UNIVERSITÀ DEGLI STUDI DI TRIESTE

UNIVERSITÀ DEGLI STUDI DI TRIESTE

XXXVIII CICLO DEL DOTTORATO DI RICERCA IN FISICA

HERMES Pathfinder and SpIRIT: From Technology Development to Operations, Data Analysis, and a Future Mission.

SETTORE SCIENTIFICO-DISCIPLINARE: ASTRONOMIA E ASTROFISICA

Candidato:

Giulia Baroni

Coordinatore:

Francesco Longo

Supervisor:

Fabrizio Fiore

Co-supervisor:

Francesco Longo

Anno Accademico 2024/2025

Abstract

The *High Energy Rapid Modular Ensemble of Satellites* Pathfinder (HERMES-PF) is a new mission concept involving the development of a constellation of six CubeSats in Low-Earth Orbit. The main HERMES-PF scientific goals are: to accurately and timely localize bright X-ray/soft γ-ray transients, such as Gamma-Ray Bursts (GRBs) and other high-energy transients, and to investigate, for the first time, the temporal structure of GRBs down to the microsecond scale and constrain the models for the GRB engine.

The mission consists of two projects: the *HERMES Technological Pathfinder* (HTP), funded by MIUR and ASI, which aims at demonstrating the feasibility of the project based on the first three nanosatellites; the *HERMES Scientific Pathfinder* (HSP), funded by the EU Horizon 2020 program, which includes three additional satellites for the purpose of enabling an initial GRBs localization experiment.

At the core of each scientific payload there is a hybrid Silicon Drift Detector (SDD)/GAGG:Ce scintillator based system for X-ray and γ-ray detection. For the HERMES-PF readout electronics, a low-noise, low-power application-specific integrated circuit (ASIC), called LYRA, was designed and developed.

The HERMES-PF also operates together with the Australian-Italian SpIRIT (*Space Industry Responsive Intelligent Thermal*) mission, which hosts an HERMES-like detector. SpIRIT is a 6U CubeSat developed by a consortium led by the University of Melbourne with Italian participation, supported by the Australian and Italian Space Agencies.

SpIRIT was launched on December 1, 2023, while HERMES-PF was launched on March 15, 2025, forming a seven-satellite mini-constellation in Sun-synchronous orbit.

An X-ray and γ-ray spectrometer, derived from the HERMES-PF payload, was also included in the TASTE (*Terrain Analyzer and Sample Tester Explorer*) mission study, with the goal of obtaining X-ray and γ-ray spectroscopy of the surface of Deimos, one of the moons of Mars. The mission is currently in phase B and is funded by ASI.

The thesis project focuses on the calibration and performance analysis of the HERMES-PF and SpIRIT flight units, from ground calibration activities to in-orbit commissioning. It also

includes contributions to TASTE mission studies for adapting the HERMES-PF payload to the Martian environment.

The first part of the work describes the ground integration and calibration of the last three HERMES-PF payloads, which were fully tested and calibrated at the FBK (Trento) and INAF/IAPS (Rome) clean-room facilities. Calibrations were performed with radioactive sources in a temperature range from -20 °C to +20 °C and the results of all seven payloads (HERMES-PF + SpIRIT) were consolidated into a Calibration Database (CALDB) for future in-orbit configuration and monitoring. The technical performance of each payload was evaluated and discussed.

The second part presents the commissioning of the HERMES-PF payload on-board SpIRIT, monitored in part at the University of Melbourne. Commissioning activities included verification of the payload's functionality and performance in the space environment. In-flight calibrations were performed, allowing detector thresholds to be optimized, background noise levels to be monitored, and the CALDB to be successfully verified and updated in orbit, demonstrating the scientific functionality of the payload. The first scientific observations were then acquired and analyzed.

Finally, the thesis describes the developments for the TASTE mission. The trade-off studies and modifications required to the HERMES-PF payload to meet the new scientific and technical requirements and survive in the Martian space environment are presented, with a focus on the new readout electronics and the development of a test board to verify its functionality. These results represent the first step in adapting HERMES-PF detector technology to operate in harsh space environments.

The thesis is organized as follows: Chapter 1 introduces γ-ray astronomy, with a focus on the evolution of high-energy instrumentation and Gamma-ray Bursts. Chapter 2 gives an overview of CubeSat applications for high-energy astrophysics. Chapter 3 describes the HERMES-PF mission: from technological and scientific objectives to a detailed description of the instrumentation. Chapter 4 reports the calibration campaigns on the HERMES-PF flight models, with a related discussion on the results obtained. Chapter 5 presents the SpIRIT in-orbit results. And Chapter 6 summarizes the TASTE mission, describing the proposed payload modifications.

Contents

Chapter 1

An overview of Gamma-Ray Bursts

1.1 Introduction to Gamma-ray Astronomy

The study of X-ray and γ-ray radiation has shown a violent and rapidly changing aspect of the Universe that has profoundly revolutionized modern astronomy. This is particularly true for γ-ray astronomy, which represents nearly 15 orders of magnitude in energy in the electromagnetic spectrum, covering the range $\sim 10^5$ eV–10^{15} eV.

These energetic photons provide us with a fascinating insight of our Universe under extreme conditions where the laws of physics are taken to their limits[1]. The study of this high-energy radiation involves a large field of research, interesting for many reasons: looking at the γ-ray window of the electromagnetic spectrum allows us to explore the most energetic celestial phenomena happening on very different astronomical scales.

In our Galaxy, there are different kinds of sources in which such an energetic radiation has been detected: supernova remnants, a number of pulsars, pulsar wind nebulae and microquasars. Outside the Milky Way, γ-rays have been observed from galaxies with an exceptional rate of star formation, and from ultra-relativistic jets of particles escaping supermassive black holes located in the center of some galaxies. In addition, the γ-ray sky is populated by extremely energetic transient events called *Gamma-Ray Bursts* (GRBs) [2]. The low probability of interaction with matter that characterizes γ-rays means that, by studying this radiation, it is possible to observe, with relative ease, sources at a considerable distance from us. In particular, γ-ray photons travel in straight lines, enabling an accurate determination of their origin. Finally, the γ-ray emission is seen not only from localized sources, but also from diffuse regions in our Galaxy and beyond.

In Figure 1.1 the Fermi/LAT five years image shows the entire sky at energies higher than 1 GeV.

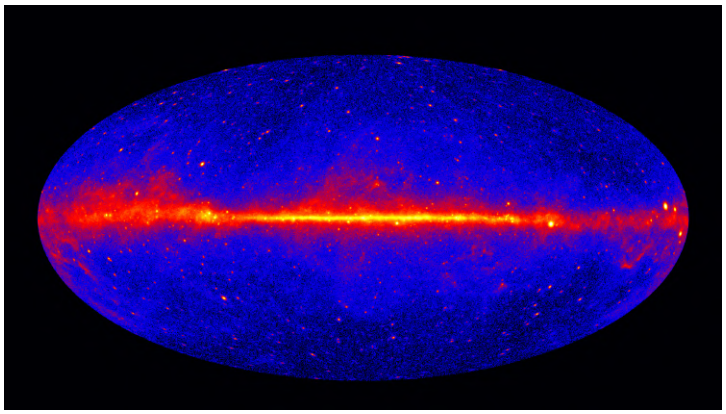

Figure 1.1: The Fermi/LAT five years image showing the entire sky at energies higher than 1 GeV. Brighter colors indicate brighter γ-ray sources. The most prominent feature is the bright band of diffuse glow along the map center, which marks the central plane of our Milky Way galaxy. Credit: NASA/DOE/Fermi LAT Collaboration.

However, this is not the end of the story: the Universe is observed not only through the different windows of the electromagnetic spectrum, but also through other cosmic messengers, i.e. via Cosmic Rays (CRs), neutrinos and Gravitational Waves (GWs) and γ-ray are the perfect companion for multi-messenger astronomy [3]. These reasons have led to the widespread interest in γ-ray astronomy in recent decades. Gamma-ray astronomy could also give new insights on cosmology (through the measurement of infrared background or by studying primordial black holes) and to particle physics beyond the Standard Model (evidence of supersymmetric particles or dark matter). The number of present and planned experiments demonstrates the continuing growing interest of the scientific community in this field.

1.1.1 The evolution of high-energy instruments

Because of the wide energy range covered by γ-rays, no single technique or instrument can cover it entirely. The Earth's atmosphere blocks γ-rays from reaching the ground, therefore, their direct detection requires space-based instruments. At higher energies, the sensitivity of space-based detectors is insufficient, so a ground-based technique is required [4]. As a consequence, there are two types of γ-ray instruments: *space-based*, that work at low energies between 100 keVs to 100 GeV, where γ-rays are mostly absorbed by the Earth's atmosphere, and *ground-based* detectors, that work typically with energies above 100 GeV and and are therefore complementary to the former ones. Here the focus is on the firs category of detectors, as they are of most interest in this work. The design of a space-borne detector sensitive to

γ-rays involves several challenges both in terms of logistics in satisfying certain mass, power, and cost requirements, and regarding the constraints characterizing the launch and operation of the instrument in the space environment. The most important design problem, however, is finding an efficient way to deal with the intense charged particle environment experienced by any space-based instrument [5]. Thus, in addition to pursuing scientific objectives, the design must consider the complexities of space operations: noise, vibration, and acceleration to which a rocket is subjected, as well as thermal stresses and changes in performance due to temperature variations. The space radiation environment also requires radiation-resistant electronic circuits to minimize failures since repairing an instrument once it is in space is not practical [5].

History of space-based γ-ray detectors

The development of space-based γ-ray astronomy began in the late 1960s and early 1970s: the OSO-3 satellite, *Orbiting Solar Observatory* 3, a sandwich of crystal scintillators (CsI and NaI) and a Lucite Cherenkov counter, surrounded by a plastic anti-coincidence scintillator, in 1967–1968 provided the first evidence that the Milky Way was a bright source of γ-rays above 50 MeV [3]. The first significant results were obtained in 1972–73 with the SAS-2, *Small Astronomy Satellite 2*, with an on board instrumentation made of a wire spark-chamber, which revealed the Galaxy's diffuse emission and discovered the Crab and Vela nebulae and the periodic signals of their pulsars [3]. In 1975 the first satellite of the newly formed European Space Agency (ESA) was launched: COS-B [6], with a spark chamber γ-ray detector and a proportional counter mounted on the side of the γ-ray detector, which produced a catalog of 25 sources, all Galactic except one, the quasar 3C 273.

Coming to our closest times, a turning point for γ-ray astronomy was the 90's: the satellites began to be equipped with instrumentation capable of achieving much better angular resolution (typically up to $\sim 0.1^\circ$). In 1991, the United States launched the first orbiting satellite fully dedicated to γ astronomy: the *Compton Gamma-ray Observatory* (CGRO) [7]. It comprised four instruments that covered six decades of the electromagnetic spectrum, from 30 keV to 30 GeV. The *Burst And Transient Source Experiment* (BATSE) was the smallest one, consisting of eight modules. Each unit included a large flat NaI(Tl) scintillator and a smaller, thicker scintillator for spectral measurements, combined to cover an energy range from 15 keV to over 1 MeV.

The *Oriented Scintillation Spectrometer Experiment* (OSSE), with four large, collimated NaI scintillator detectors to study γ-rays within the range 60 keV–10 MeV, allowed for alternating observations of a γ-ray source and nearby background regions. The *Imaging Compton Telescope* (COMPTEL), for the detection of medium–energy γ-rays between 0.8 and 30 MeV, consisted

in two detector arrays, using a liquid scintillator as passive material and NaI crystals as active material absorbing the scattered photon.

The *Energetic Gamma Ray Experiment Telescope* (EGRET) had a tracker made of spark chamber modules and a calorimeter a block of of NaI. The entire instrument was covered by a plastic scintillator anti-coincidence dome to prevent triggering from events not associated with γ-rays. The Third EGRET catalog revealed 271 sources, among which were many Active Galactic Nuclei (AGN), inaugurating the field of extragalactic γ-ray astronomy at high energies [3].

At lower energies, in the range 100 keV–few MeV, Swift (2004) and INTEGRAL (2002) played a key role in monitoring the sky for nearly two decades (although the effective area of Swift's BAT instrument decreases significantly above $\sim$150 keV). Earlier missions, such as GRBM aboard BeppoSAX, which detected over 1000 GRBs, also contributed crucially to the study of X-ray and soft γ-ray transients [8].

The scientific objectives of the *International Gamma-ray Astrophysics Laboratory* [9] have been addressed through the use of high-resolution spectroscopy (2 keV at 1 MeV) with accurate imaging (angular resolution of 12 arcmin) and positioning of celestial sources in the soft γ-ray domain in the range 15 keV–10 MeV. Its payload consists of a spectrometer (SPI), an imager (IBIS) differently optimized to complement each other. These are supported by two monitor instruments that provide complementary observations in the X and optical energy bands: the Joint European X-ray monitor (JEM-X) and the Optical Monitoring Camera (OMC).

SPI, IBIS and JEM-X share a common principle of operation: they are all coded-mask telescopes. A coded mask basically consists of a position-sensitive detection plane (PSD) and a mask model placed at a certain distance above it. By exploiting the pinhole camera principle, a point source in a large field of view casts a mask shadow on the sensing plane.

In November 2004, the *Swift Gamma Ray Burst Explorer* [10] was launched with three on board instruments: the Burst Alert Telescope (BAT), a large field of view telescope capable of observing a huge section of the sky in the energy interval between 15 and 150 keV, the X-ray Telescope (XRT) sensitive in the energy band between 0.2 and 10 keV, and an Ultraviolet/Optical Telescope (UVOT).

Swift is still operational, while INTEGRAL concluded its scientific operations on February 28, 2025 [11].

In high-energy γ-ray astrophysics, the two main missions are Fermi, launched in 2008, and its entirely Italian precursor AGILE, launched in 2007.

Space telescopes sensitive to γ-rays above a few MeVs detect photons through their interaction products, since they cannot be focused. As a consequence, usually to measure the direction of

incoming γ-rays and their energy two subdetectors are required: a *tracker* and a *calorimeter*. In addition, an anti-coincidence detector is critical to reject background due to cosmic-rays.

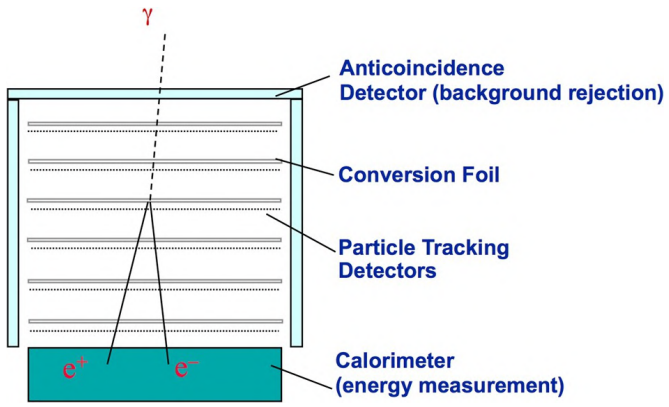

Figure 1.2: Generic tracker based γ-ray detector showing the transformation of an incident γ-ray into an electron-positron pairs by tracker conversion foils [5]. The particles are tracked through the instrument, allowing the original direction of the γ-ray to be reconstructed, and deposit their energy in the calorimeter, which measures the energy of the γ-ray.

In Figure 1.2 we can see a sketch of this structure: the tracker detects the electron-positron pair created in the conversion of photons on the converter plates, being able to measure the deposited energy and the position of each interaction, allowing to determine the direction of arrival of the γ-ray. The calorimeter is a device that measures the energy of the secondary particles. The anti-coincidence system is the first instrument a particle encounters when it makes contact with the satellite and is formed by a shielding scintillator that surrounds the main detector. It is used to reject charged particles, background like cosmic rays, that consist mainly of protons and heavier nuclei.

The *Astrorivelatore Gamma ad Immagini Leggero* [12] is the first of a new generation of high-energy space missions based on solid-state silicon technology combining for the first time two sophisticated co-axial instruments, a γ-ray detector and a hard X-ray detector.

The first one, the *Gamma-Ray Imaging Detector* (GRID), covers a range between 30 MeV and 50 GeV, while *SuperAGILE*, the hard X-ray imager, operates in the 18–60 keV energy band. The instrument is completed by a Mini-Calorimeter and by an anti-coincidence system. The very large field of view of the γ-ray imager coupled with the hard X-ray tracking capability makes AGILE suitable for studying galactic and extragalactic sources, as well as GRBs and other fast transients. AGILE re-entered the atmosphere on February 14, 2024, bringing its intense activity to an end [13].

The *Fermi* observatory [14] was launched in 2008 and is still operational. The main instrument on board is the *Large Area Telescope* (LAT), a high-energy γ-ray imaging telescope covering the energy range from 20 MeV to about 300 GeV and above, with a tracker, an ACD and a

calorimeter and a field of view covering about 20% of the sky. The *Gamma-ray Burst Monitor* (GBM) is the other Fermi instrument, consisting of two sets of detectors: twelve NaI scintillators and two BGO scintillators, and complements the LAT observations of transient sources.

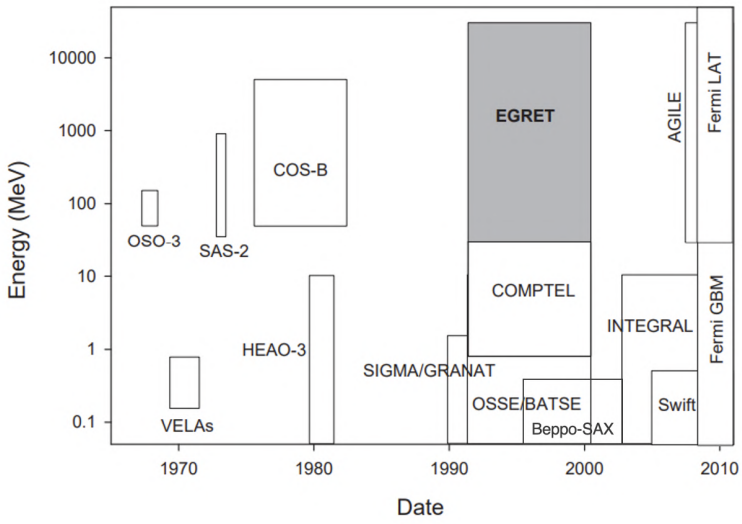

Figure 1.3: Some of the γ-ray space missions mentioned in the text, showing the energy coverage and time of each mission adapted from [15].

In Figure 1.3 some of the γ-ray space missions mentioned showing the energy coverage and time of each mission. For space telescopes that detect γ-rays in the energetic range between 100 keV and tens of MeV there is a lack of high resolution and high sensitivity observations [16]. The most sensitive observations to date have been obtained by COMPTEL with an energy resolution of 8.8% FWHM at 1.27 MeV, quite modest performance when compared to the improvements achieved today in the other energy bands, and SPI, the spectrometer on INTEGRAL, which has been taking data since 2002, but with a worse sensitivity and field of view than COMPTEL. This lack is mainly due to the difficulty of observations in this energy band: photons, because of their small cross section to interact with matter, interact mainly through Compton scattering, which makes it difficult to reconstruct the direction of the incoming photon.

Several large-scale missions dedicated to MeV γ-rays, such as newASTROGAM [17] and AMEGO-X [18] have been proposed, but most of them are still in the design or conceptual phase, with launches not expected until the next decade [19]. In this context, ASTENA is another mission concept proposed in response to the ESA Voyage 2050 call [20, 21].
Among NASA's Small Explorer missions there is COSI, scheduled for launch in 2027, which will operate in the 0.2–5 MeV band [22].
At the same time, there has been a significant increase in projects based on CubeSats, which provide economical and rapidly deployable platforms. A CubeSat dedicated to MeV γ-rays

could therefore serve as a key demonstrator for both technological and scientific objectives, providing useful information for the design and construction of future large-scale MeV observatories [19].

1.2 Gamma Ray Bursts

Gamma-Ray Bursts are transient sources and are the most energetic bursting events in the Universe, releasing energies up to 10^{53-54} erg and can last from a fraction of seconds to several hours [23]. GRBs are the result of at least two very different types of stellar death. They can occur as a result of the merger of two compact objects or from the collapse of massive stars.
They are absolutely random in their occurrence on the sky and it is impossible to predict when and where they originate. The rate observed across the entire sky depends on the sensitivity of the detector: for instruments like BATSE it's typically 2-3 events per day. The variable emission of radiation that lasts for tens of seconds is called *prompt* emission, whose rapid variability imposes constraints on the size of the emission source. The next phase is called *afterglow*: a long-lasting multi-wavelength emission produced by the interaction of the relativistic jet with the surrounding medium. It can persist for days or even months, depending on the energy band observed. GRBs are brief and bright and can eclipse other γ-rays sources, during their short lifetimes. This makes them easy to detect with small omnidirectional detectors outside the atmosphere.
They were accidentally discovered in 1967 by the Vela satellite network, a group of American military satellites [10], which was used to monitor possible nuclear explosions outside and inside the Earth atmosphere and announced to the public in 1973 as an astronomical phenomenon. A turning point came with BATSE aboard CGRO, which, during 9 years of activity, obtained positions for more than 2700 GRBs [10] by identifying their isotropic angular distribution, an early clue to their extragalactic nature. However, BATSE was unable to position them with sufficient precision in the sky to allow follow-up observations at other wavelengths.
This was later confirmed by the *BeppoSAX* satellite [24], launched in 1996, which made it possible to locate and detect GRBs. It covered an energy range from 0.1–300 keV, with four Narrow field Instruments (NFI), two Wide Field Cameras (WFCs), sensitive in the 2–30 keV band, which observed the region where the GRB came from, and the Gamma-Ray Burst Monitor (GRBM), operating in the 40–700 keV range. It made possible to detect for the first time the long-lived *afterglow* [25], which fades with time, i.e., a fainter emission that accompanies the immediate emission that lasts up to days and moving from the X-ray to the infrared band. This has made it possible to measure some GRBs that directly prove their extragalactic origin: once the GRB was detected in the γ band, the satellite first analyzed its X-ray emission and

then sent an alert signal, so that the optical telescopes could be pointed toward the source with an accuracy of several arcseconds and the optical afterglow could be observed from the ground. The optical follow-up allowed the host galaxy to be identified and the redshift to be tracked, confirming the extragalactic origin of these phenomena.

After these first results, several satellites were designed to study these energetic objects: one of the most important is Swift (see Section 1.1.1) which opened a new era for the study and understanding of the GRB phenomenon. The BAT instrument continuously monitors a large area of the sky and, after detecting a GRB, calculates its position within about 10 seconds. Then Swift quickly re-points itself, aiming XRT and UVOT towards the source, starting observations, thanks also to ground observers and other satellites to which the GRB coordinates are immediately sent. This has allowed us to obtain a large number of GRBs with redshift measurements, discovering GRBs at high redshift, like GRB 090423 at $z \sim 8.1$ [26]. Also Fermi plays an important role: GBM observes about 250 GRBs per year [14], while LAT detect ~ 10 GRBs per year above 100 MeV [27].

Therefore, one of the primary mission objectives of several current satellites is to rapidly detect and optionally localize GRBs, and rapidly transmit this information on ground to alert other satellites and ground observers for a refined localization through triangulation of the signal observed by different instruments, and follow-up observations at other wavelengths. Based on this principle, there is the *InterPlanetary Network* [28](IPN), a project operating since 1976 that combines data from existing γ-ray detectors on multiple spacecraft to provide GRB localizations through cross-correlation of light curves. Localization accuracy is proportional to spacecraft distances, and can be improved by increasing detector spacing and more accurate receiver timing. In this way, it is possible to observe a GRB at several wavelengths. A disadvantage of the IPN method is the delay in acquiring data from all spacecraft up to about 1 day. Despite this, many GRB positions were determined quickly enough to allow identification of their counterparts so that redshift measurements and other observations could be made [28].

1.2.1 Temporal and Spectral Properties

Only a limited number of GRBs have similar properties, while most bursts differ significantly, making it difficult to summarize their fundamental characteristics. The time profile may have several peaks or spikes or may simply be without a fine structure [10]. The distribution of burst durations shows a bimodal pattern [29], which is why they are divided into two classes: short and long. The former are pulses lasting <2 seconds, while the longest >2 seconds (see 1.2.1). There is a correlation between variability and brightness: the brighter the GRBs are, the more variable they are. Hence, what characterizes the morphology of the light curves is a

great diversity: except for a few cases of random similarity, each GRB seems to have its own signature. The variability observed in the prompt emission of GRBs provides constraints on the size of the emission source: the typical minimum timescales of variability are of the order of ∼10 ms (with only rare cases reaching ∼1 ms)[30], implying a compact central engine with a characteristic size of $\sim 10^6$–10^7 cm. However, this scale does not correspond to the size of the γ-ray emitting region. Due to the relativistic expansion of the outflow, with typical bulk Lorentz factors $\Gamma \gg 100$, γ-ray emission is expected to originate at much larger radii, of the order of $\sim 10^{13}$–10^{14} cm, consistent with photosphere and internal shock models [30].
An other important aspect is that GRBs do not repeat: they are one-time events, since the progenitor system undergoes an irreversible transformation that prevents repetition on observable timescales.
The energy spectrum of a burst have a spectral energy peak often on the order of hundred of keV. Thus, most of all of the energy produced is emitted in the X-ray and γ-ray regime: they emit most of their power at photon energies of tens to hundreds of keV, while some have been detected at energies of GeV.
In the near half century since the announcement of their discovery, GRBs have moved from a niche question to the astrophysical mainstream and are one of very few classes of sources to be identified from the very high-energy γ-ray to the low frequency radio regimes [23]. As previously mentioned, the emission occurs in two stages: the prompt emission and the afterglow.

Prompt Emission

Prompt emission is the first emission phase of a GRB, the brightest and shortest in duration. It is typically observed in the 10 keV–1 MeV range with a duration from 0.1 s up to a few hundred seconds ($\sim 10^3$s), characterized by a non-thermal spectrum which varies from one GRB to another. Operationally, it is defined as the period of time during which the γ-ray detector detects a signal above the background.
Prompt GRB spectra are often fitted by a phenomenological broken power-law function known as the Band function [31]:

$$N(E) = \begin{cases} A \left(\frac{E}{100\,\mathrm{keV}}\right)^{\alpha} e^{-\frac{E}{E_0}} & E < (\alpha - \beta)\, E_0 \\ A \left(\frac{(\alpha-\beta)E_0}{100\,\mathrm{keV}}\right)^{\alpha-\beta} e^{\beta-\alpha} \left(\frac{E}{100\,\mathrm{keV}}\right)^{\beta} & E \geq (\alpha - \beta) E_0 \end{cases} \tag{1.1}$$

where E_0 is the break energy of the spectrum, A is the normalization factor, α the low-energy photon spectral index, β the high-energy photon spectral index. Although this is the main component of the spectra, some GRBs show an additional (quasi) thermal component and/or a high energy power-law component is necessary to explain the spectral data [32].

There is no definitive explanation for how physical mechanisms can generate the spectral components observed in the emission, so various models have been developed to interpret the emission processes involved.
The Band component, which spans several orders of magnitude in terms of energy, clearly indicates a non-thermal origin. Relativistic electrons accelerated by internal shocks or magnetic dissipation are expected to radiate mainly via synchrotron emission [33]. However, discrepancies have been found between the observed keV-MeV spectral slopes and those predicted by simple synchrotron models. Recent studies suggest that synchrotron radiation in a moderately fast cooling regime could explain the observed spectra [32]. On the other hand, the presence of a blackbody or quasi-thermal component indicates emission from the photosphere of the relativistic flux, where photons decouple from matter after multiple Compton scatterings. This thermal emission had already been predicted in one of the first models developed to describe the central engine: the fireball model, described in Section 1.2.2.

Most of the prompt emission is highly variable, showing 100% flux variation on a time scale much shorter than the overall duration of the burst. The prompt emission has, generally, an irregular course whose structure can often be broken down into many pulses. The shape of the pulses varies significantly and randomly as shown in Figure 1.4, while their duration follows a bi-modal distribution as shown in Figure 1.5.
The most commonly used measure of duration is T_{90}, defined as the time in which 90% of the GRB counts arrive.
A classification based on their duration can be introduced. Kouveliotou et al. in [29] showed that GRBs can be divided into two distinct groups: *long bursts* with $T_{90} > 2$ s and *short bursts* with $T_{90} < 2$ s. These two classes also have different spectral hardness ratios (HR), i.e., the ratio of photons observed in the hard (100–300 keV) and soft (50–100 keV) energy band.
The hardness ratio reflects either the count rate, or the energy contained in one band, relative to another and represents a characteristic that emerges from the analysis of spectral properties of the different populations:short bursts are mainly harder emitting more high-energy radiation, while long bursts are softer, with comparatively lower high-energy emission.
Long GRBs are characterized by wide variety of temporal structures. While some exhibit short-lived pulses consisting of consecutive “single spikes” separated by quiet intervals, most long bursts have simpler profiles, such as shapes that rise rapidly and decay exponentially, or light curves with only a few distinct pulses. This behavior reflects the intrinsic diversity of their light curves [34].
They show substantial evidences for different origins. The host galaxies of long GRBs are predominantly irregular and star-forming, with a few being spiral galaxies with active star

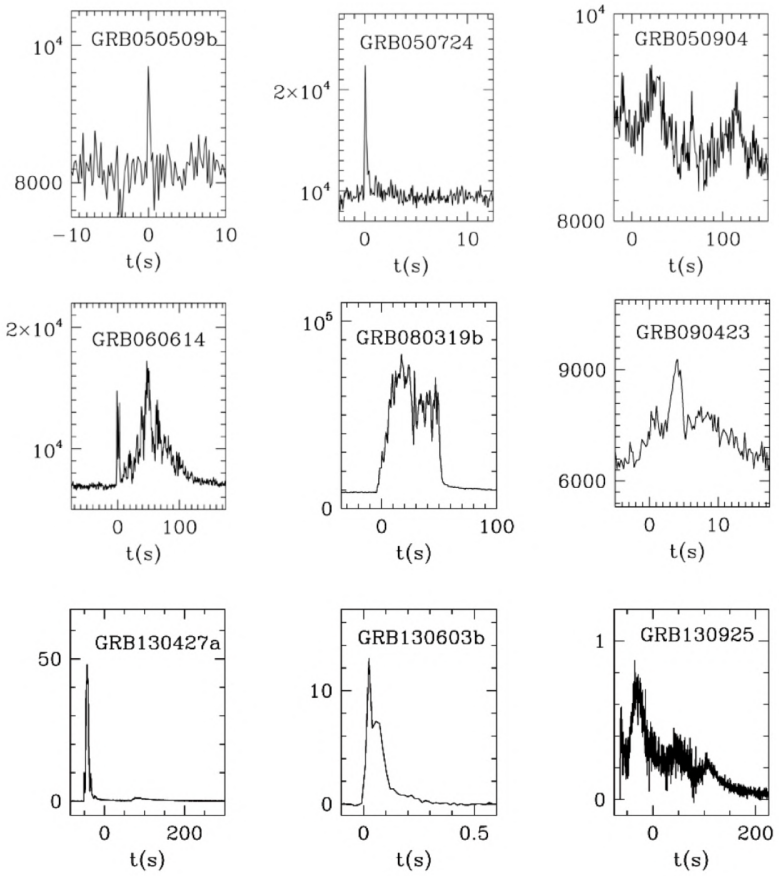

Figure 1.4: A selection of the wide variety of temporal profiles of GRBs, as detected by Swift-BAT. Note the wide range of durations and morphologies of the bursts, highlighting the diversity of the prompt GRB emission [23].

formation [32], therefore they are the endpoints in the lives of massive stars and their rate is roughly proportional to the star formation rate of the host galaxy. Within the host galaxy, they are preferentially located in the brighter central regions. Since long GRBs originate from the collapse of massive stars and occur in regions of active star formation, they are expected to be associated with supernovae, specifically of type Ic [35].

In contrast, a significant fraction of the host galaxies of short GRBs are quiescent, with little or no star formation, however, the majority are actively star-forming galaxies[36]. They often occur several kiloparsecs away from their host galaxies, with locations only weakly correlated with the stellar light distributions of their hosts [36]. Short GRBs are typically less energetic (their isotropic equivalent energy is of the order of 10^{49}–10^{51} erg) than long GRBs and occur at lower redshift.

The main difference between long and short GRBs is in their progenitor systems and collapse processes. Short GRBs originate from the merger of compact binaries, which involves three

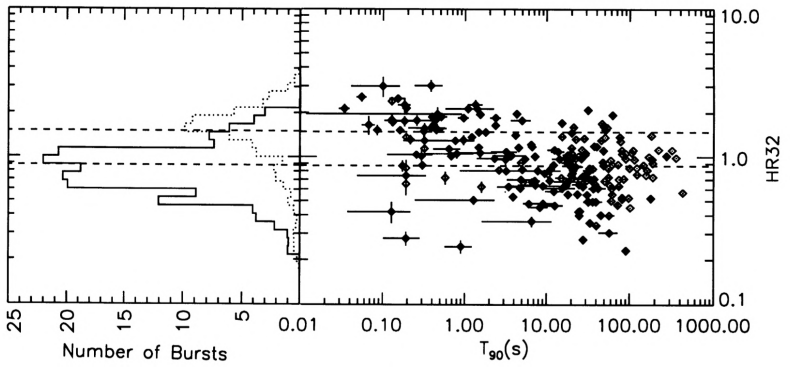

Figure 1.5: GRB classification into short and long according to their T_{90} and BATSE HR [29]. The solid line shows the long GRBs ($T_{90} > 2$ s) and the dashed line the short GRBs ($T_{90} < 2$s). The dashed lines correspond to the average HR of the two classes of GRBs.

phases: spiraling, merger, and the formation of an accretion disk capable of launching a relativistic jet. Long GRBs, on the other hand, result from the collapse of the core of a massive star. During this collapse, the non-spherical symmetry allows the formation of an accretion disk around the newly formed black hole, which feeds a relativistic jet.

To get a long GRBs is necessary but not sufficient having a massive BH. It is also necessary that the accretion disk is in non-spherical collapse: in a binary system, the interaction of the pair can cause the star that then explodes as a SN to acquire a very high rotational velocity, and as a result the collapse will not be perfectly spherical. A moment before the explosion can be created the binomial BH - accretion disk and the jet starts, it lasts very little but it is very energetic.

Afterglow Emission

The afterglow emission, i.e. the phase that follows the prompt, was identified firstly in 1997 by BeppoSAX (1.2), and consists of a considerably longer emission with energies ranging from X-ray then optical, IR and finally radio and can last from days to months [10].

Afterglows are necessary for locating GRBs, measuring their redshift and thus defining their energy, identifying the galaxies that host them and detecting the nascent supernovae or kilonovae[1] that locate the progenitors of long and short GRBs. Any model of the afterglow is defined by two parts: a hydrodynamic description of the deceleration of the relativistic ejecta of the burst by the circumstellar medium and an identification of the radiative processes at work [37]. The afterglow is believed to originate in the external shock produced by the shock wave of the explosion colliding with and sweeping away material in the surrounding interstellar medium.

[1]Transient events due to the merger of two neutron stars (or a neutron star and a black hole), which produce three observable phenomena: a gravitational wave signal; a short γ-ray burst and heavy elements.

Its temporal structure changes depending on the spectral band. The origin of the spectrum is also non-thermal and the emission is well described by synchrotron emission, as expected by the *standard shock model*. The emission at progressively lower wavelengths (X-ray, optical, radio) are due to the expanding shock wave that sweeps away more and more material, making it slow down and lose energy.

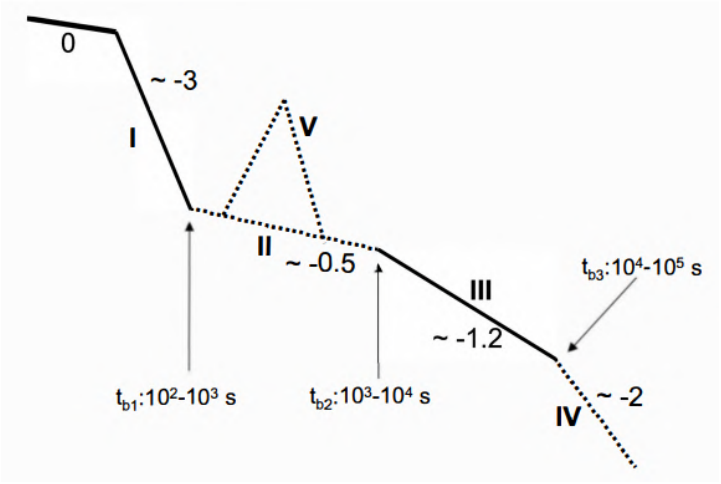

Figure 1.6: A schematic illustration of the X-ray afterglow light curve based on the observations of the Swift XRT. The phase "0" denotes the prompt emission, "I" is the rapid decay phase, "II" the shallow decay phase or plateau, "III" the normal decay, "IV" the post jet-break phase and "V" the flaring phase. Typical temporal indices in the four main steps are also indicated [32].

As shown in Fig. 1.6, typical X-ray light curves can be summarized into five components, namely a distinct component of rapid decay (I), a shallow decay component (II), a normal decay component (III), a jet breaking component (IV) and X-ray flares (V).
The main characteristics of each of these component are listed [38, 32]:

I *Steep decay phase* behaves as the "tail" of the prompt emission and the decay slope is typically in the range of ~ 3 to ~ 10;

II *Shallow decay phase* has a typical slope is in the range between 0 and $\sim$0.7. If the slope of the shallow decay component is close to 0, it is also called a plateau. This phase begin at $\sim$100-1000 s after the trigger, lasting until 10^4 s;

III *Normal decay* usually follows the shallow decay component, or sometimes directly follows the II component. It has a decay slope of $\sim$1.

IV *Post jet break phase* often follows the normal decay segment, as is also expected in the external shock model;

V *X-ray flares* are "superimposed" on the background power-law decay components hence considered to be of different origin. Their light curves typically show rapid rises and falls with steep indices. Many properties of X-ray flares, both in the time and spectral domains, are similar to those of prompt emission, suggesting that that they could be directly powered by the central GRB engine.

Compared with the X-ray afterglow, the optical afterglow exhibits more complicated behavior. The optical light curve can also consist of shallow decay, normal decay, and jet-break phases. To understand both prompt emission and afterglow, the fireball model is used, which provides a consistent description of the different emission phases observed in GRBs.

1.2.2 The fireball shock model

The isotropic energy involved in GRBs can reach the order of 10^{54} erg. This high amount of energy, combined with the short variability observed in prompt emission, which implies a compact central engine, leads to extreme energy densities, which limit the physical processes plausible for the creation of GRBs.
This huge energy within a very small volume implies the formation of a e^+, e^-, γ fireball [10]. Standardizing the countless aspects of GRBs emission under a common theory is not easy: the numerous observations of GRBs and of their afterglows constrain the *fireball model* [39], shown in Figure 1.7, that describes the emitting regions.

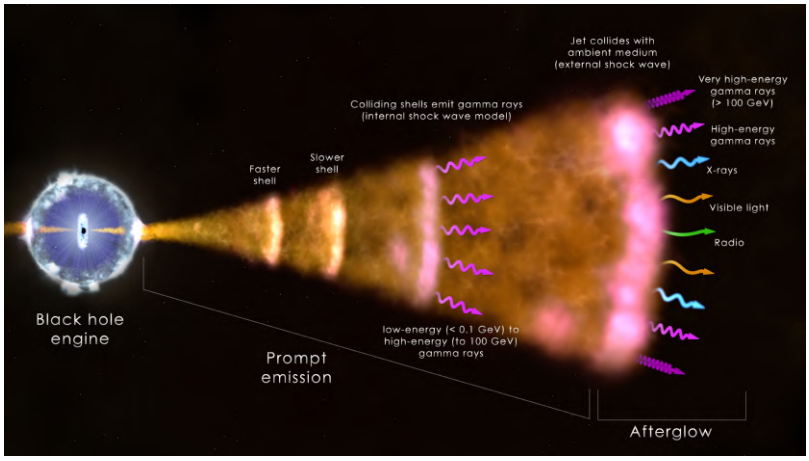

Figure 1.7: Illustration of the fireball model [40].

The GRB is produced by a central engine that releases a large amount of energy in a very compact region, generating an ultra-relativistic outflow that expands to increasingly larger radii. If the engine remains active for a finite time, it can eject multiple shells with different Lorentz factors.

Initially, the internal energy of the outflow is converted into kinetic energy during an acceleration phase, allowing the shells to reach Lorentz factors, typically of the order of $\Gamma \sim 10^2$–10^3. After this acceleration phase, the outflow enters the coasting regime in which the Lorentz factor remains approximately constant with radius [41].

The ejected shells do not all propagate at the same speed: a faster shell that follows a slower one will surpass it, and the interaction will produce a shock that transfers energy to the particles and the magnetic field. The accelerated particles emit non-thermal radiation, mainly through synchrotron emission and, in some cases, inverse Compton scattering, giving rise to the observed emission of γ-rays.

There is γ-ray emission every interaction between the shells, and since this occurs randomly, all the GRBs are different from each other.

In summary, the fireball model can be divided into several phases:

Fireball phase: a central engine provides the energy to convert into kinetic energy and generate the subsequent shocks;

Prompt phase: the energy is transferred to the particles and the magnetic field and conditions are generated to have the γ-ray flashes. This is an "internal" mechanism in which the shells ejected from the central engine collide with each other. Their interaction leads to the formation of shock waves: a forward shock propagating into the slower shell and a reverse shock that propagates backward in the rest frame of the fast shell and is responsible for its deceleration. The electrons accelerated in these shocks emit synchrotron radiation in the presence of magnetic fields. Each shock produces its own emission, and the resulting prompt emission (spectrum and variability) is the addition of simultaneous emission from multiple shocks;

Afterglow phase: as the relativistic outflow propagates outward, it begins to interact with the interstellar medium. The interaction gives rise to external shocks, in which the total kinetic energy of the flow is progressively transferred to the surrounding medium, accelerating it. For these reasons, the afterglow phase is called "external" phase. The afterglow follows a distribution in energy that decreases with time in both frequency and energy: $F(E,t) \sim t^{-\alpha}\nu^{-\beta}$ [42], passing from X-ray , then optical and finally radio frequencies.

Therefore, as the speed decreases for the braking action of the external medium, the emission is at gradually lower frequencies. Particles scattered across the shock interface will be accelerated at a relativistic velocity, leading to non-thermal synchrotron radiation and IC, meanwhile the outflow continues to expand outward, gradually slowing down due to its interaction with the external medium.

1.2.3 Multimessenger Astronomy

One of the most interesting aspects of studying Gamma-ray bursts is that their extreme progenitor systems represent the most natural places for the production of additional astrophysical messengers. These "non-photon" signals include very high-energy cosmic rays, neutrinos, and gravitational waves [23]. The combined observation of these different messengers constitutes Multi-messenger astronomy, which offers a unique opportunity to understand the behavior of the most extreme astrophysical systems. Gamma-ray bursts arise from some of the most extreme conditions in nature, and thus their progenitors are among the most likely sources of multi-messenger signals [23]. Here, the focus is on the relationships to GRBs as multi-messenger sources.

Gravitational Waves

Gravitational Waves are ripples in space-time, produced from accelerating, non-spherically symmetric systems. They can be associated with GRBs, particularly short GRBs, presumably the result of coalescence of two compact objects (BH+NS, NS+NS). The mergers of compact objects have, in fact, been studied as potential sources of GWs. The crucial breakthrough for multimessenger astronomy occurred in August 2017, when Fermi and INTEGRAL detected a short-lived GRB about two seconds after LIGO (Laser Interferometer Gravitational Wave Observatory) and VIRGO observed the first merger of a binary system of neutron stars [23, 43]. This became increasingly clear as location information became available. The event is shown in Figure 1.8. The position triangulated by the two LIGO detectors and by VIRGO was in agreement with that of Fermi, and INTEGRAL enabled a refined electromagnetic position.

Since short-lived GRBs are rare, the connection between the two based on timing alone was very suggestive.
Since GRBs are bright and easily identifiable in the sky, monitoring programs such as Swift and Fermi, which cover the entire sky or smaller, deeper areas, offer promising opportunities to detect GW counterparts.
Being rare events, with detection rates of only a few per week, their frequency is sufficiently low that the coincident detection of a GRB and a GW trigger within seconds of each other has a low probability. This means that the association of a GRB with a GW transient, can occur via temporal information alone even in the absence of any positional information. This is extremely interesting. Indeed, the error boxes derived from these γ-ray detectors can often be much smaller than those obtained from the GW event alone, providing a much easier search for afterglows or host galaxies.

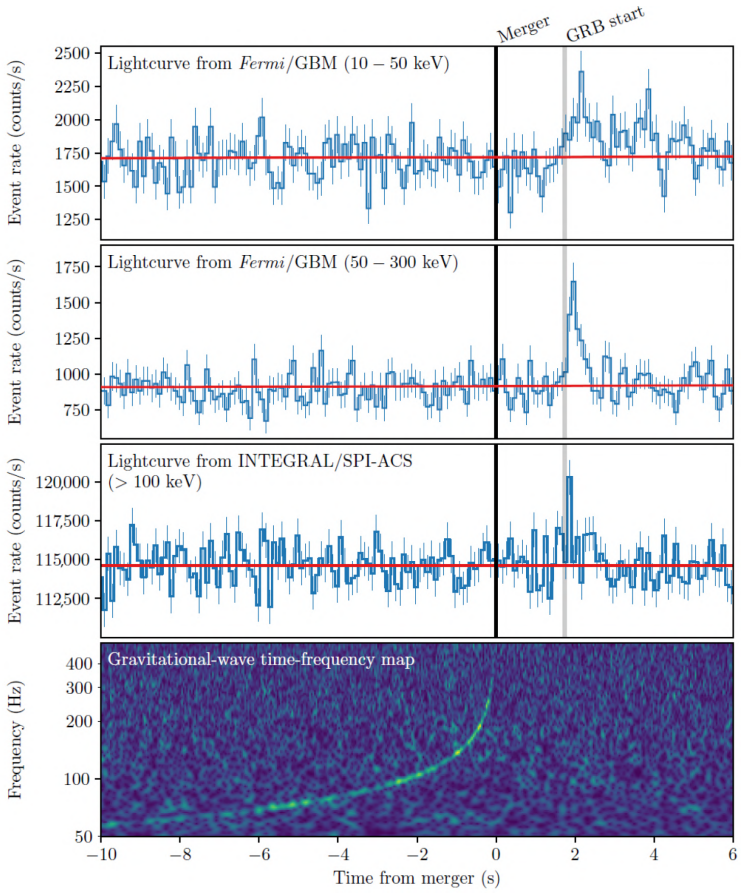

Figure 1.8: The detection of GW170817 and GRB170817A [44]. The bottom panel shows the frequency of the gravitational wave signal plotted against the time from the merger. The top panel shows the γ-ray light curves recorded by Fermi (in two different energy bands) and Integral. The GRB occurred within about 2 seconds from the merger [23].

Finally, the precise timing of GRBs also narrows the window for searching for GW, lowering the associated background. This means that even in the absence of a gravitational wave trigger, the data stream can be analyzed only around the time of the GRBs, increasing the effective sensitivity (and hence distance) by a factor of ~ 2.

The detection of a GW signal coincident with a GRB is a very exciting discovery. The fact that GW is emitted in close proximity to the central engine provides direct evidence of the progenitor, its nature, and its mass distribution. The main facilities are now in operation for the detection of GW: in this way, the operation of an efficient all-sky X-ray and γ-ray monitor with good localization capabilities will play a key role in bringing multi-messenger astrophysics to maturity, and to fully exploit the enormous benefits of adding an additional dimension to our ability to study cosmic sources [45].

1.2.4 Current and Future Perspectives

The joint detection of GW170817 and GRB170817A demonstrated the power of multi-messenger astrophysics and highlighted the need for a new generation of instruments capable of observing the Universe simultaneously in Gravitational Waves, X-rays, γ-rays and high-energy neutrinos. Indeed, over the past 50 years, GRBs have driven the development of cutting-edge technologies for high-energy astrophysics, leading to the launch and success of numerous space missions dedicated to studying these phenomena[46]. Based on these legacy, several space missions are currently underway or in development, with the aim of expanding our ability to detect and locate transient phenomena across multiple messengers.

Among recent space missions dedicated to X-rays and γ-rays, SVOM, *Space-based multi-band astronomical Variable Objects Monitor*, (a joint Chinese-French project) was launched on June 22, 2024. The payload includes a γ-ray monitor, GRM (15 keV-5 MeV), the ECLAIRs X-ray imager and trigger (4-150 keV), the MXT lobster-eye telescope (0.2-10 keV), and an optical telescope [47, 48]. Therefore, ECLAIRs and GRM perform GRB prompt observations, while MXT and VT are dedicated to follow-up observations in the X-ray and optical energy bands, respectively.

Another important future mission is THESEUS [49] (*Transient High-Energy Sky and Early Universe Surveyor)*; already studied by ESA in 2018-2021 as an M5 candidate mission, it was selected again for a Phase A study in the framework of the ESA M7 call. If selected, its launch is scheduled for 2035. THESEUS is designed to study the early Universe by detecting high-redshift GRBs and enable the identification of electromagnetic counterparts of gravitational wave sources, which are expected to become increasingly common with the commissioning of new detection facilities. The mission will carry three main instruments: a Soft X-ray Imager (SXI, 0.3–5 keV) based on a lobster eye focusing system, an X-ray and γ-ray imaging spectrometer (XGIS, 2 keV–10 MeV) for GRB detection and localization, and a 70 cm infrared telescope (IRT, 0.7.–1.8 µm) with both imaging and spectroscopic capabilities to identify the infrared counterparts of GRBs and measure their redshift [48].

In parallel with these large missions, continuous advances in compact low-power detectors, readout electronics, and flight computers have opened up new opportunities for X-ray and γ-ray detection using CubeSat platforms [50]. This type of missions are therefore able to bridge the gap between satellites launched in the 2000s and already been operational for more than 10 years, and their successors, since they require a much shorter development time scale, a minor cost and have less overall complexity. γ-ray detection CubeSats are expected to play an increasingly important role in the new era of time-domain and multi-messenger astronomy, making an increasingly significant contribution to the detection and localization of Gamma-Ray

Bursts (GRBs). This aspect will be discussed in more detail in Chapter 2.

An example of this type of mission is HERMES-PF (*High Energy Rapid Modular Ensemble of Satellites*) Pathfinder, a constellation of six CubeSats designed to detect and localize high-energy transients such as GRBs. Each satellite is equipped with a compact detector capable of measuring X-ray and γ-ray photons with high temporal precision. The mission is described in detail in Chapter 3.

Chapter 2

CubeSats for High Energy Astrophysics

A *nanosatellite* is defined as any satellite with a mass between 1 kg and 10 kg, a category that includes CubeSats [51]. The term CubeSat refers to a class of small satellites built to standardized dimensions and form factors. The basic unit, known as "1U", is a cube of 10 cm $\times$ 10 cm $\times$ 10 cm and a typical mass of up to 2 kg. A 2U CubeSat is formed by stacking two of these units, with dimensions of approximately 10 cm $\times$ 10 cm $\times$ 20 cm and a maximum mass of approximately 4 kg. Larger configurations, such as 3U, 6U, 8U, 12U, and 16U, can be created by combining multiple 1U units in a modular way [52]. To date, more than 2,000 nanosatellites have been launched, the most common being 3U CubeSats [51].

The CubeSat concept was introduced in 1999 by R. J. Twiggs at Stanford University to make satellite mission development accessible within academia [53]. This entails the need for short development times, compatible with master's and doctoral programs, and costs low enough to be accessible to universities. At that time, the high cost of launches per kilogram restricted spacecraft mass to only a few kilograms. In the following two decades, CubeSats have expanded far beyond their educational origins and are now employed extensively in commercial, scientific, and defense applications [53].

CubeSat missions offer numerous advantages in several areas. They benefit from lower production and launch costs, the possibility of sharing launch opportunities, and the miniaturization and commercialization of space-grade electronic components. The wide availability of commercial CubeSat manufacturers, combined with standardized structural and electronic designs, further facilitates development. In addition, space agencies provide financial, programmatic, and technical support, making CubeSat missions increasingly accessible. As a result, the number of CubeSats orbiting Earth has grown significantly in recent years, as shown in Figure 2.1,

a trend that is expected to continue in the coming decades.

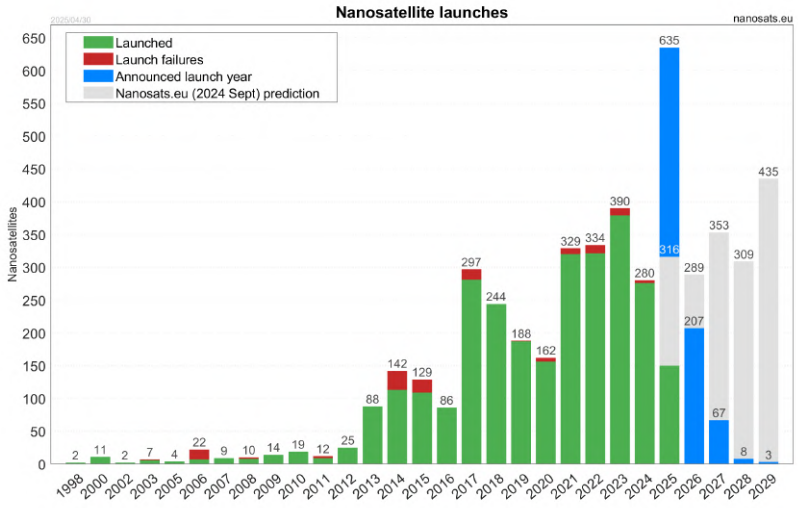

Figure 2.1: Total number of nanosatellite launches between 1998 and 2025, with forecasted launches between 2025 an 2029 [51].

The reduction in costs in current CubeSat projects can be mainly attributed to four factors [53, 52]:

- miniaturization, which leads to lower mass and smaller volumes; the miniaturization of electronic components has enabled the integration of complete satellite subsystems into compact and lightweight modules.
- hardware standardization, which is often based on Commercial Off-The-Shelf (COTS) components; today, processors, memory chips, optics, and batteries originally developed for commercial applications often satisfy the stringent quality standards of space missions. As a result, CubeSat developers can adopt COTS electronic equipment, substantially reducing costs compared to custom-designed solutions. Standardization extends to multiple aspects of CubeSat development, including structural components, electronic interfaces and communication protocols.
- lower labor costs at universities and research institutes compared to traditional space industries;
- less stringent quality control requirements. For example, ESA's In-Orbit Demonstration (IOD) CubeSat projects must comply with requirements and risk levels that are about ten times lower than other programs.

The cost of a standard CubeSat weighing approximately 5 kg varies between 0.02$ and 0.08$ million per kg, which is much lower than large missions (including bus and payloads). For

example, IXPE (330 kg) costs approximately 0.42$ million per kg [53]. Standard CubeSats are generally simple and have limited capabilities. A more interesting comparison can be made with advanced CubeSats, which are specifically designed for scientific missions. A representative example is the HERMES Pathfinder (HERMES-PF, see Chapter 3). The net cost of each HERMES-PF 3U CubeSat, including its payload, is approximately $860,000. This is 2 to 7 times higher than the cost of a standard 3U CubeSat, but still only about one-third of the cost of an Explorer-class mission [53].

2.1 CubeSats for Gamma-ray Astronomy

The relatively low cost of CubeSat-based scientific missions has expanded the space science community, encouraging participation from both academia and small and medium-sized enterprises.

Mission	Type	Objective(s)	Energy range	Status
BlackCAT [54]	6U	High-z GRBs; Transients	0.5–20 keV	Launch late 2025
BurstCUBE [55]	6U	GRBs	50 keV–1 MeV	Launch 03/2024
COMCUBE [56, 57]	6U	GRBs; Polarization	50 keV–few MeV	Study phase
COMPOL [58]	3U	Cyg X-1 Polarization	160 keV–few MeV	Launch 2026
CUSP [59]	6U	Solar Flares; Polarization	20–100 keV	Study phase
EIRSAT-1 [60]	2U	GRBs; Education; Tech Demo	30 keV–2 MeV	Launch 12/2023
GIFTS [61]	6U	GRBs	50–300 keV	In development
GRID [62]	6U	GRBs	∼10 keV–2 MeV	Launch 10/2018; 11/2020; 02/2022
GRBAlpha [63, 64]	1U	GRBs; Solar Flares	70 keV–890 keV	Launch 03/2021
GRBBeta [64]	1U	GRBs; Solar Flares	70 keV–890 keV	Launch 07/2024
GTM [65]	2×1U payloads	GRBs	50 keV–2 MeV	Launch 2026
HERMES PF [66]	7×1U payload	GRBs	5–500 keV	Launch 03/2025
IGOSat [67]	3U	γ-rays; Education	20 keV–2 MeV	Launch 2026
IMPRESS [68]	3U	Solar Flares	4–100 keV	Launch 2026
LECX [69]	2U	GRBs	30–200 keV	Launch 2025
LIGHT-1 [70]	3U	TGFs; Education	20 keV–3 MeV	Launch 12/21
MAMBO [71]	12U	Cosmic diffuse background	0.3–10 MeV	Launch 2025
MeVCube [72, 73],	6U	GRBs	200 keV–4 MeV	Launch 2025
Min-XSS1 [74]	3U	Solar Flares; Education	0.4–30 keV	Launch 12/2015
Min-XSS2 [75]	3U	Solar Flares; Education	0.4–30 keV	Launch 12/2018
SOCRATES [76]	3U	GRBs; Tech Demo; Education	200 keV–1.3 MeV	Launch 11/2019
VZLUSAT-2 [63, 64]	3U	GRBs	30–890 keV	Launch 01/2022
3UTRANSAT [77]	3×3U	GRBs	15–200 keV	Study phase

Table 2.1: Planned and operational CubeSats for high-energy astrophysics adapted from [50].

In recent years, CubeSats have increasingly been employed for astronomical observations, thanks to their modularity and low cost, which make them attractive alternatives to larger,

more expensive platforms. They have participated in numerous missions aimed at studying a variety of cosmic phenomena, including exoplanets, interstellar matter, and other astrophysical targets. The primary instruments flown on these missions include UV, visible, and infrared telescopes, X-ray and solar X-ray spectrometers, γ-ray detectors, particle detectors, and radio interferometers [52].

In this work, the emphasis is mainly on the contribution of CubeSats to γ-ray astronomy. In particular, Table 2.1, adapted from [50], lists some operational and planned CubeSat missions. The primary scientific objectives generally include the observation of transient phenomena such as GRBs, Solar Flares, and Terrestrial Gamma-ray Flashes (TGFs). In addition to their scientific role, CubeSats also provide a valuable test bed for innovative technologies in orbit, helping to increase their technology readiness level (TRL) to the point where they can be adopted in large-scale missions by major space agencies. With the advent of multi-messenger astronomy, the impact and scope of CubeSat-based research is constantly increasing [50].

The following subsections summarize just a few of the most interesting recent CubeSat missions that have contributed to high-energy astrophysics, highlighting the growing potential of CubeSats in this field.

2.1.1 GRBAlpha/VZLUSAT-2

GRBAlpha is a 1U CubeSat launched on March 22, 2021, into a Sun-Synchronous polar orbit (SSO) at an altitude of 550 km [78]. The detector on board consists of a CsI(Tl) scintillator read by eight silicon photomultipliers (SiPMs) [63]. GRBAlpha is the first 1U CubeSat to successfully detect multiple confirmed Gamma-ray Bursts (GRBs) [50]. Figure 2.2 shows an example of a light curve detected by GRBAlpha. The mission serves as a technological pathfinder for a future constellation of CAMELOT nanosatellites that will monitor and locate GRBs using a time-based cross-correlation technique [63].

GRBAlpha's detectors have also been installed on VZLUSAT-2, a 3U CubeSat built by the Czech Aerospace Research Center. The satellite was launched on January 13, 2022, into a SSO orbit at an altitude of 550 km [63]. GRBAlpha detected over 140 transients, of which approximately 81 were identified as GRBs, while VZLUSAT-2 recorded approximately 83 transients, of which approximately 44 were GRBs, confirmed by larger GRB missions [64]. These results demonstrate the potential of nanosatellites for the regular detection of these events. GRBAlpha re-entered Earth's atmosphere on June 9, 2025.

The successor to GRBAlpha, GRBBeta, was launched on July 9, 2024. It includes minor improvements to the readout electronics and new down-link capabilities that should allow sampled data to be downloaded at a much higher rate [64]. The satellite is currently operational

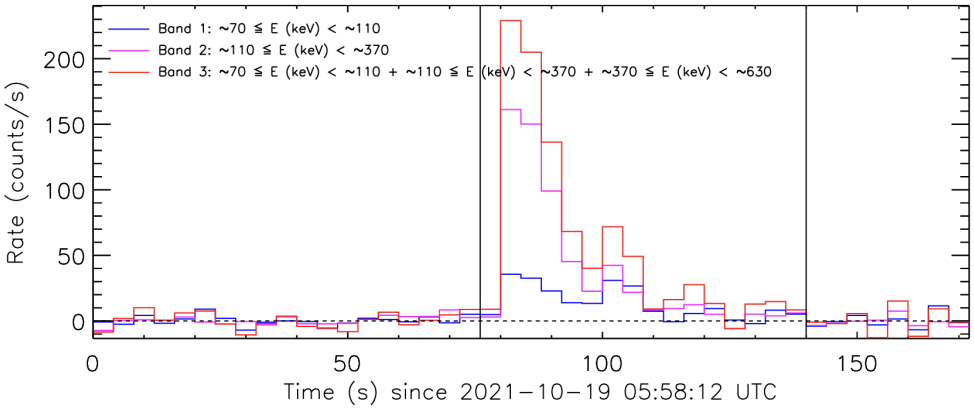

Figure 2.2: Light curve of GRB 211019A detected by GRBAlpha [79, 50].

and functioning nominally.

2.1.2 EIRSAT-1

The Educational Irish Research Satellite 1 is the Ireland's first satellite and it is supported by the second edition of the European Space Agency's (ESA) Fly Your Satellite! program [60]. It was launched on December 1, 2023, into a Sun-Synchronous orbit at an altitude of ∼520 km. It is a 2U CubeSat with three payloads on-board; GMOD, a scintillator and SiPM based detector for detecting GRBs; EMOD, a thermal materials experiment, and WBC, an attitude control and determination software test bed [80]. EIRSAT-1 detected several Gamma-ray Bursts during its mission: one example is GRB 240821B on August 21, 2024, detected by the GMOD γ-ray module and also confirmed by Fermi GBM [81]. The satellite reentered Earth's atmosphere on September 4, 2025.

2.1.3 BurstCube

BurstCube is a 6U CubeSat designed to detect GRBs and enable multimessenger observations, launched on March 21, 2024 [55]. BurstCube is funded via NASA's APRA program [50]. The instrument consists of four CsI(Tl) scintillator detectors read by SiPM arrays. BurstCube successfully detected GRB 240629A [55] and it was decommissioned on September 16, 2024.

Chapter 3

The HERMES Pathfinder mission

The *High Energy Rapid Modular Ensemble of Satellites* Pathfinder (HERMES-PF) is an in-orbit demonstration mission that aims to develop a constellation of six nanosatellites (3U CubeSats, see Chapter 2) in low Earth orbit, hosting compact and innovative X-ray and γ ray detectors. The main goal is to monitor high-energy cosmic transients, such as Gamma Ray Bursts (GRBs) and the electromagnetic counterparts of Gravitational Wave Events (GWEs) [82, 66].

	Timelines	Modules	Launch
HTP (ASI)	2017–2022	3 nanosatellites	March 15, 2025
HSP (Horizon 2020)	2018–2022	3 nanosatellites	March 15, 2025
SpIRIT (ASI-ASA-UniMelbourne)	2019–2022	1 HERMES Payload	December 1, 2023
HERMES Full Constellation	On going studies		

Table 3.1: Summary table of HERMES-PF mission steps and timelines.

The mission consists of two projects: the *HERMES Technological Pathfinder* (HTP), funded by the Ministry of Education, University and Research and the Italian Space Agency, which aims at demonstrating the feasibility of the project based on the first three nanosatellites, and the *HERMES Scientific Pathfinder* (HSP), funded by the European Union Horizon 2020 research and innovation program, which includes three additional satellites for the purpose of enabling an initial GRB localization experiment, for a total of six flight units. A HERMES-like detector is also be hosted on board the SpIRIT (*Space Industry Responsive Intelligent Thermal*) project, coordinated by the Australian Space Agency (ASA) and the University of Melbourne. The Italian participation has been approved and funded by ASI.
The HERMES-Pathfinder mini-constellation thus consists of six satellites plus SpIRIT. SpIRIT was launched on December 1, 2023, while HERMES-PF was launched on March 15, 2025 in a Sun-synchronous orbit. In October 2025, HERMES-PF is still under commissioning because of some communication issues between the spacecraft and the Ground Antennas.

The final step will be the realization of the *HERMES Full Constellation* (HFC), a network composed by tens of units, designed to continuously monitor the full sky for GRBs, GWEs, and other high-energy events. The main information and timelines for each project are summarized in Table 3.1.
Compared with the usual mission design, HERMES-PF provides a different approach, aiming to achieve a network of modular, low-cost, and small ($10\times10\times30$ cm^3) units. This strategy offers several advantages: it prevents mission failure due to the loss of one (or even more) units, if one or more units fail, the constellation and the experiment remain operational; it allows hardware to be tested during the first launches, with the possibility of improving the design in subsequent launches; it allows for a gradual deployment strategy: starting with reduced Pathfinder versions of HERMES to demonstrate feasibility, before deploying the entire constellation.

3.1 Scientific Goals

The three main scientific goals of HERMES are [45]:

1. accurate and timely localization of bright X-ray/soft γ-ray transients, such as GRBs and other high-energy transients, including the electromagnetic counterparts of GWEs;

2. investigate, for the first time, the time structure of GRBs down to microseconds, to constrain the models related to GRBs engine;

3. study the radiative mechanisms responsible for the emission of GRBs through systematic measurements in the energy range below 10 keV.

3.1.1 Transient detection and localization with HERMES

The localization strategy adopted by HERMES for the determination of the position on the celestial sphere of the GRBs is determined by measuring the delay between the arrival time of the transient signal at the different detectors. This is a well-known technique, adopted for locating GRBs since their first discovery by the VELA satellites[10] and used routinely by the InterPlanetary Network (Section 1.2). Delay times are calculated using the cross-correlation function between the light curves recorded by different detectors. The accuracy in determining the position σ_{PA} is given by the following formula [45]:

$$\sigma_{\mathrm{PA}} \approx \frac{c\sqrt{\sigma_{\mathrm{CC}}^2 + \sigma_{\mathrm{TPOS}}^2 + \sigma_{\mathrm{TIME}}^2 + \sigma_{\mathrm{sys}}^2}}{AB\sqrt{N-1-2}} \tag{3.1}$$

where σ_{CC} is the error on the cross-correlation calculated between two light curves, $\sigma_{\mathrm{TPOS}}=\sigma_{\mathrm{POS}}/\mathrm{c}$ is the error due to the uncertainty on the location of the satellite, σ_{TIME} is the uncer-

tainty on absolute time, $\sigma_{\rm sys}$ is a systematic uncertainty, AB is the Average Baseline, namely the average distance between detectors, and N is the number of detectors which detect a given event. The requirement on the localization capability, 1 arcmin or less for long and short GRBs with variability down to ∼ms and ∼1° for all short GRBs, imply that $\sigma_{\rm TPOS}$, $\sigma_{\rm TIME}$ and $\sigma_{\rm sys}$ should be smaller than a few tens μs. By including these values in Eq. 3.1 and considering a base distance between the different spacecraft similar to the Earth's radius $AB \sim R \sim 7000$ km, a simplified equation is obtained:

$$\sigma_{\rm PA} \approx \frac{2.4^{\circ} c \sqrt{\sigma_{\rm CC}^2 + \sigma_{\rm sys}^2}}{\sqrt{N-3}} \tag{3.2}$$

The magnitude of $\sigma_{\rm CC}$ depends on multiple factors: a) the temporal resolution of the detector; b) the temporal structure of the transient; c) the number of photons per temporal bin in the light-curve, which is basically given by the intensity of the transient and by the collecting area of the detector, and d) the level of the background. Experience gained from operating a small fleet of units in orbit prototype will be crucial to verify the various expected contributions.

3.1.2 The GRB inner engine

The main observational characteristics of GRBs are their enormous luminosity and rapid variability, typically on timescales of tens of milliseconds to seconds, with millisecond variability being rare [83, 84]. These characteristics led to the development of the fireball model [85] (see 1.2.2). Although successful in explaining GRBs observations, this model implies the presence of a thick photosphere, which hampers direct observations of the hidden internal engine, which accelerates the mass flow. The fast variability of GRBs offers a possibility for investigation of their internal engines. In particular, numerical simulations [86, 87] and analytical studies [88] suggest that the light curves of GRBs reproduce the activity of their internal engine. However, there are alternative interpretations, according to which the variability on a short time scale derives from dissipation processes that occur occurring at larger radii in the jet [89].
Light curves have been studied in detail as low as 1 ms or so [90], while the μs-ms window is essentially unknown, just as little is also known about the actual duration of the prompt event. We do not know how many shells are ejected by the central engine, what the ejection frequency is, and its length. This leads to the conclusion that accurate and sensitive GRB timing, including the μs/ms window, should help answer at least some of these questions [45].
One of the most important open issues in GRBs is also the composition of the jets. It is not clear yet whether the energy of the jet energy is carried out by the central engine in the form of Poynting flux (magnetic jet) or as kinetic energy of matter (baryonic jet). The two scenarios predict different variability properties which is why the detection of sub-millisecond variability

is also critical to place constraints on both models and on the composition of the jet itself [45]. Fast timing, at the level of fractions of μs, is at the heart of the HERMES concept. Once the position of the GRB has been deduced from the time delays of the signals detected by the different detectors, the same signals can be realigned in time and summed to improve the GRB statistics. The total collecting area needed to provide a few counts per 10 μs for GRBs with a photon count rate of 10 ph/s/cm^2 in the energy band 50–300 keV is of a few m^2, which translates into ∼50–100 detectors simultaneously looking at the source, each of which having a collecting area of $\sim$ 200 cm^2 [45].
This photon count rate corresponds to relatively bright bursts, which are expected to occur a few times per month across the full sky.
Studies conducted using BATSE data [91] have suggested two trends: a positive correlation between luminosity and variability, and a negative correlation between width and amplitude of individual pulses in a burst. Both trends support the search for short-duration variations in bright bursts.
More recent analyses on a much larger samples of GRBs show that the correlation between luminosity and the traditional variability estimator is weaker than previously thought [84, 92]. Instead, it has been found that the luminosity of GRBs is more strongly correlated with the minimum variability timescale, defined as the shortest timescale over which the signal shows uncorrelated temporal variability in the prompt light curve [93]. This parameter could reflect the activity of the central engine and the emitting regions, reinforcing the scientific relevance of fast-timing observations.

3.1.3 The HERMES Pathfinder Goals

The Pathfinder and the Final Constellation have a specific program of objectives. The main goal of the **HERMES Pathfinder** program is to demonstrate the feasibility of the HERMES approach and, in particular, to [45]:

- develop instrumentation and miniaturized scientific technologies for the detection and study of GRBs and other high-energy transients;
- demonstrate that accurate localization of GRBs can be achieved by measuring the signal arrival delay time of different detectors hosted by miniaturized satellites;
- demonstrate the applicability of disruptive technologies and Commercial Off-The-Shelf components to a challenging space mission.

The two main high-level scientific requirements are:

- to detect GRBs with peak fluxes $>$ 0.5–1 ph/s/cm^2 in the 50–300 keV band;

- to detect ≥ 40 long GRBs and ≥ 8 short GRBs simultaneously in at least 3 units during a nominal 2-year phase and be able to assess their position by analysis of the time delay in signal arrival on different detectors.

3.1.4 The HERMES Full Constellation Goals

The **HERMES Full Constellation** should be able to reach the following high-level scientific goals [45] :

- to cover each location of the celestial sphere using 20–30 detectors with maximum off-axis angle, i.e. the distance from the optical axis of the detector, equal to 60 degrees.The full sky should be accessible at each given moment;
- to achieve sensitivity to weak GRBs with flux ~ 0.2 ph/s/cm^2 in the energy band 50–300 keV allowing the observation of events similar to GRB170817 at distance 120–150 Mpc;
- to achieve localization accuracy better than 15 arcmin for long bursts and 1 degree for short bursts, where accuracy is a function of the GRB flux for the long and short GRB, respectively. Stronger GRBs allow to recover time delays with a better accuracy [94]. This would allow prompt identification of the electromagnetic counterpart of a GWE and guide multiwavelength follow-up;
- to disseminate to the astrophysical community the positional data of transient events within few minutes from the trigger time;
- to deploy a sufficient number of units to achieve a total collective area of the order of a few m^2;
- to achieve better than µs photon timing accuracy.

3.2 The expected scientific performances

The HERMES-PF pre-launch expected scientific performances are reported in [95]. The predicted number of short and long GRBs events detected with HERMES-PF per year is shown in Table 3.2.

HERMES-PF is expected to detect short GRBs at a rate of 19^{+5}_{-3} per year and long GRBs at a rate of $\sim 195^{+22}_{-21}$ per year. Short GRBs are detected mainly by the γ instrument, because of their harder spectra [96]. The effective area of HERMES-PF (HP) is smaller than that of Fermi-GBM, which explains its lower detection rate of short GRBs ($\sim$40 yr^{-1}, [97]) . For long GRBs, approximately 26% of detections are made possible by the extended sensitivity in

GRB Class	S-mode	X-mode	X-mode only	Total
Long	147^{+13}_{-11}	131^{+17}_{-19}	51^{+12}_{-13}	195^{+22}_{-21}
Short	19^{+5}_{-3}	$0.3^{+0.4}_{-0.2}$	< 0.1	19^{+5}_{-3}

Table 3.2: Predicted number od Short and Long GRBs events detected with HERMES-PF per years adapted from[95]. For each GRB class, the table shows the total rate and partial rates in X and S modes (see text 4.1 for discussion). X-only refers to events detected only by the X instrument.

the soft X-ray energy range (3-20 keV). Combined with the possible implementation of burst fluence-based trigger algorithms, this makes HP competitive with Fermi-GBM, which observes long GRBs at an average rate of $\sim$200 yr^{-1} [97].

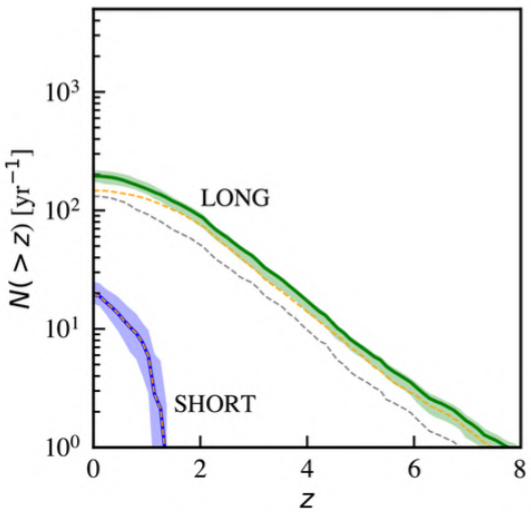

Figure 3.1: GRBs detection rates expected from HERMES-PF (events per year) as a function of redshift z [98].

The GRB detection rate has been estimated under the assumption of a 50% duty cycle (as expected in a Sun-Synchronous Orbit) and with the six satellites organized into two triplets, each oriented toward different regions of the sky. In this configuration, each triplet provides a field of view of about 5.20 sr in S-mode and about 3.14 sr in X-mode [95].

Thanks to the extension of the energy band to soft X-rays (3 keV), HERMES-PF will be able to detect approximately 3.4 GRBs per year with redshift z$\geq$6 as shown in Figure 3.1 . This estimate was derived from the sample of 8 high-redshift GRBs observed over the last two decades. With follow-up in the near-infrared (NIR) from ground-based and/or space-based facilities, HERMES-PF will therefore be able to significantly expand the current sample of high-z GRBs already during its operational lifetime [98].

3.3 Payload Design

Parameter	Value
Payload peak effective area (X-mode & S-mode)	52 cm^2
Field of View	3.2 sr FWHM
Low energy threshold	$\leq$ 3 keV
Energy resolution X-mode (@ 6 keV)	$\leq$ 800 eV FWHM
Energy resolution S-mode (@ 60 keV)	$\leq$ 5 keV FWHM
Time resolution (68% c.l.)	320 ns
Time accuracy (68% c.l.)	181 ns
Background rate 50–300 keV	72 counts/s
Background rate 3–2000 keV	510 counts/s
Payload mass	1.55 kg
Payload power in Observation	1.8 W
Payload Telemetry (scientific + engineering)	610 Mbits/day (50% duty cycle)

Table 3.3: Summary of HERMES-PF anticipated performance [98]. The background rates were estimated for an equatorial orbit, originally planned for the launch.

The scientific requirements of HERMES-PF determine ambitious payload (P/L) requirements summarized in Table 3.3: wide energy bandwidth, good efficiency, good energy resolution, high time resolution, extremely compact design, reliable operation in a wide range of space environments (e.g., temperature, radiation damage, etc.) [98].
To meet these requirements within the mass, volume, and power constraints of a CubeSat, HERMES-PF was designed with an innovative and customized design.

The payload structure is allocated in a 1U-CubeSat (10 cm $\times$ 10 cm $\times$ 10 cm), with a total mass $\leq$ 1.6 kg) that is composed by four major blocks represented in Figure 3.2: the Detector Assembly, the Back-End Electronic board (BEE), the Power-Supply electronic board (PSU) and the Payload Data Handling Unit (PDHU). In the following sections, these components and their principle of operation will be explained in detail. The integration of the Detector Assembly took place in the laboratories of the Fondazione Bruno Kessler (FBK) in Trento, Italy. The BEE, PSU and PDHU boards were integrated with the detector at the INAF/IAPS laboratories in Rome, where functional tests were also conducted [99].

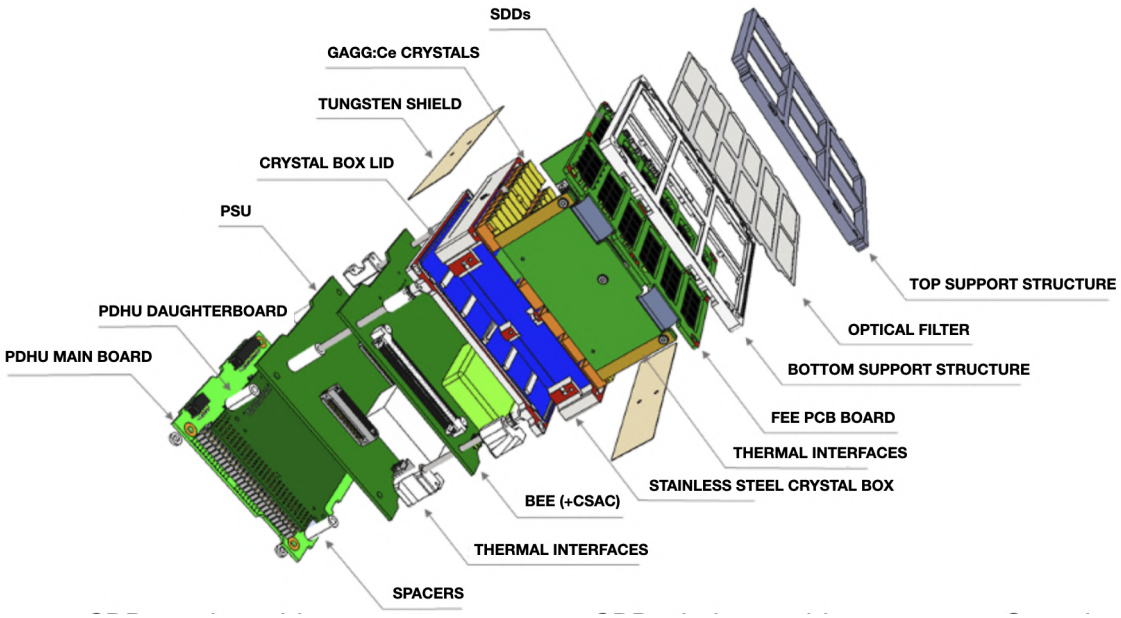

Figure 3.2: Exploded view of the HERMES-TP/SP Payload [98].

Starting from the top, the payload is composed of:

Detector support structure, mounted on top of the sensing plane. A thin **optical filter**, designed and produced by the Institute of High Energy Physics (IHEP) in Beijing, China, is placed between the top and bottom of this structure to block Optical/UV light from the environment that could degrade the performance of the detectors. The filter also plays a role in the overall thermal design of the detector assembly.

Front-End Electronics (FEE), a rigid-flex printed circuit board with a main plate located below the filter and two side wings, that hosts 12 SDD arrays, 120 LYRA-FE ASIC arrays (one for each SDD channel), 4 LYRA-BE ASICs, discrete electronic components and electrical connectors acting as the electrical interfaces with the BEE board.

60 scintillator crystals, where each crystal is optically connected to two SDD cells. They are housed in the crystal box that, along with the FEE board and the detector support structure, defines the overall mechanical structure, above the BEE. The box is shielded on the sides and on the bottom by three 200 μm thick tungsten plates.

Back-End Electronics (BEE). This board reads analog signals from the FEE, produces digital data via external ADCs, handles time marking and other operations using a Field Programmable Gate Array (FPGA) as the control logic.

Payload data handling unit (PDHU) board, with the on-board computer. It implements

all the functionality required by the experiment, with an average consumption of 400 mW. For example, it configures FEE and BEE and receives their digital data, generates the photon list, processes the data with a burst search algorithm, and produces TM telemetry data packets, the data to be sent to the ground, It also handles housekeeping (i.e., monitors the status of the payload), and the interface management with the spacecraft.

Power Supply Unit (PSU) board, responsible for the control and generation of the P/L power supplies.

3.3.1 Detector Architecture

The HERMES-PF detector is based on the "siswich" architecture described in Figure 3.3, where thin silicon detectors are coupled to scintillator crystals in a monolithic structure [82]. This architecture allows the wide energy band required to be covered. This architecture enables

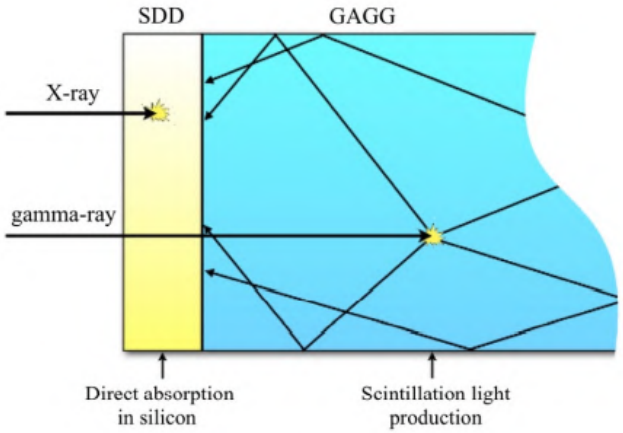

Figure 3.3: Siswich architecture: the SDD (yellow) is coupled to the GAGG:Ce scintillator (blue). Low-energy photons ($\leq$30 keV) are absorbed in the SDD, while higher-energy photons interact in the scintillator, producing light that is collected by the SDD.

the detection of both soft and hard X-rays, as well as γ-ray photons. Soft X-rays are directly absorbed by silicon, while higher-energy X-rays and γ-rays pass through the scintillator crystals. These high-energy photons are absorbed and converted into visible light, which is subsequently collected using the same silicon detector. The detector configuration is an array of 12 Silicon Drift Detector (SDD) matrices shown in Figure 3.4, each with 10 individual 0.45 cm^2 cells and a silicon thickness of 450 μm. SDD can detect X-ray radiation with good efficiency up to 20–30 keV, with low noise and a time resolution of less than μs [66]. Due to their high quantum efficiency ($\sim$90%) for optical light, SDDs also play the role of scintillator photodetectors.
The SDDs are based on results achieved within the framework of the Italian ReDSoX collaboration, with the combined design and manufacturing expertise of INFN-Trieste and Fondazione

Bruno Kessler (FBK, Trento) [100].

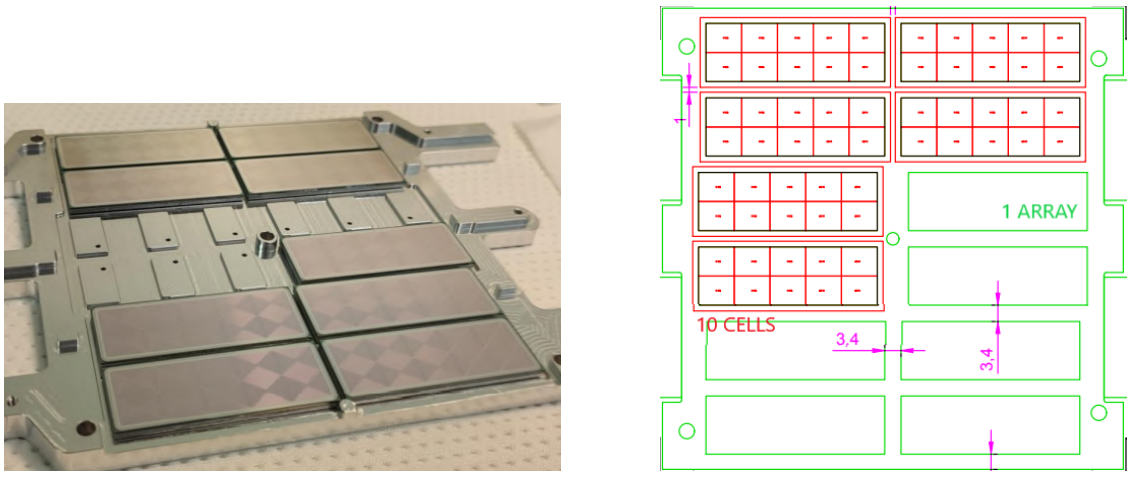

(a) (b)

Figure 3.4: HERMES-PF 12 Silicon Drift Detectors array during integration (a). Design of the structure of the SDD array and cells (b). Each SDD array is composed by 10 cells as [100].

Crystals are optically connected to the SDDs, and each is read by two SDD cells. In this way, events detected by a single SDD are associated with soft X-rays, whereas events detected simultaneously in the two adjacent detectors correspond to hard X-ray/γ-ray photons. The crystals are grouped in sub-assemblies of five crystals, with one sub-assembly coupled to an individual SDD array.

To maximize the efficiency of scintillation light collection, each crystal is wrapped in reflective material (see Figure 3.5), with the exception of the surface directly in contact with the SDD, which is optically coupled via a soft, transparent silicone layer. This layer also acts as a shock absorber, mitigating risks during launch and in-orbit operations.

The inorganic scintillator is the *Cerium-doped Gadolinium-Aluminum-Gallium Garnet* (GAGG:Ce), which was first developed in Japan (2010) and has been commercially available since 2014. In addition to mechanical robustness, to an extremely low intrinsic background and absence of hygroscopicity, it displays high light output ($\sim$ 50000 ph/MeV) and short decay time of $\sim$ 90 ns [82].

The high light output allows lower energy thresholds for high-energy detection (from 20 keV to several MeV), while fast decay times are crucial for achieving high photon timing accuracy. The 60 crystals, grouped 5 by 5, are contained in the crystal box, and each crystal has a 6.94×12.1 mm^2 cross-section and is 15 mm thick.

A common feature of almost all scintillators is the so-called non-linearity in their response, i.e., the light output is not constant with respect to energy but depends on several factors. Although there is no detailed description of this behavior for the GAGG:Ce, some studies [101, 62] have

shown a decrease in light output of a few percentage points for photon energies below a few hundred keV and the presence of a discontinuity due to the gadolinium K edge (at 50.23 keV). In order to correctly calibrate the response of the HERMES-PF detectors in the γ-ray energy band, the deviation of the light output from the reference value (usually assumed to be the 662 keV line from ^{137}Cs) was evaluated in [102], on the basis of which a correction was then obtained to be applied to future acquisitions.

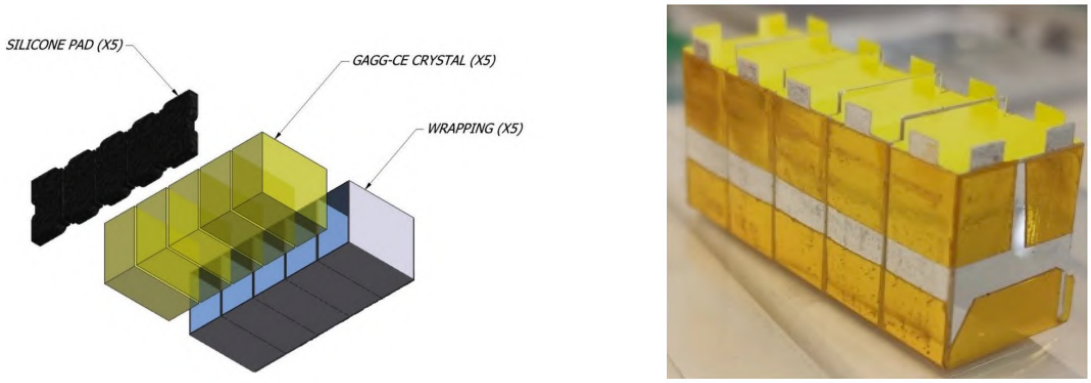

(a) **(b)**

Figure 3.5: Scintillators optical assembly design (a) and real (b). Each crystal is wrapped in a reflective material and optically connected to the SDD through a layer of soft, transparent silicone [100].

With this design, the payload detector can detect X-rays and γ-rays in the energy range 3–2000 keV, providing the following information for each detected photon:

- Timestamp of photon event
- Photon energy
- Address of the pixel where the conversion took place

3.3.2 LYRA Readout Electronics

HERMES-PF readout electronics feature an application-specific integrated circuit (ASIC) called LYRA, developed by a collaboration between Politecnico di Milano and University of Pavia [103]. It is an heritage of the VEGA ASIC project developed for the read-out of large-area SDDs [104, 105]. This ASIC is optimized for low noise and low power consumption, which is essential for achieving the high-energy resolution potential of Silicon Drift Detectors.
HERMES detector hosts four independent LYRA ASICs chipsets. Each LYRA chipset is divided into 30 Front-End ASICs (LYRA-FE) and 1 Back-End multichannel ASIC (LYRA-BE) for a total of 120 LYRA-FE and 4 LYRA-BE circuits [82], with the detector segmented into four independent quadrants, each with its own electric bias. This architecture is schematized in

Figure 3.6. (However, due to a failure in one quadrant that occurred during the final stages of ground calibration, the payload on board SpIRIT operates with only three active quadrants). The LYRA-FE ASICs are installed close to the SDD anodes to minimize the input capacitance, and they have the functions of preamplifiers, signal shapers, and transmitters. Once processed by the LYRA-FE, the signals are routed to the LYRA-BE ASICs, which are located on the side of the Front-End Electronics board. Each LYRA-BE chipset handles 32 channels (including two spare), with each channel incorporating a current-mode signal receiver, a second signal shaper, a discriminator, a peak-stretching circuit, and control logic.

The LYRA-BE is responsible for multiplexing the signals from the 32 input channels of LYRA-FE. Through the multiplexer, analog outputs from each SDD, along with event triggers, are read. A digital-to-analogue converter (DAC) on the LYRA-BE programs the threshold that determines the minimum signal level to trigger an event readout. Thresholds are expressed in 8-bit DAC units, i.e., spanning the range from 0 to 255, which correspond to an analog voltage level from 0 V to 3.3 V. This voltage serves as a reference for the discriminator circuit, which compares the incoming signals with the threshold level to decide whether an event should be recorded.

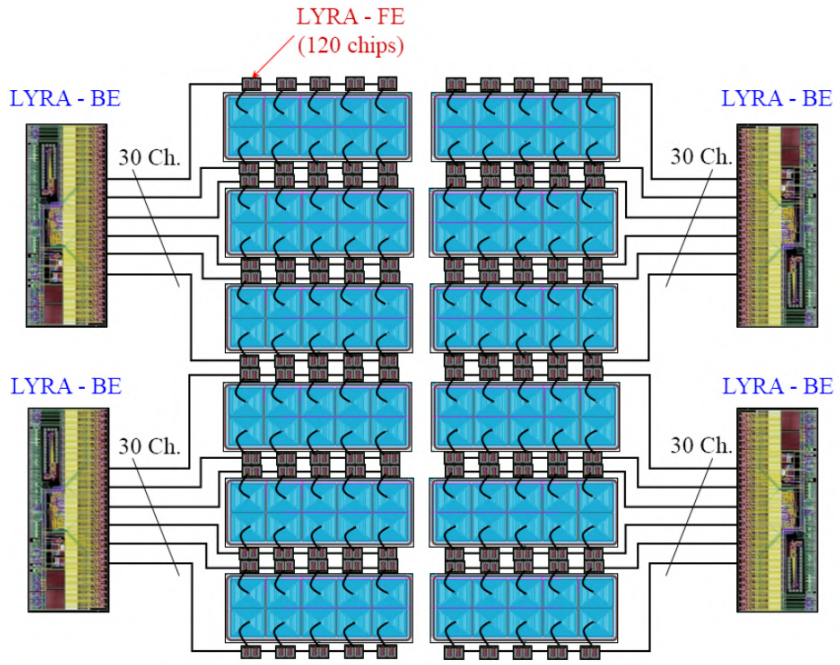

Figure 3.6: Architecture of the LYRA chipset with 120 LYRA-FE connected to 120 anodes of the SDD and 4 LYRA-BE [82]

The threshold can also be set for individual channels, and is called the fine threshold. The combined global and individual thresholds are set high enough to effectively suppress noise-induced triggers in most detector channels. The effective energy threshold is determined by the

DAC-programmed value in combination with the specific characteristics of each channel (gain, offset, and light output) and the payload temperature [106].
The number of nominal active channels together with the selected DAC threshold define the main parameters of the ASIC configuration.
The detector and the readout electronics are hosted in the FEE Electronics board, together with six temperature sensors.

LYRA ASIC Circuit

A scheme of the complete LYRA circuit is shown in Figure 3.7, where the logic blocks contained in the FE and BE sections are outlined [107].

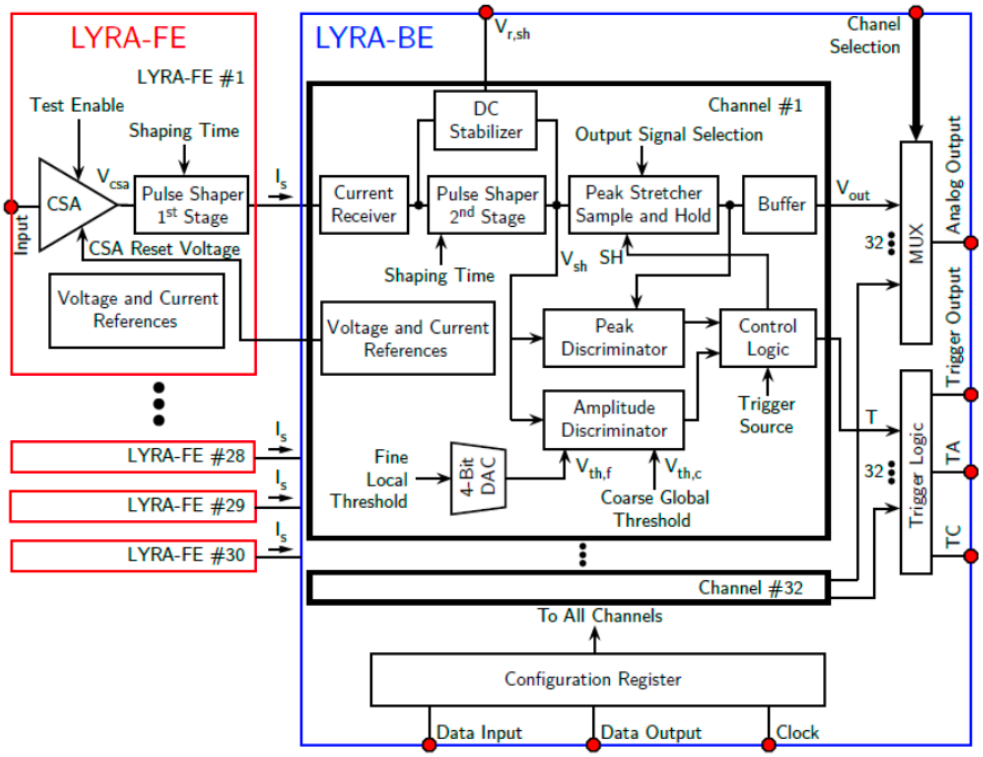

Figure 3.7: Block diagram of the LYRA ASIC chipset. The respective chains of the FE and BE sections are outlined by a red and blue rectangle [107].

The first element of the Front-End (LYRA-FE) is the *Charge Sensitive Preamplifier*(CSA), which transforms the current at the SDD anode into a voltage step. The preamplifier input is connected both to the SDD anode and to a test input V_{test}. A capacitor connected to the latter allows to simulate a signal such as an event related to the arrival of a photon. Next, the *pulse shaper* transforms the signal from a step to a quasi-Gaussian shape of which we can select the rise time, that is, the time required for the signal to reach the peak.
The LYRA-BE receives the shaped signals from up to 32 front-end units. A second shaping

stage further refines the pulse, which is then processed by the *Peak stretcher and sample-and-hold circuit*. A *discriminator* allows to select signals intense enough to be due to a photon and not to a noise fluctuation. The discriminator is set by a programmable threshold via the Digital-to-Analog Converter (DAC). The lower the value of the threshold, the more it will be sensitive to lower-amplitude events, such as low energy photons. If a signal passes the threshold, it can be converted to a digital value. The *peak stretcher* allows the analog-to-digital conversion: when the input signal reaches its peak, it is held at the maximum level and remains constant. In other words: if the signal exceeds the threshold, it arms the peak discriminator, which then enables the stretcher. Valid events generate a trigger signal, managed by the control logic.

The outputs of the individual channel triggers and of the analog stretcher signal are at the end of each channel circuit. In order to minimize the number of external connections, a *multiplexer* allows to select the routing of any given channel to the external output.

After the analog-to-digital conversion the signal chain is reset and is able to acquire triggers again. The LYRA-BE operates in two modes: configuration and operation. In the first mode, all parameters can be set, such as the trigger thresholds and the selection of active channels. In the second case, the ASIC generates an OR trigger signal each time a channel detects an event above the threshold. At the same time, the analog signal from the Peak Stretcher is routed to the output through the multiplexer.

3.3.3 Back-End electronics (BEE)

The Back-End Electronics Board is a PC/104 format board developed by INAF specifically for the HERMES-PF payload, using COTS components [66]. It is responsible for communication between the FEE board and the Payload Data Handling Unit. It uses a Field Programmable Gate Array (FPGA) as control logic to manage various operations, including reading analogue signals from the Front-End Electronics (FEE) and converting them into digital data via external ADCs, configuring the ASIC, collecting the Housekeepings and controlling the power lines for the FEE. It manages event data acquisition and transmits this information to the PDHU, while also receiving and decoding telecommands sent by the PDHU.

The BEE also houses a miniaturized chip-scale atomic clock (CSAC) that provides an extremely stable 10 MHz clock and a pulse-per-second (PPS) signal [108]. The PPS, synchronized with the onboard GPS receiver, resets a 28-bit counter, while the 10 MHz clock drives a 24-bit fast counter used to timestamp events with 100 ns resolution. This architecture allows time-tagging of events with sub-microsecond accuracy and ensures precise clock synchronization, even when the GPS signal is temporarily lost [66, 106].

On the BEE board, the analog signals generated by the detectors and processed by the FEE are

routed to an analog-to-digital converter (ADC). The system includes four independent ADC chains, each dedicated to a specific quadrant of the detection plane. This architecture allows for the simultaneous acquisition of events occurring in different quadrants [66].

3.3.4 Power Supply Unit (PSU)

All power supplies required for the P/L are handled by the Power Supply Unit (PSU) board, also developed and manufactured by INAF using COTS components [109]. In particular, it controls the power supply to the payload by managing the activation and deactivation of the required voltages. These voltages are sourced from the satellite's power bus (SBUS), which filters and distributes them across the various P/L sections. The distributed power lines are [109, 66]:

- 3V3 supplies power to the BEE, the CSAC and the Payload Data Management Unit;
- 5V0 supplies power to the FEE ASICs (5V0-FEE), specifically powering the linear voltage regulators that provide 3V3 V for the analogue and digital circuits, as well as 2V0 for the analogue of the FEE. It also powers some of the circuits on the BEE board (5V0-BEE);
- 12V power the DC-DC converter providing the High Voltage bias for the SDD detectors.

For each main power supply track, there is an Overcurrent Sensing circuit that monitors the current flowing on the line and quickly opens the line breaker if an overcurrent condition is detected, in order to prevent damage of the load [109]. The PSU hosts the electronic switches that control the voltages, while the PDHU controls them, managing the switching on and off based on predetermined operating procedures. Additionally, the BEE firmware controls another set of switches, adding an extra layer of security.

3.3.5 Payload Data Handling Unit (PDHU)

The Payload Data Handling Unit (PDHU) is the main control system at the payload level, responsible for pre-processing, storing, and preparing scientific data, as well as managing housekeeping tasks like monitoring payload status [110]. Acting as the interface between the spacecraft and the payload, the PDHU is built around the Innovative Solutions In Space (ISIS) On-Board Computer (iOBC), a high-performance, flight-proven unit featuring an ARM9 processor and a modular daughterboard architecture that facilitates the integration of mission-specific electronics. The PDHU configures the FEE and BEE, receives digital data, processes it using a burst search algorithm, generates photon lists, and creates telemetry data packets for transmission to the ground. It operates with a low average power consumption of 400 mW [66].

Operating Modes

The PDHU software is designed on the basis of a finite-state machine model [66, 110]. The P/L operating modes are described in Figure 3.8.

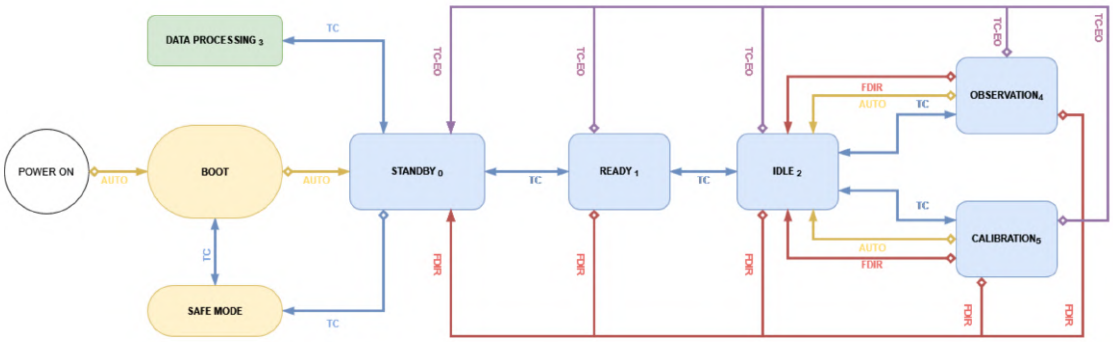

Figure 3.8: Payload operative modes. TC means that the transition between one operative mode to another is performed by executing a remote *TeleCommand*.

The system starts in **Boot** mode immediately after power-on, which is the initial start-up state triggered by the activation of the 3.3V power line. When a significant error or malfunction is detected, the system shifts to Safe Mode, where functionality is reduced to handle such exceptional situations. Once the system is powered on, the PDHU enters **Standby mode**, where the detector remains off and the system only requires the 3.3V supply line.

Following successful health checks, the PDHU switches to **Ready** mode, where all power lines (3 V, 5 V, and 12 V) are activated, but the detector's high voltage remains off. In **Idle** mode, which is similar to Ready mode, the high voltage required for the detector is turned on, generated from the 12 V line.

Observation and **Calibration** modes are used to collect scientific data, with their specific configurations set in either Idle or Standby mode. In Calibration mode, full-band photon-by-photon data are recorded; in Observation mode, Scientific Rate Meters (SRAs) are produced, which consist of light curves for each quadrant with a 100 ms temporal resolution. During Observation, a burst detection algorithm is executed in real-time while data are being collected.

The primary role of **Data Processing** mode is to prepare scientific data for transmission to the ground. This includes running a second burst detection algorithm, reducing and compressing the data, and collecting housekeeping reports.

The **Fault Detection Isolation and Recovery** (FDIR) procedure, a non-autonomous operating mode, allows automatic switching between operating modes. The on-board sensors allow monitoring of voltage, current and temperature values and comparison with the nominal values described in the on-board database. In the event that they fall outside the expected ranges,

the FDIR task issues a warning and assesses the severity of the fault. If high severity faults occur, an automatic switch to safe mode or power-cycling is performed.

The **Emergency Remote Control** (TC-EO) can be activated in the event of communication issues or other unforeseen problems, ensuring a complete and controlled shutdown sequence of the P/L. More information on the TC-EO command can be found in Section5.2.3.

Memory architecture

The PDHU incorporates its own memory architecture, organizing the file system into various sub-directories. The 'CAL' sub-directory is dedicated to storing Calibration mode photon data, with each file representing one second of data. The 'PHR' and 'PHF' directories manage photon data in the 50–300 keV range and the full-band photon lists triggered during Observation mode. The 'SRA' sub-directory, on the other hand, holds files that contain the Scientific Rate Meters, with one file generated per observation.

In addition, the system generates several `.log` files that document operational activities and events, playing a critical role in event tracking and diagnosing possible problems.

3.4 HERMES-PF payload implementation stages

The integration of each payload follows a well-defined logic and a consolidated sequence of steps. Figure 3.9 illustrates the overall strategy that guides the payload integration process [99].

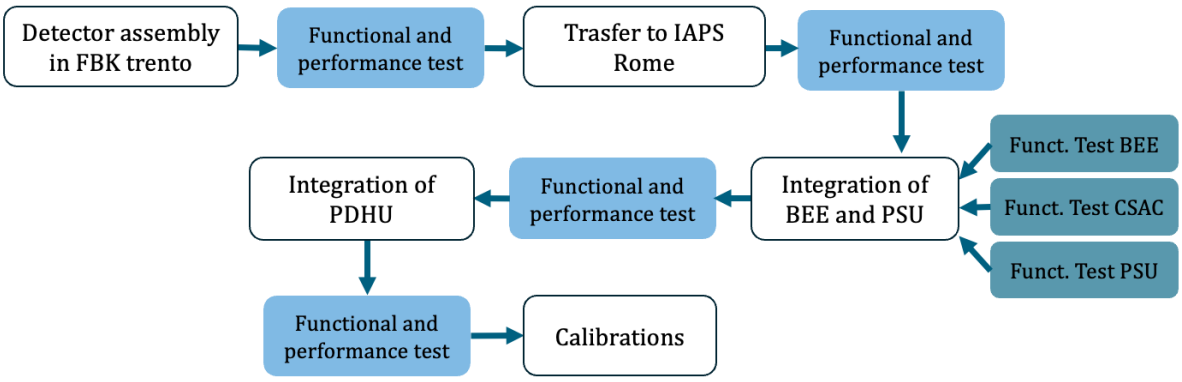

Figure 3.9: The overall strategy of the HERMES Pathfinder payload integration [99].

The first step of the integration process involves the assembly of the detector, carried out at the laboratories of Fondazione Bruno Kessler (FBK) in Trento, Italy. FBK is also responsible for the production of the SDD detectors.

Following this initial phase, including functional and performance testing, the partially assembled payload is transferred to the INAF/IAPS laboratories in Rome, Italy. Here, the integration of the remaining electronic boards, BEE, PSU, and PDHU, is completed. A schematic view of the payload is shown in Figure 3.10 (b). After the installation of each board, additional functional tests are conducted to ensure system compatibility and performance Once the full payload integration is completed, the calibration campaigns are carried out at various temperatures (in the range ±20 °C) using different radioactive sources (e.g. ^{55}Fe, ^{109}Cd, ^{137}Cs).

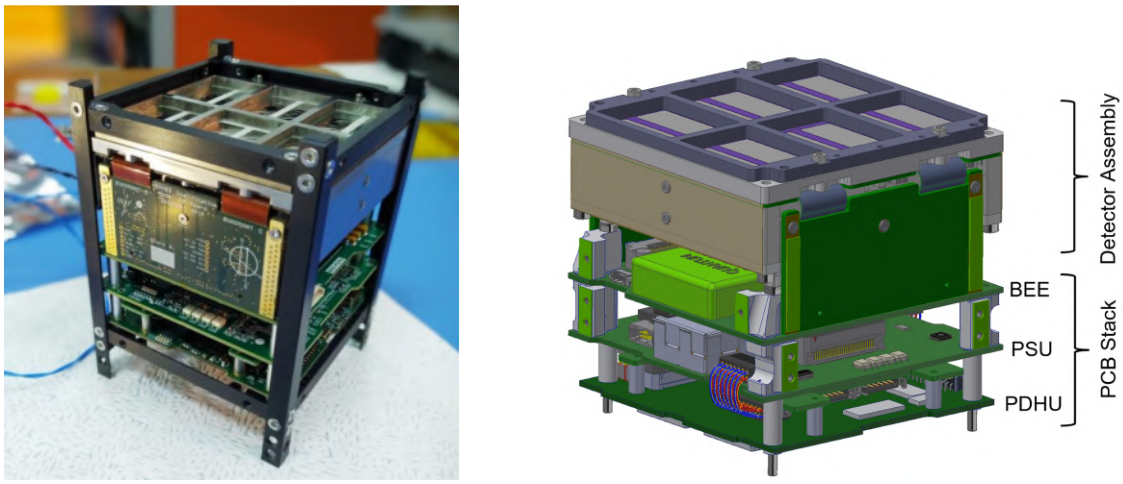

(a) (b)

Figure 3.10: Picture of the payload Demonstration Model [100] (a) and a schematic view of the HERMES-PF payload [106] (b).

Before working with real flight payloads, the Payload Demonstration Model (DM) in Figure3.10 (a) was realized: it represents the first fully integrated, non-flight HERMES payload dedicated to validate the integration procedure and to carry on functional and preliminary performance testing.
The HERMES-PF flight models are named PFM (Proto Flight Model), FM1 (the SpIRIT one), FM2, FM3, FM4, FM5, and FM6, listed in order of integration.

3.5 HERMES-Pathfinder Service Module

The HERMES-PF service module (SM) is a 3U-class CubeSat with a volume of 10 cm× 10 cm× 30 cm, with a total mass ∼ 6 kg. It has been designed and developed by Politecnico di Milano. The internal structure is divided in three main parts [98], shown in Figure 3.11:

- Top Unit: entirely dedicated to the payload;
- Central Unit: housing the batteries, control boards, and all the main electronics;
- Bottom Unit: primarily allocated to the reaction wheels.

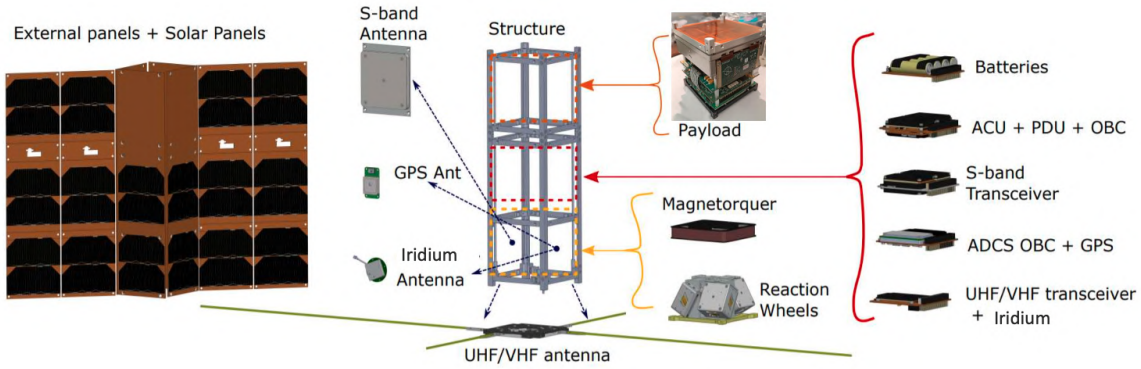

Figure 3.11: HERMES-PF Service module internal configuration [111].

The assembly, integration, verification and test (AIV/T) activities of the service module were mainly carried out in the ISO 8 clean room at the Politecnico di Milano.

Chapter 4

Calibration and Integration activities for HERMES-PF

This chapter presents the work plan for the Calibration of HERMES-PF flight models [112, 106]. Section 4.1 introduces the logical and physical principles underlying calibration, defining the main characteristic quantities to be determined. Section 4.2 is dedicated to the preliminary functional tests carried out during the integration of the detector, while section 4.3 presents the calibration setup for the official calibrations campaign described in Section 4.5. Section 4.4 describes the software pipeline developed specifically for processing calibration data. Finally, the results obtained are discussed in Section 4.6.

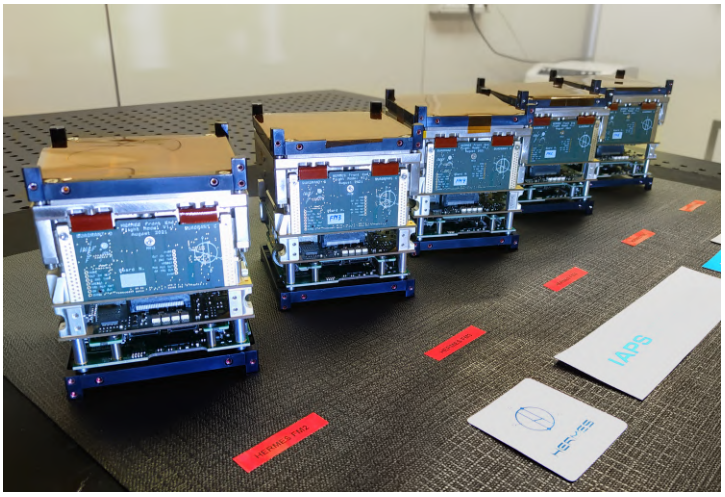

Figure 4.1: Payloads family picture from FM2 to FM6 [98].

The author's contribution to this work concerned Flight Models (FMs) 4, 5, and 6, particularly with regard to functional tests and calibration campaigns conducted in the laboratory. Calibration activities and performance analyzes were performed on all FMs. A family picture

of the payloads from FM2 to FM6 is shown in Figure 4.1.

4.1 Calibration basic principles

Calibration of the acquired spectra means converting detector amplitudes in terms of absolute energy in keV to identify high-energy emitters. In HERMES-PF, lower-energy radiation is detected in the SDD, while higher-energy X-rays and gamma-rays are absorbed in the crystal and give rise to optical scintillation photons, which are then collected by the SDD. Both signals are read out by the front-end electronics. Therefore, calibration is divided into two modes, one for X-ray sources and one for gamma-ray sources. As explained in Chapter 3, the entire detector is split into four totally independent quadrants, each of which houses a LYRA-BE ASIC that handles 30 LYRA-FE channels. Each channel reads and processes the signal coming from an SDD anode [82]. Calibration is performed for all channels of each quadrant using a set of known radioactive sources: ^{55}Fe, ^{109}Cd, ^{137}Cs. When an X-ray interaction occurs in the SDD silicon bulk, only one trigger channel is usually present and a *X-mode* event is identified. Otherwise, if the incoming photon is absorbed in a scintillator crystal, the two channels reading out the crystal are triggered and this is classified as a gamma-ray *S-mode* event.

4.1.1 X-Mode

When an X-ray is absorbed in the SDD silicon bulk, on average one electron is produced every 3.65 eV of deposited energy [113]. Consequently, there is a linear relation between X-ray energy and the anode signal amplitude in electrons. The *slope* and *intercept* of the linear fit between the measurements in a recorded spectrum of known photon line energies, versus the amplitude in electrons, define the calibration parameters called *gain* and *offset*. The main purpose of X-mode calibration is to determine the gain and offset for each channel. The linear fit is described by the following expression:

$$A[ADC] = A[e^-] \times \text{Gain}[ADC/e^-] + \text{Offset}[ADC] \tag{4.1}$$

The calibration of a given amplitude A in [e$^-$] is then performed by:

$$A[e^-] = \frac{A[ADC] - \text{Offset}}{\text{Gain}} \tag{4.2}$$

For X-mode events, the amplitude is expressed in keV as:

$$A[\text{keV}] = \frac{3.65[\text{eV}/e^-]}{1000[\text{eV/keV}]} A[e^-] = 0.00365[\text{keV}/e^-] A[e^-] = 0.00365 \frac{A[ADC] - \text{Offset}}{\text{Gain}} \tag{4.3}$$

The X-mode calibration is performed using ^{55}Fe and ^{109}Cd radioactive sources. Since the calibration parameters also depend on temperature, it is necessary to perform a data acquisition

at different temperatures (around the expected operating temperature, which is ~ 0 °C for HERMES-PF and ~ -15 °C for SpIRIT). In particular, temperature variations are due to two contributions: the intrinsic contribution of the electronic chain, and that of the digitizing part of the signal (ADCs).

Based on the activity rate[1] (activity 200 μCi for ^{55}Fe, about 50 μCi for ^{109}Cd), an integration time of 900 s is chosen for each measurement, to obtain sufficient count statistics ($\geq$10 kcts per channel) in order to minimize errors on the peak fits of the acquired spectra. The steps to be followed are summarized in Table 4.1.

Step	Mode	Measurements	Temperature	Notes	Integration time
1	X	^{55}Fe + ^{109}Cd	20 °C	$\geq$10 kcts/channel	900 s
2	X	^{55}Fe + ^{109}Cd	10 °C	$\geq$10 kcts/channel	900 s
3	X	^{55}Fe + ^{109}Cd	0 °C	$\geq$10 kcts/channel	900 s
4	X	^{55}Fe + ^{109}Cd	-10 °C	$\geq$10 kcts/channel	900 s
5	X	^{55}Fe + ^{109}Cd	-20 °C	$\geq$10 kcts/channel	900 s

Table 4.1: List of steps for X-mode calibration: the adopted sources are ^{55}Fe and ^{109}Cd and 900 s acquisitions are performed to collect a minimum of 10^4 counts for each temperature.

Each source is placed above the payload, with a suitable holder and all four quadrants are tested together. Each measurement is performed with three set ASIC thresholds (see Section 3.3.2), at values of 105, 95 and 85 (in units of the internal ASIC DAC). The use of different thresholds makes it possible to verify if there a residual dependence of the gain on this parameter, and to define the optimal one for acquisitions in orbit.

4.1.2 S-Mode

The main purpose of the S-mode calibration is the verification of the effective light output LY for each channel. The LY is defined as the number of electrons produced at the SDD anode for unit of energy absorbed in the scintillator crystal and is measured in [e$^-$/keV]. As such, it is the product of the intrinsic light output (number of scintillation photons produced per unit of absorbed gamma-ray energy), the optical contact efficiency (fraction of scintillation photons able to reach the SDD surface window) and of the SDD quantum efficiency (fraction of scintillation photons able to produce one electron of charge in the active silicon bulk. On

[1]The activity of a radioisotope source is defined as its rate of decay and is given by the fundamental law of radioactive decay

$$\frac{dN}{dt} = -\lambda N \tag{4.4}$$

where N is the number of radioactive nuclei and λ is defined as the decay constant. The historical unit of activity has been the curie (Ci), defined as exactly 3.7×10^{10} disintegrations/second [114].

average, one optical photon produces one electron). The effective light output is also known to be a non-proportional quantity, i.e., its value depends also on the energy. This effect is being measured and parameterized on the same HERMES-PF scintillator crystals with a dedicated setup [102]. The effective light output depends on the temperature, with an expected ∼20% increase by going from the room temperature value to –20 °C [115].
The signal amplitude for S-mode events is expressed in keV as:

$$A[\text{keV}] = \frac{A[e^-]}{LY[e^-/\text{keV}]} = \frac{1}{LY[e^-/\text{keV}]} \frac{A[ADC] - \text{Offset}}{\text{Gain}} \tag{4.5}$$

where LY is the light output for the given channel (and the given temperature).
To reconstruct the event read out by two channels (a, b) optically connected to the same crystal, its amplitude is given by:

$$A_{\text{tot}}[\text{keV}] = \frac{A_a[e^-] + A_b[e^-]}{LY_a[e^-/\text{keV}] + LY_b[e^-/\text{keV}]} = \tag{4.6}$$

$$= \frac{1}{LY_a[e^-/\text{keV}] + LY_b[e^-/\text{keV}]} \left(\frac{A[ADC]_a - \text{Offset}_a}{\text{Gain}_a} + \frac{A[ADC]_b - \text{Offset}_b}{\text{Gain}_b} \right)$$

For each HERMES-PF FM, the effective light output is measured by irradiating the detector using a ^{137}Cs radioactive source (monochromatic emission line at 661.65 keV). The source is placed above the center of the detector and all four quadrants are acquired simultaneously. Similarly to X-mode calibrations, each measurement is repeated with three ASIC thresholds, whose values are set at 105, 95 and 85. The steps to be followed are summarized in Table 4.2.

Step	Mode	Measurements	Temperature	Notes	Integration time
5	S	^{137}Cs	20 °C	≥10 kcts/channel	900 s
6	S	^{137}Cs	10 °C	≥10 kcts/channel	900 s
7	S	^{137}Cs	0 °C	≥10 kcts/channel	900 s
8	S	^{137}Cs	−10 °C	≥10 kcts/channel	900 s
9	S	^{137}Cs	−20 °C	≥10 kcts/channel	900 s

Table 4.2: List of steps for S-mode calibration: source used is ^{137}Cs and 900 s acquisitions are performed to collect a minimum of 10^4 counts for each temperature.

4.2 Preliminary functional tests

Calibration is essential in order to identify any problems in the electronics and detector, and to apply the necessary solutions. During each payload integration phase, a preliminary and

intermediate calibration was performed, with the aim of verifying the correct functioning of each component and, consequently, their overall integration.

As shown in Section 3.4, the first integration phase involved the assembly of the detection system and its connection to the Front-End Electronics board. The operations described in this section were carried out by the author for FM4, FM5 and FM6. They took place over a period of time from January to March 2023. The procedure described below is the same for all payloads.

4.2.1 Detector assembly

The first series of functional tests was carried out in Trento, Italy, at the Fondazione Bruno Kessler (FBK), to verify the operability of the integrated system.

After the integration of the SDD detectors into the FEE board, shown in Figure 4.2a, and the bonding of the ASICs, the first test phase was started. The second phase began with the integration of the crystal box, shown in Figure 4.2b, into the FEE.

The main purpose of these tests was to characterize the correct behavior of the LYRA circuit together with the SDDs, and in particular to identify for which channels an anomalous behavior occurs.

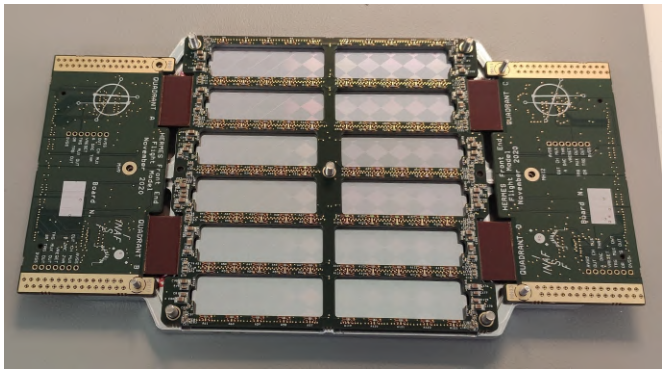

(a)

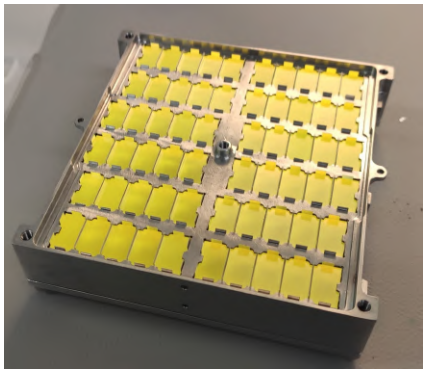

(b)

Figure 4.2: SDD detectors integrated into the FEE board. (a) The 60 crystals inside the crystal box (b). The two components will then be assembled in order to couple each pair of SDDs with its corresponding crystal.

The test equipment is shown in Figure 4.3. It consists of a power supply to feed the board (since the PSU board was not integrated at this stage), which provides low-voltage and high-voltage lines. In particular, three bias voltages were needed: 2.0 V for the LYRA-FE, and two separate 3.3 V lines for the LYRA-BE—one for the analog section (3.3A) and one for the digital section (3.3D). The HV at 120 V is required to polarize the SDD.

A digital oscilloscope, to observe the output of all 32 channels on each ASIC. The oscilloscope

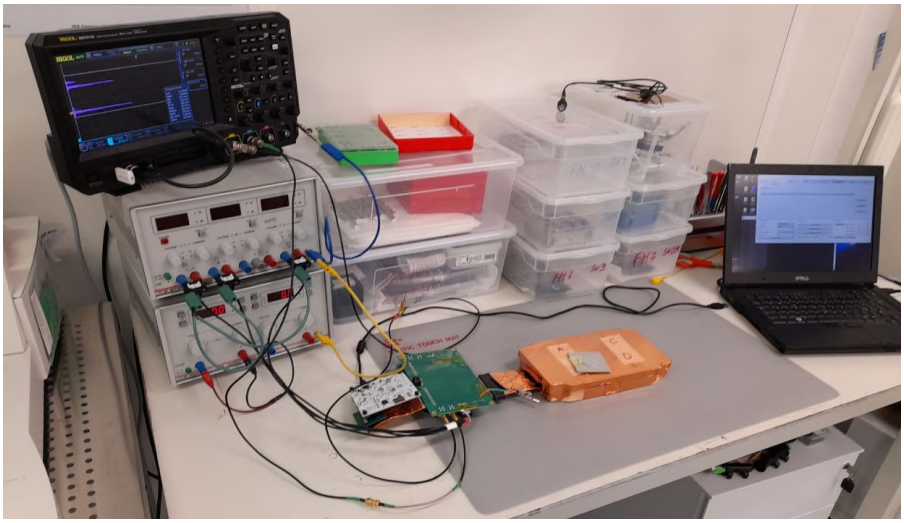

Figure 4.3: Test equipment used for preliminary calibration of the Front-End electronic board, incorporating the SDD detectors and the LYRA ASIC.

is able to produce real-time histograms and it works also as pulser, to stimulate electrically the ASIC by simulating photon signals. The pulser is monitored through the oscilloscope and connected to the test board; a Digilent™ Arty-Z7 board, equipped with an on-board FPGA (Field Programmable Gate Array) that serves as the control logic for configuring the ASIC; it is connected to the test with a custom flat cable and to the PC via an USB connection. A computer with a software interface, developed at INAF-OAS, that communicates with the Arty-Z7 board to acquire data and configure the ASIC. Configuration parameters are defined via the graphical user interface shown in Fig. 4.4, which are transferred to the internal ASIC memory registers via a serial interface handled by the FPGA. Through the interface it is possible to activate the channel to be tested and enable or disable the individual chains in the circuit and display the signal of interest.

The same test equipment was used after the integration of the GAGG:Ce crystals, with an additional cover to shield the crystals from ambient light.

The initial phase of the functionality tests consists of testing and characterizing all 120 LYRA-FE ASICs bonded to the SDDs, which are placed on the FEE board, and the 4 LYRA-BE ASICs. All acquisitions were made at room temperature between 22 and 24 degrees. Temperature is an important parameter to consider when analyzing results.

After verifying that the absorption values were nominal, 7 mA on the 3V3 line, 3 mA on the 2V0 line, the electronics of one quadrant at a time were tested. The functionality of the FE-electronics was evaluated in two operating modes: shaper and stretcher (See 3.3.2) selectable via the interface shown in Fig. 4.4 using identical configuration parameters for all tests (threshold 100, 120-bit DAC reset, internal single-channel mode). Using the pulser, the nominal behavior

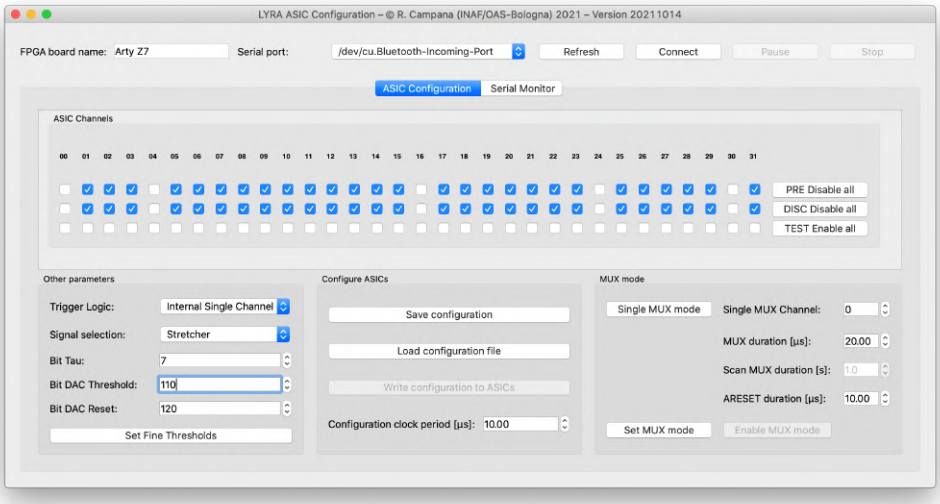

Figure 4.4: The graphical interface used to configure the ASIC parameters.

of both modes was verified for all channels in each quadrant, providing an immediate overview of noisy or strange channels. In Figure 4.5 an example of signals observed in shaper mode, on a single channel (a), and in stretcher mode, with a cycle on all 32 channels, is shown (b). The default threshold for all these preliminary acquisitions is set to 100. Fine threshold adjustments can be made on individual channels in the case of noisy channels (see 3.3.2).

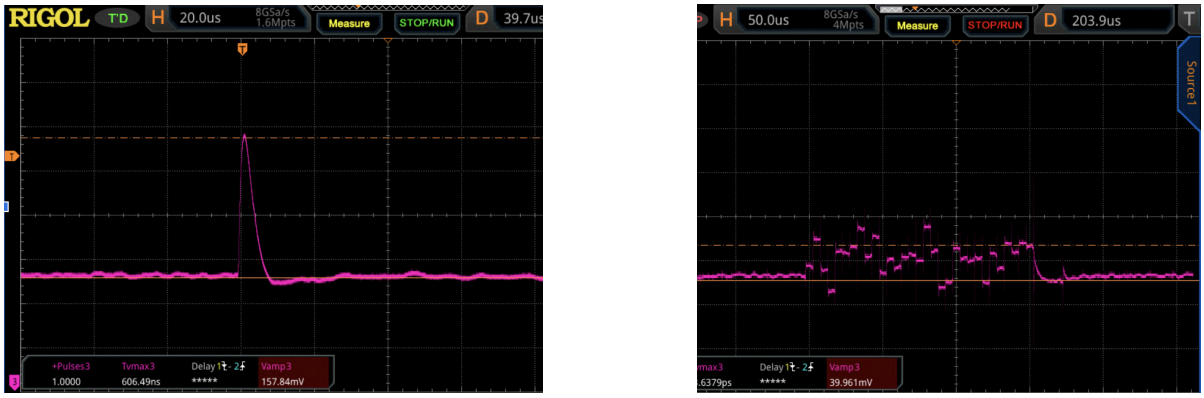

(a) **(b)**

Figure 4.5: Examples of signals observed in shaper mode, on a single channel (a), and in stretcher mode, with a cycle on all 32 channels (b).

To characterize the entire functionality of the channels, including the SDDs, spectra were acquired using radioactive X-ray sources ^{55}Fe and ^{109}Cd, followed by a preliminary calibration. During data acquisition, the sources were moved across each quadrant to ensure uniform irradiation of all channels.

Each spectrum was recorded with an oscilloscope: an example for a single channel is shown in

Figure 4.7, where three expected emission lines are clearly visible: one from ^{55}Fe at 5.9 keV, and two from ^{109}Cd at 22.1 keV and 24.9 keV.

The gain and offset values of each channel were measured using the relations described in Section 4.1.1: the peaks of the emission lines were first identified manually using the oscilloscope and then compared with the expected energies. Then, a linear regression was applied, from which the gain and offset parameters were extracted. The gain and offset distributions for quadrant B of FM4 are shown in Figure 4.6. The intrinsic dispersion of the values of the individual electronic components in the system leads to an expected variation in gain and offset between the different channels of approximately 20-30%.

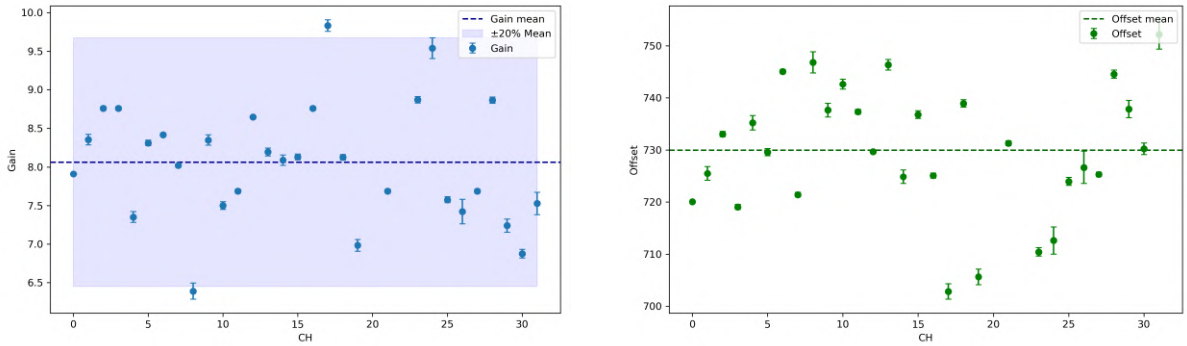

(a) **(b)**

Figure 4.6: Gain (a) and offset (b) values distribution with error bars, for each working channel of FM4 Quadrant B. The dispersion of gain and offset from channel to channel is consistent with the expected variation of ±20% from the average (blue rectangle for gain).

This initial estimate is preliminary and is intended to identify potential anomalies, since a this stage, interventions can still be made to repair or improve malfunctioning channels, or at least to attempt their recovery.

The second stage of detector assembly, carried out in Trento, involves integrating the crystal box. After cleaning it to remove any potential contamination, the 60 GAGG:Ce crystals are placed in the box and positioned in optical contact with the SDDs, with silicon pads interposed between them. The entire integration process was carried out by a dedicated specialist. Then the assembled detector module was put into the vacuum chamber for 40 minutes.

Once the module was ready for testing, the pulser was used to recheck all channels in both shaper and stretcher modes, verifying that no damage had occurred during assembly. To compare the results before and after box integration, a preliminary calibration was also performed at this stage.

The ^{55}Fe and ^{109}Cd sources were used to repeat the X-ray calibration, obtaining updated gain and offset values, while a ^{137}Cs source, with an emission line at 661.7 keV, was used to

Figure 4.7: Example of a single-channel spectrum recorded by the oscilloscope in purple. The three emission lines are clearly visible: one from ^{55}Fe at 5.9 keV, and two from ^{109}Cd at 22.1 keV and 24.9 keV.

determine the light output of the crystals. The relationships used for these calculations are those described in 4.1.2. The average effective light output was 13.5 e^-/keV for FM4, 12.8 e^-/keV for FM5, and 13.1 e^-/keV for FM6. Figure 4.8 shows the light-output distribution for FM4. At the operating temperature ($\sim$ 0°C for HERMES-PF) these values should reach the expected value (around 14-15 e^-/keV).

After testing, a definitive first picture of the behavior of each channel in all payloads was established. This information was used to define a preliminary ASIC configuration, which will be re-evaluated at each subsequent stage of integration, until the final configuration is reached once the payload is ready for orbit.

The analysis highlighted several typical issues affecting some channels: *noisy* channels, characterized by broad peaks, with reduced energy resolution. Channels affected by *retrigger*, mainly caused by residual pulses induced by the reset signal, which discharges the feedback capacitance of the preamplifier after each trigger event [106]. These channels require a higher threshold to function correctly. Channels showing a *low-energy peak*, often attributable to reset bounce effects or electronic noise. When one of these effects is too high, the channel may lose its functionality and be turned off.

Taking FM4 as a representative example, before crystal integration, 82 of the 120 channels (69.3%) were fully functional. 22 channels (18.3%) showed the low-energy peak before the ^{55}Fe line, but remained operational. Seven channels (5.8%) functioned marginally due to retriggering problems and required a higher threshold, while eight channels (6.7%) were classified as noisy, characterized by broad peaks. Only one channel (0.8%) was non-functional due to excessive retriggering. After crystal box integration, 77 channels (64.1%) remained nominal, 27 channels (22.5%) showed the low-energy peak. Five channels (4.2%) functioned marginally

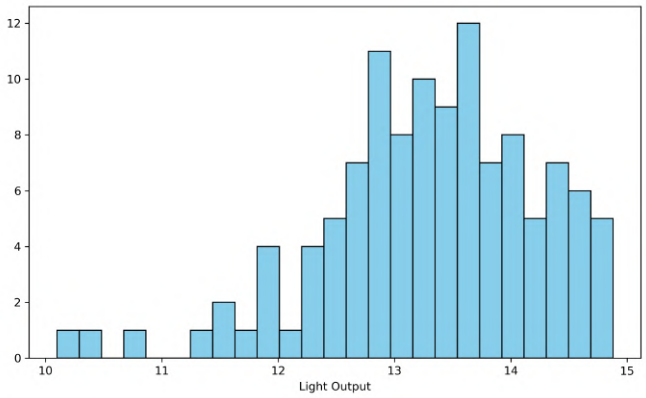

Figure 4.8: Effective light output distribution for all the active channels in FM4.

due to retriggering problems and required a higher threshold, while five channels (6.7%) were classified as noisy. Four channel (3.3%) were non-functional due to excessive retriggering.

There are no significant differences between the results obtained before and after the integration of the crystal box. The lack of a perfect match between the problematic channels in the two cases is most likely due to the configuration conditions associated with payload integration, rather than actual acquisition problems. Such variations may result from factors introduced during assembly, including the contact pressure of the silicone couplers, optical alignment, or small mechanical displacements during the integration.

Similar behavior was also observed in other flight models. After functional testing in Trento, the detector was carefully packed and prepared for transport to Rome, where a second preliminary calibration of the FEE was performed. Spectra of ^{55}Fe, ^{109}Cd and ^{137}Cs were acquired to verify the performance of the channels. The results were broadly consistent with those obtained in Trento, although some channels classified as noisy here appeared nominal and vice versa. These differences are mainly attributed to configuration conditions. A second ASIC configuration with on channels was defined. Once payload integration is complete, the final ASIC configuration will be verified and it will be determined whether the disabled channels can be recovered.

4.3 Calibration

The detector assembly was integrated with the BEE board, the PDHU and the PSU at INAF-IAPS facilities in Rome. With the payload fully integrated, official Calibration started.

4.3.1 Calibration set up

The HERMES-PF calibrations were performed in a class 10000 clean room[2] at the INAF/IAPS laboratories in Rome, Italy. The calibration experimental set up is shown in Figure 4.9.

Figure 4.9: The calibration experimental setup. The payload is in the climatic chamber, on the right [106].

The calibration parameters to be determined are the electronic gain, offset and effective light output for each channel. The calibration is performed by placing the flight unit in a suitable temperature-controlled climatic chamber, shown in Figure 4.10, and illuminating the detector with standard laboratory calibration sources (^{55}Fe, ^{109}Cd, ^{137}Cs). The radioactive sources are housed in a source holder (3D printed).

Based on the following source dimensions, specific holes were created in the holder: ^{55}Fe is a cylinder with a diameter of 8 mm and a height of 5.05 mm; ^{137}Cs and ^{241}Am are rectangular plates measuring 11.14 $\times$ 23.51 mm and 1.95 mm thick. ^{109}Cd is a cylinder with a diameter of 25.37 mm and a thickness of 5.57 mm. Therefore, a large central hole houses the ^{109}Cd and ^{109}Cs sources, while smaller side holes house the ^{55}Fe sources. A cover secures the sources in place. The source holder is mounted on a movable arm inside the climate chamber. The sources are usually positioned 18-20 cm from the top of the detector, allowing for almost uniform coverage of the detector plane.

The Electrical Ground Support Equipment (EGSE) used is shown in Figure 4.11.

[2] A *clean room* is a defined enclosed space where provisions are made to reduce particulate contamination and control other environmental parameters such as temperature, humidity and pressure. Clean rooms are classified according to the number and size of particles allowed per volume of air. In a class 10000 clean room, a maximum of 70 particles/ft^3 larger than 5 μm and less than 10,000 particles/m^3 larger than 0.3 μm is allowed.

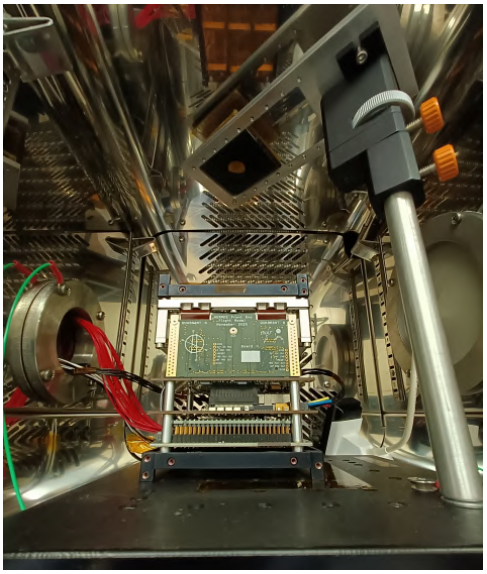

Figure 4.10: The HERMES-PF FM1 unit inside the climatic chamber, with the source holder above the detectors.

The fully integrated payload (whose components are described in Section 3.3) is placed in the climate chamber and it is powered through a monitored power supply (Keysight E36312A) and through an Uninterruptible Power Supply (UPS, an electrical apparatus that provides emergency power when the main input power source fails), which is characterized by three main voltage lines to the PSU: 12.0 V, 5.0 V, and 3.3 V.

This is completely similar to the power lines supplied to the payload from the satellite bus. The 12.0 V power line, controlled by the BEE, provides the voltage to the section of the circuit that generates the High-Voltage which polarizes the SDD detectors; the 5.0 V line gives the voltage needed to supply various loads in the FEE and the feedback network of the HV section. It also powers some BEE sections, such as the four ADCs for science event acquisition and the pulse generator for detector calibration; the 3.3 V line feeds the BEE and the ADC dedicated to housekeeping data. All payload configuration and data acquisition operations are performed using a Windows 10 computer, with remote desktop access enabled, and custom-made interface to communicate with the PDHU (see Section 3.3). A temperature sensor and logger is placed inside the climate chamber to monitor the thermal environment (humidity and temperature) through its specific software. The humidity of the environment inside the chamber is also controlled by a nitrogen cylinder. The flow of nitrogen, at around 0.5–1.5 liters per minute, is feed into the chamber through a pressure reducer set at 1 bar. The use of nitrogen is intended to minimize the rise of humidity and prevent condensation inside the chamber during thermal cycles.

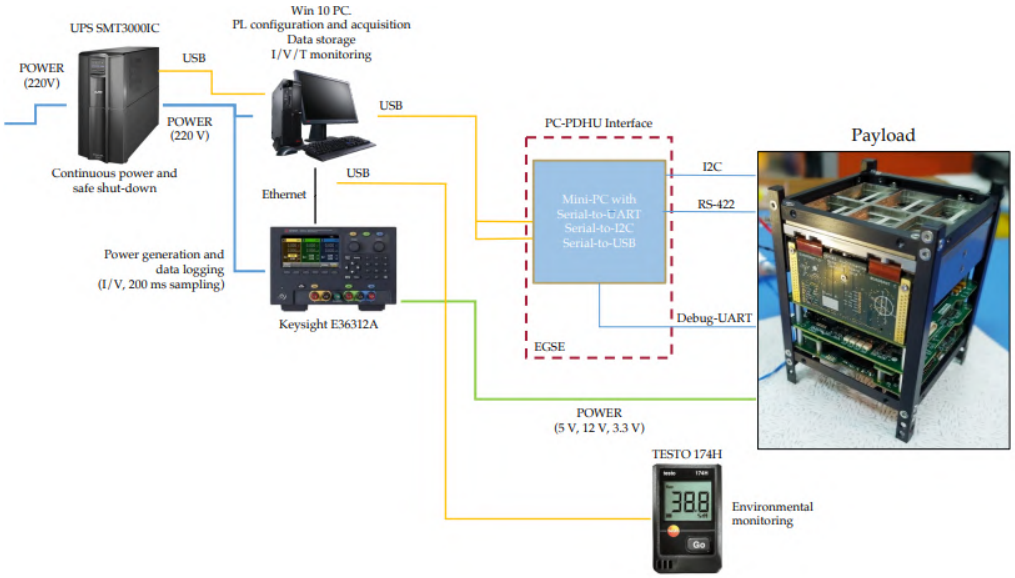

Figure 4.11: Diagram of the HERMES EGSE used for the calibrations [112].

4.4 Mescal: data reduction pipeline

During the integration and testing of HERMES-PF, a data reduction pipeline was developed to enable simple and immediate reduction of the data acquired during calibration activities [112, 116].

This pipeline will not be part of the standard HERMESDAS scientific calibration pipeline (developed by SSDC [117]).

According to the official standard defined for HERMES-PF, raw binary data acquisition files are converted to a standard FITS *Level 0* format. More in detail, the HERMES P/L (the BEE) generates a RECORD LIST for each quadrant, typically once per second (i.e., a total of 4 RECORD LISTS per second). This record list includes a 116 bytes HEADER with the temperatures, housekeepings, and GPS time at the beginning of the observation and the number of entries in the given list. After the HEADER, the EVENT DATA are reported in packets of 4 bytes (*records*). The first record contains the time and the multiplicity of the event (i.e., how many SDD channels were triggered), and is followed by a series of records with the information on the ADC counts of each triggered SDD (e.g., ASIC ID, GAGG crystal ID, SDD ID, ADC amplitude). Therefore, the number of records for each event depends on how many pixels are fired. At the rising edge of the Pulse-Per-Second (PPS) signal generated by the on-board ultra-stable atomic clock (CSAC), a special record called Absolute Time (ABT) Event is produced containing the on-board time (OBT) information.

From this *Level 0*, the HERMESDAS scientific calibration pipeline [117] generates *Level 1*, i.e., the calibrated event files. The following stage of the software pipeline involves *Level 2* files,

that is, the light curves and spectra that will be analyzed and lead to the scientific outputs. For the calibration activities, a conversion from *Level 0* format to an intermediate FITS *Level 0.5* was required, necessary to ease further processing and data analysis. This format mainly translates raw housekeeping values (voltages, currents, temperatures) into physical units; it calculates the event timestamp, in seconds, by summing the OBT of the previous ABT event; it expands multi-pixel events up to 6 separate columns (with LYRA-BE channel addresses and ADC values).

Data calibration and analysis were performed using this custom-made highly automatized pipeline of Python scripts, named `mescal`[3](herMES CALibration pipeline) [116]. The `mescal` pipeline is implemented in Python 3 and requires the Level 0.5 input file and an explicit indication of the list of radioactive sources, with their emission line energies, used for calibration data acquisition. The energy units (keV) given for the list of calibration sources will be the units of the output calibrated spectra. The working logic of the Python-implemented algorithm is summarized in Figure 4.12.

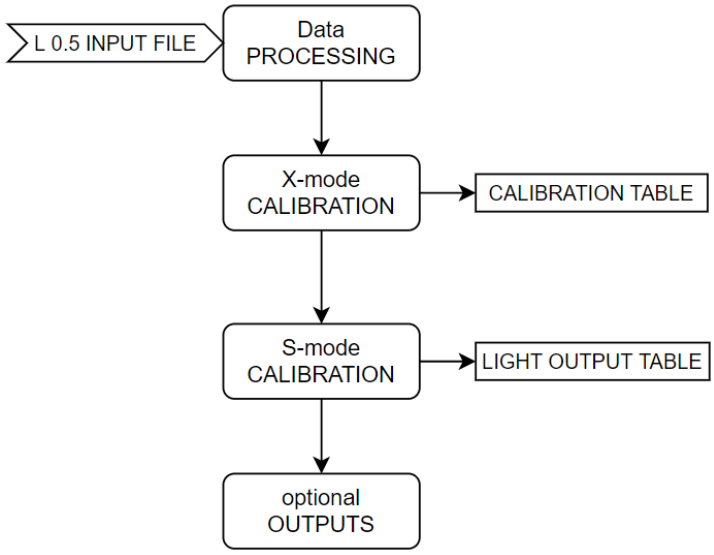

Figure 4.12: Block diagram of the `mescal` logic structure.

In detail, the algorithm proceeds as follows:

1. **Data readout**: once initialized, `mescal` accesses the detector map associated with the flight model being analyzed, containing the mapping of the raw address to SDD/crystal ID (specific to each model), as well as the acquired data file. The input data is read and organized in a Python `pandas`[4] data frame, creating a table with rows representing

[3] `https://github.com/baronig23/Hermes-Cal-SW`
[4] `https://pandas.pydata.org/`

a trigger event and columns storing the relevant information.

It is also necessary to specify the list of the used calibration sources, indicating their respective emission lines. The corresponding decay energies are stored in one of mescal's support libraries.

In this first stage, a filter is also implemented to remove events associated with electronic noise and spurious events.

2. **Event type discrimination and tagging, multiplicity filtering and histogram building:** events are tagged as "X-mode" or "S-mode" to discriminate between events generated directly in the SDDs and events generated in the scintillators. The logic of the event discrimination process is as follows: the entire list of channels which are read out in the same trigger cycle is examined. If two channels reading the same crystal simultaneously see an event (multiplicity 2), it is tagged as an "S" event, while if the event is seen by only one channel (multiplicity 1) it is called an "X" event. Tags are defined and stored for each single event. The histogram of events tagged as "X" and "S" is then constructed, obtaining two spectra for each channel. These spectra include only events with multiplicity exactly equal to 1 in the first case, and with multiplicity exactly equal to 2 in the second. Higher-multiplicity events (e.g., photons which Compton scatter between two crystals) are simply discarded, at this stage.

3. **X-mode calibration:** if at least one of the radioactive sources entered by the user is listed as an X-ray emitting calibration source, the algorithm will attempt to perform energy calibration on the X-mode spectra.

   To search for the emission lines, the software uses SciPy `findpeaks`[5] function to identify local maxima in the histogram based on parameters such as height, width, and prominence (i.e., the distance between the peak and the baseline), iterating until the desired number of lines is found.

   If there are more candidates (K) than desired lines (N), the system generates all possible combinations of N peaks on K, shuffles them to avoid ordering bias, and processes each as a potential set of lines.

   To correctly identify emission lines, `mescal` assigns a score (higher values indicate better matches) to each combination of candidate peaks based on several metrics. These metrics include [116]:

[5] `https://docs.scipy.org`

- *a prior error score*, the sum of the distances between the detected peaks and the predicted positions using an initial assumption about gain and offset.
- *linearity*, the correlation coefficient of a preliminary linear regression between the peaks and the energy values is used.
- *baseline distance*, using the preliminary gain and offset parameters from the linearity evaluation, `mescal` assigns each candidate-peak combination a score equal to the opposite of the distance of the minimum energy value (i.e., the first non-zero bin) to the expected 2 keV.
- *peaks prominence*, product of the peak heights in the combination.
- *features width* FWHM dispersion – the more homogeneous they are, the higher the score.

Each combination is assigned a rank based on each metric: the best gets rank K (the highest), the worst gets rank 1. The ranks of the different metrics are added up and the combination with the highest sum is chosen as the winner. In the event of a tie, the one with the best rank in a single metric is preferred.

In problematic cases, the user can intervene manually: the ranges in which to search for each line can be redefined via command line prompts, and the identification process can be restarted.

These lines positions are used as input to a Gaussian profile fitting algorithm (using the `lmfit`[6] package), which returns the position of the best peak and the full width at half maximum (FWHM) for each line.

The selected set of pairs composed of the ADC value for the centroid of a data line and the energy value of its corresponding calibration line are given as input to a least-squares linear fit algorithm. The fit will return gain, offset and their errors for each channel. The console standard output will list for which channels, if any, this calibration step failed. Each event will then be separately calibrated for each channel in energy units, and a final calibrated X-mode event list will be created.

4. **S-mode calibration:** if at least one of the user-input radioactive sources is listed as a gamma-ray emitting calibration source, the algorithm will attempt to perform energy calibration on the S-mode spectra. The actual light output from the scintillator is referenced to the ^{137}Cs line at 661.67 keV; the algorithm automatically uses the peak search

[6] `https://lmfit.github.io/lmfit-py/`

procedure to find this line, assuming it is the only line which is present. Then, the algorithm fits the Gaussian profile on the position given by the peak finder, returning the position of the center of the line and its FWHM.

Then, for each channel, the algorithm takes the gain and offset parameters found during the X-mode calibration and converts the S-mode spectrum in units of electrons. For each pair of channels reading the same crystal, the events are summed event by event in electrons. This yields a list of summed events per crystal in units of energy. The summed spectrum is used to derive the total light output, emitted by the crystal and read by the two channels, by fitting it to the 661.67 keV line. The next step involves deriving the light outputs of the individual channels by weighted averaging of their respective Gaussian fits. The software returns a crystal-summed event list in energy units. The console standard output will list the channels, if any, for which this calibration step failed.

5. **Visualization plots and output writing:** The pipeline produces three main types of output: results tables (reports), data plots, and event lists [116].

   The *reports* include all parameters derived from spectral fits in both X and S modes, together with the calibration parameters obtained (gain, offset, and effective light output). An additional report provides the resolution of emission features in X mode. These outputs serve as inputs for generating the final calibration files, which are stored in the standard Calibration Database (CALDB) and subsequently used by the scientific pipeline HERMESDAS [117].

   The *event list* is a table calibrated according to the energy of the photon events, exported in FITS format. It includes the amplitudes of the events expressed in both energy units and electric charge units, classified by type (X or S), together with their pixel addresses (CH and QUADID) and a time tag. The time is reported in instrumental units (seconds since the start of the most recent data acquisition), while in flight it will be expressed in Mission Elapsed Time (MET), defined as the number of seconds elapsed since January 1, 2022, at 00:00 TT.

   The *plots* produced include: raw and calibrated spectra per channel (in X and S mode), calibration parameters (gain, offset, light output with relative errors and percentiles), and a color map of counts to verify correct data acquisition. Diagnostic spectra are also generated for active and functioning channels only to verify the correct identification of calibration lines, and a linearity graph with least squares fit and residuals. The pipeline also provides a resolution map (FWHM at the lowest energy calibration line). Finally, it returns the energy-calibrated spectra for X and S modes, both for single channels and as

a single spectrum obtained by stacking the calibrated events.

Some of these plots are shown in the Section 4.5.4.

`Mescal` offers the possibility to define which results to write as output tables and which graphs to save as output. The available saving options are illustrated in Figure 4.13.

Figure 4.13: Menu of save and display options provided by `mescal`. There are ten available options that allow to save plots and tables of results.

4.5 Calibration Campaigns

The author took part in the calibration campaigns for payloads FM3, FM4, FM5, and FM6. The acquisitions were carried out from January to May 2023. The overall procedure for the calibration is the same for all the flight models.

4.5.1 Acquisition Procedure

The calibration plan performed on all the flight units follows the steps summarized below:

1. radioactive sources are placed on the source holder, which is fixed on the mechanical support inside the climatic chamber. Acquisitions are performed using several sources simultaneously;
2. open the N_2 flux, set the flow at 0.5–1.5 l/min, set the climatic chamber to the required temperature and wait until the complete thermalisation (about 1–2 hours, depending on the temperature);
3. the payload is turned on and put into the *Idle* (see Section 3.3.5) operating mode (all quadrant are configured and the detector high voltage is turned on);
4. once the payload is in a stable thermal environment (monitored by the external and internal temperature sensors), data acquisition is performed, taking care to accumulate at least 10^4 counts for each radioactive source and for each channel, as described in tables 4.14.2;
5. the data are downloaded and analyzed;
6. the climate chamber is set to another temperature and the sequence starts again.

Each payload has its own ASIC configuration in which the operating and enabled channels and the acquisition threshold are defined. Calibrations were carried out at three threshold values (105, 95, and 85 in units of the internal ASIC DAC), and for each threshold setting, tests were performed over a temperature range from -20 °C to 20 °C.

4.5.2 Flight Model 6

By way of example, the main results obtained for the FM6 payload are presented in this section. A location counts map of SDDs and scintillator crystals produced using `mescal` is shown in Figure 4.14. LYRA-BE coupled channel addresses are indicated: the grid shows the physical position of each channel in the detector plane, with the color scale indicating the total number

of events detected per channel. The four main blocks represent the four quadrants: A, B, C, D. Dashed channels are those that are switched off.

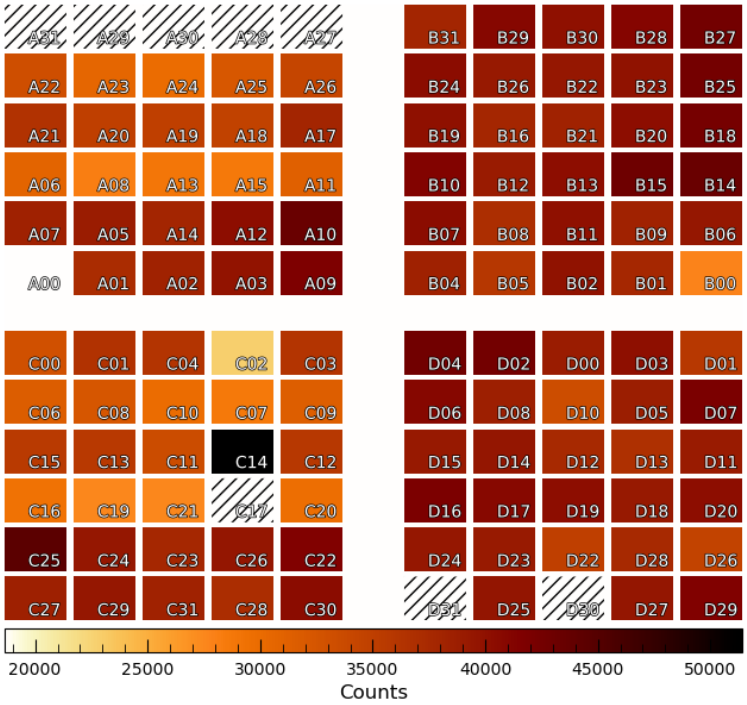

Figure 4.14: Map of FM6 payload counts produced with `mescal`. Each cell in the grid corresponds to the physical position of a channel in the detector plane,where the division into four main blocks represents the four quadrants. The color scale represents the total number of counts recorded per channel.

A total of 8 non-working channels out of 120 were identified, mainly due to excessive noise, retriggering, or other issues(see 4.2.1). This is consistent with process variations in the ASIC and SDD production and integration. The non-working channels are distributed as follows:

- Quadrant A: CH27, CH28, CH29, CH30, CH31
- Quadrant B: all working
- Quadrant C: CH17
- Quadrant D: CH30, CH31

Importantly, each crystal is read out by at least one functioning channel. Channels that are operational but paired with a channel that is turned off are called widows (See Section 4.6.5).

4.5.3 Preliminary tests

Before proceeding to the calibration campaign, several *preliminary tests* were carried out to verify the functionality of the experimental set up: the goal was to verify that it is possible

to turn on the system and acquire safely. First, the step-by-step on/off procedure was tested by verifying a smooth completion of the procedures and making acquisitions as expected. It was verified that the three low-tension supplies (3.3 V, 5 V, 12 V) coincide with the nominal ones and that the current absorptions are as expected at each different power-on step: when turned on, the absorptions are 297 mA, 60 mA, 68 mA, respectively. In *Idle* mode they are 294 mA, 73 mA, 24 mA. In *Observation* mode they are 298 mA, 85 mA, 26 mA, as shown in Figure 4.15. High voltage was also controlled by opening the 12 V line switches and ramping-up automatically the high voltage. This operation took a few tens of seconds.

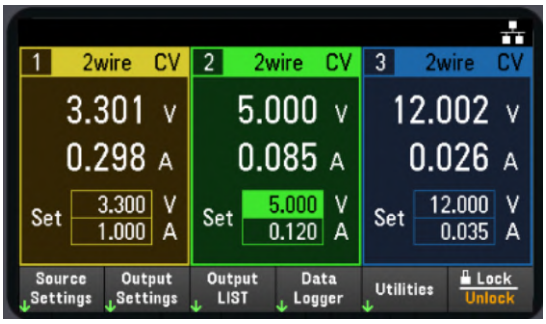

Figure 4.15: The three low-tension supplies (3.3 V, 5 V, 12 V) with the associated current absorptions (298 mA, 85 mA, 26 mA) shown on the low voltage generator screen during preliminary tests.

Likewise, the housekeeping values were also verified. The housekeeping signals (monitoring the various voltages and currents in the payload) were acquired using several ADCs implemented in the BEE board. The next step was to install the sources, verify the count rates, and check the climate chamber temperature. To limit the overall count rates, ^{55}Fe was screened with a thin kapton filter and rates were about 700–1000 counts/s/quadrant; ^{109}Cd with an aluminum filter and rates were about 2500–3500 counts/s/quadrant. The ^{137}Cs had a rate of about 3300–5000 counts/s/quadrant. After that, the chamber was thermalized at one required temperature at a time, and preliminary test acquisitions were performed for each for all sources simultaneously.

4.5.4 Acquisitions and main outputs

To start the acquisitions, the procedure is followed step by step (Section 4.5.1). The three sources are placed and the climate chamber is set at one temperature at a time. All four quadrants are tested together. Next, the main outputs of the calibrations (gain, offset, light output and spectra) for different configurations are illustrated.

As explained in the Section 4.4, in the X-mode, the calibration software finds the position of the maximum of each peak for each channel and compares the position of the measured peak with the energy of the known calibration lines. Therefore, through a linear fit of these data,

the calibration line for each channel is obtained along with the calibration parameters, gain and offset (slope and intercept of these fits).

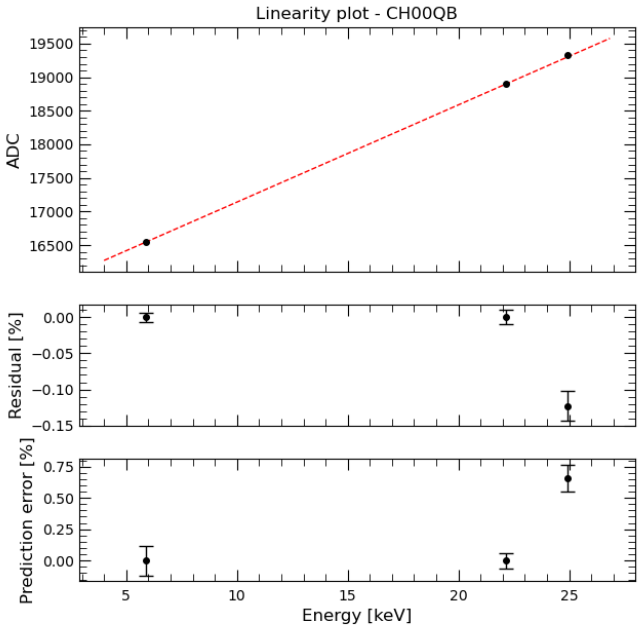

Figure 4.16: Linear fit for the 'X' mode calibration, for Channel 0 on Quadrant B, for a given acquisition. Relative residuals and their errors are plotted below.

Since this procedure is identical for all quadrants, in Figure 4.16 a representative linear plot example for Channel 0 on FM6 Quadrant B at threshold 105 is shown. After this step, the calibration parameters gain and offset for each quadrant in the different configurations are obtained.

As example, the gain and offset distributions for quadrant B at -10 °C are shown in Figure 4.17a. The inherent dispersion of the values of the individual electronic components in the system leads to an expected variation in gain and offset between different channels of around 20-30%. Thus, percentiles 25-75 are overplotted in red.

Through the calibration parameters, for all configurations, the calibrated X-spectra are obtained. Figure 4.18 shows a representative calibrated X-mode spectrum for quadrant B channel 26, showing the X-ray lines of ^{55}Fe at 5.89 keV and of ^{109}Cd at 22.1 keV and 24.9 keV.

The second part of the acquisitions is the S-mode calibration that aims at verifying the LY for each channel. Again, acquisitions were made in the different temperature and threshold configurations. As example, the light output distribution for quadrant B at -20 °C is shown in Figure 4.17b. For the LY, there is not a defined expected channel-to-channel variation, since other factors, such as mechanical or optical couplings, also come into play. However, to

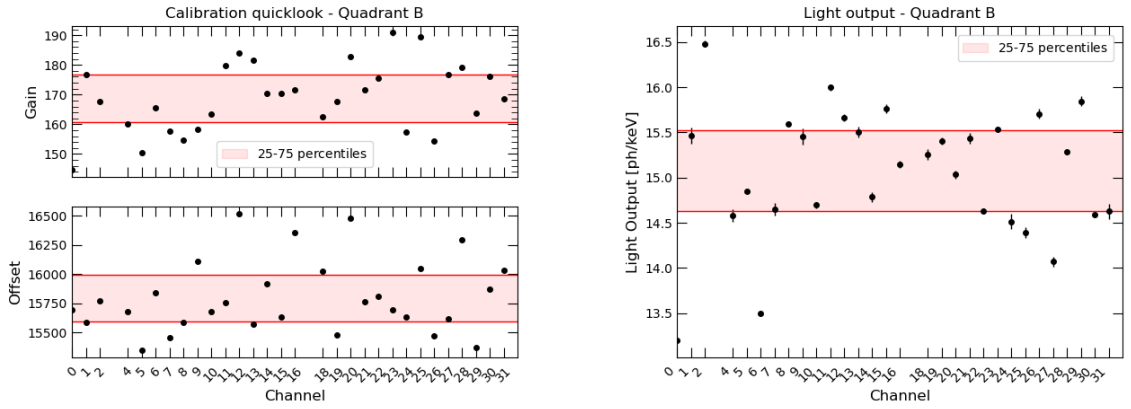

(a) **(b)**

Figure 4.17: (a) Gain (top) and offset (bottom) values distribution with error bars, for each working channel of Quadrant B at -10 °C at threshold 105. (b) Light outputs values distribution, with error bars, for each working channel of Quadrant B at -20 °C, threshold 105. 25-75 percentiles are overplotted.

guide the representation of the results, again the 25-75 percentiles are overplotted in red. A few outliers are visible, likely associated with a non-optimal optical contact between SDD and crystal.

In Figure 4.19 the S-mode calibrated spectrum of the entire FM6 HERMES detector (all quadrants) at the temperature of -20 °C, showing the gamma-ray lines of ^{137}Cs at 662 keV, is shown.

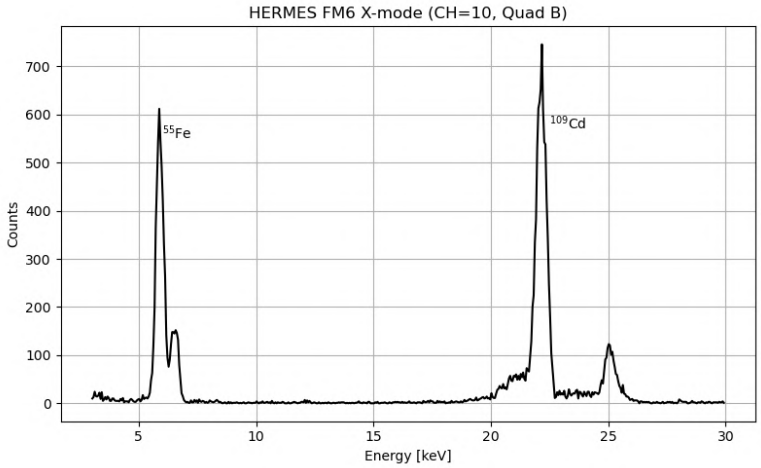

Figure 4.18: X-mode calibrated spectrum of ^{55}Fe and ^{109}Cd radioactive sources for quadrant B channel 10, at temperature of −10 °C. The X-ray lines of ^{55}Fe and ^{109}Cd around 6 keV and 25 keV, respectively, are indicated.

Similar distributions, plots and spectra are obtained for the other quadrants at the other

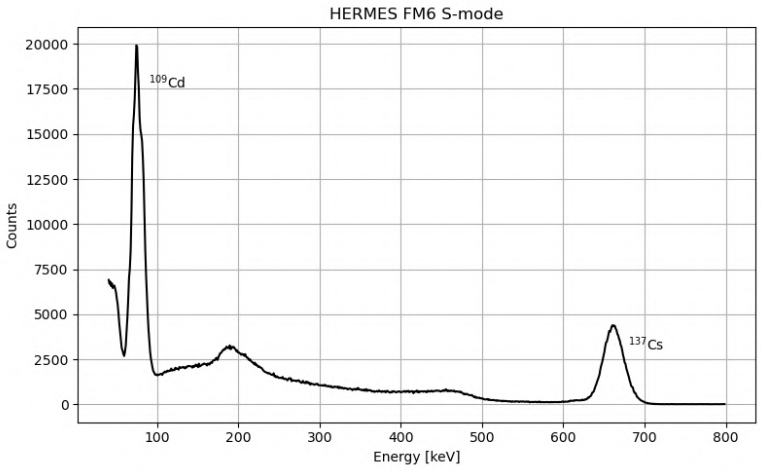

Figure 4.19: Summed S-mode calibrated spectrum of the whole FM6 HERMES detector, illuminated using the ^{137}Cs radioactive source, at a temperature of -20 °C. The Cs 662 keV line is indicated.

temperatures and thresholds. The same outputs were obtained for the remaining payloads. From the complete series of acquisitions in X and S modes, across the entire temperature range and thresholds, the calibration parameters (gain, offset and light output) for each operating channel of all flight models were derived. These results were consolidated in the Calibration Database (CALDB), which will serve as a reference for in-orbit configuration and subsequent performance monitoring.

4.6 Payload Technical Performances

For all the payloads, a statistical analysis of the calibration parameters was performed to have an overall picture of the payloads behavior under all the different conditions [106]. The operational temperature range of the HERMES-PF payloads extends from -20 °C to $+20$ °C, with the detectors expected to spend most of the time near ~ 0°C.

The first aspect analyzed is the overall fraction of calibrated channels for each payload in X- and S-mode, that are summarized in Table 4.3 [106]. In X-mode, all payloads except FM1 show calibrated fractions between 82.2% and 93.3%, corresponding to effective areas of 45.0–50.4 cm^2 out of the total 54.015 cm^2. S-mode fractions are lower, ranging from 70.0% to 83.3%. FM1, affected by a hardware issue, had only three active quadrants, yielding a geometric area of 40 cm^2, with 82.2% and 68.9% calibrated in X- and S-mode, respectively. S-mode calibration requires prior X-mode calibration of both channels reading the same crystal, therefore S-mode fractions cannot exceed X-mode. Uncalibrated channels were mainly disabled due to excessive noise, retriggering, or other issues(see Section 4.2.1).

					Energy Resolution [eV]			[%]
	f_X [%]	f_S [%]	T_X [keV]	T_S [keV]	5.9 keV	22.1 keV	24.9 keV	662 keV
PFM	91.7	83.3	1.7	34.9	374 ± 3	475 ± 3	502 ± 5	4.79 ± 0.02
FM1	82.2	68.9	2.1	45.0	390 ± 4	483 ± 4	508 ± 7	4.86 ± 0.02
FM2	83.3	70.0	2.1	43.2	317 ± 5	426 ± 3	434 ± 6	4.73 ± 0.02
FM3	90.0	80.0	2.2	42.5	300 ± 3	419 ± 3	438 ± 5	4.74 ± 0.03
FM4	90.0	80.0	2.6	46.2	295 ± 3	414 ± 3	435 ± 6	5.11 ± 0.04
FM5	90.0	80.0	2.2	43.5	295 ± 3	413 ± 3	432 ± 6	4.82 ± 0.03
FM6	93.3	83.3	2.0	39.1	293 ± 3	413 ± 2	423 ± 5	4.74 ± 0.02

Table 4.3: A summary table of the payloads performances measured at 0 °C, reporting the calibrated channel fraction in X- (f_X) and S-mode (f_S), the X-mode energy thresholds (T_X), the S-mode energy thresholds (T_S), and FWHM energy resolution as estimated from the emission lines ^{55}Fe 5.9 keV, ^{109}Cd 22.1 keV and 24.9 keV, and ^{137}Cs 662 keV.

Although the CALDB acquisitions were made under controlled temperature conditions (climatic chamber), the real temperatures used for the analysis are those measured by the temperature sensors positioned on the detector, as shown in Figure 4.20a. Each quadrant has its own reference sensor, plus two central sensors. An example of temperatures measured by FM3 sensors for an acquisition at 0°C is shown in Figure 4.20b.

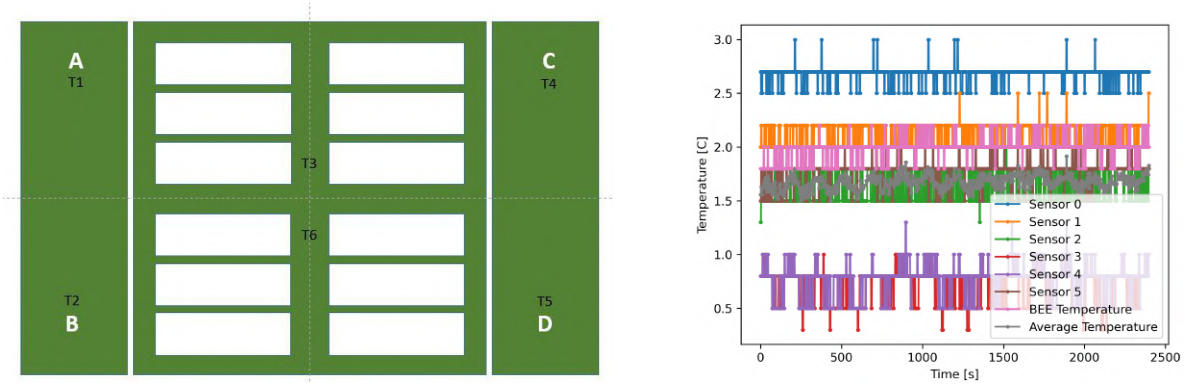

(a) **(b)**

Figure 4.20: (a) Schematic diagram of the detector seen from above showing the quadrants and the location of the temperature sensors. (b) Example of temperatures measured from FM3 sensors for one acquisition at 0°C.

4.6.1 Gain and Offset

The gain and offset parameters depend on the characteristics of the components within the spectroscopic chain, therefore some degree of dispersion is expected. Figure 4.21 shows the values measured for all 720 channels calibrated on all payloads at 0 °C.

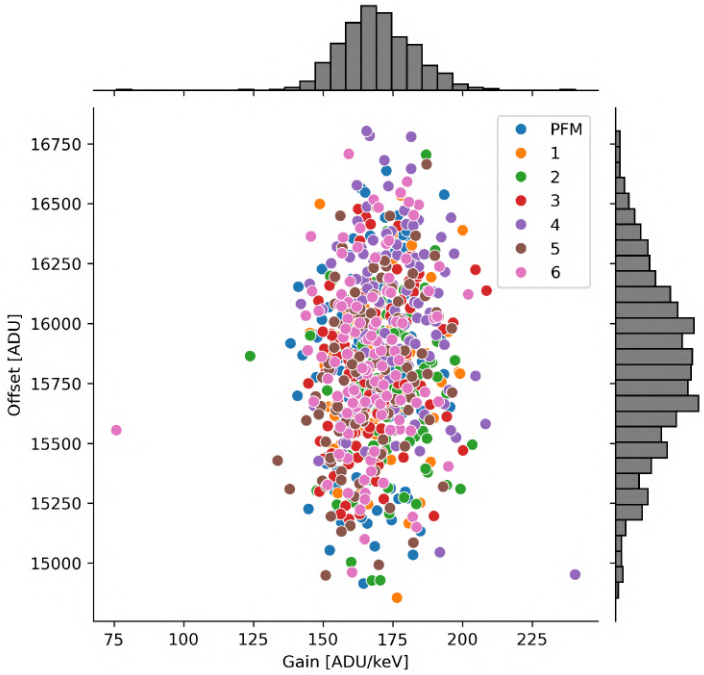

Figure 4.21: All channel gains and offsets (points) and their marginal distributions (histograms), for all payloads, at a temperature of 0 °C. Each color represents a specific PL.

When considered individually, the average values of the gain and offset distribution are 169.5 ADU/keV and 15,824 ADU, respectively, with corresponding standard deviations of 13.6 ADU/keV and 356 ADU [106].

The gain and offset calibration parameters also depend on temperature. In particular, temperature variations are due to two contributions: the intrinsic contribution of the electron chain, and that of the digitizing part of the signal (ADC). These can differently depend on temperature and have a certain range of variability. Depending on their relation, these two contributions can overlap, leading to different global variations of gain and offset with respect to the temperature. Hence, for each channel in each quadrant, and for each threshold, changes in gain and offset were analyzed and modeled as a function of different acquisition effective temperatures.

The trend as a function of temperature was modeled by the equation 4.7, a polynomial of

degree 2 for both gain and offset:

$$y = c_2 x^2 + c_1 x + c_0 \tag{4.7}$$

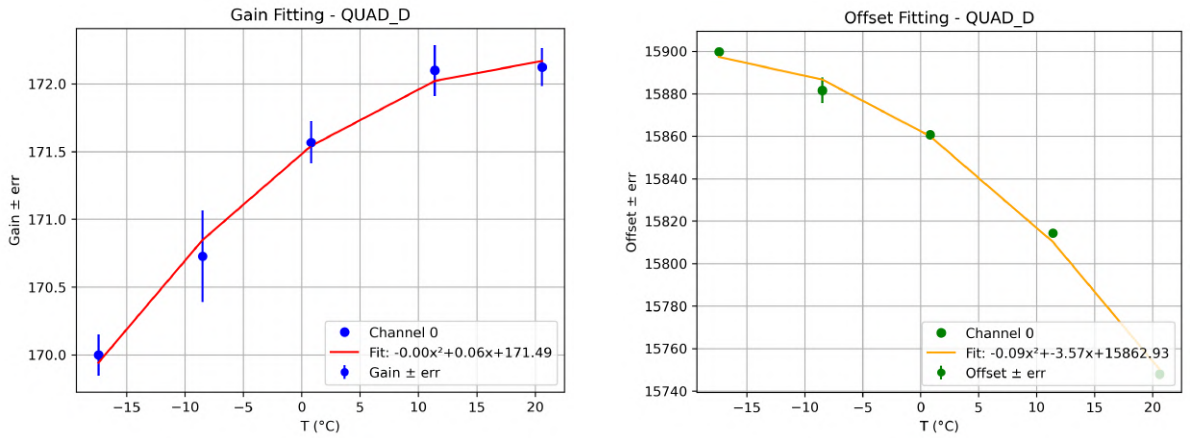

(a) **(b)**

Figure 4.22: Polynomial fit of degree two for gain (a) and offset (b) as a function of temperature for FM4 channel 0 on quadrant D. Fit equation is shown in the legend.

In Figure 4.22 an example of polynomial fits of degree two for gain and offset as a function of temperature for channel 0 on quadrant D of FM4 at threshold 105.
This parameterization made it possible to define a general model, describing the variation of parameters with temperature, applicable for almost all channels (except for the anomalous ones). It also confirmed, as expected, that the behavior of the parameters is consistent with temperature, excluding any issues in calibration.
For each individual channel in each payload, the change in gain and offset parameters between +20 °C and −20 °C remains below 1%. This confirms the stability of the X parameters and the calibration of the spectroscopic chain, as will also be confirmed by the calibration carried out after the payload integration into the service module (See Section4.6.6).

4.6.2 Light output

Light output for the 312 scintillators successfully calibrated in S-mode has a median value of 29.1 photons/keV, with a standard deviation of 2.3 photons/keV.
The effective light output also depends on temperature, with an expected intrinsic increase of ∼20% going from the value of room temperature to −20 °C [115]. Therefore, the LY variation for each channel in each quadrant was also analyzed for the different temperatures acquired. As for gain and offset, the trend as a function of temperature was modeled by the equation 4.7, a polynomial of degree 2. As an example, in Figure 4.23 the global average of light outputs

at fixed temperature as a function of the five effective temperatures for FM3 quadrant C is shown. The coefficients of the fit are shown on the graph. The goodness of fit is indicated by the residuals, which are of the order of ∼1%.

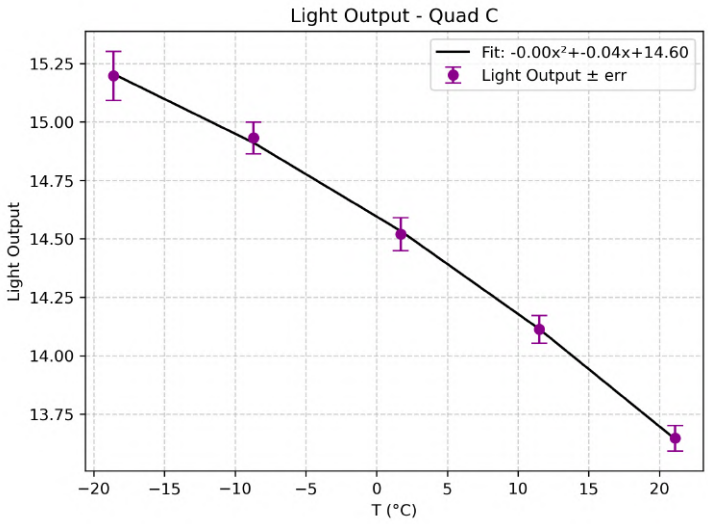

Figure 4.23: The global average of light outputs at fixed temperature as a function of the five effective temperatures for FM3 quadrant C. The polynomial fit of degree two is shown in the legend.

Similar plots are obtained for other quadrants and for the other PLs.

Analysis shows that the median difference in light output of 2.5 photons/keV between temperatures +20 °C and −20 °C, corresponding to a 9.4% percentage improvement. The slight difference from the expected variation, is due to the fact that, in addition to the intrinsic increase in light output with temperature, other factors come into play in the variation, including changes in the optical coupling between the GAGG crystal-SDD, that are due to the mechanical contractions of the system with temperature [106].

A secondary effect may contribute to the increase in light output at low temperatures. As the bulk silicon of the SDD cools, electron mobility improves, reducing the ballistic deficit of the detector. This allows a greater percentage of the photoelectrons generated by scintillation to be captured by the electronics, creating an apparent increase of the scintillator light output.

The opposite trend is observed in 26 scintillators, where light output decreases at lower temperatures. This behavior is most likely mechanical in origin and can be attributed to irregular optical coupling. In fact, scintillators exhibiting this effect also show the greatest discrepancies between the actual light collected by the two SDD channels, with one channel capturing significantly more scintillation light than the other. At low temperatures, thermo elastic deformations of the detector assembly can further degrade the optical coupling, leading to an apparent reduction in the crystal's light output.

4.6.3 Energy thresholds

One of the key features of HERMES-PF is its ability to operate at low energy thresholds. The detector energy threshold is the minimum energy required to a photon to be detected, either in X- or S-mode.

The activation threshold is set via two configuration levels: a global setting via the LYRA-BE DAC, which affects all LYRA-BE channels, and an individual 'fine threshold' setting, which allows you to equalize the threshold between individual channels, adjusting any differences (See 3.3.2).

The effective energy threshold is determined by the DAC-programmed value in combination with the specific characteristics of each channel (gain, offset, and light output) and the payload temperature [106].

The median values of the channel threshold distributions represent the minimum energy at which half of the detector is operational, as summarized in Table 4.3.

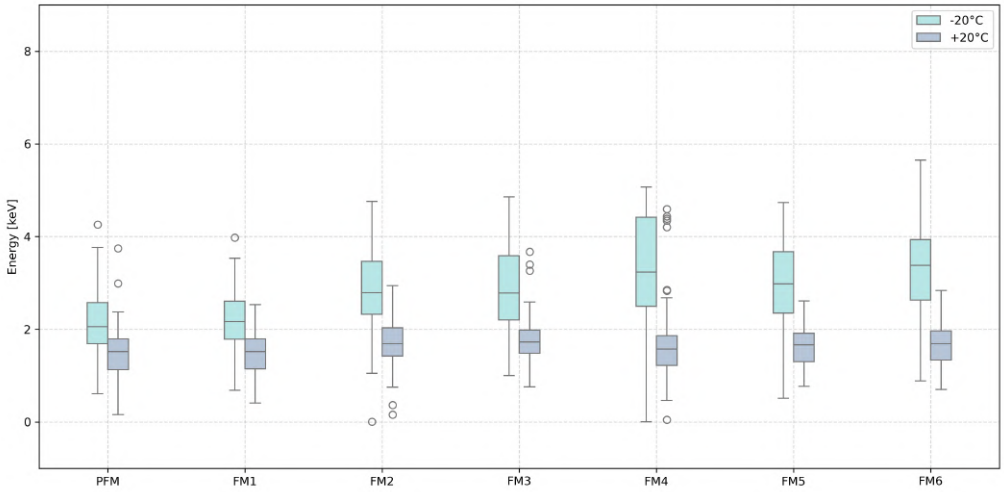

Figure 4.24: Low-energy threshold for X-mode at temperature −20 °C and 20 °C. The box-plot width is proportional to the number of correctly calibrated channels from each payload.

Changes in temperature can affect the DAC threshold reference current level, leading to variations in the energy thresholds. Specifically, we observe an increase in energy thresholds at constant DAC threshold setting for lower temperatures [106], as shown in Figure 4.24, which displays the distributions of the X-mode energy thresholds at −20°C and +20°C for all HERMES-PF payloads.

To mitigate the impact of temperature on energy thresholds, the back-end DAC threshold parameter can be lowered during operations at low temperatures. Lowering the DAC setting corresponds to a reduction of the effective energy threshold, compensating for the threshold increase induced by low-temperature conditions.

A specific calibration campaign, aimed at estimating the temperature-dependent variation of the DAC threshold, was carried out and described in [106].
Another aspect that was verified is the independence of the calibration parameters from the selected threshold. Figure 4.25 shows an example of the gain for each channel in all quadrants of FM3 at the three acquisition thresholds (105, 95, and 85) at 0 °C. Apart from a few channels, probably affected by noise or defects, the measurements overlap, confirming that the calibration parameters do not depend on the threshold.

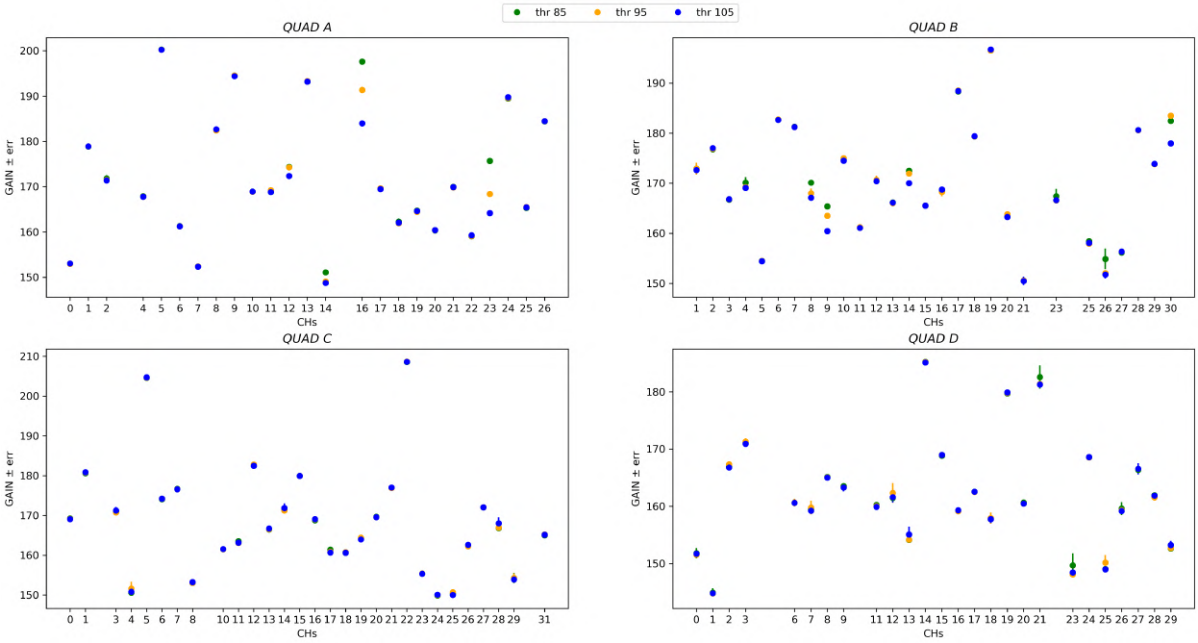

Figure 4.25: Gains of each channel in all quadrant of FM3 at the three acquisition thresholds (105, 95, and 85) at 0°C. The parameters are independent of the threshold.

4.6.4 Energy spectroscopic resolution

The energy spectroscopic resolution differs between X and S modes. A summary of the resolutions obtained from the integrated calibration spectra for each payload is reported in Table 4.3. In X-mode, the FWHM at the ^{55}Fe 5.9 keV calibration line ranges from 293 eV to 390 eV. In S-mode, the resolution is below 5%, calculated at the ^{137}Cs 662 keV calibration line, for all payloads, with the only exception of FM4, which shows 5.11%±0.04 under the same conditions. As an example, Fig. 4.26 shows the channel-by-channel FWHM energy resolution at the ^{55}Fe 5.9 keV line in X-mode, mapped onto the detector planes for all payloads. No systematic trends are visible when comparing channels located in identical positions on different payloads, with the exception of PFM and FM1, which have lower spectroscopic resolution than the other flight models [106].

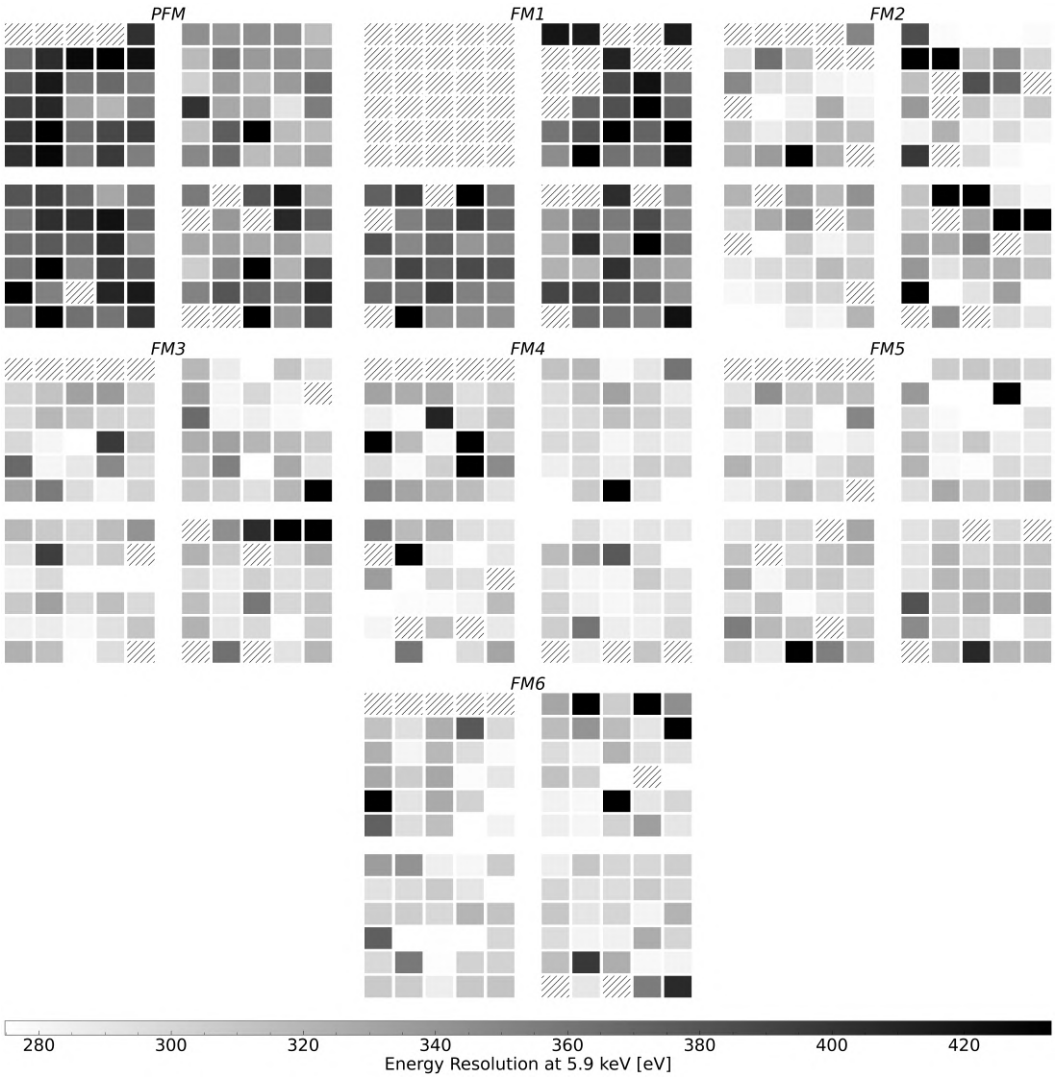

Figure 4.26: FWHM energy resolution at 5.9 keV and 0°C, mapped to channel positions on the all HERMES-PF payloads detector planes.

4.6.5 Widows channels calibration

The HERMES-PF detector operates according to the siswich principle (see Section 3.3). When two Silicon Drift Detectors (SDDs) coupled to the same scintillator register independent signals at the same time, these are combined into a single S-mode event, corresponding to one incoming high-energy photon. On the other hand, if the signals are recorded either by non-coupled SDDs or at different times, they are classified as two distinct X-mode events. In this way, the detectors can cover the full energy range from 3 keV up to 2 MeV.

If a single SDD becomes non-functional or is disabled (a dead channel), the paired SDD coupled to the same scintillator loses the ability to discriminate between X-mode and S-mode events. In this case, the operational SDD is referred to as a *widow* channel, and the signals it records are classified as widow events. In Figure 4.27 an example of a working channel able to recognize X

e S events (a), and a widow channel (b) of FM6. Although the gain and offset parameters for all channels, including widow channels, are determined during standard calibration and thus allow a reliable X-mode calibration, the S-mode calibration cannot be directly applied, since widow channels cannot intrinsically distinguish between the two event types.

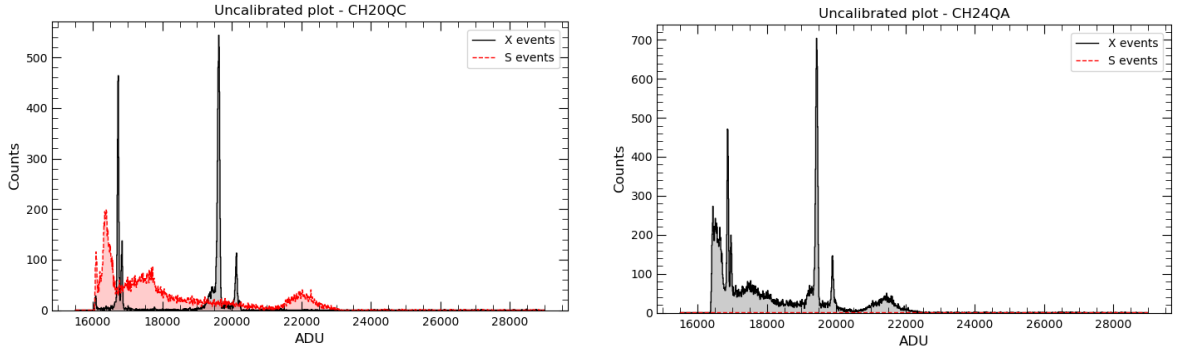

(a) **(b)**

Figure 4.27: Uncalibrated raw spectra of ^{55}Fe, ^{109}Cd and ^{137}Cs acquired with FM6. Channel D16 with a functioning coupled channel (D15), where event-type tagging correctly separates X (grey) and S-mode (red) events (a). Widow channel A22 with non-functioning coupled channel (A31), where all events are classified as X-mode (b).

To avoid losing effective detector area, a dedicated algorithm was developed to statistically assign an event type to widow events. This makes it possible to convert them into energy units and, within an acceptable uncertainty, preserve their scientific value.

Starting from the `mescal` algorithm, a new approach was developed to extend the light-output calibration to widow channels as well. The algorithm is based on statistical comparison with neighboring channels (up to a maximum of three), which have a known distribution of X and S events. It is assumed that, under the same conditions, the distribution of events in a widow channel is statistically similar to that of its neighbors, within counting errors. In fact, flux variations between a widow channel and its neighbors are minimal because each channel operates independently and the spatial resolution of a single HERMES detector unit is limited. The procedure is as follows: The spectrum is divided into bins of 200 electrons, a value chosen as a compromise between using narrower bins to preserve the equivalent energy resolution and wider bins to reduce statistical counting errors. For each interval, the probabilities P of an event being X-type or S-type are calculated from the distribution of the neighboring channels N_k. X(N_k) is the number of events of type X in the neighboring channel N_k.

$$P(X) = \frac{\sum X(N_k)}{\sum TE(N_k)}, \qquad P(S) = 1 - P(X) \tag{4.8}$$

where TE be the total number of events detected by a given channel.

The total number of events detected by the widow channel TE(W) in each interval is then distributed between X and S proportionally to these probabilities:

$$F_W(X) = TE(W) \cdot P(X), \qquad F_W(S) = TE(W) \cdot P(S) \tag{4.9}$$

For energies above 15000 electrons (∼55 keV), all events are directly assigned as S-mode, since the probability of having X-mode events at such energies is negligible(the efficiency of the SDD at energies is less than 4%). The assignment of events is performed randomly but weighted by the calculated probabilities, in order to avoid introducing systematic biases. Once separated into X and S, the events of widow channels are calibrated using the same procedure adopted for normal channels. The final outcome is that each widow event is associated with two possible calibrated energy values (one for X-mode and one for S-mode), together with a probability coefficient indicating which type is more likely. This makes it possible to retain widow channel data for scientific use, albeit with a higher uncertainty compared to standard channels.
It should be noted that, under normal conditions, the spectral characteristics detected by a scintillator in the HERMES model should be symmetrical and approximately Gaussian. In widow channels, however, events are recorded only on one side of the scintillator, resulting in asymmetric spectral characteristics, as shown in Figure 4.28. This effect inevitably introduces a slight increase in the uncertainty of the derived light output value. Note also the residuals from X mode, which appear as delta-shaped features (^{109}Cd lines), but the detection of the 661.7 keV peak remains clear.

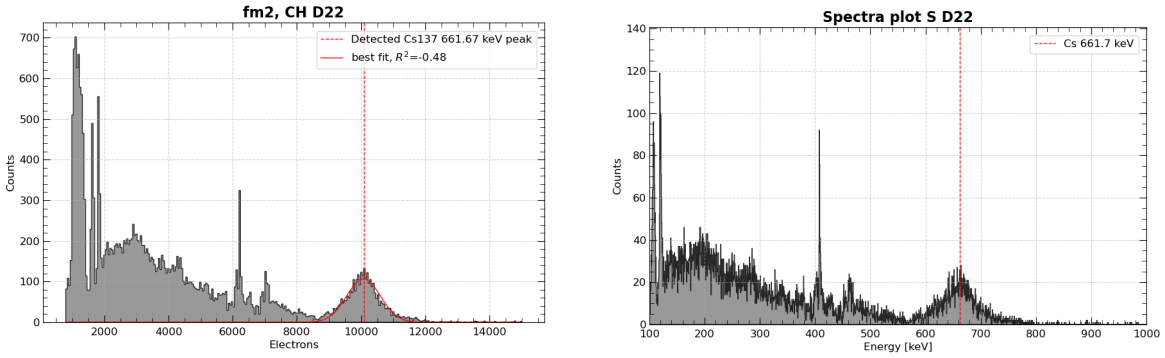

(a) **(b)**

Figure 4.28: Spectrum of the cesium widow channel 22 in quadrant D of FM2. (a) Fit of the ^{137}Cs line performed by the algorithm; (b) calibrated spectrum. The asymmetry of the line is clearly visible.

The critical step in the proper S-mode calibration of a widow channel is, thus, the event type tagging process, which, if done properly, will contribute minimal uncertainty to the calibration process. With this method, the light outputs of the widow channels have therefore been

recovered.

4.6.6 Calibration and test of the PL integrated in the spacecraft

Once characterized and calibrated, the HERMES-PF payloads were integrated into the service module (see Sect. 3.5).

The HERMES-PF satellites were subjected to a complete environmental test campaign to demonstrate that the integrated system is capable of surviving the mechanical and thermal stresses of launch and the space environment, ensuring nominal functionality for the entire mission. These tests also help identify possible defects or problems in the integration activities. The tests included vibration tests (resonance research, random and sinusoidal vibrations) performed at the shaker facility of the Politecnico di Milano and thermal vacuum tests (TVAC) performed in Thales Alenia Space Italia [98].

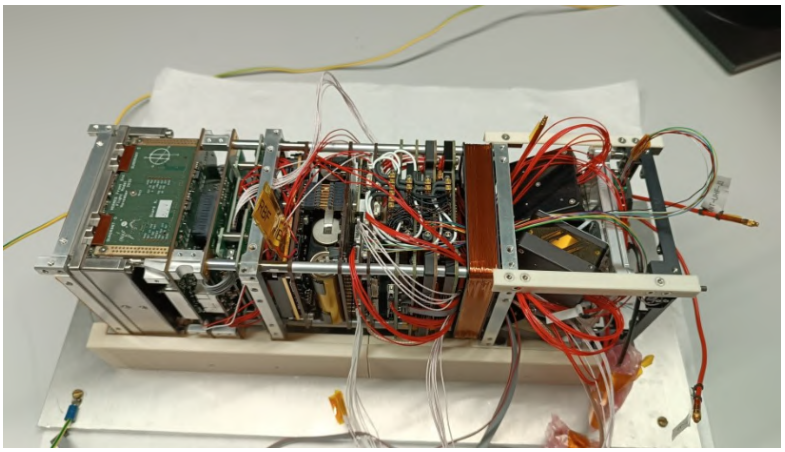

Figure 4.29: HERMES FM2 flight model during AIV/T activities in Politecnico di Milano clean-room [98].

Verification and functional tests were performed at each integration step for each payload, as well as on the fully assembled 3U module, to ensure nominal payload operation and proper communication with the spacecraft. In particular, functional tests were performed after Vibrations and TVAC tests to verify possible changes to the functionality of the integrated system. These tests involved checking the functionality of PL operating modes (See Sect. 3.3.5). After verifying the two initial modes, Standby and Ready, in which the detectors are off and housekeeping parameters are collected, the Idle mode was activated to power on the detectors. Finally, the system was set to Calibration mode.

Data acquisition was carried out in the clean room at Politecnico di Milano using a Mini-X-ray tube (Amptek Mini-X2) for X-ray calibration and a ^{176}Lu source for gamma-ray calibration. They were used to verify consistency with the ground calibration database (CALDB) and to

confirm the proper operation of the integrated system. The Mini-X tube and the ^{176}Lu source were adopted to replace the radioactive sources used for ground calibrations, as the latter cannot be transported due to safety restrictions and regulations relating to the transport of radioactive materials. In fact, the ^{176}Lu source was already available in the calibration facilities.

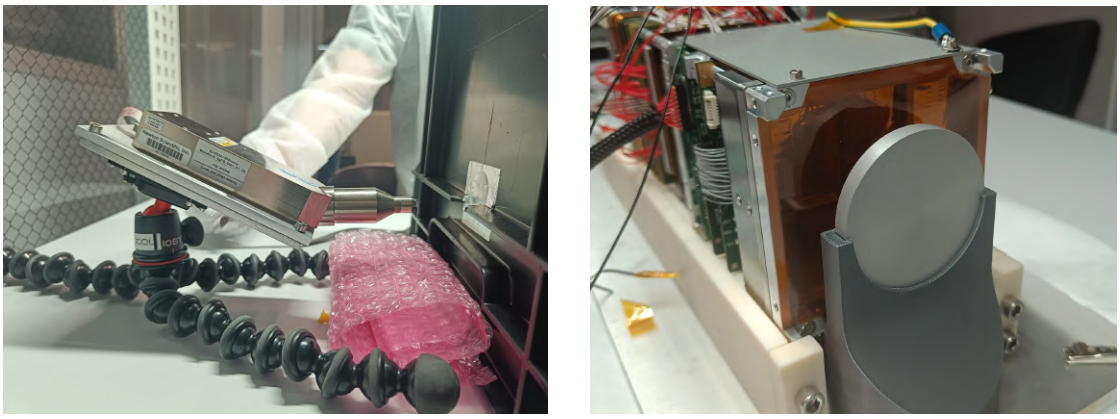

(a) **(b)**

Figure 4.30: The Mini-X tube (a) and the ^{176}Lu source (b) used during the data acquisition campaign with the spacecraft for X-ray and gamma-ray calibrations.

The Mini-X2 X-ray tube has a silver cathode and an aluminum filter a few millimeters thick, producing two characteristic Ag fluorescence lines at 22 keV and 25 keV, together with a continuous bremsstrahlung spectrum. The Cu fluorescence lines at 8.05 keV and 8.9 keV are also visible, resulting from the presence of a small copper disk that acts as an attenuator.
The ^{176}Lu source emits two main gamma-ray lines at 201.8 keV and 306.8 keV. The acquired spectra are shown in Figure 4.31. Acquisitions were performed at temperatures between 24 °C and 27 °C.

X-mode calibration

Post-TVAC Mini-X2 acquisitions were used to verify the X-mode calibration. In particular, the ground calibration parameters (CALDB, THR 105) were extrapolated for each channel at the temperature of the mini-tube acquisitions, using the parameters of the models described in Sect. 4.6.1. Once the gain and offset for each channel were obtained at the acquisition temperature, calibration was applied using `Mescal` software. A comparison between the new and reference CALDB parameters showed an average variation of less than 1%, confirming the stability of the X-mode calibration for all payloads. The gain variations were found to be within one standard deviation, while the offset exhibited an average variation of 0.2–0.3%, indicating that the calibration parameters remain consistent and stable after the environmental tests.
An example of spectra calibrated with the two different parameter sets is shown in Figure 4.32

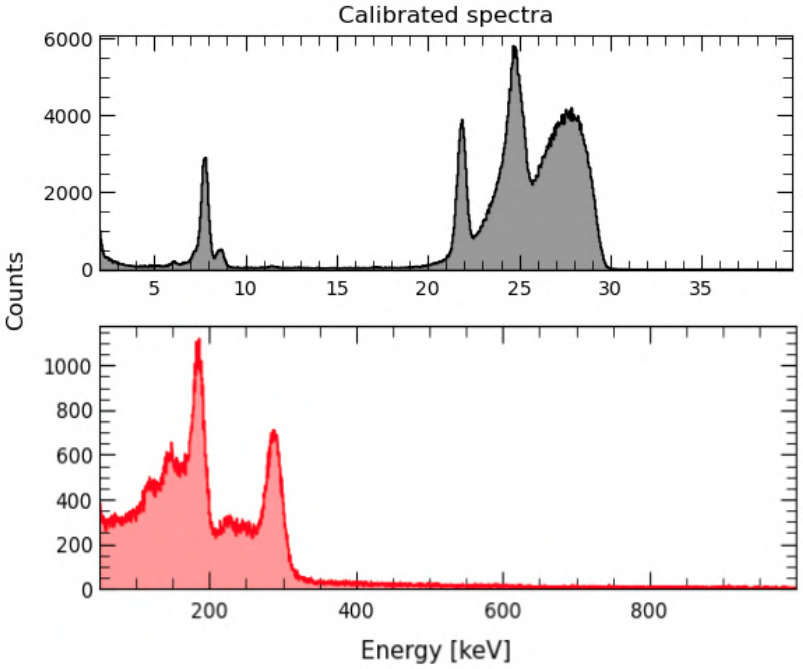

Figure 4.31: Example of calibrated spectra acquired after FM6 integration into the service module. The upper panel (grey) shows the X-ray spectrum measured with the Mini-X Tube with the two Ag fluorescence peaks at 22 keV and 25 keV. Cu fluorescence lines at 8.05 keV and 8.90 keV are also visible. The lower panel (red) shows the gamma-ray spectrum acquired with the ^{176}Lu source with lines at 201.8 keV and 306.8 keV.

for FM6. The red curve was calibrated using the reference CALDB parameters, while the black curve was calibrated using the parameters extrapolated at the acquisition temperature. The dashed purple lines indicate the nominal positions of the two Ag fluorescence peaks at 22 keV and 25 keV. The Cu fluorescence lines at 8.05 keV and 8.9 keV are also visible. In addition, a noise peak caused by retriggering can be observed in some channels close to the baseline.
The consistency of the X calibration performed with the tube and the standard confirms the stability of the X parameters and therefore the calibration of the spectroscopic chain.

S-mode calibration

Post-TVAC ^{176}Lu acquisitions were used to verify the S-mode calibration. The ground light-output (LO) calibration parameters (CALDB, THR 105) were extrapolated for each channel at the temperature of the new acquisitions, following the modeling functions described in Sect. 4.6.2. The calibration was then applied using `mescal`.
The difference between the measured position of the peak at 306.8 keV in the integrated spectrum and its nominal energy was used to derive the non-linearity correction factor (See 3.3.1). Therefore, using these acquisitions a new calibration was performed, obtaining updated LO

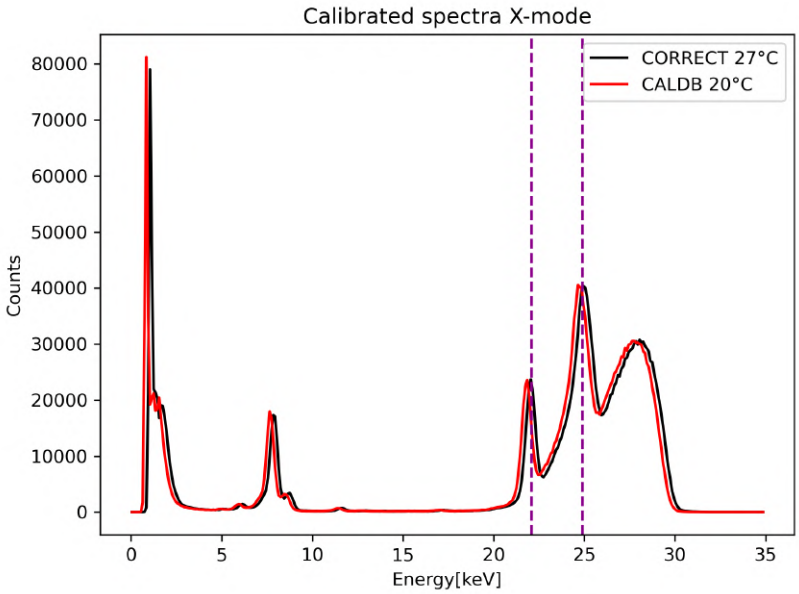

Figure 4.32: Comparison of FM5 X-ray spectra calibrated with reference CALDB parameters (red) and temperature-extrapolated parameters (black). Dashed purple lines indicate the 22 keV and 25 keV Ag peaks. Cu fluorescence lines at 8.05 keV and 8.90 keV and a noise peak from channel retriggering near the baseline are also visible.

values for each channel, which were corrected using the derived non-linearity factor.
The comparison between the light output (LO) obtained during ground calibrations and after the environmental tests showed a variation in the light output following the thermal vacuum campaign. The number of channels in which the light output varies differs for each payload. An example of this variation is shown in Figure 4.33 for FM6.
In particular, the light output decreases for some channels. This behavior is likely of mechanical origin: during TVAC cycles (from $-20°C$ to $+60°C$), the optical coupling couplers may soften and expand at high temperatures and shrink during cooling, resulting in reduced light transmission.

Following the environmental tests, a scale correction was derived to update the CALDB light output values. For each channel, the reference LO at the new acquisition temperature was first extrapolated from the two closest CALDB measurements (at $10°C$ and $20°C$) using a linear function. Then a correction factor was calculated from the difference between this extrapolated value and the new LO value obtained from the post-TVAC calibration ^{176}Lu. This channel-by-channel factor was subsequently applied to the channel-by-channel light output values at all temperature points in the CALDB.

As hypothesized, analysis of these factors confirmed the trend shown in Figure 4.33: most scale correction factors are ≤ 1. This result quantitatively confirms that TVAC tests induced

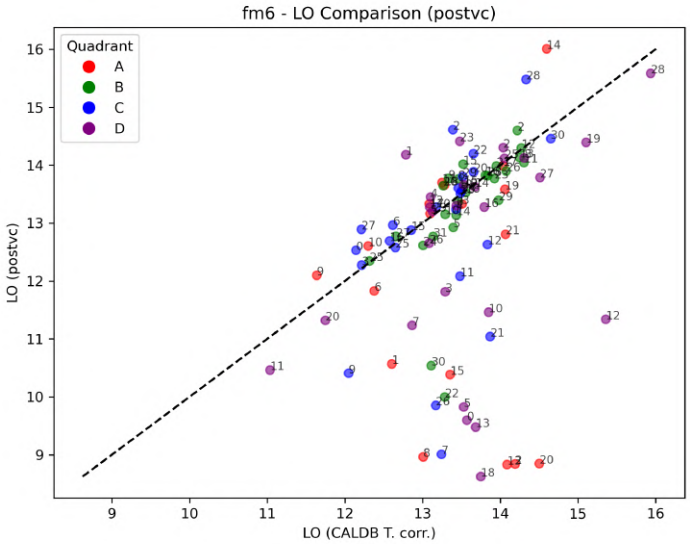

Figure 4.33: The comparison between the channels light output for FM6 before the enviromental tests (CALDB) and after the TVAC. A decrease in the light output is clearly visible in some channels.

a moderate but measurable reduction in light output, likely due to mechanical stress on the optical coupling. Although some anomalous channels showed factors $\geq$1, the dominant trend validated this recalibration phase, resulting in the update and correction of the CALDB for in-orbit operations.

Chapter 5

The HERMES-PF payload onboard SpIRIT: early operations and first data

The Space Industry Responsive Intelligent Thermal (SpIRIT) mission is a 6U CubeSat developed through a collaboration between Australia and Italy in the field of high-energy astrophysics. The satellite carries an HERMES Pathfinder payload and operates in a Sun-synchronous orbit. Launched on December 1, 2023, aboard a SpaceX Falcon 9, SpIRIT has now completed its payload commissioning.

This Chapter is organized as follows: the mission is described in Section5.1. Section 5.2 presents the first in-orbit operations, including commissioning activities, while Section 5.3 reports the analysis of in-flight calibrations. Scientific observations are discussed in Section 5.4 and Section 5.5 describes the observation strategy applied and summarizes the main lesson learned.

5.1 SpIRIT

The Space Industry Responsive Intelligent Thermal nano-satellite mission[1] is a 6U CubeSat developed by a consortium led by the University of Melbourne (UoM, PI Michele Trenti) and with Italian participation, supported by the Australian and Italian Space Agencies. The mission was successfully launched into a Polar Sun-synchronous orbit at an altitude of 513 km on December 1st, 2023, from Vandenberg Space Force Base aboard a SpaceX Falcon 9. 24 months of nominal mission duration, including commissioning, are foreseen. SpIRIT is Australia's first in-flight mission funded by the Australian Space Agency, since it was established in 2018. The

[1] `https://spirit.research.unimelb.edu.au`

space platform had no flight heritage and it consists of deployable solar panels, provided by Inovor Technologies company (Adelaide, Australia), a COTS S-band transceiver, provided by the Italian Space Agency and a novel high-efficiency ion thruster developed by Neumann Space company (Adelaide, Australia) [118].

In addition, the spacecraft main subsystems, developed by UoM, include: the *Payload Management System* (PMS), the Instrument Control Unit whose purpose is to manage communications with all SpIRIT payloads and their operations and whose main components are an On-Board Computing Unit (OBC) and a electrical power system(EPS); *Thermal Management Integrated System* (TheMIS), a subsystem designed for precision thermal management and to provide all payloads with active cooling; in addition, two deployable thermal radiators support passive thermal control. *Mercury*, a communication subsystem designed to optimize low-latency, short burst data transmission by exploiting the Iridium satellite network; LORIS, a set of visible and IR inspection cameras and an on-board Artificial Intelligence image-processing module.

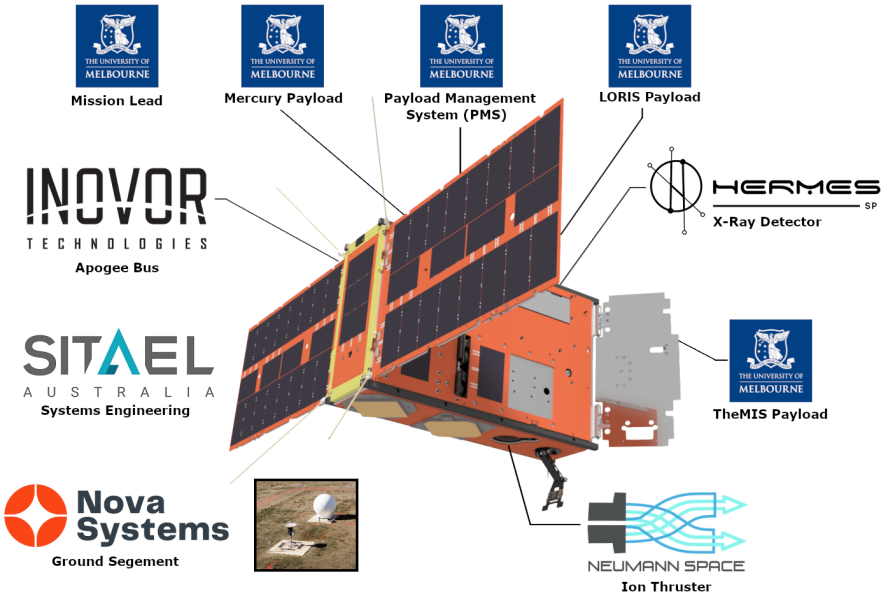

Figure 5.1: Overview of the SpIRIT CubeSat and its main collaborators. The spacecraft main subsystems are highlighted: the HERMES X-ray detector, the TheMIS thermal management system, the LORIS imaging module, the Mercury communication subsystem, and the Payload Management System (PMS). The spacecraft is also equipped with an ion thruster provided by Neumann Space [119].

The primary goal of SpIRIT is to serve as a platform for testing new technologies in space, while its scientific mission focuses on the detection and localization of high-energy astrophysical transients, such as Gamma-ray Bursts. To identify these types of sources, the main scientific instrument on board is a CubeSat 1U, equipped with a X-ray and gamma-ray compact and

advanced detector. This unit is identical to the ones on board HERMES-PF described in Chapter 3. An overview of the SpIRIT CubeSat is shown in Figure 5.1.
HERMES-PF was launched on March 15, 2025 and together with SpIRIT, the Pathfinder constellation will consist of seven units, designed to validate the performance of novel technologies in space and assess the scientific capabilities and operational procedures. SpIRIT represents a pivotal first step in evaluating the HERMES-PF payload under the harsh space environment and varying thermal conditions.

Starting from January 2024, SpIRIT entered its commissioning phase, during which the initial operations confirmed that all hardware provided by the University of Melbourne and the HERMES-PF consortium is functioning nominally and responding as expected to remote commands.
HERMES-PF detectors were switched on, reaching 'first light', on January 16, 2024, with the instrument operating in simple Geiger counter mode. On March 27, 2024, the payload switched to nominal observation mode, successfully recording scientific data.

5.2 Early operations in orbit

The commissioning phase started in January 2024, during which the operational capabilities of the HERMES-PF payload were systematically verified and evaluated [120]. The author directly participated in commissioning activities at the University of Melbourne between late January and March 2024. Through a series of tests, this phase aims to define a set of first systematic in-orbit operations to verify the functionality and performance of the payload and to establish its readiness for scientific data acquisition. In particular, this approach ensures that each P/L sub-system, as described in Section 3.3, and the communication interfaces between them, operate as expected. It also serve to ensure reliable communication between the payload and the spacecraft and identifying any potential problems that need to be addressed prior to full operational deployment.
Communication between the payload and the spacecraft is managed by the Payload Management System (PMS), which acts as an interface between the HERMES-PF Payload Data Handling Unit (PDHU) and the S/C On-Board Computer (OBC), referred to as the Main Mission Module (MMM). Payload operations are controlled via Lua scripts [121]. The scripts are first prepared and uploaded from the mission operations center to the ground station, from where they are then transmitted to the PMS via the spacecraft's UHF link. The scripts orchestrate the sequence of commands necessary for configuring operating modes and acquiring data. In particular, communication commands between the PDHU and the PMS have been

studied and implemented in these codes.

The commands are transmitted to the PMS, which forwards them to the PDHU for execution, while data collected from the HERMES-PF payload are transferred to PMS and then from PMS flash storage to the MMM. To ensure the safety of the payload, all operational scripts and command sequences were thoroughly tested on the Engineering Model at the University of Melbourne facilities before execution in orbit.

At this stage of commissioning, the primary subsystem responsible for telemetry and remote control of the HERMES-PF payload is the UHF antenna system, which communicates with Nova Systems Ground Station in Peterborough (Australia). The satellite establishes contact with the Ground Station approximately twice every 12 hours. This is currently the only ground station capable of interacting with SpIRIT, and the available bandwidth for HERMES-PF is limited to approximately 50 kBytes per day. This limited telemetry budget, together with the dependency on a single GS for communications, severely restricted the commissioning activities of the payload.

The data transmission capability will be improve via the S-Band, which will be available at the end of its current commissioning period: on 24 May 24, 2024, a test transmission of a Fibonacci sequence was successfully received by the SpIRIT GS in the S-band and decoded, verifying its functionality [118].

5.2.1 Operational mode test procedure

The test procedure is designed to verify the correct functionality of the payload by systematically checking all its operating modes (see Section 3.3.5). For each mode, the acquisition and verification of housekeeping (currents, voltages and temperatures) is performed to check the health of the payload in orbit. The sequence of activation of the payload's operating modes is summarized in Figure 5.2.

These tests make it possible to systematically check the operation of each subsystem of the P/L in each mode, ensuring nominal operation and perfect interaction between hardware components.

Housekeeping parameters include a series of status indicators that monitor the correct operation of each power supply line of each quadrant, as well as the BEE and FEE circuits. These parameters also control the activation of the Overcurrent Sensing circuits in the PSU. In the event of a line malfunction, a series of alarms are activated to signal the problem. This allows comprehensive and detailed monitoring of payload behavior, allowing targeted action to be taken on the specific fault line. This approach helps prevent serious damage or operational interruptions, minimizing the risk of permanent failure or performance degradation.

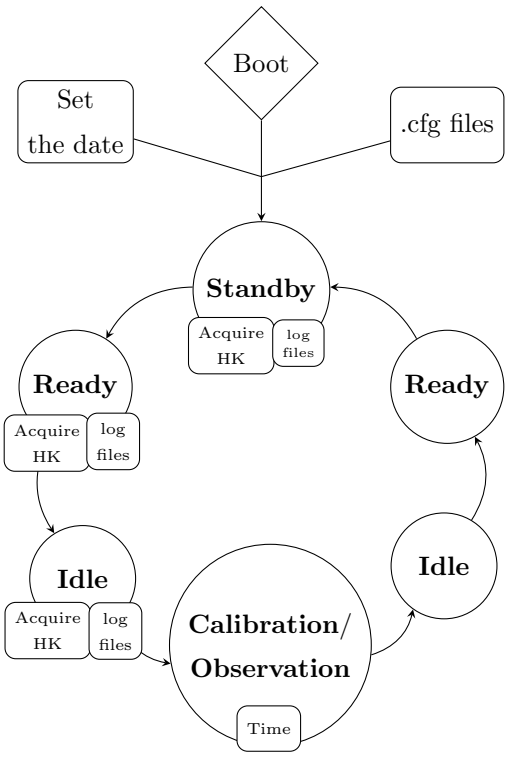

Figure 5.2: Circular graph of the sequence of activation of the payload's operating modes[120].

In the first phase, the focus is on testing the initial two modes individually: *Standby* and *Ready*, in which the detectors are switched off. The test ensures that the three switched-on low-voltage supplies (3.3 V, 5 V, 12 V) and the current consumption are consistent with the expected nominal values in each power-on phase and the P/L temperatures are monitored.

Once the nominal state of the payload in orbit during these modes is verified, the *Idle* mode is tested. The 12 V power supply activates the high voltage for polarization of the SDDs: the detectors are switched on and event triggers are recorded on-board.

The system is then set to *Calibration* mode. In this mode, photon-by-photon data are collected from the detectors, allowing continuous monitoring of the behavior of each detection channel. This step allows the ASIC configuration to be adjusted when necessary and allows the generation of calibrated spectra and light curves. Once calibration confirms nominal payload functionality, scientific operations begin in *Observation* mode. During each observation, the Payload Data Handling Unit (PDHU) generates files containing Scientific Rate Meters (SRAs), which consist of light curves with a 100 ms temporal resolution for each quadrant. These SRA involves three predefined energy bands: $3 < E_{\text{low}} < 10$ keV, $10 < E_{\text{mid}} < 100$ keV, and $E_{\text{high}} > 100$ keV.

In each operation, the activation of the payload is programmed at the desired time, e.g. during the eclipse. All the selected ground tracks and the low-energy band count rates for each

Observation performed between February and June 2024 are shown in Figure 5.3. The colored lines represent the satellite trajectories, with the intensity of the color encoding the variation in the recorded count rate along each path. The black contours delineate the approximate positions of the polar electron belts and the South Atlantic Anomaly. All Observations are described in detail in Section 5.4.

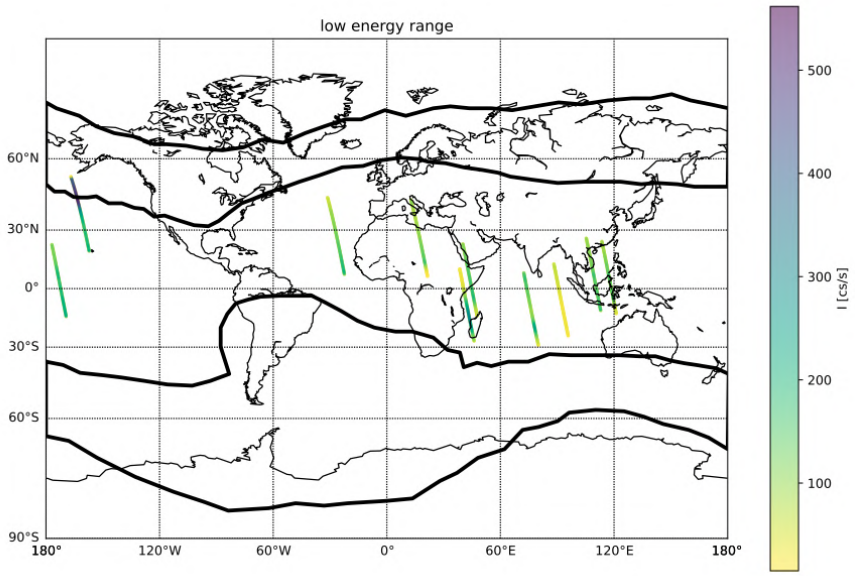

Figure 5.3: Ground tracks and low-energy band count rates for each observation performed between February and June. The black contours indicate the approximate positions of the polar electron belts and the South Atlantic Anomaly.

5.2.2 Detector switch-on: Idle mode

The first mode transition in *Standby* was performed on January 5, 2024, while in *Ready* on January 10, 2024. Housekeeping data were perfectly within the expected range by verifying the nominal status of the BEE and PSU lines.

Along with this, the `error.log` file (Section 3.3.5) revealed no errors during transitions, so the *Idle* mode was activated as the detectors were switched on, reaching 'first light' on 16 January 2024.

Housekeeping checks allow in particular the monitoring of voltages and absorption currents of the payload supply lines for the BEE and FEE circuits. An example of the nominal values acquired during an *Idle* transition are shown in Figure 5.4.

At this stage of commissioning, it is also critical to monitor the payload temperature, especially since the cooling system (TheMIS) was not yet operational. Temperature monitoring during

data acquisition is handled by six TMP235A2DCK analog temperature sensors located on the FEE Electronics board. Each quadrant has a dedicated reference sensor, supplemented by two central sensors. In addition, two sensors on the BEE PCB are used to monitor the respective BEE and CSAC temperatures (Section 4.6).

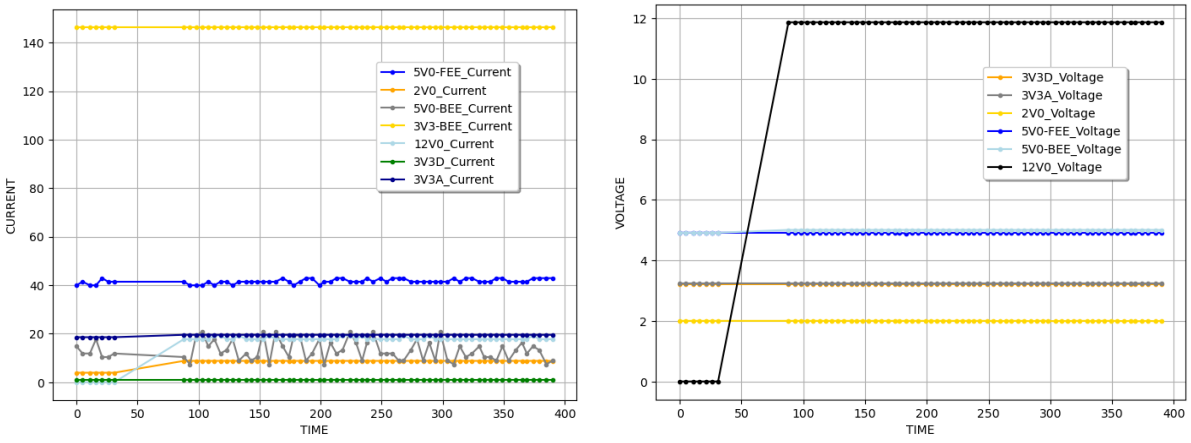

(a) **(b)**

Figure 5.4: Currents (a) and voltages (b) of payload power supply lines for BEE and FEE circuits in *Ready* (leftmost points) and *Idle* mode (rightmost points, recorded after a few seconds gap).

During this acquisition in *Idle* mode, the onboard P/L sensors reported an average temperature of approximately ~ 9 °C, as shown in Figure 5.5.

Temperatures at this level are significantly higher than those expected under optimal operating conditions. Consequently, it is essential to adjust the ASIC configuration, particularly to optimize the low-energy threshold when operating at elevated temperatures. This adjustment is critical to minimize the occurrence of occasional spikes recorded in the time-binned data, caused by the electronics' increased sensitivity to noise also due to the radiation damage already accumulated by SDD at this stage. Once the radiators have been deployed, and the cooling system activated if necessary, the temperature will return to nominal levels, allowing the ASIC original configuration to be restored and a full verification of correct operation to be carried out.

Further *Standby-Ready-Idle* transition tests were carried out between January and February 2024, where voltages and currents always turned out to be nominal and recorded temperatures varied in the range between 2–10 °C.

5.2.3 Emergency procedures

To avoid potential damage to the payload, an emergency shutdown sequence is implemented in the PDHU as a safety measure. This sequence is triggered in case of communication problems

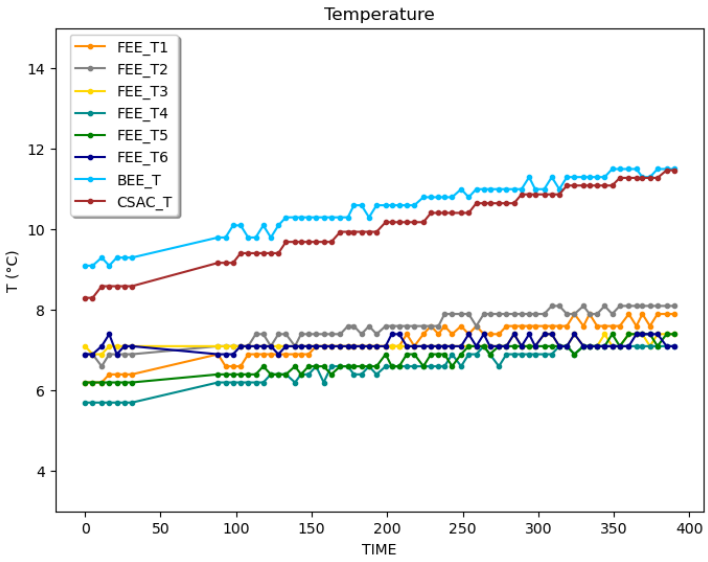

Figure 5.5: Temperature monitoring during first *Idle* acquisition. In particular, the temperature trends recorded by the six FEE sensors, along with those from the BEE and CSAC sensors.

or any other unforeseen problem, as well as if certain nominal conditions required on the status of the payload are not met. This procedure specifically helps limit damage to the SDDs that could be caused by an unexpected drop in the payload power supply. For this reason, if the HV is switched on, the system allows 30 seconds to reduce it safely.

The correct functioning of the in-orbit emergency procedure was demonstrated during five PMS reboot events that occurred while the P/L was transitioning from one operating mode to another. The root cause of the restart is still being analyzed. For each of these events, the PMS issued an emergency procedure activation command to the PDHU and provides uninterrupted backup power to the HERMES instrument through a supercapacitor-based UPS to ensure the safe shutdown of the instrument in the event of a power failure on the platform [118]. The P/L PDHU shutdown sequence was successfully executed, with all power systems safely deactivated, ensuring no damage to the detector, as confirmed by the housekeeping check following the events.

5.3 In-flight calibrations

Subsequent to verifying the complete functionality of the payload through initial operational mode tests and determining the optimal ASIC configuration for the given operating conditions, the Calibration and Observation mode tests were started for scientific data collection.

The Calibration and Observation sessions are essential for ensuring that the payload performs as anticipated and can reliably acquire the scientific data. The results of the acquisitions are

outlined below.

5.3.1 Calibration acquisitions

SpIRIT has performed, to date, ten acquisitions in **Calibration** mode, listed in Table 5.1.

Date	Acquisition Duration	P/L Temperature ~	Threshold	Description
2024-02-17	8 s	2 °C	115	Pointing Unknown.
2024-05-18	8 s	–17 °C	150	Partial overlap with souther polar electron belt. Pointing Unknown.
2024-07-04	10 s	–8 °C	150	Pointing Unknown.
2024-12-11	10 s	–17 °C	135	Pointing: Crab Nebula, ∼40° w.r.t. local zenith
2024-12-28	40 s	–17 °C	135	Pointing: Crab Nebula, ∼25° w.r.t. local zenith
2024-12-29	40 s	–16 °C	135	Pointing: Crab Nebula, ∼25° w.r.t. local zenith
2025-02-20	490 s	–18 °C	135	Pointing: Crab Nebula, ∼25° w.r.t. local zenith
2025-03-13	400 s	–17 °C	135	Pointing: Crab Nebula, ∼20° w.r.t. local zenith
2025-04-01	731 s	–18 °C	135	Pointing: Crab Nebula, ∼20° w.r.t. local zenith

Table 5.1: Summary of Calibration acquisitions performed by SpIRIT. The threshold column reports the values, expressed in DAC units, that define the minimum signal level required to trigger event acquisition (see text in Sections 3.3.2 and 5.3.1 for details).

Each of the first four CALs was scheduled to run for 10-seconds due to the telemetry budget constraints imposed by the UHF transmission (5.2). For the next two CALs, 40-seconds were acquired, while the last three exceeded 400 seconds of acquisition.

February 17, 2024

The first calibration was performed on February 17, 2024, of which only the first 20 kB of the output file could be downloaded, thus truncating the data to the first ∼8 seconds for issues with the execution of the S/C script. The pointing information was unknown with the satellite likely in tumbling mode.

Calibration was performed using data collected from ground calibration measurements [116] (Chapter 4). Figure 5.6b shows the acquired spectra: at the top the summed spectrum calibrated in X-mode, at the bottom in S-mode. Both show the background at X-ray and gamma-ray energies. The detector map in Figure 5.6a shows the four quadrants and the counts detected by each channel. The counts are filtered for ASIC re-trigger due to electronic noise and for spurious events (see Section 4.2.1). This noise is mainly associated with afterpulse noise, occasionally induced by the signal responsible for resetting a channel after a trigger [106]. This channel behavior was also characterized on ground, as described in the Chapter 4. For each channel, the filter removes events at a time distance of less than < 20 µs from the previous

one, where < 20 µs corresponds to the delay between the trigger and the reset signal. In the detector map, a more restrictive filter (< 50 µs) is applied to ensure a robust removal of all spurious events and residual noise, even considering that the operating temperature is higher than expected.

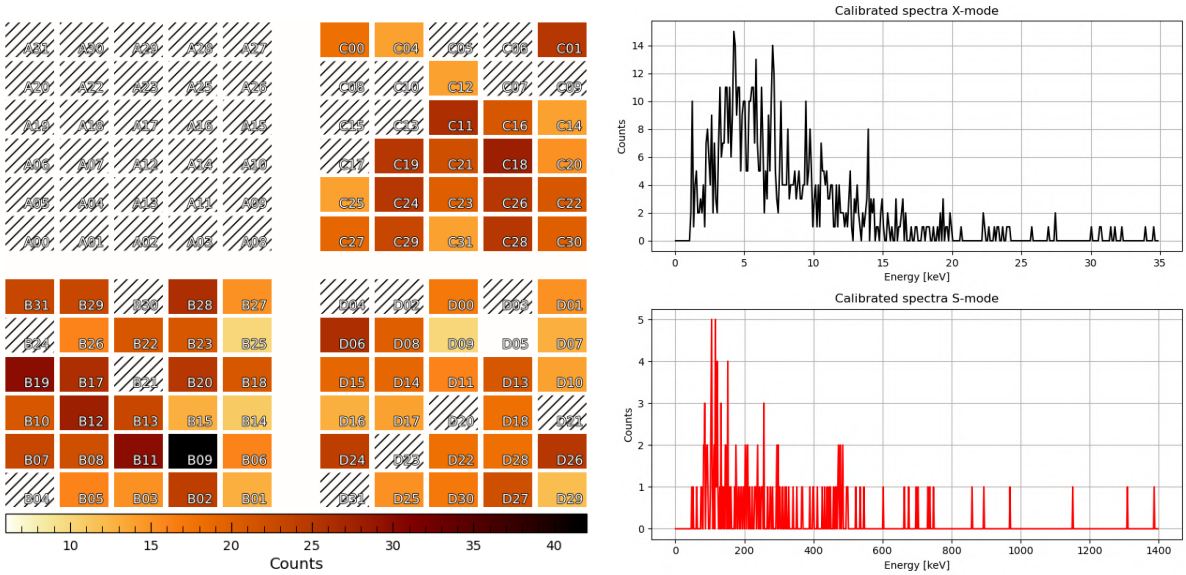

(a) **(b)**

Figure 5.6: First *Calibration* outputs (February 17, 2024): the map of detector channels counts (a), with the top left quadrant switched off due to a fault occurred during ground calibration. Calibrated summed spectrum in X-mode in black, in S-mode in red (b).

All calibration acquisitions were corrected for scintillator non-linearity (see Sect. 3.3.1) using the values obtained in [102]. Due to the failure in one quadrant that occurred during the final stages of ground calibration (a sudden short circuit on the HV voltage line), the payload operates with only three functional quadrants, resulting in no data being recorded from the affected quadrant (the one marked in gray on the map). In set ASIC configuration, some channels in the working quadrants are switched off (dashed), because during ground calibrations they were too noisy to be used [106]. During this acquisition, the payload temperature was between 2 °C and 3 °C.

Data were analyzed using HERMES software (HERMESDAS) developed by the HERMES Science Operations Center (SOC), to generate calibrated and clean scientific data from raw telemetry data [117]. The software `mescal` [116] described in Section 4.4, developed for ground-based calibrations, allowed to analyze the behavior of each channel by evaluating the detected background counts. This capability enables the assessment of noisy channels and validation of the optimal configuration for light curve acquisition during observations, in terms of which channels to keep active and the appropriate threshold settings (Sect. 3.3.2). Following the

analysis of the previous operative modes, during this acquisition, a threshold value of 115 was initially set (Sect. 3.3.2). However, analysis of channel behavior indicated the necessity of increasing the threshold to minimize noise peaks due to sub-optimal operating temperature (Sect. 5.2.2). The threshold was raised (to a value of 150) for the next two CALs.

The second 10-s calibration was performed on May 18, 2024. As before, only the first ∼8-seconds of data were downlinked. During the acquisition, the satellite's trajectory was on the boundary of the southern electron belt, resulting in contamination of the data. However, channels map was consistent with the latest loaded ASIC configuration, and the PL HKs were all nominal.

July 04, 2024

The third 10-seconds acquisition was performed on July 04, 2024, with unknown pointing information. The channel map and calibrated spectra are shown in Figure 5.7.

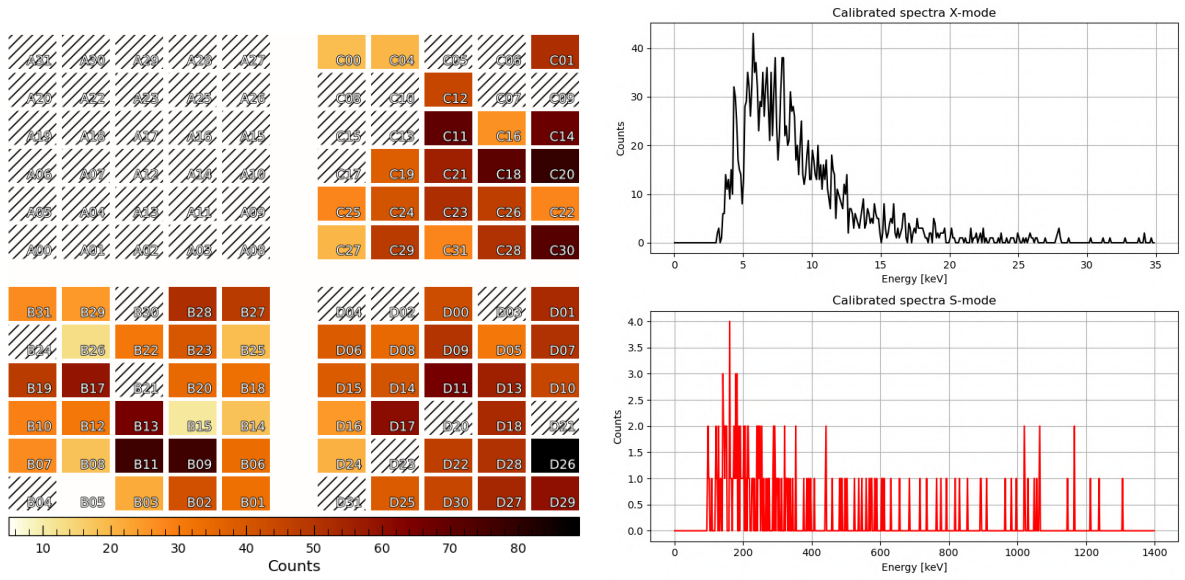

(a) **(b)**

Figure 5.7: Third *Calibration* outputs (July 04, 2024): the map of detector channels counts (a), with the top right quadrant switched off due to a fault occurred during ground calibration. Calibrated summed spectrum in X-mode in black, in S-mode in red (b).

In this acquisition, we also observe the background contribution at X-ray and gamma-ray energies. At this stage, the solar panels were deployed and the radiators were exposed (albeit not fully deployed), therefore the payload temperature was lower, between –8 °C and –10 °C. Given the decrease in operating temperatures, close to nominal levels, the ASIC configuration was updated by lowering the threshold for the next acquisitions (135).

December 11, 2024

On December 11, 2024, another 10-s calibration was performed. The channel map and calibrated spectra are shown in Figure 5.8. This acquisition was performed with the Crab Nebula positioned approximately 40° off-axis. At this phase the radiators were fully deployed and the payload temperature was around –17 °C.

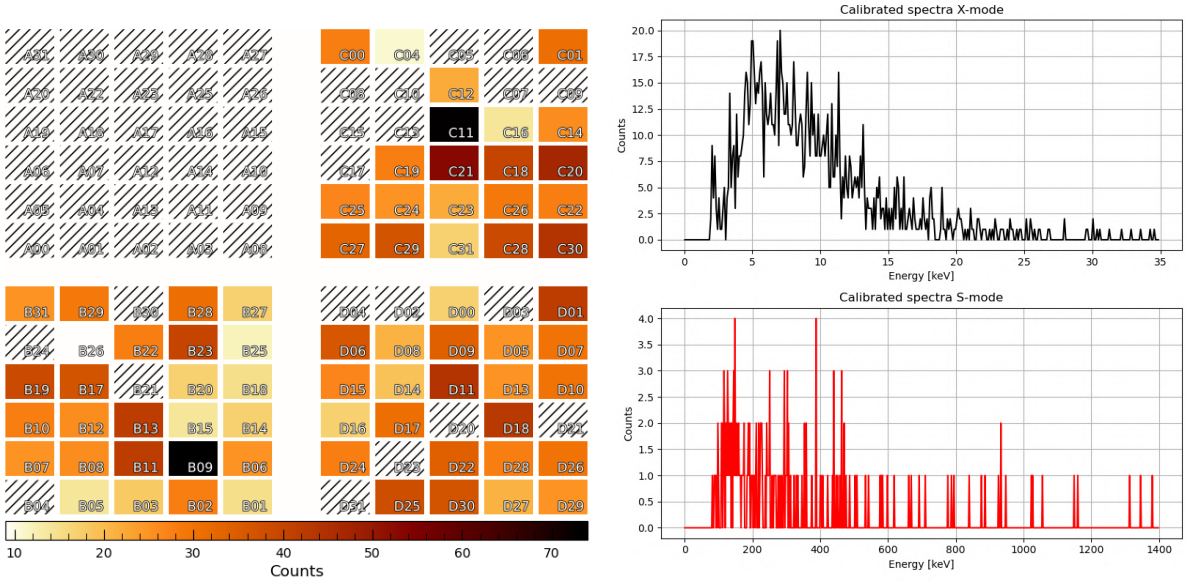

(a) (b)

Figure 5.8: Fourth *Calibration* outputs (December 11, 2024): the map of detector channels counts (a), with the top right quadrant switched off due to a fault occurred during ground calibration. Calibrated summed spectrum in X-mode in black, in S-mode in red (b).

December 28, 2024

On December 28, 2024 the first 40-s calibration was performed. The channel map and calibrated spectra are shown in Figure 5.9. This acquisition was performed with pointing towards the Crab Nebula, at an average angle of ∼25° from the local zenith. The payload temperature was around –17 °C.

December 29, 2024

On December 29, 2024 the last 40 s calibration was performed. The channel map and calibrated spectra are shown in Figure 5.10. This acquisition was performed with pointing towards the Crab Nebula, at an average angle of ∼25° from the local zenith. The payload temperature was around –16 °C.

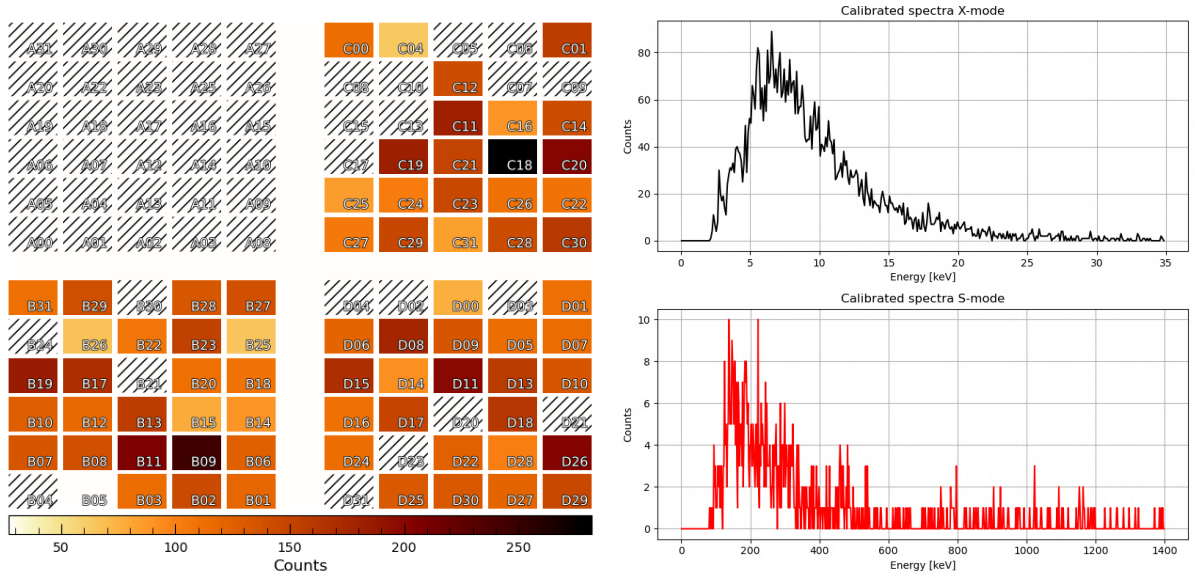

(a) **(b)**

Figure 5.9: Fifth *Calibration* outputs (December 28, 2024): the map of detector channels counts (a), with the top right quadrant switched off due to a fault occurred during ground calibration. Calibrated summed spectrum in X-mode in black, in S-mode in red (b).

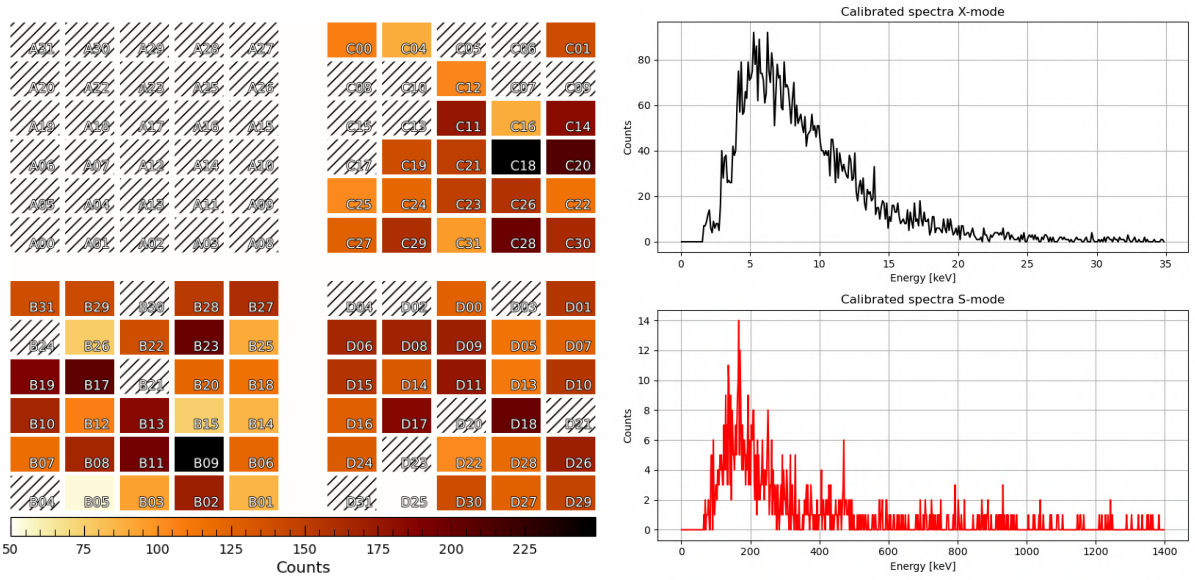

(a) **(b)**

Figure 5.10: Sixth *Calibration* outputs (December 29, 2024): the map of detector channels counts (a), with the top right quadrant switched off due to a fault occurred during ground calibration. Calibrated summed spectrum in X-mode in black, in S-mode in red (b).

February 20, 2025

On February 20, 2025 a 490 s calibration was performed. The channel map and calibrated spectra are shown in Figure 5.11. This acquisition was performed with pointing towards the Crab Nebula, at an average angle of ∼25° from the local zenith. The payload temperature was around –18 °C.

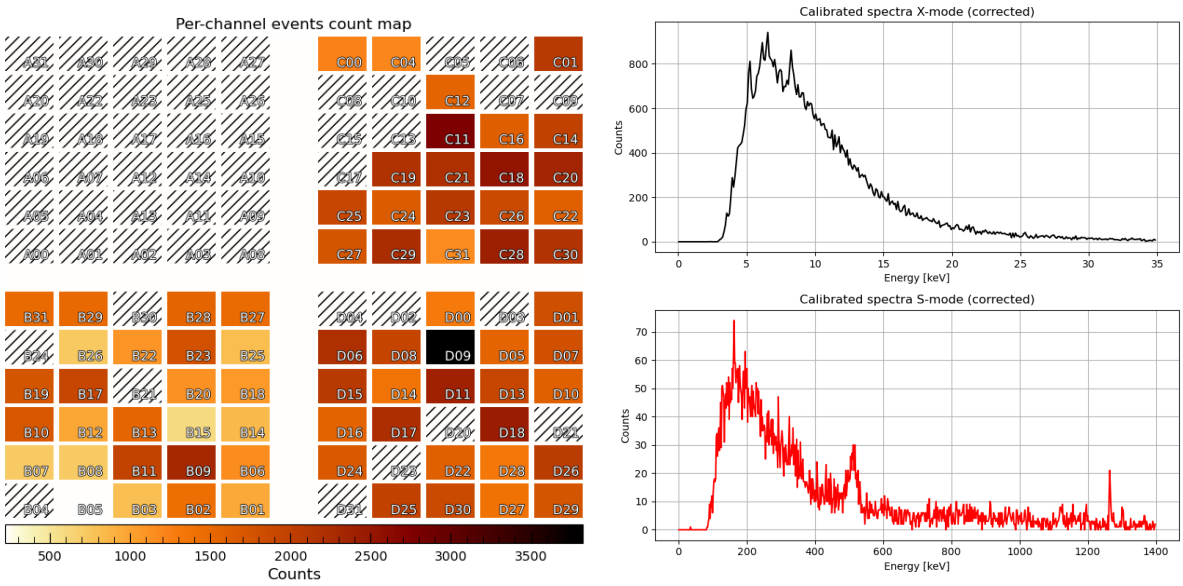

(a) **(b)**

Figure 5.11: Seventh *Calibration* outputs (February 20, 2025): the map of detector channels counts (a), with the top right quadrant switched off due to a fault occurred during ground calibration. Calibrated summed spectrum in X-mode in black, in S-mode in red (b).

A characteristic line is clearly visible in the S-mode spectrum in Figure 5.11: a peak around 511 keV. The slight shift from the nominal position reflects the degradation of the detector response over time in orbit and therefore the need to update the calibration.

After identifying the prominent line near 511 keV, another peak was also visible around 1200 keV. This second feature is probably the 1275 keV line associated with the decay of ^{22}Na. Both of these lines likely originate from crystal activation: when the detector is exposed to energetic particles such as orbiting protons, nuclear reactions can occur within the crystalline material, producing radioactive isotopes. The subsequent decay of these isotopes generates gamma-ray lines, as discussed in [122]. However, the second peak is significantly narrower than expected, given the energy resolution of the system. Therefore, its identification as ^{22}Na, consistent with the expected activation components, is still uncertain, and further studies are needed to confirm its origin (simulations in progress). Although other activation lines may also be present in the spectrum, the available statistics were insufficient to identify

them reliably.

Since the response of the GAGG:Ce crystal is not linear [102], the use of multiple lines for calibration could introduce errors. Therefore, only the 511 keV was used as reference for updating the energy calibration.

For the total spectrum, the re-calibration procedure involved fitting the line using a Gaussian function together with on a linear background, which allowed a precise determination of the line peak. The measured position was then compared with the expected energy, and the correct factor was derived. For this spectrum a correct factor of 8% was obtained, consistent with the possible degradation of the instrumental response after 18 months in orbit.

March 13, 2025

On March 13, 2025 a 400 s calibration was performed. The channel map and calibrated spectra are shown in Figure 5.12. This acquisition was performed with pointing towards the Crab Nebula, at an average angle of ∼20° from the local zenith. The payload temperature was around –17 °C. As shown in the channel map, channels C18, C23, and D09 exhibit significant noise and

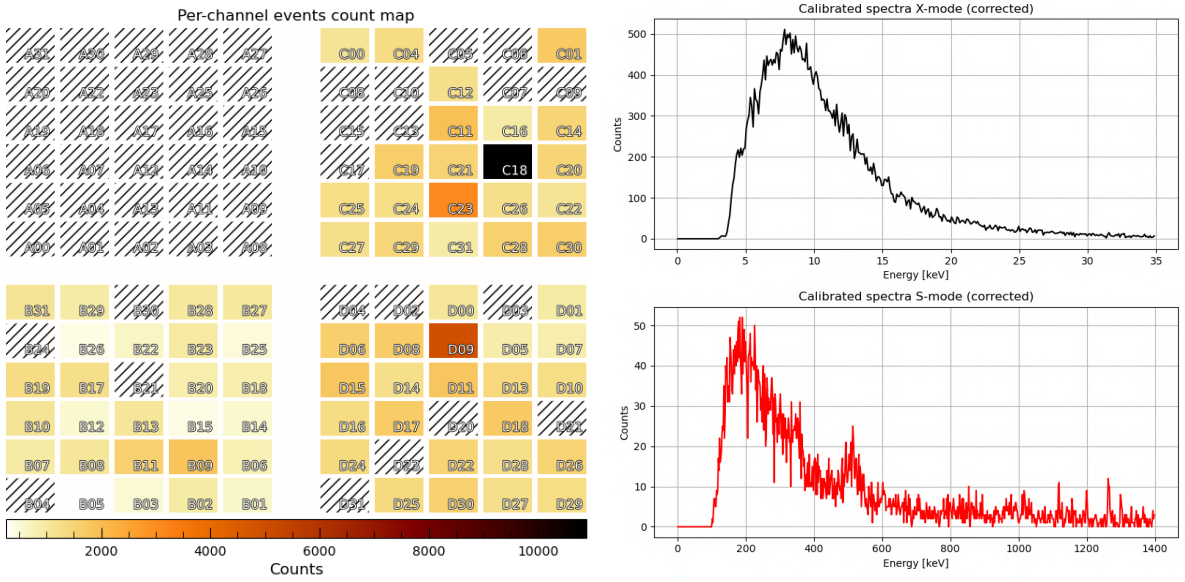

(a) (b)

Figure 5.12: Eighth *Calibration* outputs (March 13, 2025): the map of detector channels counts (a), with the top right quadrant switched off due to a fault occurred during ground calibration. Calibrated summed spectrum in X-mode in black, in S-mode in red (b).

were therefore excluded from the calibration analysis. In the calibrated summed spectrum in Figure 5.12, in the S-mode the 511 keV line is clearly visible. A calibration correction factor of approximately 9% was determined, similar to the previous data set acquired the month before.

April 01, 2025

On April 01, 2025 a 731 s calibration was performed. The channel map and calibrated spectra are shown in Figure 5.13. This acquisition was performed with pointing towards the Crab Nebula, at an average angle of ∼20° from the local zenith. The payload temperature was around –18 °C.

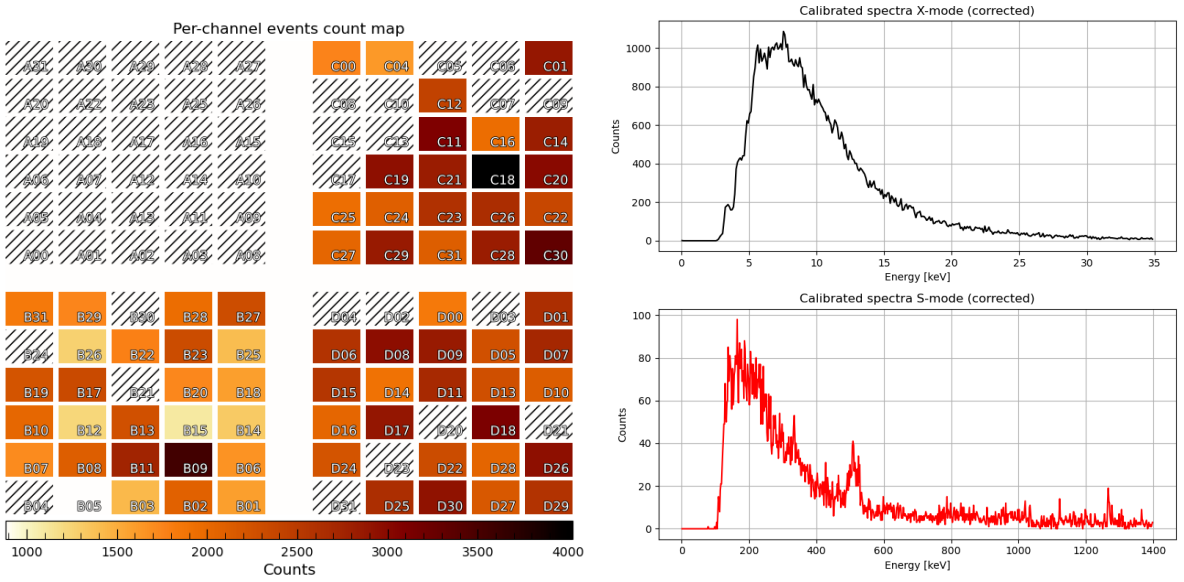

(a) **(b)**

Figure 5.13: Ninth *Calibration* outputs (April 01, 2025): the map of detector channels counts (a), with the top right quadrant switched off due to a fault occurred during ground calibration. Calibrated summed spectrum in X-mode in black, in S-mode in red (b).

In the calibrated summed spectrum in Figure 5.13, in the S-mode the 511 keV line is clearly visible. A calibration correction factor of approximately 9% was determined, similar to the previous data set acquired the month before.

5.3.2 Ground vs in-orbit calibration

All in-orbit calibration results were compared with ground calibration data [106] (Chapter 4). In particular, data collected on the ground at temperatures and threshold settings comparable to those of the acquisitions in orbit were compared. For example, the in-orbit calibration on February 17 at threshold 115 and temperature 2 °C was compared with the ground acquisition at 0 °C at threshold 105. This analysis involved all active channels and revealed a consistent pattern: channels identified as noisy during ground calibration, mainly due to ASIC re-trigger [106], showed similar behavior in orbit. This leads to an increased number of triggers, particularly near the low threshold setting. The nominal channels maintained stable perfor-

mance. Despite the low statistics of the in-orbit data, the observed consistency in channel behavior in both environments, demonstrates the stable performance of the readout electronics in different operating contexts.

As shown in the in-orbit calibration acquisitions, a calibration correction factor was calculated for the gamma-ray spectrum, which is consistent with the possible degradation of the instrumental response (Sect. 5.3.1). To define the correction factor more accurately, the total spectrum obtained by summing the last three CAL acquisitions for a total exposure time of 1131 s was analyzed, in order to increase the spectrum statistics. The original gamma-ray summed spectrum is shown in Figure 5.14 and it is corrected only for scintillator non-linearity (see Sect. 3.3.1) using the values obtained in [102]).

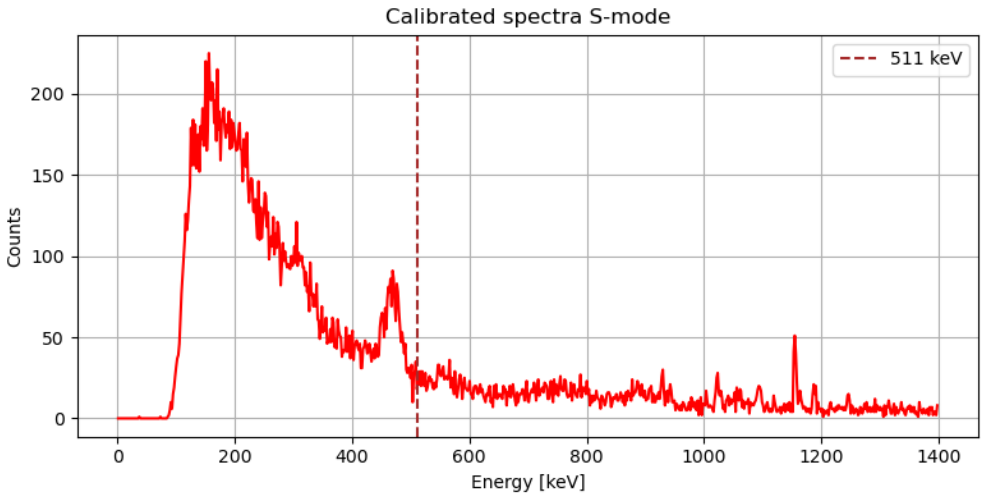

Figure 5.14: Summed gamma-ray spectrum obtained from the last three CAL acquisitions for a total exposure time of 1131 s. The spectrum is corrected for the non-linearity of the scintillator[102]. A clear line is visible around 511 keV, probably associated with the activation of the crystal.

As for single calibrations, also for the total spectrum, the re-calibration procedure involved fitting the line near 511 keV using a Gaussian function together with on a linear background, which allowed a precise determination of the line peak. The measured position was then compared with the expected energy, and the correct factor was derived. For the summed spectra a correct factor of 8% was obtained and the corrected spectrum is shown in Figure 5.15. In the events file corresponding to the last three CAL, the 511 keV line was also visible in the spectra of each individual channel. However, given the limited statistics, was not possible to determine the position of the line by a Gaussian fit, but the barycenter of the counts in the energy range where the line was expected (before correction) was calculated. Once identified, the line was compared with the expected value at 511 and a channel-by-channel correction factor was derived.

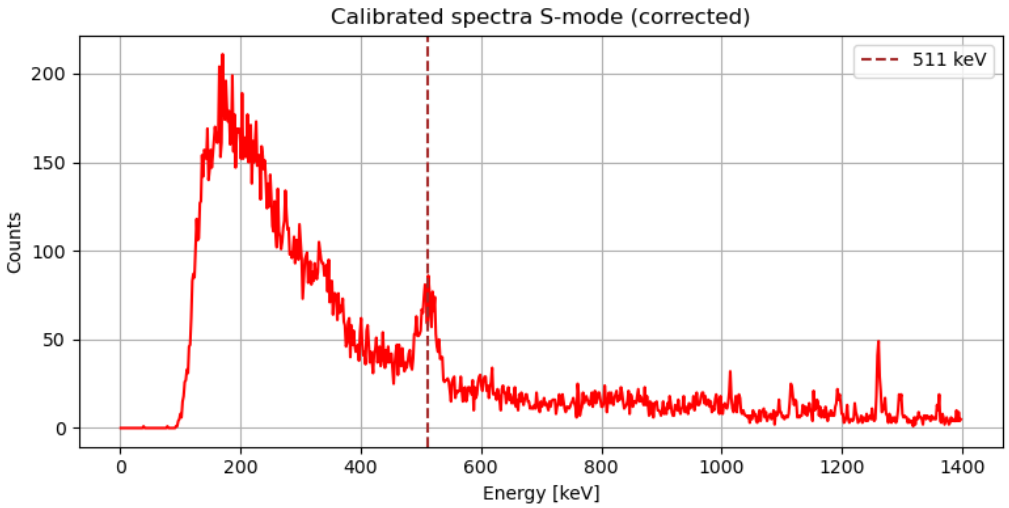

Figure 5.15: Summed gamma-ray spectrum obtained from the last three CAL acquisitions after applying the calibration correction factor derived from the line at 511 keV.

Gamma calibration was obtained using the relation described in 4.5. The stability of the parameters derived from X-mode calibration, gain, and offset, is confirmed by the consistency of the parameters measured during ground calibrations [106] (see discussion in Sect. 4.6.1) and during calibrations performed after integration of the payload into the service module (see discussion in Sect. 4.6.6). Therefore, the shift observed in the gamma-ray spectrum A[keV] was attributed to a variation in the Light Output of the crystals LY. This behavior was also observed after environmental testing carried out on the spacecraft with integrated payload. The thermal vacuum leads to a variation in light output (See Sect. 4.6.6).

The correction factors derived from the 511 keV line were then applied to the light output of the corresponding crystals, providing updated and corrected light output values.

These corrected values were then used to update the CALDB (4.5.4).

The spectrum in X-mode is also being analyzed to verify the detection of the Crab Nebula, given the pointing during these calibrations. The analysis is still ongoing and the results are not reported here.

5.3.3 Low energy threshold analysis

The low-energy threshold is a key performance feature of the HERMES-PF payload (see Section 4.6). The resulting effective energy threshold is determined by the DAC-programmed value (Sect. 3.3.2) in combination with the specific characteristics of each channel (gain, offset and light output) and the payload temperature. Consequently, a certain level of dispersion between the different channels is expected (Sect. 4.6.1). Temperature, in particular, plays a dual role: on one hand, the DAC threshold increases at lower temperatures [106] (see Section 4.6.3); on

the other hand, noise levels rise at higher temperatures. Therefore, a complete analysis of all these factors is essential to accurately characterize threshold behavior.

Given the low statistics, the minimum energy detected by each channel is used as a proxy for the effective energy threshold to study their low-energy behavior.

Each CAL acquisition was performed under different conditions. In particular, each calibration data set is characterized by a predefined threshold setting and a variable payload temperature, both of which influence the observed energy distributions. The varying operating conditions of the acquisitions make it challenging to assess the impact of leakage current.

In the following Figures, the minimum energy of the calibrated photon list detected in each channel is compared across different CAL acquisitions.

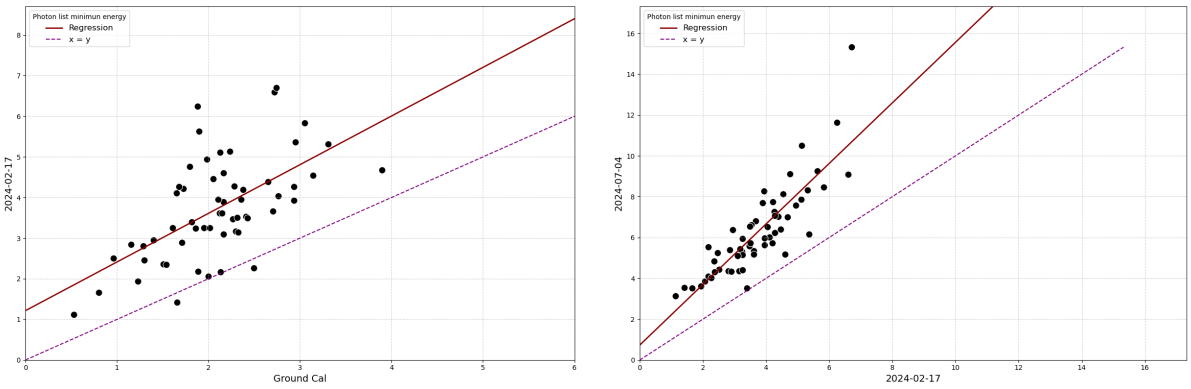

(a) **(b)**

Figure 5.16: Comparison of the minimum energy measured for different calibrations. (a) The February 17, 2024, calibration is plotted against the ground calibration. (b) The July 4, 2024, calibration is plotted against the February 17, 2024, calibration. The black scatter points represent individual detector channels, the purple dashed line corresponds to the ideal x=y reference (no variation), and the red line represents the best linear regression fit.

Figure 5.16(a) compares the minimum energy measured between the calibration performed on February 17, 2024, and the ground calibration. For the former the DAC threshold was set at 115 and the P/L temperature was ∼2 °C, while for the latter the threshold was set at 105 with a temperature of 0 °C. The black scatter points represent the individual detector channels, while the purple dashed line represents the ideal x = y reference, which indicates no change between the two calibrations. The dark red regression line shows the best linear fit to the data. The slope of the regression line is consistent with the fact that the temperature difference is just around 2 °C and the DAC threshold is higher for the 17 February CAL, resulting in a higher minimum energy.

Similarly, Figure 5.16(b) compares the July 4, 2024, calibration with the February 17, 2024, one. The slope of the regression is consistent with the trend observed in[106], confirming that

lower operating temperatures lead to a threshold shift toward higher energies.

Continuing the comparison across calibrations, another example is shown in Figure 5.17(a), where the December 11, 2024, CAL is plotted against the July 4, 2024, CAL, and in Figure 5.17(b), where the December 28, 2024, CAL is plotted against the December 11, 2024, CAL.

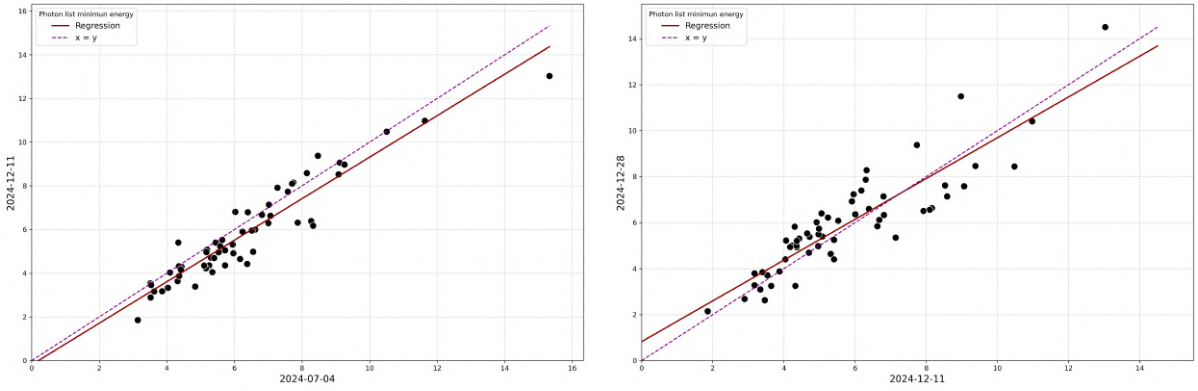

(a) **(b)**

Figure 5.17: Comparison of the minimum energy measured for different calibrations. (a) The July 04, 2024, calibration is plotted against the December 11, 2024. (b) The December 11, 2024, calibration is plotted against the December 28, 2024, calibration. The black scatter points represent individual detector channels, the purple dashed line corresponds to the ideal x=y reference (no variation), and the red line represents the best linear regression fit."

On 4 July, the DAC threshold was set at 150 with a payload temperature of approximately -8 °C, while on December 11, it was set to 135, with a temperature of approximately -17 °C. The 9-degree temperature difference compensates for the change in DAC threshold from 150 to 135, as expected, therefore the regression line is almost consistent with the ideal one.
The two December calibrations were performed with the same threshold setting (135) and the same temperature (-17 °C), again resulting in a regression line almost consistent with the ideal one. The slight deviation of the regression line from the ideal x=y is mainly due to the intrinsic variability of each channel's parameters, as well as the contribution of channels with higher noise levels, which tend to increase the dispersion around the average response.

The last three calibrations acquired are compared in the Figure 5.18. The February 20, 2025, calibration is plotted against the March 13, 2025 CAL in Figure 5.18a. In Figure 5.18b, the March 13, 2025, calibration is plotted against the April 01, 2025, CAL.
These acquisitions were all made under the same threshold conditions (135), with a difference of 1°C in temperature for the acquisition on March 13 (-17 °C), compared to the other two CALs (-18 °C).

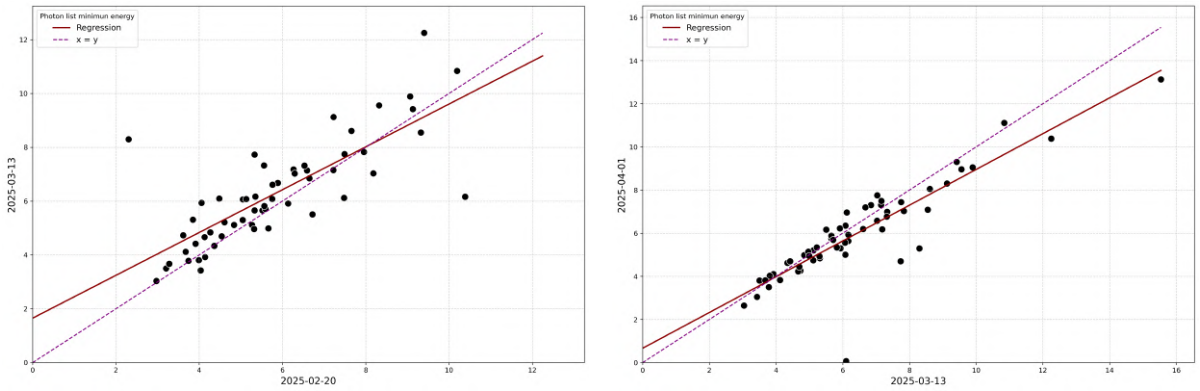

(a) **(b)**

Figure 5.18: Comparison of the minimum energy measured for different calibrations. (a) The February 20, 2025, calibration is plotted against the March 13, 2025. (b) The March 13, 2025, calibration is plotted against the April 01, 2025, calibration. The black scatter points represent individual detector channels, the purple dashed line corresponds to the ideal x=y reference (no variation), and the red line represents the best linear regression fit."

In conclusion, based on the dependence of the low-energy threshold on the DAC-programmed value, temperature, and individual channel parameters (gain, offset, and light output) [106], it can be observed that the resulting effective energy threshold of each channel has remained substantially stable over time and that the channels therefore behave nominally in orbit under different operating conditions.

The April 1, 2025 CAL was also used to update the auxiliary response file (ARF) for the HERMES-PF payload. The minimum energy detected by each channel was used to individually scale the effective threshold, and the contributions of all active channels were combined to produce an updated ARF. Rather than assuming a single threshold for all channels, this ARF reflects the behavior of each individual channel and therefore provides a more accurate representation of the detector's response under nominal operating conditions.

5.4 Ratemeters in Observation mode

SpIRIT has performed 10 Observations of 600 seconds each (for a total accumulated 100 min of observation time) summarized in Table 5.2.

Date	Acquisition Duration	P/L Temperature ∼	Description
2024-03-27	600 s	1 °C	"First light". Satellite in spinning. Pointing Unknown.
2024-04-04	600 s	1 °C	Satellite in spinning. Pointing Unknown.
2024-04-08	600 s	2 °C	Satellite in spinning. Pointing Unknown.
2024-06-01	600 s	−3 °C	Partial overlap with northern polar electron belt. Pointing Unknown.
2024-06-06	600 s	−6 °C	Pointing mostly zenith.
2024-06-13	600 s	−8 °C	Pointing and Satellite attitude unknown.
2024-06-18	600 s	−3 °C	Pointing and Satellite attitude unknown.
2024-06-23	600 s	−4 °C	Pointing and Satellite attitude unknown.
2024-06-24	600 s	−7.5 °C	Pointing and Satellite attitude unknown.
2024-06-28	600 s	−9.5 °C	Pointing and Satellite attitude unknown.

Table 5.2: Summary of Observation acquisitions performed by SpIRIT.

The first nominal *Observation* was on March 27, 2024. Each SRA file contains the light curves acquired in the three energy bands $3 < E_{\text{low}} < 10$ keV, $10 < E_{\text{mid}} < 100$ keV, and $E_{\text{high}} > 100$ keV with 100ms of resolution. The Figure 5.19 compares the light curves for each observation.

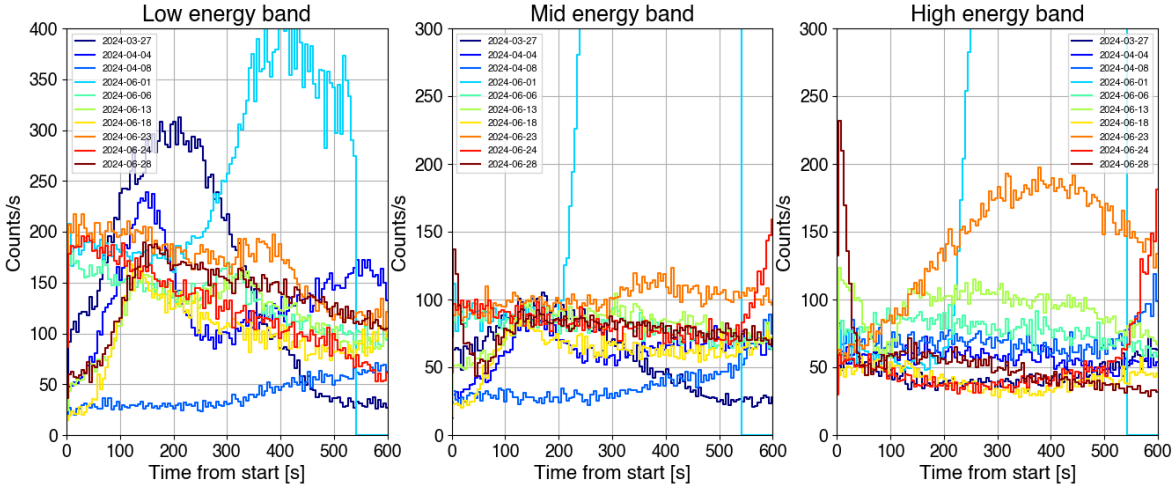

Figure 5.19: Light curves of the 10 acquisitions in observation mode of 10 minutes each in the three energy bands: 3–10 keV, 10–100 keV, 100 keV–2 MeV. The light blue curve is the observation of June 1, 2024: the rising count rate indicates the satellite entering the northern polar electron belt.

The housekeeping data recorded in *Idle* and *Ready* preceding each 10-minute observation pe-

riod confirmed the overall health of the system. During the first observations, the spacecraft's attitude changed with each data acquisition. At low and medium energies, the observed modulation was primarily due to the Earth's gradual entry into the field of view, partially obscuring the cosmic X-ray background. The background levels detected across the three energy bands aligned with pre-flight estimates.

For all other observations, a comparative analysis was performed using background simulations based on the model described in [123]. These simulations account for all the main populations of particles and photons which contribute to the on-board scientific background, fully convolved with the HERMES-PF mass model. The dominant contribution comes from the Cosmic X-ray Background (CXB). By calculating the expected modulation of the background contributions and incorporating the spacecraft's attitude, simulated light curves were generated to represent the expected background under realistic operational conditions. Since information on the spacecraft attitude was not available, multiple hypotheses were tested for each observation to identify the attitude configuration that best matched the acquired data. These configurations were very simplified, considering only a single possible S/C axis of rotation. The simulated light curves were subsequently compared with the acquired observation data for each energy band. No pointing information was available for any observation.

5.4.1 Observation mode, March 27, 2024

In the March 27, 2024 Observation, the spacecraft attitude was characterized by a time-dependent pointing direction (S/C in spinning configuration). No pointing information was available. To simulate this attitude dynamics, a linear rotation model was adopted, in which the pointing angle evolves over time according to a constant rotation speed and an initial phase. This model is defined by:

$$\theta(t) = \omega t + \phi \bmod 360^\circ \tag{5.1}$$

where $\theta(t)$ is the pointing angle at time t, ω is the rotation speed (in deg/s), and ϕ is the initial phase. The $\theta(t)$ value is always reported in the range [0°,360°]. The best configuration values, derived from the comparison between simulations and observational data, are a rotation speed of 0.6°/s and an initial phase of 60°. Figure 5.20 shows the comparison between the observational data (blue line) and the background modulation (black line) expected from the simulations in the three energy bands: 3–10 keV, 10–100 keV, 100 keV–2 MeV.

The observed background is consistent with the trend in the three bands expected, with variations consistent with the orientation of the spacecraft, and the Earth's gradual entry into the field of view, except for the low-energy band, where the observed count rate is significantly higher than predicted by the simulations. This discrepancy is probably due to the contribution

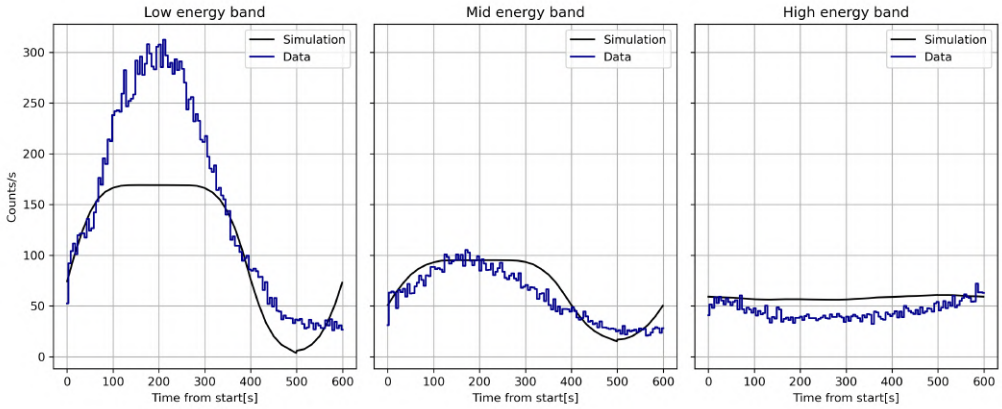

Figure 5.20: March 27, 2024 Observation. Comparison between acquired light curves (colored) and background simulated counts (black) in different energy bands.

of additional astrophysics sources, predominant in the soft X-ray band and not considered in the background model.

5.4.2 Observation mode, April 4, 2024

In the April 04, 2024 Observation, the S/C was still in spinning configuration. The the best configuration for describing the data includes a rotation speed of 1°/s and the initial phase is 20°.

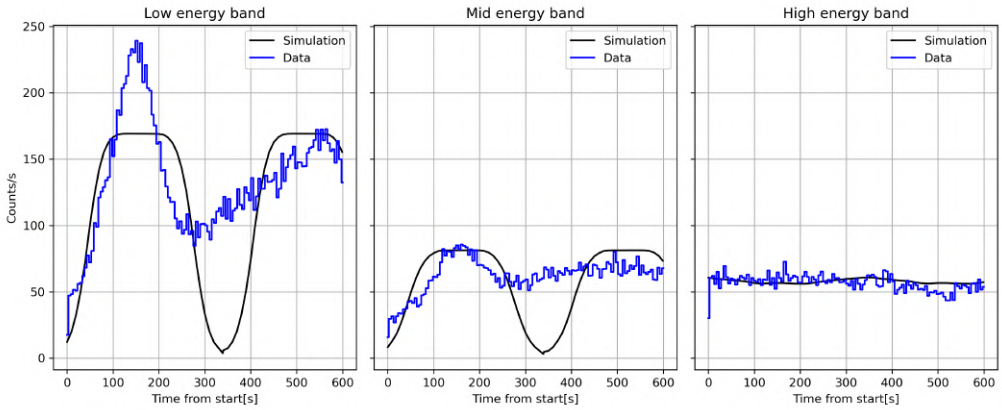

Figure 5.21: April 04, 2024 Observation. Comparison between acquired light curves (colored) and background simulated counts (black) in different energy bands.

Figure5.21 shows the overlap between data (blue) and simulation (black). As with the previous acquisition, the data show a higher count rate than the simulations, particularly during the transition between the two rotation speeds. This discrepancy is probably due to the contribution of additional X-ray sources, not included in the background model. Their impact seems to be more pronounced in the low-energy band, consistent with the presence of soft X-ray

emitters.

5.4.3 Observation mode, April 8, 2024

In the April 08, 2024 Observation, the S/C is still in spinning configuration. The data are best described by a rotation speed of 0.1°/s and no initial phase.

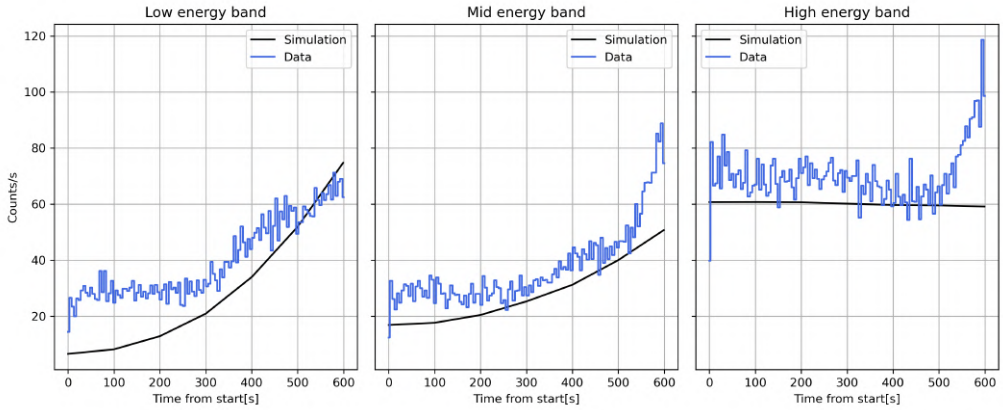

Figure 5.22: April 08, 2024 Observation. Comparison between acquired light curves (colored) and background simulated counts (black) in different energy bands.

This acquisition, shown in Figure 5.22, still shows a slight underestimation of counts in simulation. Furthermore, without detailed information on the satellite pointing, it is difficult to determine with certainty the origin of the increased count rate mostly at high energies.

5.4.4 Observation mode, June 1, 2024

In the June 1, 2024 Observation the satellite's orientation shows a certain degree of stability and the Earth remains roughly stable at the edge of the field of view, contaminating its outer regions at lower energies. Figure 5.23 shows a zoom of the first minutes of all the first observations, with the June 1 in light blue. In particular, a significant surge in counts is observed in the mid and high-energy bands due to the satellite entry into the polar electron band. Background signal levels remain stable before entering this specific zone, aligning with previous measurements and pre-launch projections, as indicated by the dotted black line.

5.4.5 Observation mode, June 6, 2024

In the June 6, 2024 Observation in Figure 5.24, the available pointing information indicates that the S/C was mainly pointing towards the zenith. Therefore, the best configuration to describe the data assumes no rotation and no initial phase.

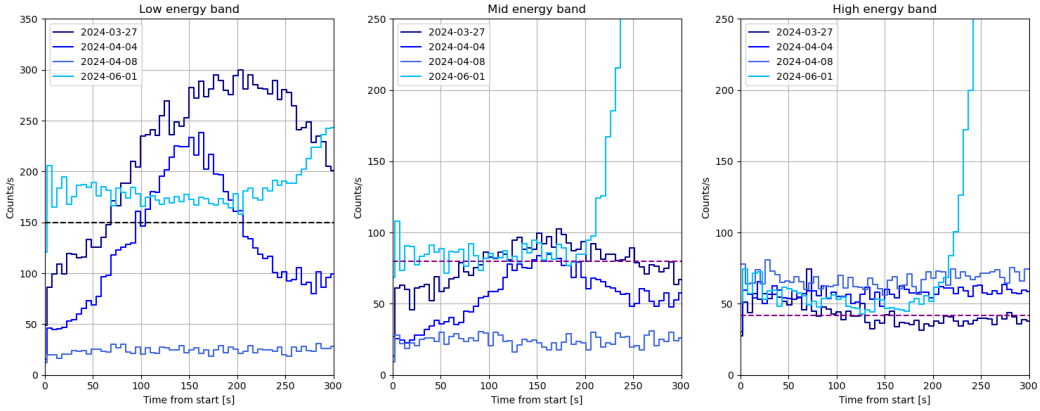

Figure 5.23: Zoomed view of the first 300 s for the first observations light curves in three energy band. The lightblue curve is the observation of June 1, 2024: the rising count rate indicates the satellite entering the northern polar electron belt. The black dotted line represents pre-launch background estimates.

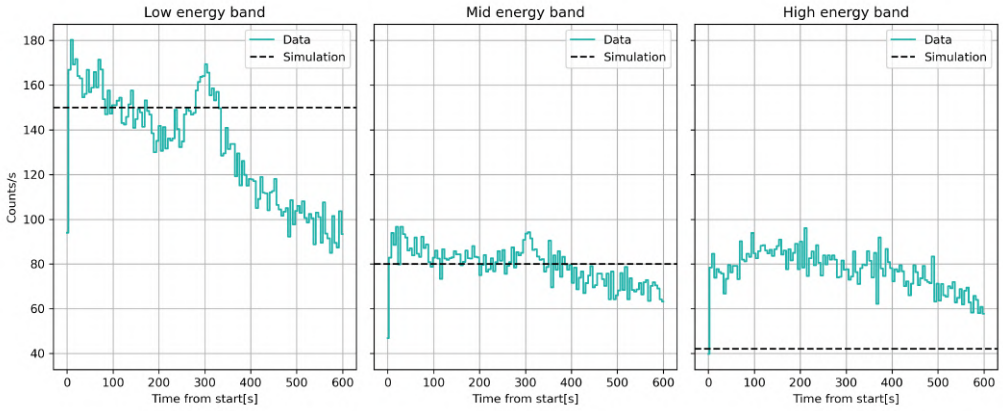

Figure 5.24: June 06, 2024 Observation. Comparison between acquired light curves (colored) and background simulated counts (black) in different energy bands.

An abnormal behavior is observed at low-energy band, together with a significantly higher count rate at high energies. The anomalous peak in the low energy band corresponds to a brief deviation from the satellite nominal zenith pointing attitude, during which Sco X-1 entered the instrument field of view.

5.4.6 Observation mode, June 13, 2024

In the June 13, 2024 Observation in Figure 5.25 and in the following ones, the S/C attitude is unknown, therefore the linear rotation model discussed in Sect. 5.4.1 is used. The the best configuration for describing the data includes a rotation speed of 0.4°/s and the initial phase is 50°.

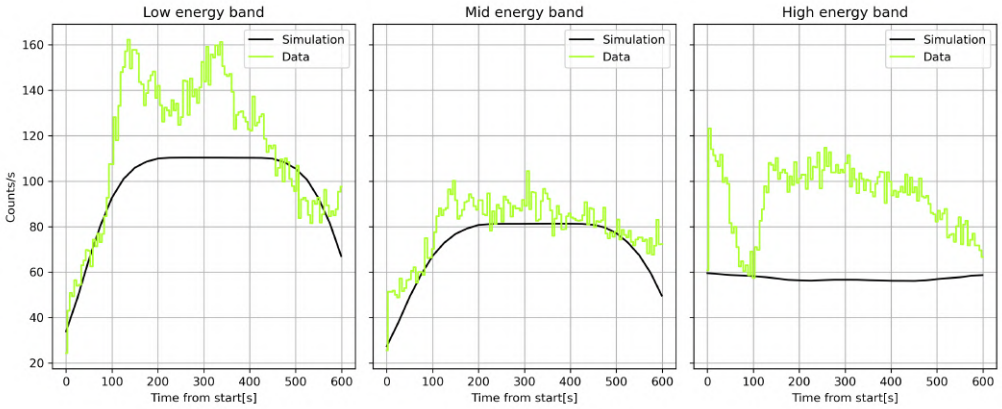

Figure 5.25: June 13, 2024 Observation. Comparison between acquired light curves (colored) and background simulated counts (black) in different energy bands.

Again, a possible contribution of X sources is observed in the low-energy band, together with a significantly higher count rate at high energies.

5.4.7 Observation mode, June 18, 2024

In the June 18, 2024 Observation in Figure 5.26, the best configuration for describing the data includes a rotation speed of 0.35°/s and the initial phase is 45°.

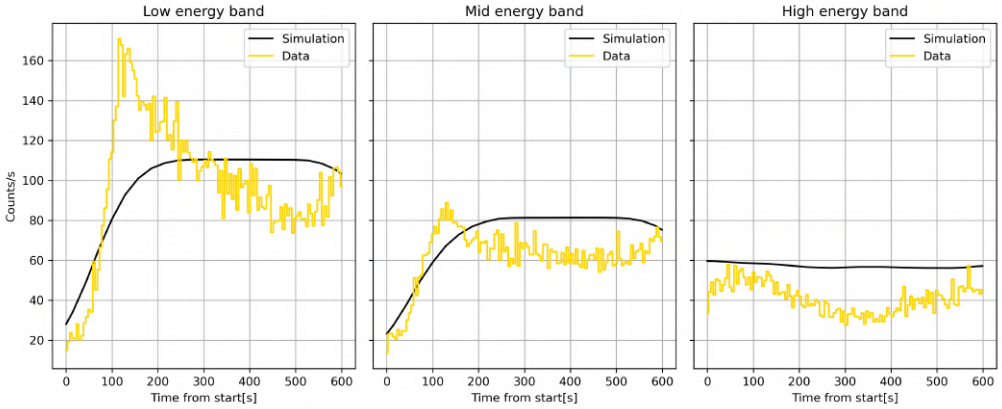

Figure 5.26: June 18, 2024 Observation. Comparison between acquired light curves (colored) and background simulated counts (black) in different energy bands.

5.4.8 Observation mode, June 23, 2024

In the June 23, 2024 Observation in Figure 5.27, the best configuration for describing the data includes a rotation speed of 0.2°/s and the initial phase is 85°.

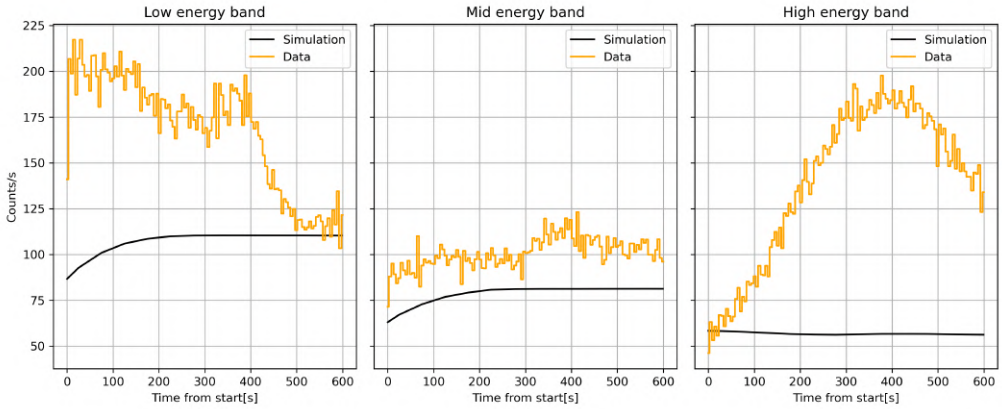

Figure 5.27: June 23, 2024 Observation. Comparison between acquired light curves (colored) and background simulated counts (black) in different energy bands.

5.4.9 Observation mode, June 24, 2024

In the June 24, 2024 Observation in Figure 5.28, the best configuration for describing the data is represented by the pre-launch background simulations that do not involve any rotation of the satellite.

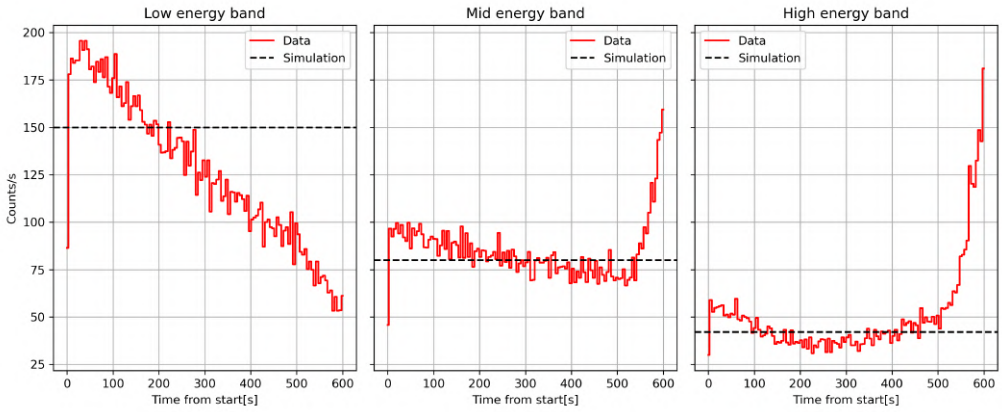

Figure 5.28: June 24, 2024 Observation. Comparison between acquired light curves (colored) and background simulated counts (black) in different energy bands.

5.4.10 Observation mode, June 28, 2024

In the June 28, 2024 Observation in Figure 5.29, the best configuration for describing the data includes a rotation speed of 0.35°/s and the initial phase is 55°.

In most observations, the low-energy band shows an excess of counts compared to simulations, suggesting the presence of additional X-ray sources in the background. In contrast, the high-energy band shows variability between different observations, probably influenced by changes

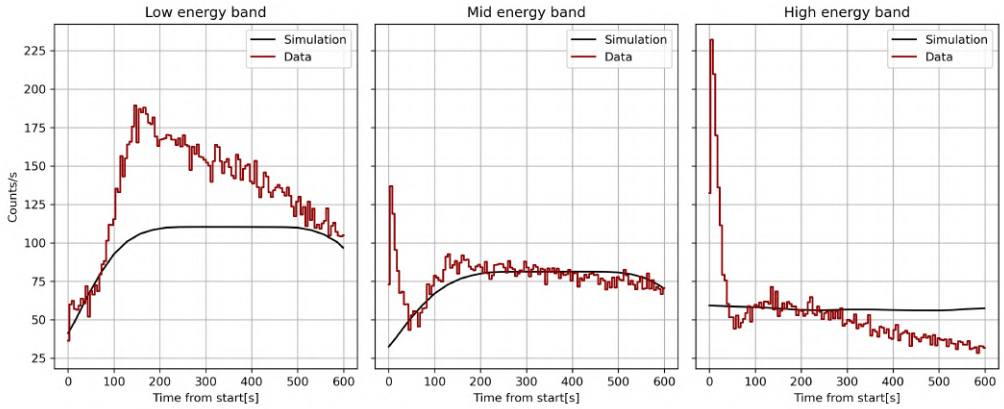

Figure 5.29: June 28, 2024 Observation. Comparison between acquired light curves (colored) and background simulated counts (black) in different energy bands.

in the spacecraft environment or background contributions such as cosmic rays or potential solar activity.

In addition, the model assumes uniform rotation so that if pointing undergoes deviations or instabilities, the time at which a source enters the field of view could differ from predictions.

Although the model is extremely simplified, it allows for indications of the satellite behavior during observations. Given the lack of precise pointing information, this analysis allows reasonable approximations to interpret and justify the observed data.

5.4.11 Scatter Plots

For all observations, potential correlations between the counts in the three working quadrants across the three different energy bands (low, medium, high) were analyzed. In particular, simultaneous counts between all pairs of quadrants were compared, including counts with a 100 μs offset. This allowed us to verify that there were no correlated high-intensity events and that the detected spikes were therefore independent and related, for example, to instrumental noise (such as noisy channels).

In Figure 5.30 an example of scatter plots for the 6 June, 2024 Observation between quadrants C and D for the three energy band 3–10 keV (a), 10–100 keV (b), 100 keV–2 MeV (c). The data show no correlation between quadrants.

The observation of June 1, 2024 is the only one in which a strong correlation is visible, as shown in Figure 5.31b. As described in 5.4.4, a significant surge in counts in the mid and high-energy bands is observed due to the satellite entry into the polar electron band.

In fact, the related counts are caused by ionization streaks produced by charged particles passing through the detectors simultaneously. The entry into the electron polar band occurs

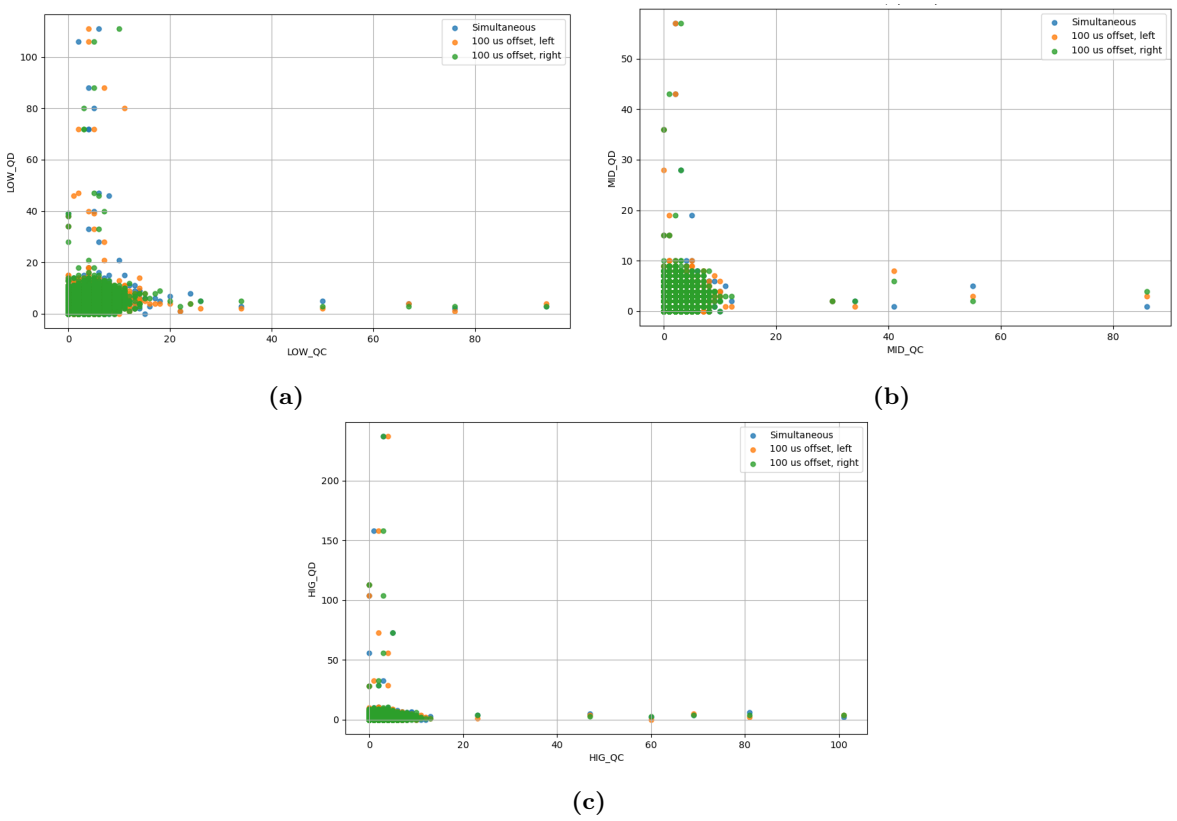

Figure 5.30: Scatter plots for the 6 June, 2024 Observation between quadrants C and D for the three energy band 3–10 keV (a), 10–100 keV (b), 100 keV–2 MeV (c). No correlation is visible in the data.

after the first 200 seconds of observation. Figure 5.31a shows the scatter plot in the high energy band between quadrants B and D during the first 200 seconds, where no correlation is visible, while Figure 5.31b shows the same plot after 200 seconds, where a clear correlation can be seen. The correlation is visible across all quadrants.

5.5 Observation strategy and lessons learned

The commissioning of SpIRIT took more than a year to complete, with the main limitation being the low data transmission rate (50 kBytes per day). Starting from June 2025, the instrument entered the standard observation phase, organized to maximize scientific efficiency despite bandwidth constraints. The strategy adopted is to keep the payload on a few tens of minutes per day, without immediately downloading the data, which remains on board. During observations, the presence of transients is monitored by consulting reports from the Gamma-ray Coordinates Network (GCN). If a transient is identified, the ratemeters relating to the period of the event are downloaded. If the ratemeters show a significant signal, the photons

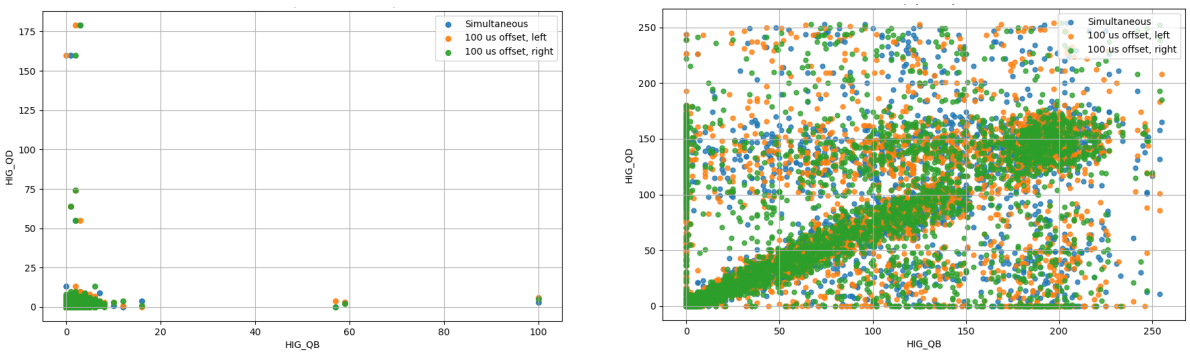

(a) **(b)**

Figure 5.31: Scatter plots of high-energy band between quadrants B and D on June 1, 2024 observation.

recorded in the same time interval are then downloaded. This procedure optimizes the use of the limited data transmission capacity, ensuring maximum scientific return and focusing the download only on events of real interest.

In addition to the scientific results, SpIRIT provided an important opportunity to evaluate the performance of key technologies and the efficiency of operational procedures. The several lessons learned, from both an organizational and technical point of view, can help optimize the in-orbit operations of HERMES-PF, as well as the operation of the TASTE mission spectrometer (Chapter 6), and to design and plan more ambitious projects, such as a complete constellation that can serve as a monitor of the entire sky for high-energy transients [124]. Some of the main lessons learned are summarized below [124].

- The key technologies for the development of the P/L include the design and production of SDDs, ASICs for signal acquisition and processing, and thin optical filters to block optical and UV light. These critical components were developed through scientific agreements within the HERMES-PF consortium. The SDDs were designed by the University of Udine, INFN, and FBK, and manufactured and tested by FBK and INFN. The ASICs were developed by PoliMI and the University of Pavia, and fabricated through EUROPRACTICE. Between 2018 and 2022, four iterations of ASIC prototypes were produced and tested to enhance reliability and performance. Optical filters, designed and manufactured by IHEP China, demonstrated excellent X-ray transparency and UV absorption in tests conducted at IHEP and INAF. These collaborations ensured full integration between technology development and scientific objectives, optimizing the design while keeping costs aligned with CubeSat constraints.

- The HERMES P/L does not use expensive radiation-resistant electrical, electronic and

electromechanical (EEE) components. In particular, it uses a flight-proven OBC (PDHU) supplied by ISIS-Space, while the P/L's other electronic boards do not use space-qualified components, and have been designed using measures to make them robust in the space environment, such as redundancy and circuits to protect against latch-ups. The most critical elements (including DC-DC and ADC converters, current-sensitive amplifiers, LDO regulators, inverters and other elements) were validated through proton beam irradiation tests at the INFN TIFPA laboratories in Trento. The P/L electronic boards on board SpIRIT operated without any problems for over eight months in the harsh space environment, demonstrating the reliability of the design and manufacturing processes. In addition, proton beam tests were conducted at TIFPA to assess the behavior of GAGG:Ce scintillator crystals and SDDs when exposed to proton doses representative of those encountered in orbit over a two-year operational period. The results confirmed the suitability of GAGG:Ce and SDDs for space applications.

- Software development and testing is one of the most complex and time-consuming activities. This process should start as soon as hardware components such as breadboards or engineering models (EM) are available. However, it is crucial to emphasize that the proper functioning of the system is guaranteed by testing the flight models. Therefore, it is essential to perform extensive and repeated tests on the FM to ensure that all functionalities are verified and validated under real operating conditions.

- The management of communications with third parties. In particular, some operational problems with spacecraft were compounded by challenges related to privacy requirements and bureaucratic constraints, which affected the timeliness and effectiveness of communications with the S/C team. These issues highlighted the importance of establishing smoother and more transparent synergies between the various stakeholders in order to reduce the latency of critical communications while improving the quality of science operations.

Chapter 6

TASTE

The experience provided by the HERMES-PF development is allowing the studies on the adaptation of its payload to more challenging radiative environments. In this contest, the X-ray and gamma-ray spectrometer derived from the one onboard HERMES Pathfinder has been selected for the TASTE (*Terrain Analyzer and Sample Tester Explorer*) mission, with the goal of obtaining XRF (X-ray Fluorescence) and gamma-ray spectroscopy of the surface of Deimos, one of the moons of Mars [125]. These measurements will provide information on the chemical composition of the surface and thus helping to discriminate between the two possible origins of Deimos: a captured asteroid or a fragment of Mars.
The mission is currently in phase B and is the result of collaboration between INAF-OAA, INAF-OATS, and Politecnico di Milano. The project is funded by the Italian Space Agency (ASI). This Chapter introduces the mission and its general architecture in Section 6.1; Section 6.2 describes the scientific objectives of the spectrometer and Section 6.3 presents the derived scientific and technical requirements. Section 6.4 details the modifications required to the HERMES-PF payload to meet the new requirements.

6.1 The mission

TASTE is CubeSat mission composed by a 12U orbiter + 4U lander, aiming to explore the Martian moon Deimos [125]. Understanding the origin and evolutionary history of Phobos and Deimos, considered key targets for studying the evolution of Mars and, more generally, terrestrial planets, requires the acquisition of accurate data on their physical and compositional properties. Currently, there is still no consensus regarding their formation process: the two main hypotheses discussed in the scientific community are their origin from a large impact with subsequent aggregation of debris, or the gravitational capture of asteroids.
To date, no space mission has had the primary objective of exploring Phobos or Deimos;

however, several probes dedicated to the study of Mars have made remote and opportunistic observations of both satellites. It is in this context that the Martian Moons Exploration (MMX) mission was conceived, led by the Japanese space agency JAXA and scheduled for launch in 2026. MMX will be a five-year robotic mission with the goal of bringing samples from the surface of Phobos back to Earth. The TASTE mission therefore aims to focus its study on Deimos, complementing MMX.

TASTE will use a set of instruments distributed across two complementary platforms: TASTE-Orbiter and TASTE-Lander. Both will be able to operate independently or in close synergy. The Orbiter will be equipped with a multispectral camera and the HERMES-PF X-ray and gamma-ray spectrometer, while the Lander will integrate a camera and a Surface Sample Analyzer (SSA), consisting of a Sample Acquisition Mechanism (SAM) and an analytical laboratory dedicated to examining the collected samples. A schematic view of TASTE 16U Cubesat before separation between lander and orbiter is shown in Figure6.1. Different payloads are indicated by the orange boxes: the spectrometer is under the responsibility of the INAF-OATS team, of which the author is a member.

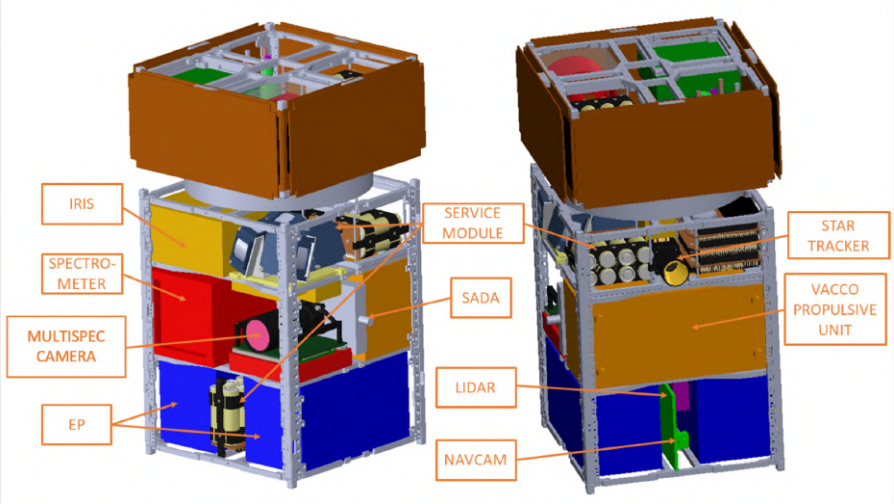

Figure 6.1: Schematic representation of the TASTE 16U CubeSat before separation between lander and orbiter. The payloads are indicated by the orange boxes.

Taking advantage of the complementarity between orbital observations and direct in situ analysis, the TASTE mission aims to achieve several scientific goals. These include: the study of the global morphology and geological context of Deimos, the determination of elemental abundance on a planetary scale, the morphological and textural characterization of the landing site, the identification of surface organic compounds, the analysis of soil composition, the comparison between local and global surface properties, as well as the measurement of the gravitational field and the investigation of the satellite's internal structure.

6.2 Spectrometer scientific goals

The X-ray and gamma-ray spectrometer is derived from the HERMES-PF instrument, described in Section 3.3. The use of X-ray and gamma-ray spectroscopy allows the elemental composition of its surface to be estimated with good accuracy, providing important information for the study of Deimos formation.

In particular, the primary objective is to investigate Deimos formation scenarios by determining its global surface elemental abundances. This will be accomplished through the comparison of mass abundance ratios derived from the detection of fluorescent lines in the X-ray band (S, Ca, Mn, Cr, Fe, Ni) and nuclear lines in the gamma-ray band (K, Si, Al, Th, C) with reference values obtained from meteorites and mineral analogs analyzed in laboratory. The energy of these emission lines are listed in Table 6.1 for the X- and gamma-ray bands.

Element (X)	*Emission line energy (keV)*	*Element (γ)*	*Emission line energy (MeV)*
S	2.308	K	1.460
Ca	3.692	Si	1.779
Mn	5.899	Al	1.809
Cr	5.415	Th	2.614
Fe	6.404	C	4.945
Ni	7.478	–	–

Table 6.1: Energies of the main emission lines of elements of interest in the X-ray and gamma-ray bands for the study of the composition of Deimos.

The *X-rays* emitted from the surface of Deimos are detected by the spectrometer, with the strongest signals expected during periods of intense solar activity. X-ray fluorescence depends in part on solar emission: even during periods of low activity, flares can trigger detectable signals, but the efficiency of the process increases significantly near solar maxima. The analysis will concentrate on the Fe/Ca, Fe/Mn, and Fe/S abundance ratios to characterize the surface composition of Deimos. These ratios will be compared with reference values obtained from meteorites and mineral analogs studied in the laboratory. The Fe/Ca ratio serves as the primary diagnostic, as the close proximity of the lines in energy minimizes uncertainties associated with the temperature of the illuminating solar flare. The Fe/Mn and Fe/S ratios act as supplementary checks to reinforce the findings, while comparisons involving lines separated by larger energy gaps, such as S and Fe, are more sensitive to variations in the solar spectrum.

So far, only a few successful experiments have been conducted with X-ray fluorescence (XRF). Missions targeting the Moon include Apollo 15 and 16 XRFS [126, 127], SMART-1 D-C1XS [128],

and Chandrayaan-1 C1XS [129]. For Mercury, XRF observations were carried out by Messenger-XRS [130] and will be further investigated by BepiColombo-MIXS [131]. For asteroids, XRF studies were conducted by NEAR-XGRS on Eros [132], Hayabusa-XRS on Itokawa [133], and OSIRIS-REx/REXIS on Bennu [134].
An example of comparison between remote sensing data and laboratory analogs for the asteroid Eros was observed by NEAR-XRS in Figure 6.2 [135].

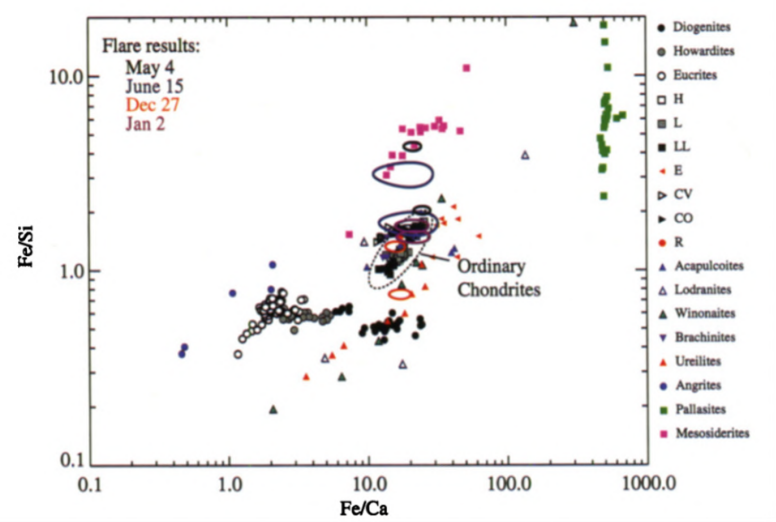

Figure 6.2: Fe/Si and Fe/Ca weight ratios inferred for asteroid Eros by NEAR-XRS and compared with ratios measured in laboratory for different meteorites [135].

The *gamma-ray* spectrometry is independent of solar activity. It will detect emissions from the decay of natural radionuclides, reactions induced by cosmic rays, neutron capture, and radioactivity caused by solar protons. Ratios such as K/Th and K/U provide reliable indicators of overall composition and provide clues about the formation environment of Deimos.

In terms of gamma-ray spectroscopy, one of the most recent missions is Kaguya-GRS [136], which produced a global map of the Moon. Other lunar investigations include the Lunar Prospector GRS and Chang'e [137]. Beyond the Moon, gamma-ray spectroscopy has been applied to other planetary bodies: Mars Odyssey-GRS at Mars [138], Messenger-GRNS at Mercury [139], NEAR-XGRS at asteroid Eros [132]. One example of a comparison between the average spectrum of lunar gamma-rays acquired during the Lunar Prospector (black) and Kaguya (red) is shown in Figure6.3 [140].

Only limited observations of X-rays and gamma-rays have been obtained in the Martian system. These include remote sensing with Chandra and XMM-Newton [143, 144], as well as in situ measurements by rover instruments [145]. The upcoming MMX mission will carry the MEGANE (Mars-moon Exploration with GAmma rays and NEutrons) instrument [146]. Since

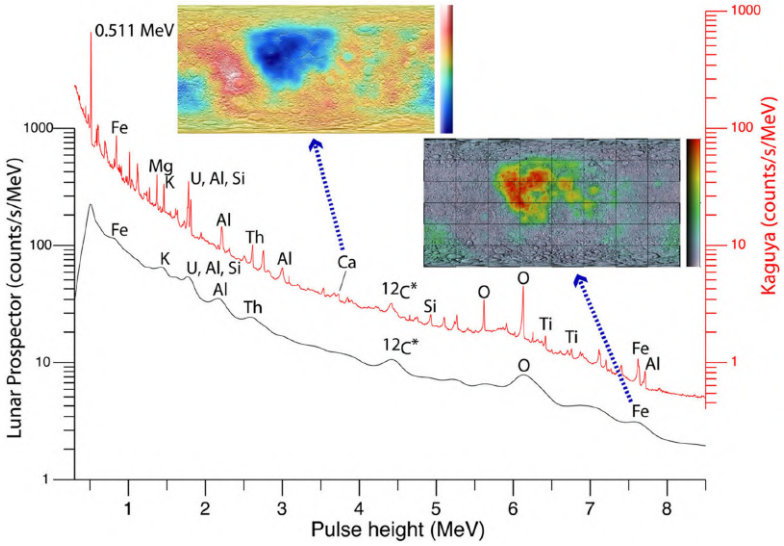

Figure 6.3: Example of a comparison between the average spectrum of lunar gamma-rays, acquired during the Lunar Prospector (black) and Kaguya (red) missions [140]. Gamma-ray peaks reveal elements such as aluminum (Al), calcium (Ca), and titanium (Ti). The insets show global maps of iron oxide (right) and calcium oxide (left) derived from Lunar Prospector and Kaguya data, respectively [141, 142].

the mission only plans flybys of Deimos, it will not be possible to collect gamma-ray data, which require long accumulation times at low altitudes. Instead, MEGANE will perform neutron measurements at Deimos, to be compared with detailed gamma- and neutron-spectroscopy data from Phobos. In this context, the TASTE spectrometers will provide the first-ever X-ray and gamma-ray observations of Deimos, enabling new insights into its surface composition and a stronger comparison with the MMX dataset from Phobos.

6.3 Spectrometer Scientific Requirements

The main objective of the Phase A study was to define the scientific requirements of the spectrometer in direct relation to the overall scientific objectives of TASTE, to which the author contributed by participating in the definition process. Specifically, the requirements are as follows:

- Fe/Ca, Fe/S, and Mn/S ratios: these must be limited with an uncertainty of 0.3–0.5 dex, where 1 dex corresponds to one order of magnitude (i.e., a difference of x dex is a variation of a factor equal to 10^x.). These measurements are essential for distinguishing ordinary chondrites from carbonaceous chondrites and other classes of meteorites.
- K/Th and K/U ratios: these must also be determined with an uncertainty margin of between 0.3 and 0.5 dex. Potassium (K) is a moderately volatile element, while thorium

(Th) and uranium (U) are highly refractory. Therefore, higher formation temperatures result in lower volatile content. Carbonaceous chondrites are characterized by high K/U and K/Th ratios, while the Moon has low values, 5 to 10 times lower than those of the Earth's continental crust. Mars, on the other hand, has values intermediate between those of the Moon and the Earth.

Based on the primary requirements,these were then divided into high-level requirements listed in Table 6.2 and low-level requirements described in Table 6.3.

The high-level requirements summarize the key performance parameters directly related to TASTE's scientific goals, such as the required energy range, resolution, field of view, and sensitivity. The low-level requirements specify the instrumental and environmental parameters necessary to meet these high-level objectives, including effective area, background levels, and radiation environment constraints.

Requirement	**Value**	**Justification**
X-ray energy band	2–15 keV	To cover Ca, Mn, Cr, Fe, Ni lines.
Gamma-ray band	50 keV–6 MeV	To cover K, Si, Al, Th, U, C lines.
X-ray energy resolution at Beginning of Life (BOL)	5 % @ 5.9 keV	To separate Mn, Fe Kα, Fe Kβ, Ni lines.
Gamma-ray energy resolution (BOL)	6 % @ 660 keV	To distinguish K, Si, Al, Th, U, C lines.
X-ray energy resolution at End of Life (EOL)	20 % @ 5.9 keV	To separate Ca, (Mn+Fe), Ni Kα lines.
Gamma-ray energy resolution (EOL)	12 % @ 660 keV	To distinguish K, Si, Al, Th, U, C lines.
Field of view	10° @ 10 keV	To cover Deimos and avoid cosmic sky.
X-ray sensitivity	0.01 ph/cm^2/s @ 3.7 keV (Ca Kα) and 5 σ; 0.04 ph/cm^2/s @ 6.4 keV (Fe Kα) and 7 σ	Constrain Fe/Ca, Fe/S, Mn/S photon ratios with a SNR=5.
Gamma-ray sensitivity	0.002 ph/cm^2/s @ 1.4 MeV (K) and 5 σ; 0.002 ph/cm^2/s @ 2.6 MeV (Th) and 5 σ	Constrain K/Th, K/U photon ratios with a SNR=5.

Table 6.2: List of TASTE spectrometer high-level scientific requirements.

Requirement	Value	Justification
X-ray total effective area	>30 cm^2 (± 10 %) @ 3–6 keV	Assuming flares > 14 MK × 1000 s.
Gamma-ray total effective area	>20 cm^2 (± 10 %) @ 600 keV; >10 cm^2 @ 2.6 MeV	
Cosmic X-ray background (CXB)	$<10^{-4}$ (± 5 %) counts/cm^2/s/keV @ 3–15 keV	FOV is assumed to be limited to Deimos, while the cosmic sky is excluded.
X-ray solar background (XSB)	<0.2 counts/cm^2/s/keV @ 3.7 keV (Ca Kα); <0.1 counts/cm^2/s/keV @ 6.4 keV (Fe Kα)	
X-ray particle induced background (PIB)	$<10^{-2}$ (± 5 %) counts/cm^2/s/keV @ 3–15 keV	
Gamma-ray particle induced background (PIB)	$<10^{-2}$ (± 5 %) counts/cm^2/s/keV @ 60–600 keV; <1 counts/cm^2/s/MeV @ 0.5–5 MeV	
Gamma-ray total background	<2.2 (± 5 %) counts/cm^2/s/MeV @ 1.4 MeV (K); <1.8 counts/cm^2/s/MeV @ 2.6 MeV (Th)	

Table 6.3: List of the TASTE spectrometer low-level scientific requirements.

6.4 HERMES-PF P/L modifications

To satisfy the scientific requirements, the X-ray and gamma-ray spectrometer need some modifications respect to the original HERMES-PF PL design (see 3.3). The goal of the Phase B study was precisely to identify and evaluate these modifications, ensuring that the instrument could meet the updated mission objectives.
The main modifications foreseen are:

- *use of longer scintillator crystals*;
- *development of new front-end ASICs* (LYRA-2/TASTE;
- *addition of a collimator.*

In particular, these modifications are necessary to satisfy the following points:

- to achieve a broad band from at least 2 keV to at least 3 MeV (with a design goal of 6 MeV); the size of the scintillator crystal directly influences the dynamic range. To achieve the required performance, the optimal crystal dimension has been determined to be 2.5 cm.
- to achieve an energy resolution consistent with the scientific requirements. The design of a new ASIC ensures both the required dynamic range coverage and the resolution necessary to detect spectral lines.

- to limit the field of view to just the photons coming from the Deimos surface, while avoiding detection of photons from the sky background. Considering the altitude of the orbit of TASTE-Orbiter (worst case ∼46 km), the field of view must be limited to a maximum of 10°.

For this studies, the activities focused on the LYRA-2/TASTE ASIC development. Work began with defining the breadboard design for testing the functionality of the new ASICs (described in Section 6.4.1) and the detector system (HERMES-like 3.3.1, with a longer scintillator), validating these modifications. In Section 6.4.2, the breadboard designed for testing is described.

6.4.1 The new ASIC

With reference to the LYRA ASICs inherited from the HERMES-PF mission, a new set of LYRA-2/TASTE ASICs has been developed for the TASTE Spectrometer. The new ASICs are designed to handle a wider dynamic range and higher spectral resolution required for scientific objectives. The LYRA-2/TASTE ASIC Front-End requirements are defined in Table6.4, where these requirements are compared with those of previous generations of ASICs.

FE Parameter	**LYRA**	**LYRA-2**
# of channels	1	1
Operating Temp. range	–30 °C to +30 °C	–30 °C to +40 °C
Dynamic range	32,700 e^-	45,000 e^- to 90,000 e^-
Shaping time	1.6 and 2.3 μs	∼2.3 and ∼3.2 μs (TBC)
Noise	20 e^- rms w/o detector	<27 e^- rms with <200 pA/50 fF
	<90 e^- rms with 500 pA/50 fF	<55 e^- rms with up to 500 pA (1000 pA goal)
Event rate	–	10..100 evt/s
Linearity	±1.5%	±1.5%
Power	270 μW/channel (FE only)	≤ 1mW/channel (FE only)

Table 6.4: Comparison of LYRA and LYRA-2/TASTE Front-End parameters. The LYRA-2 dynamic range of 45,000 e^- corresponds to 3 MeV (light output 15 e^-/keV), which is the minimum required to detect the 2.6 MeV Th line, while 90,000 e^- corresponds to 6 MeV, representing the design goal.

The main differences are:

- Dynamic range: the LYRA-2 dynamic range of 45,000 e^- corresponds to 3 MeV (light output 15 e^-/keV), which is the minimum required to detect the 2.6 MeV Th line, while 90,000 e^- corresponds to 6 MeV, representing the design goal.

- Noise: a key scientific goal is to observe Si/Al lines between 1–2 keV. To achieve a 5-sigma low X-ray detection threshold of 0.5 keV, the equivalent noise charge (ENC) must be 27 e^- rms (corresponding to ∼250 eV FWHM at 6 keV).

Regarding the Back-End – Analog circuit the modifications involved the discriminator circuit. The new version is designed to correct some issues encountered with the LYRA (such as threshold-dependent gain). The discriminator design utilizes a new threshold configuration, minimizing the temperature dependence of the threshold equivalent energy.
The final design for the digital part of the be includes 32 channels. The design is based on the LYRA architecture, which will incorporate the digital layout changes developed for NOVA ASIC (an evolution of the VEGA and LYRA ASICs, developed for the LEM-X project [147]), such as signal shielding.

6.4.2 Breadboard

The main role of the breadboard is testing and verifying the functionality of the new detector system (SDD + scintillator crystal) and the new ASICs. Therefore, the breadboard design is functionally divided into multiple sectors that involves the main circuit chains for support the operation of the ASICs and the detector:

- ASIC and Detector Hosting Area
- High-Voltage lines for SDDs polarization
- Low-Voltage lines for ASIC power supply
- Signal processing (analog and digital) chains
- Interfaces

A preliminary testing breadboard has been designed and produced in late 2024/early 2025 at INAF-OAS based on the NOVA ASIC and a small-scale SDD (2×2 cm matrix). The design is shown in Figure 6.4. Unlike the LYRA, the architecture of the NOVA ASIC is not divided into Front-End and Back-End blocks, but is unified.
The main breadboard blocks are highlighted in Figure 6.5.

1. **ASIC and Detector Hosting Area**. The board central area is dedicated to host the ASIC and the SDD, ensuring minimal signal path lengths and optimal layout for noise and interference minimization. The scintillator will be coupled with a support structure external to the breadboard, therefore the crystal size does not affect the BB.

2. **High Voltage (HV) Section.** A dedicated input connector allows interfacing with an external high-voltage generator. The circuit includes an internal voltage divider, which conditions the voltage and provides the appropriate bias for the SDD detector.

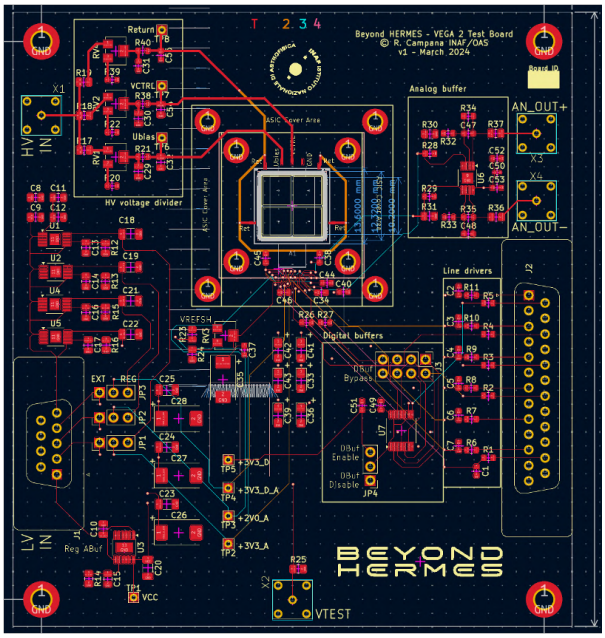

Figure 6.4: Preliminary testing breadboard design, with the main circuit chains for support the operation of the ASICs and the detector.

3. **Low Voltage (LV) Section**. A dedicated input connector allows interfacing with an external low-voltage generator. Two low-voltage inputs, provided by an external LV power source, are internally regulated to generate the required supply levels for: the ASIC, the analog signal processing chain, the digital processing chain.

4. **Signal Processing and Buffering.** The board integrates: an analog buffer with dual outputs, allowing for signal monitoring or acquisition through external equipment (e.g. oscilloscope); a digital buffer for managing the logic-level signals exchanged with external systems.

5. **Control and Data Acquisition Interface.** ASIC logic control signals are managed via an FPGA, which interfaces with the system through the IF Board connector (positioned on the right side of the board). The FPGA further connects to a laptop, which is used for real-time data acquisition and analysis.

6.4.3 Objective and development strategy

The next steps involve the development of two LYRA-2/TASTE ASICs prototypes. The first ASIC prototype was developed thanks to collaboration between the Politecnico di Milano and the University of Pavia. Sent to the foundry in July 2025, it is scheduled to be delivered in November 2025. Starting from the LYRA ASIC, the main target consists of improving

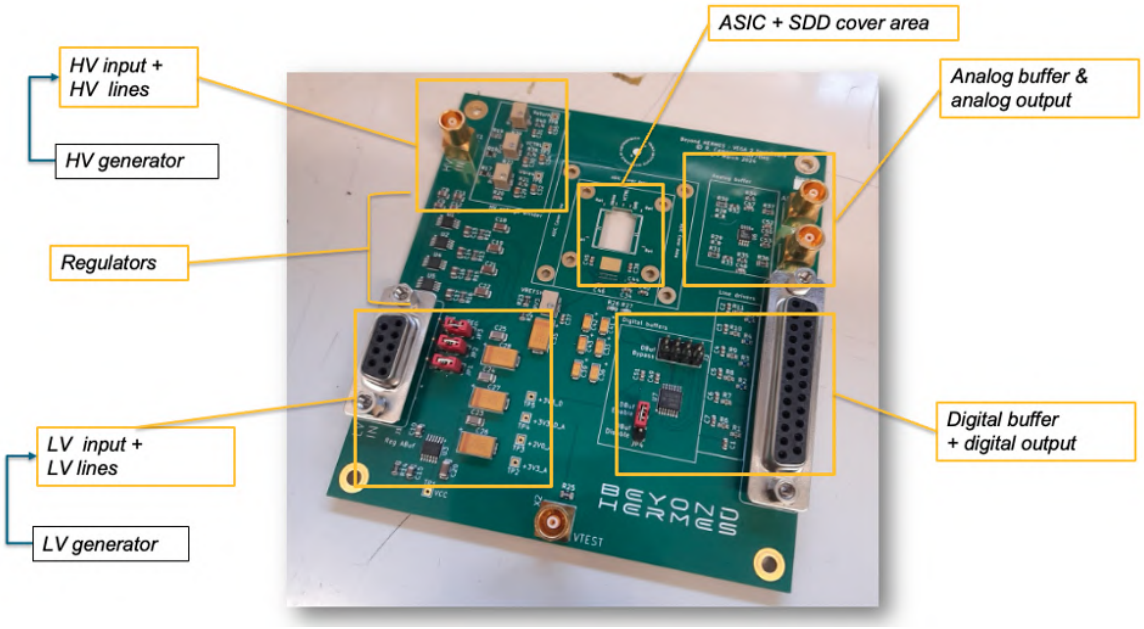

Figure 6.5: Preliminary real breadboard for testing. The main circuit chains for support the operation of the ASIC and the detector are highlighted with yellow boxes.

the dynamic range to 45,000 electrons (3 MeV in GAGG). Addressing the dynamic range of 90,000 electrons in a first iteration is considered feasible (desired, not mandatory). For this first prototype noise performance is not expected to be met (foreseen ENC $\geq$50 el.). The first prototype includes modifications on the analog front-end and analog back-end only, but with a very similar design for the digital back-end (UniPV), which will be just a pick-and-replace of the 32-channel LYRA-BE.

A new breadboard has been designed for testing the first prototype of the LYRA-2/TASTE ASIC, which is currently in production and is scheduled for delivery in October 2025. Its rendering is shown in Figure 6.6. The main modifications to the one described in Section 6.4.2 are in terms of the size of the detector and therefore the dimension of the ASIC and Detector Hosting Area (The SDD is HERMES-like, one SDD matrix of 10 cells each). The first new ASIC prototype will be connected to the breadboard and its functionality will be tested at the end of 2025.

A second ASIC prototype, to be produced in November 2025, will be based on design improvements introduced in the NOVA ASIC (developed for the LEM-X project [147], and tested with the first prototype board), including, but not limited to, current mode polarization and digital reprocessing for improved signal shielding. At this stage, the actual feasibility of the final performance in terms of noise for the dynamic range and power budget will be determined. Overall, the ASIC for TASTE will still be based on the LYRA architecture to accelerate the

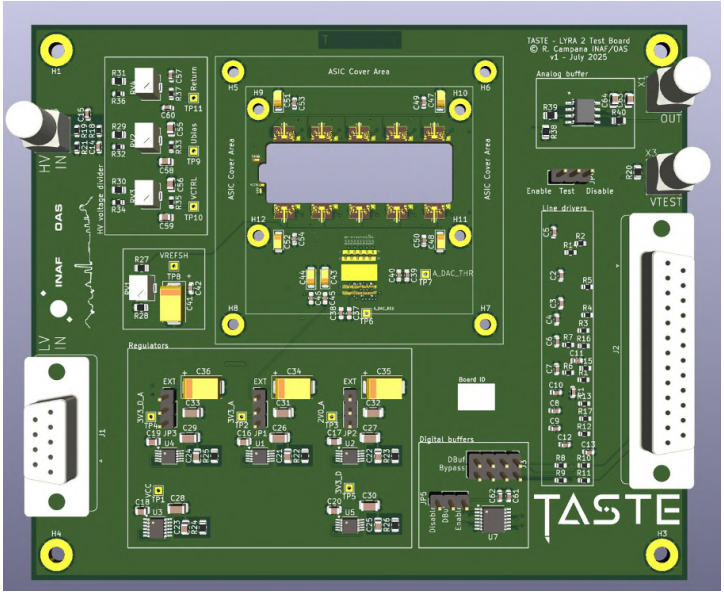

Figure 6.6: Second prototype ASIC breadboard. The ASIC and Detector Hosting Area is developed based on the HERMES-like SDD, one matrix of 10 cells each.

design and integration of a working prototype. This second TASTE ASIC prototype aims to optimize the functionality of the readout electronics.

6.4.4 Laboratory set up

Starting at the end of 2025, the breadboard and the first generation of ASICs will be ready for testing. For this reason, during Phase B, the laboratory setup necessary to carry out the tests was also studied and analyzed. A scheme of the experimental setup is shown in Figure6.7.
It consists of:

- an aluminum box that serves as a Faraday cage to provide shielding from electromagnetic interference and ambient light. The breadboard with ASIC and detector will be inserted into the box;
- a power supply for the test board, that consists of low-voltage and high-voltage lines. In particular, during the tests on the ASIC, the high-voltage line which produces the SDD drift field is not needed;
- an oscilloscope, used to monitor the output of all 32 channels on each ASIC and to check its signal output for each selected discriminator threshold and amplitude;
- a pulser to stimulate electrically the ASIC by simulating SDDs signals. The pulser is monitored through the oscilloscope and connected to the test board;

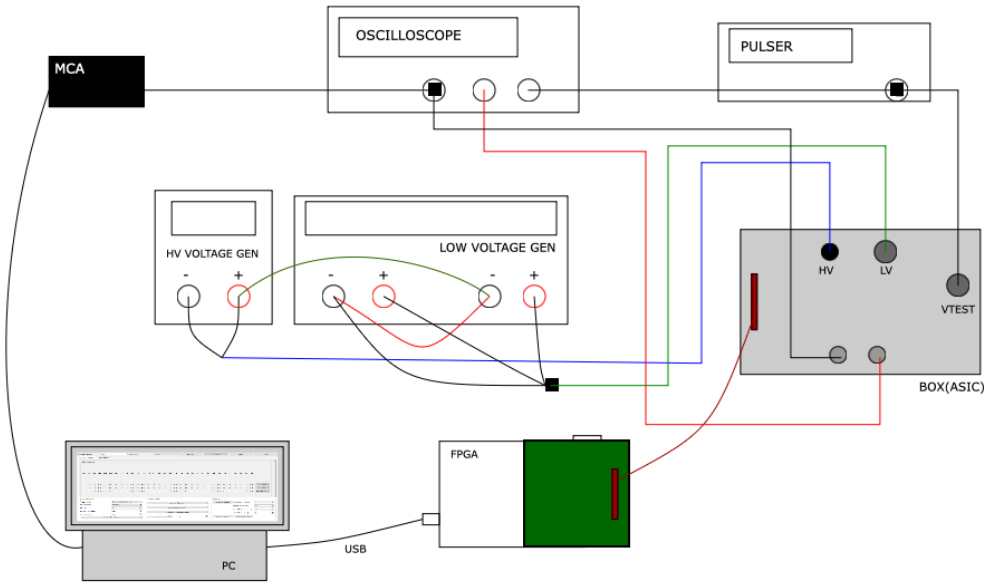

Figure 6.7: Schematic diagram of the laboratory setup for testing the breadboard. The board is powered by dedicated low- and high-voltage power supplies and is stimulated by an input test pulse generated by a pulse generator. An FPGA board, controlled by a PC, manages the ASIC configuration, while a connected multichannel analyzer (MCA) and oscilloscope acquire data for subsequent processing.

- a Digilent™ Arty-Z7 board hosting an FPGA (Field Programmable Gate Array), used as control logic to configure the ASIC and to manage the signal lines during operation. It is connected to the test with a custom flat cable and to the PC via an USB connection;
- a computer with a software interface to control the Arty-Z7 board and acquire the data from the MCA using a specific software;
- a Multi Channel Analyser connected to the board output to digitize the ASIC output.

6.4.5 Planned tests

Based on the changes that will be implemented in the new LYRA-2/TASTE ASIC, a series of tests have been defined with the aim of characterizing the new readout electronics features. The following is a list of the tests planned:

1. **Dynamic range verification** For each BE channel, for each increase in the input pulse, the amplitude of the output signal corresponding to the output of the shaper or stretcher (see Section 3.3.2) is measured. By plotting the input response against the output re-

sponse, it is possible to verify the linearity region of each channel, identify the saturation point, and therefore quantify the effective dynamic range.

2. **Analog Front-end characterization (SHAPER mode)**
   - Measurement the rise time and amplitude of each channel for the two shaping times.
   - Measurement the rise time and amplitude of a representative channel with at least three test pulse amplitudes across all shaping times.
   - Identification of channels with abnormally high noise.
3. **Full chain characterization (STRETCHER mode)**
   - Acquisition of full waveforms from all 32 channels using the Digilent Analog Discovery, for several test pulse amplitudes across all shaping times.
4. **Noise calculation** Noise is evaluated from the spreading of the impulse response: ideally, the pulser generates a delta-like input; deviations (broadening) are quantified through the standard deviation, which is adopted as the noise measure.
5. **Spectral measurements with radioactive sources** Once the detector is implemented on the board together with the ASIC:
   - Acquisition of spectra for each channel at different shaping times in SHAPER mode, using radioactive sources with a multichannel analyzer (MCA).
   - Acquisition of spectra from both channels simultaneously in STRETCHER mode, using a digitizer and the same sources.

In summary, the laboratory setup and test plan were defined in order to characterize the changes introduced in the LYRA-2/TASTE ASIC. Performing these tests will provide a complete characterization of the new chip and validate its compliance with design requirements.

Conclusions

Since the earliest observations, the observed sky at high-energies has proven to be a remarkable source of discoveries in astrophysics, especially for explosive and transient phenomena. The coalescence of compact objects, neutron stars (NSs) and black holes (BHs) is key to investigating both the physics of matter under extreme conditions and the ultimate structure of space-time. There are several discoveries that have advanced these studies in the past 30 years [45]. One of the most important is the localization of Gamma-Ray Bursts, sudden and unpredictable X-ray/soft Gamma-ray bursts with huge fluxes, up to 10^{-3} ergs/cm^2/s, which has allowed us to discover their X-ray and optical afterglows and led to the identification of their host galaxies. This definitively confirmed the extragalactic nature of GRBs and evaluated their energy balance, thus establishing them as some of the most powerful particle accelerators in the Universe.

At the same time, extraordinary advances have also involved the so-called "multi-messenger" astrophysics, beginning in August 2017 with the GW170817 event, in which new Gravitational Wave (GW) observations were added to traditional electromagnetic observations from the same astrophysical source. The nearly simultaneous detection of a GW signal by LIGO/Virgo from merging NSs — or from the merger of a NS with a BH — and a short Gamma-Ray Burst detected by Fermi and INTEGRAL, have shown that short GRBs can be associated with merging NSs, as hypothesized for about thirty years [43].

The operation of an efficient all-sky X-ray monitor with good localization capabilities will play a key role in bringing multi-messenger astrophysics to maturity [45]. The newborn multi-messenger astrophysics is acting also as a driving force for scientific innovation, aiming to propose more efficient, faster, and low-noise instruments. New mission projects are born, with the ambitious goal of combining instruments to cover a large electromagnetic band, to reveal transient phenomena and their physical origin. They also have the capacity to allow for multidisciplinary applications of new technologies and materials, through the technical and scientific effort involved in their development.

In this context, the *High Energy Rapid Modular Ensemble of Satellites* Pathfinder mission (HERMES-PF) was conceived, dedicated to the study and rapid localization of high-energy

transients with sub-microsecond time resolution and a broad energy band, ranging from a few keV to 2 MeV[66]. The HERMES-PF program offers a rapid and cost-effective complement to more complex and ambitious missions for relatively bright events; it is based on $10\times10\times10$ cm^3 satellite units following the CubeSat standard, involving costs 1–2 orders of magnitude lower than "traditional" space missions, and a much faster development timescale ($\sim$2 years, versus $\sim$10–15 years), with the downside of an usually higher risk of instrument failure (due to the use of commercial, off-the-shelf components) and a lower sensitivity of the individual instrument with respect to full-scale, "traditional" space instruments [53].

For the detection of X-ray and γ-rays, HERMES-PF involves the use of Silicon Drift Detectors coupled with scintillator crystals, which are treated as a single-detector element. This detector architecture is called "siswich": the silicon detector plays dual roles as a readout device for the scintillator signal and as an independent X-ray detector [82]. The readout electronics, a low-noise, low-power application-specific integrated circuit (ASIC), called LYRA, was designed and developed.

The HERMES-PF also operates together with the Australian-Italian SpIRIT (*Space Industry Responsive Intelligent Thermal*) mission, which hosts an HERMES-like detector. SpIRIT is a 6U CubeSat developed by a consortium led by the University of Melbourne (PI Michele Trenti) and with Italian participation, supported by the Australian and Italian Space Agencies [118]. SpIRIT was launched on December 1, 2023, while HERMES-PF was launched on March 15, 2025, forming a seven-satellite mini-constellation in Sun-synchronous orbit.

The experience provided by the development and in-flight use of HERMES-PF will also enable future studies on the adaptation of its payload to more challenging radiative environments. This may allow future CubeSat-based experiments to be designed for monitoring high-energy transients even, for example, in deep space or lunar environments, while also giving the opportunity to perform multiple distributed in-situ measurements of planetary surface composition and space weather conditions. In this contest, an X-ray and γ-ray spectrometer, derived from that of HERMES-PF, has been included in the TASTE (Terrain Analyzer and Sample Tester Explorer) mission study, with the goal of obtaining X-ray fluorescence spectroscopy and γ-ray spectroscopy of the surface of Deimos, one of the moons of Mars [125]. The goal is to obtain information on the chemical composition of the surface, and thus help to distinguish between the two possible origins of Deimos: a captured asteroid or a fragment of Mars.

The thesis project presents the study, calibration, and performance analysis of the HERMES-PF and SpIRIT flight units, with a particular focus on ground calibration activities, SpIRIT's in-orbit operations, and the contribution to the TASTE mission studies for adapting the HERMES-PF payload to the Martian environment.

Ground Activities: Calibration of HERMES-PF

The first part of the thesis reports on the calibration work for the HERMES-PF payloads (Chapter 4). In particular, it describes the functional tests carried out during the integration of the detector and readout electronics for Flight Models 4, FM5, and FM6 in Trento at the Bruno Kessler Foundation (FBK). These tests provided an initial complete characterization of the payload's functionality during the various integration steps. Once integration was complete, the calibration campaigns were described: from the design of the experimental setup for the calibration of the flight detectors and the related functional tests for data acquisition, to the development of the calibration software pipeline, written in Python [116]. During the acquisitions carried out in the clean room of the INAF/IAPS in Rome, each payload was placed in a climatic chamber, and the sources were placed on a specially designed mechanical support to allow almost uniform radiation coverage across all quadrants of the detector. Calibration acquisitions were performed with radioisotopes of ^{55}Fe, ^{109}Cd, and ^{137}Cs at different operating temperatures from -20 °C and +20 °C.

The calibration was divided into two phases: one with X-ray sources (X-mode) and one with γ-ray sources (S-mode). The main purpose of the X calibration was to determine the characteristic calibration parameters of each acquisition chain, such as gain and offset, while for the γ-ray calibration was the measurement of the effective light output of the scintillators for each channel, which is defined as the number of electrons produced at the SDD anode for unit of energy absorbed in the scintillator crystal, and is measured in units of e^-/keV.

Afterwards, calibrated spectra were obtained, and a statistical analysis of the calibration parameters at different thresholds and temperatures was performed for each payload, to have an overall characterization under the different conditions. The dispersion of calibration parameters in the channels of the four quadrants falls within the 30% expected values from the electronic design, as well as the variation of light output, which does not exceed the expected 20% [115]. Furthermore, the gain, offset, and light output were modeled according to the different actual operating temperatures using a quadratic equation. The low energy threshold of the instrument was also quantified, both in X and S modes, and the spectroscopic resolution of the instrument was estimated at energies of 5.9 keV and 662 keV. The technical performance of all payloads was summarized [106].

The results of all seven payloads (HERMES-PF + SpIRIT) were consolidated into a Calibration Database (CALDB) for future in-orbit configuration and monitoring. In conclusion, all HERMES-PF flight models have been successfully integrated and calibrated.

Subsequently, all payloads were integrated with the HERMES-PF service module at the Politecnico di Milano. At each stage of the complete integration of the satellite, appropriate

measurements were taken to check and verify the validity of the ground calibrations. Based on the results obtained, the CALDB parameters were updated for future configurations in orbit. HERMES-PF was launched on March 15, 2025, into a sun-synchronous orbit and is still undergoing commissioning due to some communication issues between the spacecraft and ground antennas.

In-Orbit Commissioning and Early Performance of SpIRIT

This part of the work reports the results obtained during the commissioning activities of the HERMES-PF payload on-board SpIRIT (Chapter 5). These activities provided important information on the functionality and performance of the PL in orbit [120]. The commissioning involved testing of each PL operational mode, to ensure system reliability in orbit. This required a sequential, iterative approach in which housekeeping data, such as voltages, currents, and temperatures, were monitored. Each step was carefully executed to confirm the payload's readiness for scientific data acquisition.

Following the completion of initial checks, the detectors were activated on January 16, 2024, achieving "first light" with the instrument operating in a basic mode similar to a Geiger counter. On February 17, 2024, the payload transitioned to Calibration mode, enabling the recording of full spectral and temporal photon data. By March 27, 2024, HERMES-PF had successfully entered nominal *Observation* mode, collecting scientific data in the form of light curves.

SpIRIT has performed, to date, 10 acquisitions in Calibration mode: the calibration acquisitions performed provided valuable insights into the operational performance of the HERMES payload. Despite the truncated data from the first two calibration sessions, which limited the analysis to around 8 seconds due to a telemetry budget restriction, the information gathered was crucial in refining the system's parameters. A key outcome of these calibrations is the identification of the optimal configuration to minimize the noise associated with the electronics. Data were analyzed using HERMES software (HERMESDAS) developed by the HERMES Science Operations Center (SOC) to generate calibrated and clean scientific data [117]. In addition, the use of calibration software developed during calibrations, such as the `mescal` software, proved to be key to analyzing and identifying problematic channels and optimizing threshold settings for future scientific observations. Although the failure of one of the quadrants limits the overall sensitivity of the instrument, the remaining three quadrants performed nominally and the detector response in these regions remains robust. This demonstrates the resilience of the system under partial failure conditions, but underscores the importance of redundancy in these missions.

The calibration data also highlighted the importance of operating temperature in detector

performance. The payload temperature during the first acquisition phase ranged from 2°C to 3°C, which, while within operational limits, necessitated adjustments to the threshold settings to compensate for noise introduced by sub-optimal thermal conditions.

After installing the solar panels and exposing the radiators, the calibrations reached the optimal operating temperature between -16 °C and -18 °C. The calibrations in orbit were compared with those on the ground, confirming the consistency of channel behavior and the stability of the readout electronics in different operating contexts. The comparison made it possible to identify noisy channels already known from the ground and to optimize the thresholds. Analysis of the total γ-ray spectrum revealed characteristic lines at 511 keV and 1275 keV, probably due to the activation of crystals by energetic particles. The 511 keV line was used as a reference to update the energy calibration, obtaining a correction factor of 8%. The Light Output values of the crystals were updated accordingly and entered into the calibration database (CALDB), ensuring the accuracy of future scientific acquisitions.

SpIRIT has performed, to date, 10 acquisitions in Observation mode: the analysis of the light curves obtained during the observations revealed a significant modulation in the low and medium energies, primarily attributable to the partial occultation of the cosmic X-ray background by the Earth. Additionally, a peak in the count rate was observed in the June 1 observation as a result of the satellite's entry into the polar electron belt. The remaining observations did not exhibit notable anomalies. The low-energy band generally shows an excess of counts compared to the simplified simulations introduced to interpret the data, suggesting the presence of additional X-ray sources in the background; the high-energy band, on the other hand, shows variability between observations, probably due to changes in the satellite environment or the contribution of cosmic radiation and solar activity. Despite the simplicity of the model used to analyze the acquired data and the lack of precise pointing information, the simulations provide useful insight into the behavior of the satellite and allow for a reasonable interpretation of the collected data.

The SpIRIT mission presented a significant opportunity to evaluate and validate the functionality and efficacy of the HERMES-PF payload in a harsh space environment and under different thermal conditions. Commissioning and in orbit operational activities led to the following conclusions:

- all University of Melbourne and HERMES-PF consortium hardware responded nominally to telecommands;

- in-orbit calibration and observation data confirmed that the HERMES-PF payload is functioning nominally;

- the next commissioning activities will prioritize extended payload operation, enabling continuous collection of scientific data. Starting in June 2025, SpIRIT entered the standard observation phase: the payload is activated for a few minutes each day, the data remains on board, and only data relating to transients identified through the Gamma-ray Coordinates Network (GCN) is downloaded.

TASTE: future developments and perspectives

Finally, the last part of the work presents the studies for the TASTE mission (Chapter 6). TASTE is a Cubesat mission consisting of a 12U orbiter and a 4U lander: the orbiter houses a multispectral camera and the new X- and γ-ray spectrometer, while the lander integrates a camera and an analytical laboratory for surface samples. The combination of orbital observations and in situ measurements will make it possible to characterize the global morphology, elemental composition, and local properties of the soil, and more generally, to investigate the internal structure of Deimos.

The scientific objectives of the spectrometer include determining the abundance ratios of key elements (Fe/Ca, Fe/S, Mn/S, K/Th, K/U) with sufficient accuracy to distinguish between different meteorite classes and formation scenarios.

The scientific requirements and necessary compromises have been defined in order to establish the modifications to be made to the basic design of the HERMES-PF payload to meet these requirements and withstand the Martian space environment. The main modifications to the HERMES-PF payload involve the use of longer scintillators, a new readout electronics called LYRA-2/TASTE ASICs, and a collimator to limit the field of view. In particular, phase B included the design of dedicated breadboards and laboratory configurations to test the new ASICs and the SDD + scintillator detection chain through dynamic range measurements, analog and digital characterization, noise calculation, and spectral acquisition with radioactive sources. The development plan includes two LYRA-2 prototypes. Laboratory work and characterization of the prototypes will ensure validation of the new design and compliance with scientific requirements, preparing the spectrometer for operational use on TASTE.

The HERMES-PF and SpIRIT missions demonstrated the technical and scientific feasibility of CubeSat-based X-ray/γ-ray monitoring, providing valuable experience for upcoming CubeSat missions, including TASTE.

List of Figures

List of Tables

Bibliography

[1] D. Bose and V.R. Chitnis. Very-high-energy gamma-ray astronomy. *European Physical Journal Special Topics*, 231:1–2, 2022.

[2] A. De Angelis and M. Mallamaci. Gamma-ray astrophysics. *The European Physical Journal Plus*, 133(8), August 2018.

[3] A. De Angelis and M. Mallamaci. Gamma-ray astrophysics. *The European Physical Journal Plus*, 133(324), 2018.

[4] Stefan Funk. Ground- and space-based gamma-ray astronomy. *Annual Review of Nuclear and Particle Science*, 65(1):245–277, oct 2015.

[5] David J. Thompson. Space detectors for gamma rays (100 mev–100 gev): From egret to fermi lat. *Comptes Rendus Physique*, 16(6):600–609, 2015.

[6] G. F. Bignami, G. Boella, J. J. Burger, P. Keirle, H. A. Mayer-Hasselwander, J. A. Paul, E. Pfeffermann, L. Scarsi, B. N. Swanenburg, B. G. Taylor, W. Voges, and R. D. Wills. The cos-b experiment for gamma-ray astronomy. *Space Science Instrumentation*, 1:245–268, August 1975.

[7] Giuseppe Di Sciascio. Ground-based gamma-ray astronomy: an introduction. *Journal of Physics: Conference Series*, 1263(1):012003, jun 2019.

[8] F. Frontera, C. Guidorzi, E. Montanari, F. Rossi, E. Costa, M. Feroci, F. Calura, M. Rapisarda, L. Amati, D. Carturan, M. R. Cinti, D. Dal Fiume, L. Nicastro, and M. Orlandini. The gamma-ray burst catalog obtained with the gamma-ray burst monitor aboard bepposax. *The Astrophysical Journal Supplement Series*, 180(1):192, dec 2008.

[9] ESA. Integral: Spacecraft, 2019.

[10] G. Vedrenne and J.L. Atteia. *Gamma-Ray Bursts: The brightest explosions in the Universe*. Springer Berlin Heidelberg, 2009.

[11] SCIENCE & EXPLORATION. Integral overview. `https://www.esa.int/Science_Exploration/Space_Science/Integral/Integral_overview?utm_source=chatgpt.com`, 2025.

[12] M.Tavati et al. Science with agile, 2004.

[13] Stefano Vercellone, Carlotta Pittori, and Marco Tavani. Scientific highlights of the agile gamma-ray mission. *Universe*, 10(4), 2024.

[14] Charles Meegan, Giselher Lichti, P. N. Bhat, Elisabetta Bissaldi, Michael S. Briggs, Valerie Connaughton, Roland Diehl, Gerald Fishman, Jochen Greiner, Andrew S. Hoover, Alexander J. van der Horst, Andreas von Kienlin, R. Marc Kippen, Chryssa Kouveliotou, Sheila McBreen, W. S. Paciesas, Robert Preece, Helmut Steinle, Mark S. Wallace, Robert B. Wilson, and Colleen Wilson-Hodge. The Fermi Gamma-ray Burst Monitor. *ApJ*, 702(1):791–804, 2009.

[15] D J Thompson. Gamma ray astrophysics: the EGRET results. *Reports on Progress in Physics*, 71(11):116901, 2008.

[16] H. Fleischhack and Amego X Team. AMEGO-X: MeV gamma-ray Astronomy in the Multi-messenger Era. In *37th International Cosmic Ray Conference. 12-23 July 2021. Berlin*, page 649, 2022.

[17] D. Berge, M. N. Mazziotta, M. Tavani, V. Tatischeff, and U. Oberlack. newastrogam – the new mev to gev gamma-ray observatory, 2025.

[18] Regina Caputo, Marco Ajello, Carolyn A. Kierans, Jeremy S. Perkins, Judith L. Racusin, Luca Baldini, Matthew G. Baring, Elisabetta Bissaldi, Eric Burns, Nicholas Cannady, Eric Charles, Rui M. Curado da Silva, Ke Fang, Henrike Fleischhack, Chris Fryer, Yasushi Fukazawa, J. Eric Grove, Dieter Hartmann, Eric J. Howell, Manoj Jadhav, Christopher M. Karwin, Daniel Kocevski, Naoko Kurahashi, Luca Latronico, Tiffany R. Lewis, Richard Leys, Amy Lien, Lea Marcotulli, Israel Martinez-Castellanos, Mario Nicola Mazziotta, Julie McEnery, Jessica Metcalfe, Kohta Murase, Michela Negro, Lucas Parker, Bernard Phlips, Chanda Prescod-Weinstein, Soebur Razzaque, Peter S. Shawhan, Yong Sheng, Tom A. Shutt, Daniel Shy, Clio Sleator, Amanda L. Steinhebel, Nicolas Striebig, Yusuke Suda, Donggeun Tak, Hiro Tajima, Janeth Valverde, Tonia M. Venters, Zorawar Wadiasingh, Richard S. Woolf, Eric A. Wulf, Haocheng Zhang, and Andreas Zoglauer. All-sky medium energy gamma-ray observatory explorer mission concept. *Journal of Astronomical Telescopes, Instruments, and Systems*, 8(04), October 2022.

[19] Rishank Diwan, Kees de Kuijper, Partha Sarathi Pal, Andreas Ritter, Pablo M. Saz Parkinson, Andy C. T. Kong, and Quentin A. Parker. Performance evaluation of a silicon-based 6u cubesat detector for soft γ-ray astronomy. *Space: Science & Technology*, 4, January 2024.

[20] C. Guidorzi, F. Frontera, G. Ghirlanda, G. Stratta, C. G. Mundell, E. Virgilli, P. Rosati, E. Caroli, L. Amati, E. Pian, S. Kobayashi, G. Ghisellini, C. Fryer, M. Della Valle, R. Margutti, M. Marongiu, R. Martone, R. Campana, F. Fuschino, C. Labanti, M. Orlandini, J. B. Stephen, S. Brandt, R. Curado da Silva, P. Laurent, R. Mochkovitch, E. Bozzo, R. Ciolfi, L. Burderi, and T. Di Salvo. A deep study of the high-energy transient sky. *Experimental Astronomy*, 51(3):1203–1223, June 2021.

[21] F. Frontera, E. Virgilli, C. Guidorzi, P. Rosati, R. Diehl, T. Siegert, C. Fryer, L. Amati, N. Auricchio, R. Campana, E. Caroli, F. Fuschino, C. Labanti, M. Orlandini, E. Pian, J. B. Stephen, S. Del Sordo, C. Budtz-Jorgensen, I. Kuvvetli, S. Brandt, R. M. Curado da Silva, P. Laurent, E. Bozzo, P. Mazzali, and M. Della Valle. Understanding the origin of the positron annihilation line and the physics of supernova explosions. *Experimental Astronomy*, 51(3):1175–1202, June 2021.

[22] John A. Tomsick, Steven E. Boggs, Andreas Zoglauer, Dieter Hartmann, Marco Ajello, Eric Burns, Chris Fryer, Chris Karwin, Carolyn Kierans, Alexander Lowell, Julien Malzac, Jarred Roberts, Pascal Saint-Hilaire, Albert Shih, Thomas Siegert, Clio Sleator, Tadayuki Takahashi, Fabrizio Tavecchio, Eric Wulf, Jacqueline Beechert, Hannah Gulick, Alyson Joens, Hadar Lazar, Eliza Neights, Juan Carlos Martinez Oliveros, Shigeki Matsumoto, Tom Melia, Hiroki Yoneda, Mark Amman, Dhruv Bal, Peter von Ballmoos, Hugh Bates, Markus Böttcher, Andrea Bulgarelli, Elisabetta Cavazzuti, Hsiang-Kuang Chang, Claire Chen, Che-Yen Chu, Alex Ciabattoni, Luigi Costamante, Lente Dreyer, Valentina Fioretti, Francesco Fenu, Savitri Gallego, Giancarlo Ghirlanda, Eric Grove, Chien-You Huang, Pierre Jean, Nikita Khatiya, Jürgen Knödlseder, Martin Krause, Mark Leising, Tiffany R. Lewis, Jan Peter Lommler, Lea Marcotulli, Israel Martinez-Castellanos, Saurabh Mittal, Michela Negro, Samer Al Nussirat, Kazuhiro Nakazawa, Uwe Oberlack, David Palmore, Gabriele Panebianco, Nicolo Parmiggiani, Tyler Parsotan, Sean N. Pike, Field Rogers, Hester Schutte, Yong Sheng, Alan P. Smale, Jacob Smith, Aaron Trigg, Tonia Venters, Yu Watanabe, and Haocheng Zhang. The compton spectrometer and imager, 2023.

[23] Andrew Levan. *Gamma-Ray Bursts*. 2514-3433. IOP Publishing, 2018.

[24] NASA. Bepposax, 2020.

[25] M. Feroci, L. A. Antonelli, M. Guainazzi, J. M. Muller, E. Costa, L. Piro, J. Heise, J. J. M. in 't Zand, F. Frontera, D. Dal Fiume, L. Nicastro, M. Orlandini, E. Palazzi, G. Zavattini, P. Giommi, A. N. Parmar, A. Owens, A. J. Castro-Tirado, M. C. Maccarone, and R. C. Butler. Bepposax follow-up search for the x-ray afterglow of grb970111. *Aap*, 1998.

[26] Rubén Salvaterra, M Della Valle, S Campana, G Chincarini, S Covino, P D'avanzo, A Fernández-Soto, C Guidorzi, F Mannucci, R Margutti, et al. Grb 090423 at a redshift of z∼8.1. *Nature*, 461(7268):1258–1260, 2009.

[27] Bandet al. Prospects for GRB Science with the Fermi Large Area Telescope. *ApJ*, 701(2):1673–1694, 2009.

[28] NASA. Interplanetary gamma-ray burst timing network (ipn), 2020.

[29] Chryssa Kouveliotou, Charles A. Meegan, Gerald J. Fishman, Narayana P. Bhat, Michael S. Briggs, Thomas M. Koshut, William S. Paciesas, and Geoffrey N. Pendleton. Identification of two classes of gamma-ray bursts. *Apj*, 413:L101, 1993.

[30] V. Zach Golkhou, Nathaniel R. Butler, and Owen M. Littlejohns. The energy dependence of grb minimum variability timescales. *The Astrophysical Journal*, 811(2):93, September 2015.

[31] D. Band, J. Matteson, L. Ford, B. Schaefer, D. Palmer, B. Teegarden, T. Cline, M. Briggs, W. Paciesas, G. Pendleton, G. Fishman, C. Kouveliotou, C. Meegan, R. Wilson, and P. Lestrade. Batse observations of gamma-ray burst spectra. i. spectral diversity. *ApJ*, 413:281, 1993.

[32] Yun-Wei Yu, He Gao, Fa-Yin Wang, and Bin-Bin Zhang. Gamma-Ray Bursts. *arXiv e-prints*, page arXiv:2204.04417, 2022.

[33] P. Meszaros and M. J. Rees. Gamma-ray bursts: Multiwaveband spectral predictions for blast wave models. *The Astrophysical Journal*, 418:L59, December 1993.

[34] R. Maccary, M. Maistrello, C. Guidorzi, M. Sartori, L. Amati, L. Bazzanini, M. Bulla, A. E. Camisasca, L. Ferro, F. Frontera, and A. Tsvetkova. Distribution of the number of peaks within a long gamma-ray burst: The full fermi/gbm catalogue, 2024.

[35] Paolo A. Mazzali. Supernovae and gamma-ray bursts. *Proceedings of the International Astronomical Union*, 7(S279):75–82, 2011.

[36] Wen-fai Fong, Anya E. Nugent, Yuxin Dong, Edo Berger, Kerry Paterson, Ryan Chornock, Andrew Levan, Peter Blanchard, Kate D. Alexander, Jennifer Andrews,

Bethany E. Cobb, Antonino Cucchiara, Derek Fox, Chris L. Fryer, Alexa C. Gordon, Charles D. Kilpatrick, Ragnhild Lunnan, Raffaella Margutti, Adam Miller, Peter Milne, Matt Nicholl, Daniel Perley, Jillian Rastinejad, Alicia Rouco Escorial, Genevieve Schroeder, Nathan Smith, Nial Tanvir, and Giacomo Terreran. Short grb host galaxies. i. photometric and spectroscopic catalogs, host associations, and galactocentric offsets. *The Astrophysical Journal*, 940(1):56, nov 2022.

[37] Olivier Godet and Robert Mochkovitch. Afterglows after Swift. *Comptes Rendus Physique*, 12:276–287, 2011.

[38] J. A. Nousek, C. Kouveliotou, D. Grupe, K. L. Page, J. Granot, E. Ramirez-Ruiz, S. K. Patel, D. N. Burrows, V. Mangano, S. Barthelmy, A. P. Beardmore, S. Campana, M. Capalbi, G. Chincarini, G. Cusumano, A. D. Falcone, N. Gehrels, P. Giommi, M. R. Goad, O. Godet, C. P. Hurkett, J. A. Kennea, A. Moretti, P. T. O'Brien, J. P. Osborne, P. Romano, G. Tagliaferri, and A. A. Wells. Evidence for a Canonical Gamma-Ray Burst Afterglow Light Curve in the Swift XRT Data. *The Astrophysical Journal*, 642(1):389–400, May 2006.

[39] G. Cavallo and M. J. Rees. A qualitative study of cosmic fireballs and γ-ray bursts. *Monthly Notices of the Royal Astronomical Society*, 183(3):359–365, 1978.

[40] ESA. Fermi: Gamma-ray space telescope, 2016.

[41] P Mészáros. Gamma-ray bursts. *Reports on Progress in Physics*, 69(8):2259–2321, July 2006.

[42] Re'em Sari, Tsvi Piran, and Ramesh Narayan. Spectra and light curves of gamma-ray burst afterglows. *The Astrophysical Journal*, 497(1):L17–L20, April 1998.

[43] B. P. Abbott, R. Abbott, T. D. Abbott, F. Acernese, K. Ackley, C. Adams, and et al. GW170817: Observation of Gravitational Waves from a Binary Neutron Star Inspiral. *Physical Review Letters*, 119(16):161101, 2017.

[44] Rosa Poggiani. Gw170817: A short review of the first multimessenger event in gravitational astronomy. *Galaxies*, 13(5), 2025.

[45] Fabrizio Fiore, Luciano Burderi, Michelle Lavagna, Roberto Bertacin, Yuri Evangelista, Riccardo Campana, Fabio Fuschino, Paolo Lunghi, Angel Monge, Barbara Negri, et al. The HERMES-technologic and scientific pathfinder. In Jan-Willem A. den Herder, Kazuhiro Nakazawa, and Shouleh Nikzad, editors, *Space Telescopes and Instrumentation 2020: Ultraviolet to Gamma Ray*, volume 11444, pages 214–228. SPIE, 2020.

[46] Enrico Bozzo, Lorenzo Amati, Wayne Baumgartner, Tzu-Ching Chang, Bertrand Cordier, Nicolas De Angelis, Akihiro Doi, Marco Feroci, Cynthia Froning, Jessica Gaskin, Adam Goldstein, Diego Götz, Jon E. Grove, Sylvain Guiriec, Margarita Hernanz, C. Michelle Hui, Peter Jenke, Daniel Kocevski, Merlin Kole, Chryssa Kouveliotou, Thomas Maccarone, Mark L. McConnell, Hideo Matsuhara, Paul O'Brien, Nicolas Produit, Paul S. Ray, Peter Roming, Andrea Santangelo, Michael Seiffert, Hui Sun, Alexander van der Horst, Peter Veres, Jianyan Wei, Nicholas White, Colleen Wilson-Hodge, Daisuke Yonetoku, Weimin Yuan, and Shuang-Nan Zhang. Future perspectives for gamma-ray burst detection from space, 2024.

[47] J.-L. Atteia, B. Cordier, and J. Wei. The svom mission. *International Journal of Modern Physics D*, 31(05), December 2021.

[48] Filippo Frontera. A short history of the first 50 years: from the grb prompt emission and afterglow discoveries to the multimessenger era, 2024.

[49] L. Amati, P.T. O'Brien, D. Götz, E. Bozzo, A. Santangelo, N. Tanvir, F. Frontera, S. Mereghetti, J. P. Osborne, A. Blain, S. Basa, M. Branchesi, L. Burderi, M. Caballero-García, A. J. Castro-Tirado, L. Christensen, R. Ciolfi, A. De Rosa, V. Doroshenko, A. Ferrara, G. Ghirlanda, L. Hanlon, P. Heddermann, I. Hutchinson, C. Labanti, E. Le Floch, H. Lerman, S. Paltani, V. Reglero, L. Rezzolla, P. Rosati, R. Salvaterra, G. Stratta, and C. Tenzer. The theseus space mission: science goals, requirements and mission concept. *Experimental Astronomy*, 52(3):183–218, November 2021.

[50] Peter Bloser, David Murphy, Fabrizio Fiore, and Jeremy Perkins. *CubeSats for Gamma-Ray Astronomy*, page 1–33. Springer Nature Singapore, November 2022.

[51] Erik Kulu. What is a CubeSat & other picosatellites. `https://www.nanosats.eu/cubesat`, 2025. Accessed: 2025-10-23.

[52] Konstantinos-Panagiotis Bouzoukis, Georgios Moraitis, Vassilis Kostopoulos, and Vaios Lappas. An overview of cubesat missions and applications. *Aerospace*, 12(6), 2025.

[53] Fabrizio Fiore and Martin Elvis. Space science & the space economy. *Space Policy*, page 101713, 2025.

[54] Abraham D. Falcone, Joseph M. Colosimo, Mitchell Wages, Michael Betts, William A. Bevidas, Brynn Bortree, Jacob C. Buffington, David N. Burrows, Zachary E. Catlin, Timothy Emeigh, Thomas Forstmeier, Derek B. Fox, Killian M. Gremling, Md. Arman Hossen, Kadri M. Nizam, David M. Palmer, Collin S. Reichard, Ana C. Scigliani,

Lukas R. Stone, Anthony J. Tavana, Ian Thornton, Daniel Washington, and Michael E. Zugger. BlackCAT: an upcoming soft x-ray coded aperture telescope on a 6U CubeSat. In Jan-Willem A. den Herder, Shouleh Nikzad, and Kazuhiro Nakazawa, editors, *Space Telescopes and Instrumentation 2024: Ultraviolet to Gamma Ray*, volume 13093 of *Society of Photo-Optical Instrumentation Engineers (SPIE) Conference Series*, page 1309317, August 2024.

[55] I. Martinez-Castellanos, A. Myers, D. Violette, L. Angellini, J. Asercion, M. S. Briggs, R. Caputo, J. Cox, G. de Nolfo, K. Gasaway, S. Griffin, D. Hartmann, B. A. Hristov, A. Joens, P. Nuessle, J. S. Perkins, J. Racusin, S. Semper, P. Shawhan, J. Smith, L. Tian, and BurstCube Team. GRB 240629A: First GRB Detected by BurstCube. *GRB Coordinates Network*, 37340:1, August 2024.

[56] A. Laviron, I. Cojocari, N. de Séréville, G. Fernandez, C. Hamadache, L. Hanlon, P. Laurent, J. Lommler, S. McBreen, A. Morselli, D. Murphy, H. Neves, U. Oberlack, R. Silva, V. Tatischeff, A. Ulyanov, V. Vitale, and P. von Ballmoos. COMCUBE: A constellation of CubeSats to measure the GRB prompt emission polarization. In A. Siebert, K. Baillié, E. Lagadec, N. Lagarde, J. Malzac, J. B. Marquette, M. N'Diaye, J. Richard, and O. Venot, editors, *SF2A-2021: Proceedings of the Annual meeting of the French Society of Astronomy and Astrophysics*, pages 105–108, December 2021.

[57] Nathan Franel, Vincent Tatischeff, Clarisse Hamadache, Alexey Uliyanov, David Murphy, Lorraine Hanlon, and Caimin Mc Kenna. COMCUBE : GRB prompt emission polarimetry with a swarm of CubeSats. In *EAS2024, European Astronomical Society Annual Meeting*, page 1574, July 2024.

[58] Ion Cojocari, Matthias Meier, Philippe Laurent, Adrien Laviron, Marco Arrigucci, Marco Carminati, Griseld Deda, Carlo Fiorini, Katrin Geigenberger, Cynthia Glas, Jochen Greiner, Peter Hindenberger, Pietro King, Peter Lechner, Martin Losekamm, Susanne Mertens, David Meßmann, Sebastian Rückerl, Lorenzo Toscano, Ulrich Walter, and Michael Willers. Calorimeter calibration of the ComPol CubeSat gamma-ray polarimeter. *Nuclear Instruments and Methods in Physics Research A*, 1046:167662, January 2023.

[59] Sergio Fabiani, Ettore Del Monte, Ilaria Baffo, Sergio Bonomo, Daniele Brienza, Riccardo Campana, Mauro Centrone, Gessica Contini, Enrico Costa, Giovanni Cucinella, Andrea Curatolo, Nicolas De Angelis, Giovanni De Cesare, Andrea Del Re, Sergio Di Cosimo, Simone Di Filippo, Alessandro Di Marco, Giuseppe Di Persio, Immacolata Donnarumma, Pierluigi Fanelli, Paolo Leonetti, Alfredo Locarini, Pasqualino Loffredo, Giovanni Lombardi, Gabriele Minervini, Dario Modenini, Fabio Muleri, Silvia Natalucci, Andrea Negri,

Massimo Perelli, Monia Rossi, Alda Rubini, Emanuele Scalise, Paolo Soffitta, Andrea Terracciano, Paolo Tortora, Emauele Zaccagnino, and Alessandro Zambardi. The cubesat solar polarimeter (cusp) mission overview, 2024.

[60] M. Doyle, A. Gloster, C. O'Toole, J. Mangan, R. Dunwoody, and J. Thompson. Assembly integration and verification activities for a 2u cubesat eirsat-1. In *Proceedings of the 3rd Symposium on Space Educational Activities*, page 128–132. University of Leicester, 2020.

[61] Alexey Uliyanov, Cuán de Barra, David Murphy, Derek O'Callaghan, Padraig McDermott, Joseph Thompson, Lorraine Hanlon, and Sheila McBreen. GIFTS: A 6U CubeSat for the detection and localisation of gamma-ray bursts. *Experimental Astronomy*, 59(3):40, June 2025.

[62] Huaizhong Gao, Dongxin Yang, Jiaxing Wen, Xutao Zheng, Ming Zeng, Jirong Cang, Weihe Zeng, Xiaofan Pan, Qimin Zhou, Yihui Liu, Hua Feng, Binbin Zhang, Zhi Zeng, and Yang Tian. On-ground calibrations of the grid-02 gamma-ray detector. *Experimental Astronomy*, 53(1):103–116, December 2021.

[63] Jakub Rípa, András Pál, Masanori Ohno, Norbert Werner, László Mészáros, Balázs Csák, Marianna Dafcikova, Vladimír Dániel, Juraj Dudáš, Marcel Frajt, Peter Hanák, Ján Hudec, Milan Junas, Jakub Kapus, Miroslav Kasal, Martin Koleda, Robert Laszlo, Pavol Lipovsky, Filip Münz, Maksim Rezenov, Miroslav Šmelko, Petr Svoboda, Hiromitsu Takahashi, Martin Topinka, Tomáš Urbanec, Jean-Paul Breuer, Teruaki Enoto, Zsolt Frei, Yasushi Fukazawa, Gábor Galgóczi, Filip Hroch, Yuto Ichinohe, László Kiss, Hiroto Matake, Tsunefumi Mizuno, Kazuhiro Nakazawa, Hirokazu Odaka, Helen Poon, Nagomi Uchida, and Yuusuke Uchida. Early results from grbalpha and vzlusat-2. In Jan-Willem A. den Herder, Kazuhiro Nakazawa, and Shouleh Nikzad, editors, *Space Telescopes and Instrumentation 2022: Ultraviolet to Gamma Ray*, page 57. SPIE, August 2022.

[64] Filip Munz, Jakub Rípa, Andras Pal, Marianna Dafcikova, Norbert Werner, Masanori Ohno, Laszlo Meszaros, Vladimír Dániel, Peter Hanak, Jan Hudec, Marcel Frajt, Jakub Kapus, Petr Svoboda, Juraj Dudáš, Miroslav Kasal, Tomáš Vítek, Martin Kolář, Lea Szakszonová, Pavol Lipovský, Michaela Ďuríšková, Ivo Vertat, Martin Sabol, Milan Junas, Roman Maroš, Pavel Kosík, Zsolt Frey, Hiromitsu Takahashi, Yasushi Fukazawa, Gabor Galgoczi, Balázs Csák, Robert Laszlo, Tsunefumi Mizuno, Nikola Husarikova, and Kazuhiro Nakazawa. Grbalpha and vzlusat-2: Grb observations with cubesats after 3 years of operations. In Jan-Willem A. den Herder, Kazuhiro Nakazawa, and Shouleh Nikzad, editors, *Space Telescopes and Instrumentation 2024: Ultraviolet to Gamma Ray*, page 250. SPIE, August 2024.

[65] Hsiang-Kuang Chang, Chi-Hsun Lin, Che-Chih Tsao, Che-Yen Chu, Shun-Chia Yang, Chien-You Huang, Chao-Hsi Wang, Tze-Hsiang Su, Yun-Hsin Chung, Yung-Wei Chang, Zi-Jun Gong, Jr-Yue Hsiang, Keng-Li Lai, Tsu-Hsuan Lin, Chia-Yu Lu, and Chien-Ying Yang. The Gamma-ray Transients Monitor (GTM) on board Formosat-8B and its GRB detection efficiency. *Advances in Space Research*, 69(2):1249–1255, January 2022.

[66] Fabrizio Fiore, Alejandro Guzman, Riccardo Campana, and Yuri Evangelista. *HERMES-Pathfinder*. Springer Nature, Singapore, 2022.

[67] H. Phan, H. Halloin, and P. Laurent. IGOSat - A 3U Cubesat for measuring the radiative/electrons content in low Earth orbit and ionosphere. *Nuclear Instruments and Methods in Physics Research A*, 912:389–394, December 2018.

[68] William Setterberg, Lindsay Glesener, Demoz Gebre Egziabher, John Glen Sample, Amir Caspi, David Miles Smith, Allan Faulkner, Arch Robison, Lestat Clemmer, Kate Hildebrandt, Evan Skinner, Annsley Greathouse, Ty Kozic, Mansour Savadogo, Mel Nightingale, and Trevor Knuth. The Impulsive Phase Rapid Energetic Solar Spectrometer (IMPRESS) CubeSat Science and Status. In *AGU Fall Meeting Abstracts*, volume 2022 of *AGU Fall Meeting Abstracts*, pages SH23A–09, December 2022.

[69] J Braga, O S C Durão, M Castro, F D'Amico, P E Stecchini, S Amirábile, F Gonzalez Blanco, C Strauss, W Silva, V R Schad, and L A Reitano. Lecx: a cubesat experiment to detect and localize cosmic explosions in hard x-rays. *Monthly Notices of the Royal Astronomical Society*, 493(4):4852–4860, February 2020.

[70] A. Di Giovanni, F. Arneodo, A. Al Qasim, H. Alblooshi, F. AlKhouri, L. Alkindi, A. Al-Mannei, M. L. Benabderrahmane, G. Bruno, V. Conicella, O. Fawwaz, G. Franchi, S. Kalos, P. Oikonomou, L. Perillo, C. Pittori, M. S. Roberts, and R. Torres. Raad: Light-1 cubesat's payload for the detection of terrestrial gamma-ray flashes, 2023.

[71] Peter Bloser, W. Thomas Vestrand, Markus Hehlen, Kim Katko, Lucas Parker, Darrel Beckman, James Sedillo, Justin McGlown, Lee Holguin, John Michel, Rory Scobie, Tony Nelson, Daniel Poulson, Christopher Fryer, Aimee Hungerford, and Matthew Mumpower. The Mini Astrophysical MeV Background Observatory (MAMBO) CubeSat Mission. In *AAS/High Energy Astrophysics Division*, volume 19 of *AAS/High Energy Astrophysics Division*, page 108.37, April 2022.

[72] Giulio Lucchetta, Markus Ackermann, David Berge, and Rolf Bühler. Introducing the mevcube concept: a cubesat for mev observations. *Journal of Cosmology and Astroparticle Physics*, 2022(08):013, August 2022.

[73] Akash Kumar Saha. Searching for dark matter with mevcube, 2025.

[74] James P. Mason, Thomas N. Woods, Amir Caspi, Phillip C. Chamberlin, Christopher Moore, Andrew Jones, Rick Kohnert, Xinlin Li, Scott Palo, and Stanley C. Solomon. Miniature x-ray solar spectrometer: A science-oriented, university 3u cubesat. *Journal of Spacecraft and Rockets*, 53(2):328–339, 2016.

[75] James Paul Mason, Thomas N. Woods, Phillip C. Chamberlin, Andrew Jones, Rick Kohnert, Bennet Schwab, Robert Sewell, Amir Caspi, Christopher S. Moore, Scott Palo, Stanley C. Solomon, and Harry Warren. Minxss-2 cubesat mission overview: Improvements from the successful minxss-1 mission. *Advances in Space Research*, 66(1):3–9, July 2020.

[76] Josiah DeLange, Seth Frick, Joel Runnels, Demoz Gebre-Egziabher, and Kale Hedstrom. Sensor for small satellite relative pnt in deep-space. In *2016 IEEE/ION Position, Location and Navigation Symposium (PLANS)*, pages 955–963, 2016.

[77] Jean-Yves Heloret, Olivier Godet, Laurent Bouchet, Jean-Luc Atteia, and Guillaume Orttner. 3u transat: a cubesat constellation to boost the multi-messenger astronomy, 2024.

[78] Jakub Řípa, Marianna Dafčíková, Pavel Kosík, Filip Münz, Masanori Ohno, Gábor Galgóczi, Norbert Werner, András Pál, László Mészáros, Balázs Csák, Yasushi Fukazawa, Hiromitsu Takahashi, Tsunefumi Mizuno, Kazuhiro Nakazawa, Hirokazu Odaka, Yuto Ichinohe, Jakub Kapuš, Jan Hudec, Marcel Frajt, Maksim Rezenov, Vladimír Dániel, Petr Svoboda, Juraj Dudáš, Martin Sabol, Róbert László, Martin Koleda, Michaela Ďuríšková, Lea Szakszonová, Martin Kolář, Nikola Husáriková, Jean-Paul Breuer, Filip Hroch, Tomáš Vítek, Ivo Veřtát, Tomáš Urbanec, Aleš Povalač, Miroslav Kasal, Peter Hanák, Miroslav Šmelko, Martin Topinka, Hsiang-Kuang Chang, Tsung-Che Liu, Chih-Hsun Lin, Chin-Ping Hu, and Che-Chih Tsao. Characterization of more than three years of in-orbit radiation damage of sipms on grbalpha and vzlusat-2 cubesats. *Nuclear Instruments and Methods in Physics Research Section A: Accelerators, Spectrometers, Detectors and Associated Equipment*, 1076:170513, 2025.

[79] J. Ripa, M. Ohno, H. Takahashi, A. Pal, L. Meszaros, B. Csak, N. Werner, M. Topinka, F. Munz, F. Hroch, T. Urbanec, M. Kasal, A. Povalac, J. Hudec, J. Kapus, M. Frajt, R. Laszlo, M. Koleda, M. Smelko, P. Hanak, P. Lipovsky, G. Galgoczi, Y. Uchida, H. Poon, H. Matake, N. Uchida, T. Bozoki, G. Dalya, T. Enoto, Zs. Frei, G. Friss, Y. Fukazawa, K. Hirose, S. Hisadomi, Y. Ichinohe, K. Kapas, L. L. Kiss, T. Mizuno,

K. Nakazawa, H. Odaka, J. Takatsy, and K. Torigoe. GRB 211019A: Detection by GRBAlpha. GCN Circular, 2021.

[80] Rachel Dunwoody, Maeve Doyle, David Murphy, Gabriel Finneran, Derek O'Callaghan, Jack Reilly, Joseph Thompson, Sai Krishna Reddy Akarapu, Cuán. de Barra, Laura Cotter, Aaron Empey, Joseph Fisher, Joseph Mangan, Caimin McKenna, Bas Stijnen, Lorraine Hanlon, David McKeown, William O'Connor, Alexey Uliyanov, Ronan Wall, Brian Shortt, and Sheila McBreen. Development, description, and validation of the operations manual for EIRSAT-1, a 2U CubeSat with a gamma-ray burst detector. *Journal of Astronomical Telescopes, Instruments, and Systems*, 9:037001, July 2023.

[81] D. Murphy, C. McKenna, C. de Barra, A. Ulyanov, P. McDermott, M. Doyle, R. Dunwoody, J. Mangan, G. Finneran, L. Cotter, A. Empey, J. Fisher, F. Gibson Kiely, J. Thompson, D. McKeown, A. Martin-Carrillo, L. Hanlon, S. McBreen, and Eirsat-1 Team. GRB240821B: First GRB Detected by EIRSAT-1 GMOD. *GRB Coordinates Network*, 37231:1, August 2024.

[82] Fabio Fuschino, Riccardo Campana, Claudio Labanti, Yuri Evangelista, Fabrizio Fiore, Massimo Gandola, Marco Grassi, Filippo Mele, Filippo Ambrosino, Francesco Ceraudo, et al. An innovative architecture for wide band transient monitor on board hermes nanosatellite constellations. In *Space Telescopes and Instrumentation 2020: Ultraviolet to Gamma Ray*, volume 11444. International Society for Optics and Photonics, 2020.

[83] Vahid Z. Golkhou and Nathaniel R. Butler. Uncovering the intrinsic variability of gamma-ray bursts. *The Astrophysical Journal*, 787(1):90, may 2014.

[84] A. E. Camisasca, C. Guidorzi, L. Amati, F. Frontera, X. Y. Song, S. Xiao, S. L. Xiong, S. N. Zhang, R. Margutti, S. Kobayashi, C. G. Mundell, M. Y. Ge, A. Gomboc, S. M. Jia, N. Jordana-Mitjans, C. K. Li, X. B. Li, R. Maccary, M. Shrestha, W. C. Xue, and S. Zhang. Grb minimum variability timescale with insight-hxmt andswift: Implications for progenitor models, dissipation physics, and grb classifications. *Astronomy & Astrophysics*, 671:A112, March 2023.

[85] P. Mészáros. The Fireball Model of Gamma-Ray Bursts. *Progress of Theoretical Physics Supplement*, 143:33–49, January 2001.

[86] Shiho Kobayashi, Tsvi Piran, and Re'em Sari. Can internal shocks produce the variability in gamma-ray bursts? *Astrophysical Journal*, 490:92–102, November 1997.

[87] Brian J. Morsony, Davide Lazzati, and Mitchell C. Begelman. The origin and propagation of variability in the outflows of long-duration gamma-ray bursts. *The Astrophysical Journal*, 723(1):267–276, October 2010.

[88] Eyal Nakar and Tsvi Piran. Gamma-ray bursts light-curves – another clue on the inner engine. *Astrophysical Journal Letters*, 572:L139–L142, 2002.

[89] Bing Zhang and Huirong Yan. The internal-collision-induced magnetic reconnection and turbulence (icmart) model of gamma-ray bursts. *The Astrophysical Journal*, 726(2):90, dec 2010.

[90] G. A. MacLachlan, A. S. Shenoy, E. Sonbas, W. C. Parke, M. Wats, and N. Gehrels. Minimum variability timescales of long and short grbs. *Monthly Notices of the Royal Astronomical Society*, 432(2):857–865, 2013.

[91] E. E. Fenimore and E. Ramirez-Ruiz. Redshifts for 220 batse gamma-ray bursts determined by variability and the cosmological consequences, 2000.

[92] C. Guidorzi, R. Maccary, A. Tsvetkova, S. Kobayashi, L. Amati, L. Bazzanini, M. Bulla, A. E. Camisasca, L. Ferro, D. Frederiks, F. Frontera, A. Lysenko, M. Maistrello, A. Ridnaia, D. Svinkin, and M. Ulanov. New results on the gamma-ray burst variability–luminosity relation. *Astronomy & Astrophysics*, 690:A261, October 2024.

[93] R. Maccary, C. Guidorzi, A. E. Camisasca, M. Maistrello, S. Kobayashi, L. Amati, L. Bazzanini, M. Bulla, L. Ferro, F. Frontera, and A. Tsvetkova. Gamma-ray burst minimum variability timescales with fermi/gbm. *Astronomy & Astrophysics*, 702:A95, October 2025.

[94] Andrea Sanna, Luciano Burderi, Tiziana Di Salvo, Fabrizio Fiore, Alessandro Riggio, Angelo Gambino, Michèle Lavagna, Roberto Bertacin, Yuri Evangelista, Riccardo Campana, et al. Timing techniques applied to distributed modular high-energy astronomy: the hermes project. In *Space Telescopes and Instrumentation 2020: Ultraviolet to Gamma Ray*, volume 11444, pages 844–862. SPIE, 2020.

[95] G. Ghirlanda, L. Nava, O. Salafia, F. Fiore, R. Campana, R. Salvaterra, A. Sanna, W. Leone, Y. Evangelista, G. Dilillo, S. Puccetti, A. Santangelo, M. Trenti, A. Guzmán, P. Hedderman, G. Amelino-Camelia, M. Barbera, G. Baroni, M. Bechini, P. Bellutti, G. Bertuccio, G. Borghi, A. Brandonisio, L. Burderi, C. Cabras, T. Chen, M. Citossi, A. Colagrossi, R. Crupi, F. De Cecio, I. Dedolli, M. Del Santo, E. Demenev, T. Di Salvo, F. Ficorella, D. Gačnik, M. Gandola, N. Gao, A. Gomboc, M. Grassi, R. Iaria, G. La Rosa,

U. Lo Cicero, P. Malcovati, A. Manca, E. J. Marchesini, A. Maselli, F. Mele, P. Nogara, G. Pepponi, M. Perri, A. Picciotto, S. Pirrotta, J. Prinetto, M. Quirino, A. Riggio, J. Řípa, F. Russo, D. Selčan, S. Silvestrini, G. Sottile, M. L. Thomas, A. Tiberia, S. Trevisan, I. Troisi, A. Tsvetkova, A. Vacchi, N. Werner, G. Zanotti, and N. Zorzi. Hermes: Gamma-ray burst and gravitational wave counterpart hunter. *Astronomy & Astrophysics*, 689:A175, September 2024.

[96] Giancarlo Ghirlanda, Gabriele Ghisellini, Davide Lazzati, and Claudio Firmani. Gamma-ray bursts: New rulers to measure the universe. *The Astrophysical Journal*, 613(1):L13–L16, August 2004.

[97] S. Poolakkil, R. Preece, C. Fletcher, A. Goldstein, P. N. Bhat, E. Bissaldi, M. S. Briggs, E. Burns, W. H. Cleveland, M. M. Giles, C. M. Hui, D. Kocevski, S. Lesage, B. Mailyan, C. Malacaria, W. S. Paciesas, O. J. Roberts, P. Veres, A. von Kienlin, and C. A. Wilson-Hodge. The fermi-gbm gamma-ray burst spectral catalog: 10 yr of data. *The Astrophysical Journal*, 913(1):60, may 2021.

[98] Yuri Evangelista, Fabrizio Fiore, Riccardo Campana, Giulia Baroni, Francesco Ceraudo, Giovanni Della Casa, Evgeny Demenev, Giuseppe Dilillo, Mauro Fiorini, Giancarlo Ghirlanda, Marco Grassi, Alejandro Guzmán Cabrera, Paul Hedderman, Ezequiel J. Marchesini, Gianluca Morgante, Filippo Mele, Lara Nava, Paolo Nogara, Alessio Nuti, Samuel Pliego-Caballero, Irina Rashevskaya, Francesco Russo, Giuseppe Sottile, Michèle Lavagna, Andrea Colagrossi, Stefano Silvestrini, Matteo Quirino, Michele Bechini, Andrea Brandonisio, Francesco De Cecio, Alice Dottori, Ivan Troisi, Roberto Bertacin, Pierluigi Bellutti, Giuseppe Bertuccio, Luciano Burderi, Tianxiang Chen, Marco Citossi, Tiziana Di Salvo, Marco Feroci, Francesco Ficorella, Na Gao, Chiara Grappasonni, Claudio Labanti, Giovanni La Rosa, Wladimiro Leone, Piero Malcovati, Barbara Negri, Giancarlo Pepponi, Matteo Perri, Raffaele Piazzolla, Antonino Picciotto, Simone Pirrotta, Simonetta Puccetti, Alexander Rashevsky, Alessandro Riggio, Marianna Rinaldi, Andrea Sanna, Andrea Santangelo, Christoph Tenzer, Alessandra Tiberia, Michele Trenti, Sara Trevisan, Andrea Vacchi, Shaolin Xiong, Gianluigi Zampa, Nicola Zampa, Shuangnan Zhang, Nicola Zorzi, Jakub Ripa, and Norbert Werner. The hermes (high energy rapid modular ensemble of satellites) pathfinder mission. In Jan-Willem A. den Herder, Kazuhiro Nakazawa, and Shouleh Nikzad, editors, *Space Telescopes and Instrumentation 2024: Ultraviolet to Gamma Ray*, page 74. SPIE, August 2024.

[99] R. Campana. Design and development of the HERMES Pathfinder payloads. In Jan-Willem A. den Herder, Shouleh Nikzad, and Kazuhiro Nakazawa, editors, *Space Tele-*

scopes and Instrumentation 2024: Ultraviolet to Gamma Ray, volume this volume of *Society of Photo-Optical Instrumentation Engineers (SPIE) Conference Series*, August 2024.

[100] Yuri Evangelista, Fabrizio Fiore, Fabio Fuschino, Riccardo Campana, Francesco Ceraudo, Evgeny Demenev, Alejandro Guzman, Claudio Labanti, Giovanni La Rosa, Mauro Fiorini, et al. The scientific payload on-board the hermes-tp and hermes-sp cubesat missions. In *Space Telescopes and Instrumentation 2020: Ultraviolet to Gamma Ray*, volume 11444. International Society for Optics and Photonics, 2020.

[101] Pawel Sibczynski, Joanna Iwanowska-Hanke, Marek Moszyński, Lukasz Swiderski, Marek Szawłowski, Martyna Grodzicka, Tomasz Szcześniak, Kei Kamada, and Akira Yoshikawa. Characterization of GAGG:Ce scintillators with various Al-to-Ga ratio. *Nuclear Instruments and Methods in Physics Research A*, 772:112–117, February 2015.

[102] Riccardo Campana, Chiara Evola, Claudio Labanti, Lisa Ferro, Miguel Moita, Enrico Virgilli, Ezequiel J. Marchesini, Filippo Frontera, and Piero Rosati. Measurement of the non-linearity in the γ-ray response of the GAGG:Ce inorganic scintillator. *Nuclear Instruments and Methods in Physics Research A*, 1056:168587, November 2023.

[103] M. Gandola, F. Mele, M. Grassi, P. Malcovati, and G. Bertuccio. Multi-chip front-end electronics LYRA for X and γ Ray detector for HERMES mission. *Journal of Instrumentation*, 16(12):T12013, December 2021.

[104] Mahdi Ahangarianabhari, Daniele Macera, Giuseppe Bertuccio, Piero Malcovati, and Marco Grassi. Vega: A low-power front-end asic for large area multi-linear x-ray silicon drift detectors: Design and experimental characterization. *Nuclear Instruments and Methods in Physics Research Section A: Accelerators, Spectrometers, Detectors and Associated Equipment*, 770:155–163, 2015.

[105] R Campana, Y Evangelista, F Fuschino, M Ahangarianabhari, D Macera, G Bertuccio, M Grassi, C Labanti, M Marisaldi, P Malcovati, A Rachevski, G Zampa, N Zampa, L Andreani, G Baldazzi, E Del Monte, Y Favre, M Feroci, F Muleri, I Rashevskaya, A Vacchi, F Ficorella, G Giacomini, A Picciotto, and M Zuffa. Characterization of the vega asic coupled to large area position-sensitive silicon drift detectors. *Journal of Instrumentation*, 9(08):P08008–P08008, August 2014.

[106] G. Dilillo, E. J. Marchesini, G. Baroni, G. Della Casa, R. Campana., Y. Evangelista, A. Guzmán, P. Hedderman, P. Bellutti, G. Bertuccio, F. Ceraudo, M. Citossi, D. Cirrincione, I. Dedolli, E. Demenev, M. Feroci, F. Ficorella, M. Fiorini, M. Gandola, M. Grassi,

G. La Rosa, G. Lombardi, P. Malcovati, F. Mele, P. Nogara, A. Nuti, M. Perri, S. Pliego-Caballero, S. Pirrotta, S. Puccetti, I. Rashevskaya, F. Russo, G. Sottile, C. Tenzer, M. Trenti, S. Trevisan, A. Vacchi, G. Zampa, N. Zampa, and F. Fiore. The ground calibration of the HERMES-Pathfinder payload flight models. *arXiv e-prints*, page arXiv:2410.06056, October 2024.

[107] M. Grassi, M. Gandola, F. Mele, G. Bertuccio, P. Malcovati, F. Fuschino, R. Campana, C. Labanti, M. Fiorini, Y. Evangelista, R. Piazzolla, M. Feroci, G. Zampa, N. Zampa, A. Rachevski, P. Bellutti, G. Borghi, E. Demenev, F. Ficorella, A. Picciotto, N. Zorzi, I. Rashevskaya, A. Vacchi, F. Fiore, and L. Burderi. X-/γ-ray detection instrument for the hermes nano-satellites based on sdds read-out by the lyra mixed-signal asic chipset. In *2020 IEEE International Instrumentation and Measurement Technology Conference (I2MTC)*, pages 1–6, 2020.

[108] Microchip Technology Inc. *Chip-Scale Atomic Clock (CSAC) SA.45s User's Guide*, 2022. Available at: `https://www.microchip.com/en-us/product/CSAC-SA45S#document-table`.

[109] Paolo Nogara, Giuseppe Sottile, Francesco Russo, Giovanni La Rosa, Fabio Paolo Lo Gerfo, Melania Del Santo, Yuri Evangelista, Riccardo Campana, Fabio Fuschino, and Fabrizio Fiore. The power supply unit onboard the HERMES nano-satellite constellation. In *Space Telescopes and Instrumentation 2022: Ultraviolet to Gamma Ray*, volume 12181, pages 1396–1410. SPIE, 2022.

[110] A Guzman, S Pliego, J Bayer, Y Evangelista, G La Rosa, G Sottile, S Curzel, R Campana, F Fiore, F Fuschino, et al. The Payload Data Handling Unit (PDHU) on-board the HERMES-TP and HERMES-SP CubeSat Missions. In *Space Telescopes and Instrumentation 2020: Ultraviolet to Gamma Ray*, volume 11444, pages 844–854. SPIE, 2020.

[111] Francesca Scala, Giovanni Zanotti, Serena Curzel, Mirela Fetescu, Paolo Lunghi, Michèle Lavagna, and Roberto Bertacin. The hermes mission: A cubesat constellation for multi-messenger astrophysics. In *5th IAA Conference on University Satellite Missions and CubeSat Workshop*, Roma, Italy, January 2020.

[112] Riccardo Campana, Giulia Baroni, Giovanni Della Casa, Giuseppe Dilillo, Ezequiel J. Marchesini, Francesco Ceraudo, Alejandro Guzman, Paul Hedderman, and Yuri Evangelista. Calibration of the first detector flight models for the HERMES constellation and the SpIRIT mission. *Society of Photo-Optical Instrumentation Engineers (SPIE) Conference Series*, 2022.

[113] Mazziotta et al. Electron–hole pair creation energy and fano factor temperature dependence in silicon. *Nuclear Instruments and Methods in Physics Research Section A: Accelerators, Spectrometers, Detectors and Associated Equipment*, 584(2):436–439, 2008.

[114] G.F. Knoll. *Radiation Detection and Measurement*. Wiley, 2010.

[115] M. Yoneyama, J. Kataoka, M. Arimoto, T. Masuda, M. Yoshino, K. Kamada, A. Yoshikawa, H. Sato, and Y. Usuki. Evaluation of GAGG:ce scintillators for future space applications. *Journal of Instrumentation*, 13(02):P02023–P02023, feb 2018.

[116] G. Dilillo, E.J. Marchesini, G. Della Casa, G. Baroni, R. Campana, E. Borciani, S. Srivastava, S. Trevisan, F. Ceraudo, M. Citossi, Y. Evangelista, A. Guzmán, P. Hedderman, C. Labanti, E. Virgilli, and F. Fiore. The HERMES calibration pipeline: mescal. *Astronomy and Computing*, 46:100797, January 2024.

[117] S. Puccetti, M. Perri, R. Campana, E. Marchesini, G. Baroni, G. Dilillo, Y. Evangelista, A. Sanna, L. Burderi, and F. Fiore. HERMES SOC activities at the ASI space science data center (SSDC). In Chris R. Benn, Antonio Chrysostomou, and Lisa J. Storrie-Lombardi, editors, *Society of Photo-Optical Instrumentation Engineers (SPIE) Conference Series*, volume 13098 of *Society of Photo-Optical Instrumentation Engineers (SPIE) Conference Series*, page 130980O, July 2024.

[118] Michele Trenti, Miguel Ortiz del Castillo, Robert Mearns, Jack McRobbie, Clint Therakam, Airlie Chapman, Andrew Woods, Jonathan Morgan, Simon Barraclough, Ivan Rodriguez Mallo, Giulia Baroni, Fabrizio Fiore, Yuri Evangelista, Riccardo Campana, Alejandro Guzman, and Paul Hedderman. Spirit mission: In-orbit results and technology demonstrations, 2024.

[119] University of Melbourne. Spirit — space industry – responsive – intelligent – thermal nanosatellite, 2025. Accesso: 28 ottobre 2025.

[120] G. Baroni, R. Campana, Y. Evangelista, A. Guzmán, P. Hedderman, G. Dilillo, E. J. Marchesini, G. Della Casa, M. Trenti, J. McRobbie, R. Mearns, M. Ortiz Del Castillo, M. Thomas, C. Therakam, A. Chapman, S. Pirrotta, S. Puccetti, M. Perri, A. Santangelo, W. Leone, S. Trevisan, M. Citossi, and F. Fiore. The commissioning and early operations of the high-energy HERMES payload onboard SpIRIT. In Jan-Willem A. den Herder, Shouleh Nikzad, and Kazuhiro Nakazawa, editors, *Space Telescopes and Instrumentation 2024: Ultraviolet to Gamma Ray*, volume 13093 of *Society of Photo-Optical Instrumentation Engineers (SPIE) Conference Series*, page 130935O, August 2024.

[121] PUC RIO. LUA the programming language. `https://www.lua.org`, 2024.

[122] Melody Pallu, Damien Pailot, Eric Bréelle, Philippe Laurent, Jérôme Carron, François Lebrun, Charbel Koumeir, Claude Chapron, and Kévin Biernacki. Studies of gagg:ce scintillators for space missions dedicated to terrestrial gamma-ray flashes and gamma-ray bursts observation. *Nuclear Instruments and Methods in Physics Research Section A: Accelerators, Spectrometers, Detectors and Associated Equipment*, 1069:169997, 2024.

[123] Riccardo Campana, Fabio Fuschino, Yuri Evangelista, Giuseppe Dilillo, and Fabrizio Fiore. The hermes-tp/sp background and response simulations. In *Space Telescopes and Instrumentation 2020: Ultraviolet to Gamma Ray*, volume 11444, pages 817–824. SPIE, 2020.

[124] F. Fiore, M. Trenti, Y. Evangelista, R. Campana, G. Baroni, F. Ceraudo, M. Citossi, G. Della Casa, G. Dilillo, M. Feroci, M. Fiorini, G. Ghirlanda, C. Labanti, G. La Rosa, E. J. Marchesini, G. Morgante, L. Nava, P. Nogara, A. Nuti, M. Perri, F. Russo, G. Sottile, M. Lavagna. A. Colagrossi, S. Silvestrini, M. Quirino, M. Bechini, L. Bianchi, A. Brandonisio, F. De Cecio, A. Dottori, I. Troisi, G. Bertuccio, F. Mele, B. Negri, R. Bertacin, C. Grappasonni, R. Piazzolla, S. Pirrotta, S. Puccetti, M. Rinaldi, A. Tiberia, L. Burderi, A. Sanna, A. Riggio, C. Cabras, A. Tsvetkova, A. Santangelo, A. Guzman, P. Hedderman, S. Pliego Cagallero, C. Tenzer, A. Vacchi, N. Zampa, R. Crupi, P. Bellutti, E. Demenev, F. Ficorella, D. Novel, G. Pepponi, A. Picciotto, N. Zorzi, M. Grassi, P. Malcovati, T. Di Salvo, W. Leone, S. Trevisan, I Rashevskaya, A. Rachevski, G. Zampa, T. Chen, N. Gao, S. Xiong, S. Yi, S. Zhang, M. Ortiz del Castillo, R. Mearns, J. McRobbie, A. Chapman, M. Thomas, A. Woods, J. Morgan, S. Barraclough, N. Werner, J. Ripa, F. Munz, A. Pal, D. Gacnik, A. Hudrap, D. Selkan, and G. Molera Calves. HERMES Pathfinder & SpIRIT: a progress report. *arXiv e-prints*, page arXiv:2502.17952, February 2025.

[125] John Robert Brucato, Michèle Roberta Lavagna, and Fabrizio Fiore. TASTE mission - a smallaste and miniaturized lander to Deimos. In *45th COSPAR Scientific Assembly*, volume 45, page 175, July 2024.

[126] I. Adler, J. Gerard, J. Trombka, R. Schmadebeck, P. Lowman, H. Blodget, L. Yin, E. Eller, R. Lamothe, P. Gorenstein, P. Bjorkholm, B. Harris, and H. Gursky. The Apollo 15 x-ray fluorescence experiment. *Lunar and Planetary Science Conference Proceedings*, 3:2157, January 1972.

[127] I. Adler, J. I. Trombka, P. Lowman, R. Schmadebeck, H. Blodget, E. Eller, L. Yin, R. Lamothe, G. Osswald, J. Gerard, P. Gorenstein, P. Bjorkholm, H. Gursky, B. Har-

ris, J. Arnold, A. Metzger, and R. Reedy. Apollo 15 and 16 Results of the Integrated Geochemical Experiment. *Moon*, 7(3-4):487–504, September 1973.

[128] M Grande, R Browning, N Waltham, D Parker, S.K Dunkin, B Kent, B Kellett, C.H Perry, B Swinyard, A Perry, J Feraday, C Howe, G McBride, K Phillips, J Huovelin, P Muhli, P.J Hakala, O Vilhu, J Laukkanen, N Thomas, D Hughes, H Alleyne, M Grady, R Lundin, S Barabash, D Baker, P.E Clark, C.D Murray, J Guest, I Casanova, L.C d'Uston, S Maurice, B Foing, D.J Heather, V Fernandes, K Muinonen, S.S Russell, A Christou, C Owen, P Charles, H Koskinen, M Kato, K Sipila, S Nenonen, M Holmstrom, N Bhandari, R Elphic, and D Lawrence. The d-cixs x-ray mapping spectrometer on smart-1. *Planetary and Space Science*, 51(6):427–433, 2003.

[129] M. Grande, B.J. Maddison, C.J. Howe, B.J. Kellett, P. Sreekumar, J. Huovelin, I.A. Crawford, C.L. Duston, D. Smith, M. Anand, N. Bhandari, A. Cook, V. Fernandes, B. Foing, O. Gasnaut, J.N. Goswami, A. Holland, K.H. Joy, D. Kochney, D. Lawrence, S. Maurice, T. Okada, S. Narendranath, C. Pieters, D. Rothery, S.S. Russell, A. Shrivastava, B. Swinyard, M. Wilding, and M. Wieczorek. The c1xs x-ray spectrometer on chandrayaan-1. *Planetary and Space Science*, 57(7):717–724, 2009.

[130] Charles E. Schlemm, Richard D. Starr, George C. Ho, Kathryn E. Bechtold, Sarah A. Hamilton, John D. Boldt, William V. Boynton, Walter Bradley, Martin E. Fraeman, Robert E. Gold, John O. Goldsten, John R. Hayes, Stephen E. Jaskulek, Egidio Rossano, Robert A. Rumpf, Edward D. Schaefer, Kim Strohbehn, Richard G. Shelton, Raymond E. Thompson, Jacob I. Trombka, and Bruce D. Williams. *The X-ray Spectrometer on the MESSENGER Spacecraft*, pages 393–415. Springer New York, New York, NY, 2007.

[131] G.W. Fraser, J.D. Carpenter, D.A. Rothery, J.F. Pearson, A. Martindale, J. Huovelin, J. Treis, M. Anand, M. Anttila, M. Ashcroft, J. Benkoff, P. Bland, A. Bowyer, A. Bradley, J. Bridges, C. Brown, C. Bulloch, E.J. Bunce, U. Christensen, M. Evans, R. Fairbend, M. Feasey, F. Giannini, S. Hermann, M. Hesse, M. Hilchenbach, T. Jorden, K. Joy, M. Kaipiainen, I. Kitchingman, P. Lechner, G. Lutz, A. Malkki, K. Muinonen, J. Näränen, P. Portin, M. Prydderch, J. San Juan, E. Sclater, E. Schyns, T.J. Stevenson, L. Strüder, M. Syrjasuo, D. Talboys, P. Thomas, C. Whitford, and S. Whitehead. The mercury imaging x-ray spectrometer (mixs) on bepicolombo. *Planetary and Space Science*, 58(1):79–95, 2010. Comprehensive Science Investigations of Mercury: The scientific goals of the joint ESA/JAXA mission BepiColombo.

[132] J. O. Goldsten. The NEAR X-Ray/Gamma-Ray Spectrometer. *Johns Hopkins APL Technical Digest*, 19(2):126–135, June 1998.

[133] T. Okada, K. Shirai, Y. Yamamoto, T. Arai, K. Ogawa, K. Hosono, and M. Kato. X-Ray Fluorescence Experiments of Asteroid Itokawa by the XRS Onboard Hayabusa. In *37th Annual Lunar and Planetary Science Conference*, Lunar and Planetary Science Conference, page 1596, March 2006.

[134] R. A. Masterson, R. Binzel, J. Grindlay, B. Allen, and J. Hong. The REXIS (Regolith X-Ray Imaging Spectrometer) Student Experience: From Concept to Operation. In *AAS/Division for Planetary Sciences Meeting Abstracts #52*, volume 52 of *AAS/Division for Planetary Sciences Meeting Abstracts*, page 413.05, October 2020.

[135] L. R. Nittler, R. D. Starr, L. Lim, T. J. McCoy, T. H. Burbine, R. C. Reedy, J. I. Trombka, P. Gorenstein, S. W. Squyres, W. V. Boynton, T. P. McClanahan, J. S. Bhangoo, P. E. Clark, M. E. Murphy, and R. Killen. X-ray fluorescence measurements of the surface elemental composition of asteroid 433 Eros. *Meteoritics & Planetary Science*, 36(12):1673–1695, December 2001.

[136] M. Kobayashi, N. Hasebe, T. Miyachi, M. Fujii, E. Shibamura, O. Okudaira, Y. Karouji, M. Hareyama, T. Takashima, S. Kobayashi, C. d'Uston, S. Maurice, N. Yamashita, and Robert C. Reedy. The Kaguya gamma-ray spectrometer: instrumentation and in-flight performances. *Journal of Instrumentation*, 8(4):P04010, April 2013.

[137] Meng-Hua Zhu, Tao Ma, and Jin Chang. Chang'E-1 gamma ray spectrometer and preliminary radioactive results on the lunar surface. *Planetary and Space Science*, 58(12):1547–1554, October 2010.

[138] W. V. Boynton, W. C. Feldman, I. Mitrofanov, J. I. Trombka, J. R. Arnold, P. A. J. Englert, A. E. Metzger, R. C. Reedy, S. W. Squyres, C. D'Uston, H. Wänke, J. Brückner, D. M. Drake, L. G. Evans, R. Starr, C. Shinohara, and F. S. Anderson. Expected Performance and Initial Results From The 2001 Mars Odyssey Gamma Ray Spectrometer (grs) Instrument Suite. In *EGS General Assembly Conference Abstracts*, EGS General Assembly Conference Abstracts, page 6602, January 2002.

[139] John O. Goldsten, Edgar A. Rhodes, William V. Boynton, William C. Feldman, David J. Lawrence, Jacob I. Trombka, David M. Smith, Larry G. Evans, Jack White, Norman W. Madden, Peter C. Berg, Graham A. Murphy, Reid S. Gurnee, Kim Strohbehn, Bruce D. Williams, Edward D. Schaefer, Christopher A. Monaco, Christopher P. Cork, J. Del Eckels, Wayne O. Miller, Morgan T. Burks, Lisle B. Hagler, Steve J. Deteresa, and Monika C. Witte. The MESSENGER Gamma-Ray and Neutron Spectrometer. *Space Science Reviews*, 131(1-4):339–391, August 2007.

[140] SPIE. Ultra-bright scintillators for planetary gamma-ray spectroscopy. `https://spie.org/news/6162-ultra-bright-scintillators-for-planetary-gamma-ray-spectroscopy`, October 2015. Accessed: 21-Oct-2025.

[141] T. H. Prettyman, J. J. Hagerty, R. C. Elphic, W. C. Feldman, D. J. Lawrence, G. W. McKinney, and D. T. Vaniman. Elemental composition of the lunar surface: Analysis of gamma ray spectroscopy data from lunar prospector. *Journal of Geophysical Research: Planets*, 111(E12), 2006.

[142] N. Yamashita, O. Gasnault, O. Forni, C. d'Uston, R.C. Reedy, Y. Karouji, S. Kobayashi, M. Hareyama, H. Nagaoka, N. Hasebe, and K.J. Kim. The global distribution of calcium on the moon: Implications for high-ca pyroxene in the eastern mare region. *Earth and Planetary Science Letters*, 353-354:93–98, 2012.

[143] K. Dennerl. Discovery of X-rays from Mars with Chandra. *Astronomy & Astrophysics*, 394:1119–1128, November 2002.

[144] K. Dennerl, C. M. Lisse, A. Bhardwaj, V. Burwitz, J. Englhauser, H. Gunell, M. Holmström, F. Jansen, V. Kharchenko, and P. M. Rodríguez-Pascual. First observation of Mars with XMM-Newton. High resolution X-ray spectroscopy with RGS. *Astronomy & Astrophysics*, 451(2):709–722, May 2006.

[145] J. A. Berger, R. Gellert, M. E. Schmidt, N. Boyd, E. Desouza, D. W. Ming, C. O'Connell-Cooper, E. B. Rampe, L. M. Thompson, S. VanBommel, and A. Yen. Elevated Zinc and Germanium Discovered by Curiosity's APXS in the Murray Formation of Gale Crater, Mars, Indicate Hydrothermal Enrichment and Possible Diagenetic Fractionation. In *AGU Fall Meeting Abstracts*, volume 2017 of *AGU Fall Meeting Abstracts*, pages P33B–2873, December 2017.

[146] David J. Lawrence, Patrick N. Peplowski, Andrew W. Beck, Morgan T. Burks, Nancy L. Chabot, Michael J. Cully, Richard C. Elphic, Carolyn M. Ernst, Samuel Fix, John O. Goldsten, Erin M. Hoffer, Hiroki Kusano, Scott L. Murchie, Brian C. Schratz, Tomohiro Usui, and Zachary W. Yokley. Measuring the Elemental Composition of Phobos: The Mars-moon Exploration with GAmma rays and NEutrons (MEGANE) Investigation for the Martian Moons eXploration (MMX) Mission. *Earth and Space Science*, 6(12):2605–2623, December 2019.

[147] Filippo Mele, Marco Grassi, Irisa Dedolli, Piero Malcovati, Riccardo Campana, Ettore Del Monte, Yuri Evangelista, Marco Feroci, and Giuseppe Bertuccio. The front-end charge readout ic for the lem-x mission concept. In Maurizio Valle, Paolo Gastaldo, and

Ernesto Limiti, editors, *Proceedings of SIE 2024*, pages 170–176, Cham, 2025. Springer Nature Switzerland.